



**Synthesis, Electrochemical and Electrocatalytic  
Properties of Transition Metal Complexes based  
on Cyclohexane-Supported *bis*-Imino Pyridines**

A thesis submitted to the University of East Anglia

For the degree of Doctor of Philosophy

Submitted September 2017

**Simon Nicholas Child**

Energy Materials Laboratory

School of Chemistry

Norwich

This copy of the thesis has been supplied on the condition that anyone who consults it is understood to recognise that its copyright rests with the author and that use of any information derived there from must be in accordance with current UK Copyright Law. In addition, any quotation or extract must include full attribution.

## Abstract

This thesis concerns the design and synthesis of transition metal complexes based on cyclohexane-supported *bis*-imino pyridines for use as electrocatalysts for hydrogen evolution, towards the aim of renewable energy storage.

To investigate the effect of secondary coordination interactions on electrochemistry and electrocatalytic response to protons, a series of transition metal complexes with the same fundamental *bis*-imino pyridine chelating groups, but with different ligand backbones of cyclohexane and cyclohexanol were synthesised. Two isomers of the cyclohexanol ligands were synthesised giving the hydroxyl groups positioned either distal or proximal to the metal centre, due to the conformational lock that occurs on metal coordination.

Coordination of these ligands to metal salts of Zn, Mn, Co, Ni and Cu gives a range of geometries. Ligands with no hydroxyl group (**10**, **L1**) or a distal (*trans*) hydroxyl (**5**, **L2**) both give octahedral geometries, whereas a proximal (*cis*) alcohol (**9**, **L3**) gives trigonal prismatic geometry for Zn, Mn and Co, but square-pyramidal geometry for Cu.

All of the complexes synthesised were shown to give rich electrochemistry, largely due to the redox non-innocent *bis*-imino pyridine ligands. The presence or absence and position of the hydroxyl group are shown to have a large effect on the cyclic voltammetry. This includes evidence for molecular motion involving the interconversion between different geometries: specifically trigonal prismatic and octahedral or square-based pyramidal.

Electrocatalysis is focused on the series of cobalt complexes as these were shown to give the largest response to acetic acid. Catalytic parameters,  $\eta$ , and  $\text{TOF}_{\text{max}}$ , of the cobalt complexes follow a trend in increasing  $\eta$  and  $\text{TOF}_{\text{max}}$  from the propane backbone, to cyclohexane backbone, to the distal cyclohexanol, to the proximal cyclohexanol. However bulk electrolysis of **CoL3N** with acetic acid indicates that proton reduction to hydrogen is not the primary electrocatalytic process for this complex, and suggests reduction of solvent. Future studies must address the nature of this process, and unambiguously establish those of the other complexes.

## Acknowledgements

First, I would like to thank my supervisor, Dr. John Fielden, for his guidance, inspiration over the duration of this research, his day-by-day guidance and supporting help during my research and writing this thesis.

I would like to thank the past and the present members of the Fielden group, Pickett group, and Wright group, especially Dr. Joseph Wright, Dr. Hani El Moll, Dr. Anil Reddy, Dr. Trevor Simmons and Dr. Ahmed Al-Yasari for their friendship, guidance, support and assistance in the laboratory.

I would also like to thank Dr. John Fielden, Dr. Hani El Moll, Dr David Hughes and the National Crystallography Service for solving crystal structures with this work.

I would like to thank Ben Howchen and Adam Sach for the complexes **CoL4N**, **CoL1B**, **CoL3B** and **CoL4B** which were synthesised under my guidance and supervision during their undergraduate MChem projects.

Many thanks to my great friend Chris Prior for taking the time to meander round the lake at lunch, and our endless discussions on a wide range of topics, and also for his DFT calculations.

I would also like to thank the University sailing club and its members for the fun and happy memories together over the years.

Thanks to all my family and friends who have supported me in various ways over the years.

Lastly I would very much like to thank my girlfriend, Emily, for her endless love, patience and support.

## Contents

1	Introduction	11
1.1	Background for research	12
1.2	Renewable energy resources	14
1.3	Energy storage	15
1.3.1	Energy storage methods	16
1.3.2	Batteries	16
1.3.3	Chemical Fuels	19
1.4.1	Water splitting for energy storage	20
1.4.2	Overview of Electro-Catalysts for water splitting	22
1.4.3	Operating Potential	23
1.5	Natural Systems for hydrogen evolution and synthetic functional models	24
1.6	Molecular catalyst based on earth abundant metal cobalt for hydrogen evolution	26
1.7	Proton coupled electron transfer, proton relays and thermodynamics of protonation	30
1.8	Proton reduction catalysts with organic ligands incorporating proton relays in the secondary coordination sphere	32
1.9	Homogenous proton reduction catalysts with organic ligands incorporating proton relays in the outer coordination sphere.	34
1.10	Hangman Cobalt and Nickel Porphyrins	35
1.11	The Coordination Complexes of 1,3,5-substituted cyclohexanes and their Catalytic Properties	37
1.12	Outline and Aims of Thesis	40
2.0	<b>Chapter 2</b>	42
2.1	Synthesis	43
2.1.1	Overview of ligand synthesis	43
2.1.2	Synthesis of 5, L2	44
2.1.3	Synthesis of 9, L3	45
2.1.4	Synthesis of 18, L4 and 10, L1	47
2.2	Ligands Based on a <i>cis</i> , <i>cis</i> -triaminocyclohexane core: demonstration of synthetic feasibility	48
2.2.1	Route 1: Protection of <i>cis</i> -TACH	48
2.2.2	Route 2: Via <i>cis</i> -1,3-dihydroxy- <i>trans</i> -5-amino cyclohexane	50
2.3	NMR of cyclohexanes	53
2.3.1	Coupling constants	53

2.3.2	Steric Compression	54
2.3.3	Axial and Equatorial Cyclohexane Shifts	54
2.4	<sup>1</sup> H-NMR Spectroscopy and characterisation of L4	55
2.5	<sup>1</sup> H-NMR Spectroscopy of Cyclohexane based Ligands	57
2.6	<sup>1</sup> H-NMR Spectroscopy of <i>cis</i> -TACH based products and precursors	60
3.0	<b>Chapter 3</b>	66
3.1	Synthesis of Metal Complexes	67
3.1.1	Cobalt complexes	69
3.1.2	Non- coordinating anion – BF <sub>4</sub>	70
3.1.3	Characterisation and synthesis of cobalt(II) tetrafluoroborate complexes	71
3.2	Crystal structures	74
3.2.1	X-ray crystal structures of cobalt complexes	75
3.2.2	X-ray crystal structures of copper complexes	78
3.2.3	X-ray crystal structures of zinc complexes	80
3.2.4	Manganese x-ray crystal structures	81
3.2.5	Nickel x-ray crystal structures	83
3.3	Octohedral versus trigonal prismatic geometry	84
3.4	<sup>1</sup> H- NMR of diamagnetic zinc complexes	88
3.4.1	<sup>1</sup> H- NMR of diamagnetic zinc complexes aliphatic region	88
3.4.2	<sup>1</sup> H- NMR of diamagnetic zinc complexes: aromatic region	91
3.5	Paramagnetic NMR	92
3.5.1	Introduction to paramagnetic NMR	92
3.5.2	Paramagnetic NMR assignment	93
3.5.3	Paramagnetic <sup>1</sup> H -NMR of CoL3N, CoL2N, and CoL1N.	96
3.5.4	Comparison of paramagnetic NMR of nitrate and tetrafluoroborate complexes	101
4.0	<b>Chapter 4 Electrochemistry of coordination complexes</b>	106
4.1.1	Electrochemistry introduction – General aspects of electrochemistry Cyclic voltammetry	107
4.1.2	Explanation of a cyclic voltammogram	110
4.1.3	Electrochemical reversibility	111

4.1.4	Effect of scan rate	112
4.1.5	Diagnostic criteria of reversible and irreversible systems	113
4.1.6	Temperature dependence	114
4.2	Electrochemistry of metal complexes with redox non-innocent ligands	115
4.2.1	Redox non-innocent ligands - $\alpha$ -iminopyridines	115
4.2.2	Series of comparable bis( $\alpha$ -iminopyridine)metal complexes	117
4.3	Understanding electrochemistry through computation: Density Functional Theory (DFT)	118
4.4.1	Electrochemistry of iminopyridine ligand	119
4.4.2	Electrochemistry of Zinc complexes – ZnL1N, ZnL2N and ZnL3N	121
4.4.3	Electrochemistry of Manganese complexes – MnL1N, MnL2N and MnL3N	129
4.4.4	Electrochemistry of Nickel complex - NiL2C	135
4.4.5	Electrochemistry of Copper complexes – CuL1N, CuL2n and CuL3N	137
4.5.1	Spin cross over in cobalt complexes	141
4.5.2	Electrochemistry of Cobalt complexes	142
4.5.3	Effect of adding distal hydroxyl ‘proton relay’ to the cyclohexane backbone	146
4.5.4	Effect of adding proximal hydroxyl ‘proton relay’ to the cyclohexane backbone	147
4.5.5	Effect of going from non-coordinating BF <sub>4</sub> to coordinating nitrate	148
4.5.6	Effect of rigidity going from propane to cyclohexane backbone	150
4.5.7	DFT and cyclic voltammetry of CoL1N	151
4.5.8	DFT and cyclic voltammetry of CoL2N	152
4.5.9	DFT and cyclic voltammetry of CoL3N	154
4.6.1	Electronic communication between redox centres	157
5.0	<b>Chapter 5 Electrocatalysis</b>	160
5.1	Introduction to electrocatalysis	161
5.2	Screening of Complexes for Activity in Electrocatalytic Proton Reduction	166
5.2.1	Cobalt complexes	166
5.2.2	Copper complexes	168
5.2.3	Manganese complexes	171
5.2.4	Nickel complex	173
5.2.5	Aqueous buffered studies of CoL2N	174
5.3.0	Electrocatalysis using cobalt complexes at GCE	178

5.3.1	Electrocatalysis using cobalt complexes at GCE – nitrate complexes	179
5.3.2	Electrocatalysis using cobalt complexes at GCE - Tetrafluoroborate complexes	188
5.4.1	Boron Doped Diamond (BDD) background	194
5.4.2	Electrochemistry with Boron Doped Diamond (BDD)	196
5.5.1	Electrocatalysis of CoL1N, CoL2N and CoL3N at BDD electrode	197
5.6.0	Bulk electrolysis using CoL3N catalyst at BDD	205
5.6.1	Conclusions from initial bulk electrolysis studies and further work	210
6.0	<b>Chapter 6</b>	213
6.1	Conclusions	214
6.2	Further work	215
7.0	<b>Chapter 7</b>	217
7.1.1	Materials	218
7.1.2	Methods	218
7.1.3	DFT methods	219
7.1.4	Instrumentation	219
7.1.5	Compound numbering	220
7.1.6	Notation for NMR, MS and IR spectra	220
7.1.7	A note on the purity of imine ligands	221
7.1.8	Electrochemical methods	221
7.1.9	Preparation of [NBu <sub>4</sub> ] [BF <sub>4</sub> ] electrolyte	222
7.2.0	Ligand synthesis	223
7.2.1	<i>cis</i> - 1,3-Ditosyloxy- <i>trans</i> -5-hydroxycyclohexane (1) and <i>cis</i> - 1,3-dihydroxy-5-tosylooxycyclohexane	223
7.2.2	<i>cis</i> - 3,5-Diazido- <i>trans</i> -hydroxycyclohexane (3)	224
7.2.3	<i>cis</i> - 3,5-Diamino- <i>trans</i> -hydroxycyclohexane (4)	224
7.2.4	<i>cis</i> - 3,5-Bis[2-Pyridinylenaemin]- <i>trans</i> -hydroxycyclohexane (5, L2)	225
7.2.5	<i>cis</i> , <i>cis</i> -3,5-Diazidocyclohexyl benzoate (6)	226
7.2.6	<i>cis</i> -3,5-Diazido- <i>cis</i> -hydroxycyclhexane (7)	227
7.2.7	<i>cis</i> -3,5-Diamino- <i>cis</i> -hydroxycyclohexane (8)	227
7.2.8	<i>cis</i> -3,5-Bis[2-Pyridinyleneamin]- <i>cis</i> -hydroxycyclohexane (9, L3)	228
7.2.9	<i>cis</i> -1,3-Bis[2-Pyridinyleneamin] cyclohexane (10, L1)	229

7.2.10	<i>cis</i> -1,3-Dihydroxy- <i>trans</i> -5-azidocyclohexane (11)	229
7.2.11	<i>cis</i> -1,3-Dihydroxy- <i>trans</i> -5-aminocyclohexane (12)	230
7.2.12	<i>cis</i> -3,5-Dihydroxy- <i>trans</i> -cyclohexylaminocyclohexane (13)	231
7.2.13	<i>cis</i> -3,5-Ditosyloxy- <i>trans</i> -cyclohexylaminocyclohexane hydrochloride (14)	232
7.2.14	<i>cis</i> -3,5-Diazido- <i>cis</i> -cyclohexylaminocyclohexane (15)	233
7.2.15	<i>cis</i> -3,5-Diamino- <i>cis</i> -cyclohexyl-cyclhexylanime (16)	234
7.2.16	<i>cis</i> -3,5-Bis[2-Pyridinyleneamin]- <i>cis</i> -(aminocyclohexyl)-cyclohexane (17)	234
7.2.17	N,N-Bis[2-pyridylmethylene]-1,3-diaminopropane (, L4 18)	235
7.3.0	Metal complex synthesis	236
7.3.1	Synthesis of CoB	236
7.3.2	Synthesis of CoL4B	236
7.3.3	Synthesis of CoL1B	237
7.3.4	Synthesis of CoL3B	237
7.3.5	Synthesis of CoL4N	238
7.3.6	Synthesis of CoL1N	239
7.3.7	Synthesis of CoL2N	239
7.3.8	Synthesis of CoL3N	240
7.3.9	Synthesis of MnL1N	241
7.3.10	Synthesis of MnL2N	241
7.3.11	Synthesis of MnL3N	242
7.3.12	Synthesis of CuL1N	243
7.3.13	Synthesis of CuL2N	243
7.3.14	Synthesis of CuL3N	244
7.3.15	Synthesis of ZnL1N	245
7.3.16	Synthesis of ZnL2N	246
7.3.17	Synthesis of ZnL3N	247
7.3.18	Synthesis of NiL2C	248
	<b>References</b>	249



## Abbreviations

GtCO <sub>2</sub>	Gigatons of carbon dioxide
DC	direct current
b.p.	Boiling point
BDD	boron doped diamond
CI <sup>+</sup> -MS	Positive ion chemical ionisation mass spectrometry
<i>cis,cis</i> -DAHC	<i>cis</i> -3,5-Diamino- <i>cis</i> -hydroxycyclohexane
<i>cis,trans</i> -DAHC	<i>cis</i> -3,5-Diamino- <i>trans</i> -hydroxycyclohexane
<i>cis</i> -TACH	<i>cis</i> -1,3,5-Triaminocyclohexane
COSY	Correlated spectroscopy
CSD	Cambridge Structural Database
CV	Cyclic voltammetry
Cys	Cystine amino acid
DEPT	Distortionless enhancement by polarisation transfer
DEAD	Diethyl azodicarboxylate
DFT	Density functional theory
DMF	Dimethylformamide
DMFH <sup>+</sup>	Protonated dimethylformamide
EPR	Electron paramagnetic resonance
ESI <sup>+</sup> -MS	Positive ion electrospray mass spectrometry
Et <sub>2</sub> O	Diethyl ether
FAB <sup>+</sup> -MS	Positive ion fast atom bombardment mass spectroscopy
Fc/Fc <sup>+</sup>	Ferrocene/ ferrocenium couple
GCE	Glassy carbon electrode
HER	Hydrogen evolution reaction
HOMO	Highest occupied molecular orbital
HS	High spin

IR	Fourier transform infrared spectroscopy
LS	Low spin
LUMO	Lowest unoccupied molecular orbital
MALDI	Matrix-assisted laser desorption ionisation
MeOH	Methanol
NHE	Normal hydrogen electrode
ORTEP	Oakridge Thermal Ellipsoid Plotter
PCET	Proton-coupled electron transfer
RCSC	Redox coupled spin cross-over
rt	Room temperature
SCE	Saturated calomel electrode
SOJT	Second order Jahn-Teller distortions
TBAF	Tetrabutylammonium fluoride
TBDMS	<i>tert</i> -Butyldimethylsilyl
TBDMSCl	<i>tert</i> -Butyldimethylsilyl chloride
TEA	Triethylamine
TLC	Thin layer chromatography
TM	Transition metal
TMS	Tetramethylsilane
TOF	Turn over frequency
TOF <sub>max</sub>	Maximum turn over frequency
Tosyl, OTs	<i>para</i> -Toluenesulfonyl

# Chapter 1

## *Introduction*

*“I’d put my money on the sun and solar energy. What a source of power!*

*I hope we don’t have to wait until oil and coal run out before we tackle that.”*

Thomas Edison in conversation with Henry Ford and Harvey Firestone – (1931).<sup>1</sup>

## 1.1 Background for research

The influence of humans on the climate is clear. The recent anthropogenic emissions of greenhouse gases are the highest in human history.<sup>2</sup> These recent changes in the climate are having widespread impacts on human and natural systems. Warming of the climate system is explicit, and since the 1950s, many of the observed changes are unprecedented over global history. The atmosphere and ocean have warmed, the amount of snow and ice has diminished, ocean acidity has increased and sea levels have risen.<sup>2</sup>

The globally averaged combined land and ocean surface temperature data, as calculated by a linear trend, show a warming of 0.85 [0.65 to 1.06] °C, over the period from 1880 to 2012.<sup>2</sup> Anthropogenic greenhouse gas emissions have increased dramatically since the pre-industrial era, largely driven by economic, technological and population growth. Anthropogenic greenhouse gas (GHG) emissions, since the pre-industrial era, have driven large increases in the atmospheric concentrations of carbon dioxide (CO<sub>2</sub>), methane (CH<sub>4</sub>) and nitrous oxide (N<sub>2</sub>O). Between 1750 and 2011, cumulative anthropogenic CO<sub>2</sub> emissions to the atmosphere were 2040 ± 310 GtCO<sub>2</sub> (UN climate change panel IPCC: n×10<sup>12</sup> tonnes of CO<sub>2</sub> equivalent (GtCO<sub>2</sub> eq)). About 40% of these emissions have remained in the atmosphere (880 ± 35 GtCO<sub>2</sub>); the rest removed from the atmosphere and stored on land (in plants and soils) and in the ocean. The ocean has absorbed about 30% of the emitted anthropogenic CO<sub>2</sub>, causing ocean acidification.<sup>2</sup>

The concentrations of carbon dioxide (CO<sub>2</sub>), methane (CH<sub>4</sub>) and nitrous oxide (N<sub>2</sub>O) have increased since 1750 by 40%, 150% and 20%, respectively, with roughly half of the anthropogenic CO<sub>2</sub> emissions between 1750 and 2011 occurring in the last 40 years. Their effects, together with those of other anthropogenic drivers, have been detected throughout the climate system and are the only credible factor to have been the dominant cause of the observed warming since the mid-20th century.<sup>2</sup>

Continued emission of greenhouse gases will cause further warming and long-lasting changes in all components of the climate system, increasing the likelihood of severe,

pervasive and irreversible impacts for people and ecosystems. Surface temperature is projected to rise over the 21st century under all assessed emission scenarios. It is very likely that heat waves will occur more often and last longer, and that extreme precipitation events will become more intense and frequent in many regions. The ocean will continue to warm and acidify, and global mean sea level to rise. Climate change will amplify existing risks and create new risks for natural and human systems. Risks are unevenly distributed and are generally greater for disadvantaged people and communities in countries at all levels of development. Without additional mitigation efforts beyond those in place today, and even with adaptation, warming by the end of the 21st century will lead to high risk of severe, widespread, and irreversible impacts globally.

In 2013 the world's energy consumption was estimated to be 108,150 TWh (where 1 TWh = 0.086 Mtoe; 9301 Mtoe),<sup>3</sup> with fossil fuels accounting for 81.4% and the other 18.6% from nuclear and renewables such as biofuels and waste, hydroelectric, solar, wind and geothermal.<sup>4</sup> Global energy needs are projected to double by mid-century and triple by the turn of the century even with an increase in appliance efficiencies.<sup>5,6</sup> The main driver of this growth is the projected growth of population from 7.1 billion in 2013 to 9.7 billion by 2050.<sup>7</sup> In addition to the 2.6 billion new people, another 3 billion people in the Third World will be seeking a higher standard of living.<sup>8</sup>

World fossil fuel reserves are finite and their extraction is becoming more challenging.<sup>9,10</sup> It is clear that a shift from fossil fuels to sustainable renewable carbon-neutral sources is needed over the next few decades to give near zero emissions of CO<sub>2</sub> and other greenhouse gases and provide political, environmental, and economic security. Delivering the additional energy needed to the world by 2050 is not a simple task, however. Most energy sources are insufficient to keep pace with the world's appetite for energy.<sup>11,12</sup>

## 1.2 Renewable energy resources

Energy source	Max. power/ TW
Total surface solar	85,000
Desert solar	7,650
Ocean thermal	100
Wind	72
Geothermal	44
River hydroelectric	7
Biomass	7
Open ocean wave	7
Tidal wave	4
Costal wave	3

**Table 1.1** Power available from renewable sources<sup>10</sup>

Nuclear fission, and commercially viable nuclear fusion, are possible energy resources, however they both have problems associated with them. Nuclear fission is embedded with economic uncertainty, hidden costs and safety concerns as well as limited uranium resources at reasonable extraction cost; it also only has the ability to supply a fraction of our energy requirements.<sup>10</sup> Fusion seems optimistic by 2050, as there are still a number of technical problems. Even if these are solved, obtaining an adequate supply of tritium (obtained from industrially and commercially valuable lithium<sup>10,13</sup>) at an acceptable cost will be challenging.

As shown in **table 1.1** there are a number of renewable energy resources suitable to provide the world with energy. Biomass, however, is limited as an energy resource due to the inefficiency of photosynthesis.<sup>14</sup> As an example, if all the biomass on the planet was in the form of sugar cane, which is the most efficient at converting solar energy into biomass at 8% (most crops and plants are 0.1-0.2% efficient), only 7 TW of energy would be obtained from its combustion with the needless reintroduction of greenhouse gases.<sup>10</sup>

Hydroelectric power is an excellent source of clean energy providing 20% of the world's electricity, and there is room for expansion as only a quarter of the world's 45,000 dams are exploited for hydroelectricity.<sup>15</sup> This is limited, however, by the availability of strategic waterways and has the potential to damage aquatic ecosystems.<sup>16</sup> Geothermal sources are reliable and cost-effective, providing 1 GW of power worldwide, and do not have the intermittency problems found with some renewables such as wind power. Only a fraction of the maximum potential is feasible, however, as energy is very diffuse and thus unrecoverable.<sup>17</sup> Wind power is increasingly used as a renewable energy source especially in colder climates producing 456 GW of energy worldwide in 2016.<sup>18</sup> It has a large potential maximum energy, however, in practise it is likely to only expand to a fraction of this owing to a number of factors that restrict possible locations such as bird fatalities,<sup>19</sup> the distance from highly populated areas and sites of natural beauty, and positioning turbines in areas of consistent wind patterns. Other problems include noise, intermittency and unpredictability of supply, sudden surges, and mechanical failure.<sup>10</sup>

By far the biggest renewable source of energy is solar, which dwarfs world anthropogenic energy consumption. The sun's 166 TW,<sup>10</sup> is more than 10,000 times the world energy consumption of 16.2 TW in 2007.<sup>8</sup> The surface solar energy drops to half, however, as 19% is absorbed by the clouds and another 30% reflected back into space. This is still, however, 5000 times more than the world energy consumption. This excess in energy means that solar energy makes a lot of economic sense, as conversion inefficiencies can be more than compensated for by nonrecurring costs of more solar collectors.<sup>10</sup> The major challenge confronting the deployment of solar energy and most other renewable energy sources on a large scale is storage - society relies on a continuous energy supply, and solar energy is diurnal and subject to intermittency arising from the variable atmospheric conditions. An inexpensive storage method is required for solar to become a large contributor to the primary energy supply.<sup>8</sup>

### **1.3 Energy storage**

There are two extremes of energy storage: large-scale centralised storage (the grid) and small-scale decentralised storage. Centralised storage makes the grid more stable and reliable by stabilising short term fluctuations. It also allows energy to be supplied to meet demand by permitting load shifts, allowing excess energy to be stored through periods of

high energy input, and distribute energy in periods of low energy input. Decentralised storage gives the same benefits as centralised storage, with the addition that energy is stored near the site of demand, providing greater reliability due to the non-linear transmission and distribution losses. In addition, small scale, highly distributed energy generation and storage is thought to be of great importance to the distribution of energy in the Third World, where infrastructure is not already in place, due to the large cost of transmission and distribution hardware required.<sup>8</sup> Decentralised renewable energy may also be the key for the world in terms of sustainability. As the energy is harvested, stored and used all at the same source, energy usage is self-regulating.

### **1.3.1 Energy storage methods**

There are a number of energy storage methods adapted to solar, wind and the other renewable energies. Fundamentally, these break down into potential energy, and chemical energy storage. Potential energy storage methods include pumped-hydroelectric, compressed air, electric charge in super/ultra-capacitors, superconducting magnetic energy storage (SMES), flywheel energy storage of kinetic energy (FES), and thermal energy. Here, we focus on chemical methods: batteries, and fuels - they are the most commonly used for centralised and decentralised storage over a range of storage time scales and most relevant to the research undertaken from a chemical perspective.

### **1.3.2 Batteries**

Batteries are the most common electrochemical energy storage technology at present. In a battery, electrons flow in an external circuit from the anode to the cathode. To maintain neutrality, cations also flow in the same direction but along a separate path within the electrolyte; so that the battery does not short circuit. The flow of electrons and cations during the batteries discharge allows for external work energy. Energy storage is achieved by reversing the electron and cation flow by applying an external energy source in the form of DC electricity.

Batteries are however, fairly low energy density storage device, but as shown from the theoretical limiting energy densities of **table 2** there is room for improvement. In a battery, the electrons must reside on atoms within the anode and cathode. The volume the



electron and cation occupy, and that for transference of charge is limited by the physical density of the materials composing the cathode, anode and electrolyte. Some of the lightest elements and hence the lowest physical densities are already used and consequently storage capacity can be expected to soon reach a ceiling. For instance, lithium is the third lightest element, and therefore its use in batteries leads to increased energy densities. All liquid batteries and metal-air batteries (metals = zinc, magnesium, lithium) have the highest theoretical energy densities due to the reduction of oxygen from the atmosphere at the cathode, which therefore gives a low physical density. Thus, most advances in batteries are from new architectural designs of anode and cathode, giving increases in power densities; the rate at which energy can be extracted and cycle life: the number of charge/discharge cycles until power output reaches 80%.<sup>20</sup>

Batteries are described in terms of the cell reactions on discharge, the open circuit potential for a charged cell, and the maximum energy density based on the cell reactions and mass of active material. **Table 2.1** gives the characteristics of various battery technologies receiving the widest attention for storage of renewable energy.<sup>21,22</sup>

Battery	Anode	Cathode	Potential/ V	Energy density/ Wh Kg <sup>-1</sup> (Theoretical limiting energy densities)	Cycle life
<b>Lead-acid</b>	$\text{Pb} + \text{SO}_4^{2-} \rightarrow \text{PbSO}_4 + 2\text{e}^-$	$\text{PbO}_2 + 4\text{H}^+ + \text{SO}_4^{2-} + 2\text{e}^- \rightarrow \text{PbSO}_4 + 2\text{H}_2\text{O}$	2.1	35 (252)	800
<b>Nickel-alkaline</b>	$\text{M} + 2\text{OH}^- \rightarrow \text{M}(\text{OH})_2 + 2\text{e}^-$	$2\text{NiO}(\text{OH}) + 2\text{H}_2\text{O} + 2\text{e}^- \rightarrow 2\text{Ni}(\text{OH})_2 + 2\text{OH}^-$			
	M = Cd		1.3	35 (240-300)	700-2000
	M = Zn		1.6	70-120 (240-300)	500
	M = Fe		1.4	30-50 (240-300)	3000
	Or				
	$2\text{MH} + \text{OH}^- \rightarrow 2\text{M}^+ + \text{H}_2\text{O} + 2\text{e}^-$		1.2	75(240-300)	600-1000
	Or				
	$\text{H}_2 + 2\text{OH}^- \rightarrow 2\text{H}_2\text{O} + 2\text{e}^-$		1.2	60 (240-300)	6000
<b>Lithium-ion</b>	$\text{LiC}_6 \rightarrow \text{Li}^+ + \text{e}^-$	$\text{MO}_x + \text{Li}^+ + \text{e}^- \rightarrow \text{LiMO}_x$	2.5 - 4.5	150 (400)	1200
<b>High T-sodium</b>		(M = Co, Ni, Mn, V)			
	$2\text{Na} \rightarrow 2\text{Na}^+ + 2\text{e}^-$	$2\text{Na}^+ + 2\text{e}^- + \text{xS} \rightarrow \text{Na}_2\text{S}_x$	2.1	170 (750-790)	1800
		Or			
<b>Liquid flow</b>		$2\text{Na}^+ + 2\text{e}^- + \text{NiCl}_2 \rightarrow \text{Ni} + 2\text{NaCl}$	2.6	115	
	$\text{Zn} \rightarrow 2\text{Zn}^{2+} + 2\text{e}^-$	$\text{Br}_2 + 2\text{e}^- \rightarrow 2\text{Br}^-$	1.3		1000
	Or	Or			
<b>Metal-air</b>	$\text{V}^{2+} \rightarrow \text{V}^{3+} + \text{e}^-$	$\text{VO}^{2+} + 2\text{H}^+ + \text{e}^- \rightarrow \text{VO}^{2+} + \text{H}_2\text{O}$	1.6	29	
	$\text{Zn} \rightarrow 2\text{Zn}^{2+} + 2\text{e}^-$	$\text{O}_2 + 2\text{H}_2\text{O} + 4\text{e}^- \rightarrow 4\text{OH}^-$	1.2	300	0

Data taken from refs 21 and 22, Theoretical limiting energy densities/ Wh Kg<sup>-1</sup>; metal – air, Li 13000, Cd 4600, Mg 6800, Al 8100, Zn 1300, Fe 1200 (note: these quoted energy densities do not correct for the weight of the metal oxide product at the cathode; when this is included, the energy density of all of these metal air batteries are greatly reduced).

**Table 1.2** Characteristics of various battery technologies receiving the widest attention for storage of renewable energy<sup>21,22</sup>

### 1.3.3 Chemical Fuels

Chemical fuels are the best storage medium for renewable energies, having the highest energy densities of all the renewable storage sources, and covering the whole range of time scales for storage. These high-energy densities are achieved through the storage of electrons in the small space (the scale of ångström) as chemical bonds between light elements (i.e. H-H, C-H, and N-H etc). Hydrogen (H<sub>2</sub>) has the largest energy density by mass (143 MJ kg<sup>-1</sup>) but suffers in volumetric energy density because it is a gas at standard temperature and pressure. Therefore, it is best used for stationary energy storage, or large-scale transportation such as ships and trains, therefore, has its place in the future for energy storage.<sup>8</sup>

Hydrogen as a renewable energy storage medium from water splitting gives additional benefits, in terms of water security. ‘Dirty’ water (waste, polluted, sea water) could be split into hydrogen and oxygen which are both gases and very thus easily separable from the ‘dirty’ source. If this hydrogen is then consumed in a sterile environment to release energy, clean potable water can be obtained. These benefits, particularly in Third World countries, could have potential to greatly improve the quality of life, and help to stem issues of water scarcity coupled with global warming and climate change.

Hydrocarbon fuels, however, have optimum energy supply in terms of energy density by mass and volume. This, in combination with the availability of fossil fuels, is the basis of the choice of hydrocarbon fuels in present society. The key however, is to switch from hydrocarbon based source, obtained from oil and gas deposits, to a renewable energy storage medium, where renewable energy is converted into hydrocarbons to store the energy as required. The use of hydrocarbons as a storage medium may also provide the additional benefit of carbon dioxide sequestration, as for example solar energy could be stored as methanol or another hydrocarbon fuel by the reduction of carbon dioxide from the atmosphere and direct sources. The atmosphere presents a challenge due to the low atmospheric CO<sub>2</sub> concentration of <0.1%, however, its possibility is illustrated by nature in plants using RuBisCO.<sup>23</sup> This would then allow control of equilibria within the carbon cycle. This effectively allows control of carbon dioxide as a greenhouse gas, through the sequestration of more carbon dioxide than is required for energy needs and giving a

method to reverse the emission of green-house gases and thus global warming and climate change.

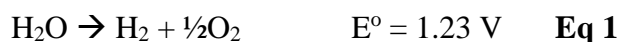
The reduction of carbon dioxide to methanol or another such hydrocarbon fuel as opposed to hydrogen could also give some additional benefits in term of transportation and intermediate infrastructure. As being liquid fuels they are easy to handle, and have high volumetric energy density and energy density. Current infrastructure can also be used allowing for a progression, rather than building whole new systems and thus a more economically friendly green energy transition. However, clean hydrogen production is a likely first step which then enables access to hydrocarbons via Fisher-Tropsch chemistry.<sup>24</sup>

#### **1.4.1 Water splitting for energy storage**

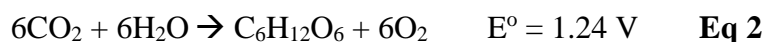
There are a number of methods of water splitting; renewable energy in the form of DC electricity from transducers of solar, wind and other renewable energy resources is used by an electrolyser containing catalysts for hydrogen evolution and oxygen evolution. For example, solar hydrogen production can be achieved by two main approaches: artificial photosynthesis is achieved either by *indirect* solar fuel conversion, where separated electron-hole pairs give a potential difference provided by a photovoltaic cell connected to an external electrolyser of water oxidation and reduction catalysts, or by *direct* solar fuel conversion approach, (monolithic devices), where the water splitting catalysts are integrated with the semiconductor and which capture the photo-generated electron-hole pairs directly, such as in Nocera's artificial leaf.<sup>25</sup> For either *direct* or *indirect* approaches the catalysts use the electron-hole pairs generated to mediate the PCET reactions of water splitting.<sup>8</sup>

Most of the energy that sustains life has been stored in the form of chemical fuels via photosynthesis, including all the fossil fuel reserves. Photosynthesis is the process in which solar energy is stored as organic compounds (such as sugars) and oxygen by the conversion of carbon dioxide and water. Natural photosynthesis, and water splitting, both start with oxidation of water.

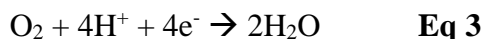
Reduction potential for water splitting:



Reduction potential for carbon dioxide fixation to carbohydrates:

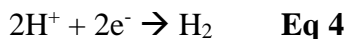


Half reaction for water oxidation:



$$E_{\text{anodic}} = 1.23 \text{ V} - 0.059 (\text{pH}) \text{ V vs NHE} \quad \text{Eq 3a}$$

Half reaction for proton reduction:



$$E_{\text{cathodic}} = 0 \text{ V} - 0.059 (\text{pH}) \text{ V vs NHE} \quad \text{Eq 4a}$$

On an electron equivalent basis the production of carbohydrate stores only 0.01 eV more energy than water splitting, as shown by **Eq 2**, and therefore the main storage of energy comes from water splitting. The carbohydrate, however, acts as a convenient storage medium for the hydrogen produced from water splitting.

Water splitting is thus a key reaction for renewable energy storage as a fuel. The first and most difficult step is oxidation of water, where four O-H bonds of two water molecules must be broken and a double O=O bond formed. The four electrons and protons released from this process may be combined to give two molecules of H<sub>2</sub>, or combined with CO<sub>2</sub> to produce organic molecules; such as alcohols, carbohydrates, and other such hydrocarbons. Combustion of the fuel obtained gives the energy when required and completes the energy cycle.<sup>26</sup>

Water splitting to H<sub>2</sub> and O<sub>2</sub> as shown in **Eq 1** appears as if it should be a pH independent reaction. However, it is comprised of two separate proton-coupled electron transfer (PCET) half reactions, shown in **Eq 3** and **Eq 4**. As shown by equations **Eq 3a** and **4a**, water splitting stores 237 kJ mol<sup>-1</sup> (at 298 K and 1 atm).<sup>8</sup> If however, the electrons were uncoupled from the protons, the reaction would be confined to one electron steps. For example, in the hydrogen evolution reaction, the proton is reduced by a single electron to produce an H• radical with the energy cost of 2.3V vs NHE. The addition of the second electron and second proton give the H<sub>2</sub> and the release of 2.3 V. This thermodynamically neutral process would have a large kinetic barrier (activation energy) of 2.3 V.<sup>8</sup>

Proton-coupled electron transfer (PCET) is a term introduced in 1981 to describe an elementary step, like electron transfer or proton transfer, but in which electrons and protons are transferred together.<sup>27-29</sup> Photosynthesis is a remarkable example of PCET in action with the transfer of 24 e<sup>-</sup> and 24 H<sup>+</sup> from *ca.* 48 photons, storing *ca.* 10<sup>18</sup> kilojoules of energy as carbon based fuels annually.<sup>30</sup>

#### 1.4.2 Overview of Electro-Catalysts for Water Splitting

Research into catalysts for **Eq (3)** and **(4)** can be split up into two main categories molecular catalysts (homogenous) and extended solids (heterogeneous catalysts), however, there are also intermediate cases, such as, when homogenous catalysts are immobilised on surfaces.<sup>31</sup> This work will focus on homogenous electrocatalysts for water/ proton reduction **Eq (4)**. Electrocatalysts can be described by two main parameters: the kinetic parameter indicated by the turn-over frequency (TOF) and the rate of reaction,  $k_{\text{obs}}$ ; and the thermodynamic parameter described by the overpotential ( $\eta$ ). The overpotential is the difference between the applied potential and the thermodynamic potential, the energy required to drive the reaction. A good catalyst would therefore have a high TOF and a small overpotential ( $\eta$ ).

### 1.4.3 Operating Potential

To split water at an appreciable rate, voltages in excess of the thermodynamic potential must be applied. The effective operational photovoltage,  $V_{op}$ , is described by:

$$V_{op} = E_{rev} + \eta_a + |\eta_c| + \eta_{\Omega}$$

Where  $E_{rev}$  is the thermodynamic water splitting potential, and  $\eta_{\Omega}$  is the voltage required to overcome the resistance losses in the cell from solution resistance and contact resistance of the catalyst with the electrode etc.  $\eta_a$  and  $|\eta_c|$  represent the over-potentials required to overcome the kinetic barriers from half reactions **Eq 3** and **4**. Better catalysts and thus lower overpotentials mean that the operational voltage will approach the thermodynamic potential for water splitting, and therefore, the overall efficiency of the processes is improved. When the efficiency of photovoltaic converters and electrolyzers are 20% and 80% respectively, the total efficiency of solar to hydrogen energy is *ca.* 16%.<sup>32,33</sup>

The anodic and cathodic overpotentials come from the activation barriers for the half equations **Eq 3** and **4** occurring at the electrode-solution interface (activation overpotential), and also the limitations from mass transport of reactants and electrocatalyst to and from the electrode. Mass transport limitations can be minimised through cell design.

Platinum based electro-catalysts are generally considered the best catalysts for hydrogen evolution (HER).<sup>34,35</sup> However, platinum is expensive and has low natural abundance, and thus its use in energy storage infrastructure is not commercially viable.<sup>10</sup> The research and development of active, stable and inexpensive electrocatalysts for water splitting is the key to the use of hydrogen as a renewable storage medium.

## 1.5 Natural systems for hydrogen evolution and synthetic functional models

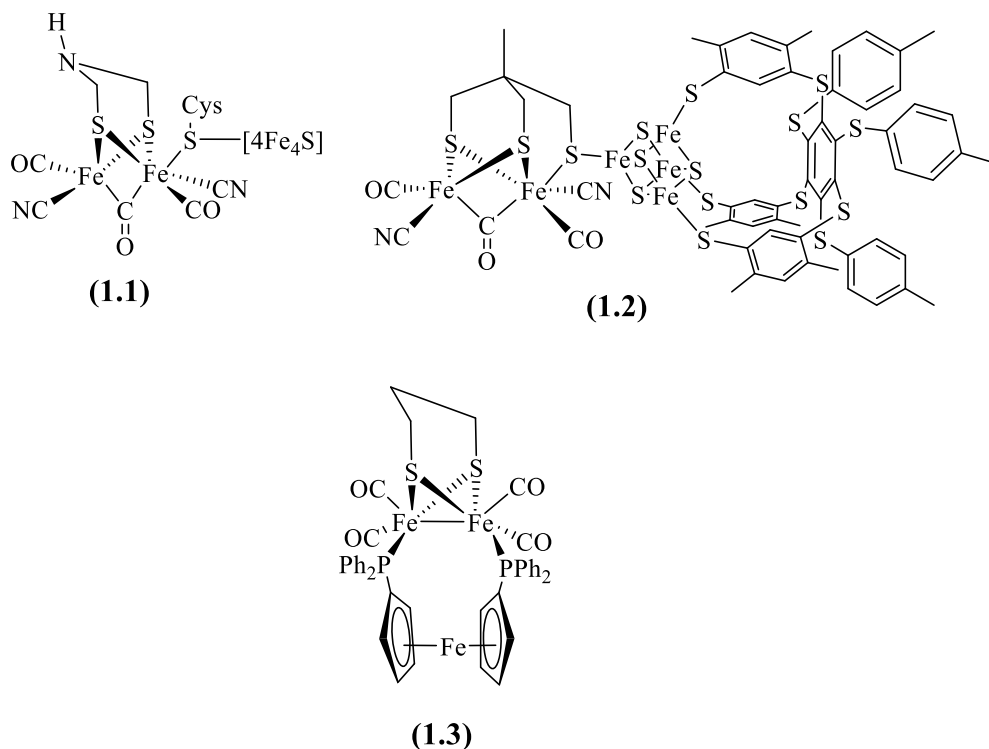


**Figure 1.1** Natural and synthetic functional active site models of the diiron hydrogenase.<sup>36-41</sup>

Nature reduces protons to hydrogen under neutral aqueous conditions using hydrogenase enzymes possessing iron or nickel cofactors. These show TOF of 100–10,000 mol H<sub>2</sub> per mole of catalyst per second at the thermodynamic potential. To achieve these multielectro multiproton transformations, these enzymes use secondary coordination sphere interactions to relay protons and electrons to the active site, stabilising key intermediates and creating a high concentration of electrons and protons around the active centre. The large size of these enzymes and their instability under aerobic ambient conditions, however, mean that their use as catalysts for hydrogen evolution is limited.<sup>36,37</sup> Nevertheless, the study of processes used by nature can be used as a guide through the synthesis of biological mimics to make more active molecular catalysts.

The most studied hydrogenase is the so called [FeFe]H<sub>2</sub>ase, with active site containing a di-iron core as illustrated in (1.1). This can catalyze the reduction of protons to hydrogen, and the oxidation of hydrogen.<sup>36,37</sup> A number of structural and functional active site



models of these have been synthesized with the majority being based on the di-iron systems.<sup>38</sup>

One such functional model was reported by Pickett and co-workers,<sup>39</sup> in which they synthesised an H-cluster analogue consisting of a di-iron subsite linked to a {4Fe4S} cluster illustrated in (1.2). This H-cluster analogue was shown to catalyse proton reduction at diffusion-controlled rate with an  $E_p = -1.33\text{V}$  versus (Ag/AgCl,  $\text{CH}_2\text{Cl}_2$ , 0.45M TBABF<sub>4</sub>, 0.05 TBACl).

Until recently no functional hydrogenase models had shown activity both for the catalytic reduction of protons to hydrogen and the oxidation of hydrogen to protons and electrons. Hogarth and co-workers,<sup>40</sup> however, have shown a di-iron analogue with a ferrocene diphosphine (dppf) ligand, which can catalyse both reduction and oxidation. Redox-active ligands containing ferrocene moiety had been developed previously as substitutes for the [4Fe4S] ferredoxin cluster (1.3).<sup>40,41</sup> In the presence of 1-10 equivalents of HBF<sub>4</sub>•Et<sub>2</sub>O in MeCN (1.3) gives a catalytic proton reduction wave with an  $E_p = -1.70\text{ V}$  vs Fc/Fc<sup>+</sup>. In addition, in the presence of equimolar pyridine in MeCN under H<sub>2</sub> results in an increase in the oxidative peak of the second oxidation process by 10 mA, which reaches 22 mA upon addition of 10 equivalents of pyridine.

## 1.6 Cobalt Based Molecular Catalysts for Hydrogen Evolution

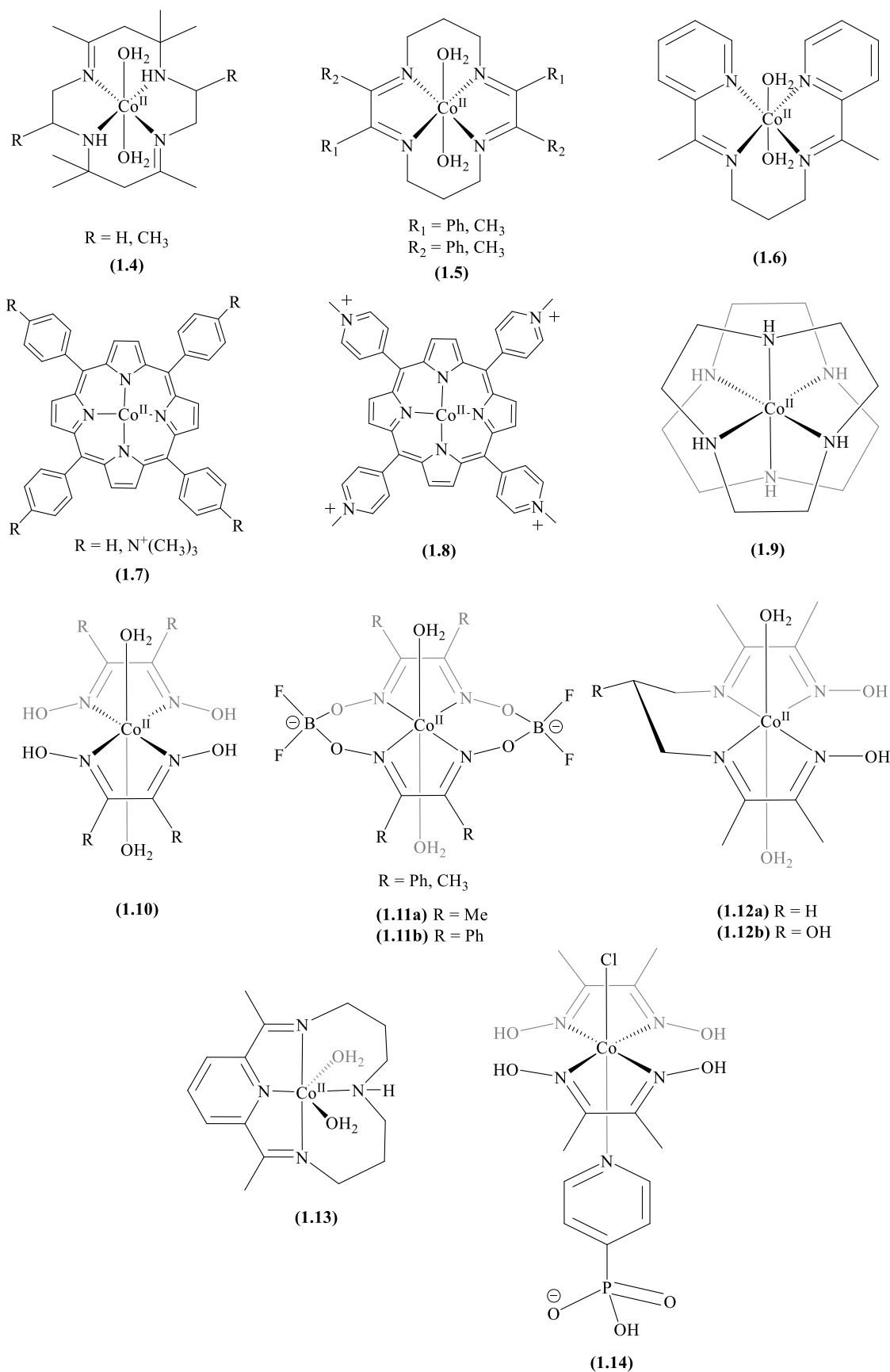


**Figure 1.2** Relevant molecular catalyst based on earth abundant metal cobalt for hydrogen evolution.<sup>48-54</sup>

Some of the most active catalysts known for hydrogen evolution are square-planar macrocyclic or pseudo macrocyclic cobalt complexes; one of the first examples of such molecular hydrogen evolution catalysts were [14]diene-N<sub>4</sub> macrocycle complexes (**1.4**) developed in 1980 by Fisher and Eisenberg,<sup>42</sup> with either a cobalt or nickel metal centre. These have been shown to catalyse the reduction of water to hydrogen at an electrode potential of -1.25 V *vs* NHE, in aqueous solution (water in acetonitrile). The nickel compounds are also competent for carbon dioxide reduction, giving carbon monoxide in a 1:1 ratio to hydrogen in aqueous solution at -1.25 V *vs* NHE. Interestingly, with a completely aliphatic ligand the ratio of carbon monoxide to hydrogen produced was found to be 2:1, suggesting that electronics of these ligands (i.e. the basicity of the metal complex formed) influence selectivity between carbon dioxide and water reductions.

Peters and co-workers<sup>43</sup> more recently developed a number of tetraimine macrocycle based cobalt complexes (**1.5**), which were found to catalyse hydrogen evolution at low overpotentials in acetonitrile. When R<sub>1</sub> and R<sub>2</sub> = methyl, the overpotential ( $\eta$ ) for hydrogen evolution is 380 mV. Furthermore, the study highlights the effect of the electron-withdrawing ability of the ligand framework on electrode potential and the subsequent effects on hydrogen evolution. When R<sub>1</sub> and R<sub>2</sub> = methyl the Co(II/I) redox couple resides at -0.35 V *vs* SCE. However, if R<sub>1</sub> is changed to a phenyl group, which withdraws electron density from the metal centre, the potential shifts ~50 - 60 mV more positive to -0.2 V *vs* SCE. If R<sub>2</sub> is also replaced by phenyl groups, then the potential shifts a further ~50 mV more positive to -0.08 V. However, with increasing substitution for the phenyl groups, the catalyst requires stronger acid to achieve hydrogen evolution. Where R<sub>1</sub> and R<sub>2</sub> are methyl groups, tosylic acid with a pK<sub>a</sub> of 8<sup>3</sup> can be used to achieve hydrogen evolution. However if R<sub>1</sub> is changed for phenyl groups, then a stronger acid HBF<sub>4</sub>·Et<sub>2</sub>O (pK<sub>a</sub> = 0.1) is required to give catalytic hydrogen evolution.

Gray, Peters and co-workers<sup>44</sup> recently reported a cobalt bis(iminopyridine) (**1.6**) which shows high activity for hydrogen evolution from aqueous buffered solutions at pH-independent operating potential of -1.3 V *vs* SCE. Bulk electrolysis at operating potentials of -1.0 and -1.4 V *vs* SCE at pH 2, 5, and 8, gave faradaic efficiencies of up to 90% and TOF's up to 50 L H<sub>2</sub> (mol cat)<sup>-1</sup> (cm<sup>2</sup> Hg)<sup>-1</sup>, with more hydrogen being produced at -1.4

V vs SCE. It was postulated that hydrogen evolution proceeds via a different route depending on the pH, both pathways start and finish in the same way, however, beginning with reduction of  $\text{Co}^{2+}$  and terminating with  $\text{H}_2$  evolution via bimolecular combination or protonation of the Co-H intermediate. At  $\text{pH} \leq 6$ , protonation of  $\text{Co}^{1+}$  is proposed to be the turnover limiting step. At  $\text{pH} \geq 7$ , protonation of  $\text{Co}^{1+}$  was found to be slow on the timescale of the CV experiment, and therefore is not the primary pathway for hydrogen evolution. Instead, it was proposed to be the formation of the doubly reduced complex. In addition it was suggested that a complementary ligand based pathway is in operation at  $\text{pH} \leq 6$ , where hydrogen evolution is faster than ligand decomposition.

Kellet and Spiro,<sup>45</sup> showed that a number of water soluble porphyrin Co(II) complexes (**1.7**) and (**1.8**) can catalyse hydrogen evolution on a mercury drop electrode at -0.71 V vs SHE in 0.1 M trifluoroacetic acid with a faradaic yield of over 90%. They however suffer from adsorption onto electrode surfaces, therefore precluding the proper evaluation of electrode kinetics and mechanism of hydrogen evolution. Refat Abdel-Hamid et al,<sup>46</sup> reported a bis(1,4,7-triazacyclodecane)cobalt (III) complex (**1.9**) which can catalyse hydrogen evolution from Britton-Robinson universal buffers at pH 2 to 10 at -1.29 V vs SHE on a mercury dropping electrode.

Connolly and Espenson in the 1980's reported a cobaloxime system, initially made as a vitamin B<sub>12</sub> mimic,  $\text{Co(II)(dmgBF}_2)_2(\text{H}_2\text{O})_2$  (**1.10**) ( $\text{dmgBF}_2 = (\text{difluoroboryl})\text{dimethylglyoxime}$ ), that catalyses the reduction of protons to hydrogen by  $\text{Cr}^{2+}$  ions at slow rates in acidic aqueous solution. Inner-sphere electron transfer via the chloride ligand was proposed as the rate determining step.<sup>47</sup> Peters, Lewis and co-workers,<sup>48</sup> studied the electrocatalytic hydrogen evolution of methyl and phenyl (**1.10**) cobaloximes in acidic acetonitrile solutions, in the prospect that electron-transfer from a solid-state electrode might be more rapid. Their studies indicated that both catalyse the evolution of hydrogen from a range of acids. Where  $\text{R}=\text{Me}$  (**1.11a**) the complex mediates the production of hydrogen at -0.55 V vs SCE corresponding to the  $\text{Co}^{\text{II/I}}$  redox couple, and when  $\text{R} = \text{Ph}$  the complex (**1.11b**) mediates hydrogen production at -0.28 V vs SCE in acetonitrile solution, using trifluoroacetic acid ( $\text{pK}_a = 12.7$  in acetonitrile).<sup>49</sup> Catalysis was found to occur in the presence of acids with modest (8.7–12.7) to low (0.1)  $\text{pK}_a$  values in acetonitrile. Bulk electrolysis of a 0.5 mM solution of (**1.15a**) in the presence of 45 mM  $\text{CF}_3\text{CO}_2\text{H}$  in 100 mL  $\text{CH}_3\text{CN}$  at -0.72 V consumed 96 coulombs of charge after

1 hour, corresponding to 20 turnovers. The identity of the axially coordinating ligands was found to affect catalysis. With the chloride-bound catalyst for example, the  $\text{Co}^{\text{II/I}}$  redox couple was shown to shift cathodically to -0.8 V vs SCE. The parent  $\text{Co}(\text{dmgH})_2$  (**1.10**) exhibits no electrocatalytic reduction under aqueous conditions within the window of the glassy carbon electrode. However, incorporation of  $\text{BF}_2$  bridges into the macrocycle results in a positive shift of the reduction potential, and gives hydrogen evolution from aqueous solutions. Without the oxime functionality, the tetraamines produce hydrogen at slow rates in 0.25 M HCl.

Peters and co-workers<sup>50</sup> recently reported that two diimine-dioxime cobalt complexes (**1.12a**) and (**1.12b**) which were shown to be efficient homogenous catalysts for hydrogen evolution from acidic aqueous solution, with identical overpotentials of 390 mV, turn over numbers of 23, 18, and faradaic efficiencies of 81% and 80% respectively, over 2 hour bulk electrolysis at -0.93 V vs SCE comparable to that of tetraazamacrocyle complexes<sup>51</sup> and  $\text{Ni}(\text{diphosphine})_2$ <sup>52</sup> complexes in acetonitrile using organic acids. In the same work they also showed that a diiminopyridine macrocycle (**1.13**) is able to catalyse the evolution of hydrogen at an overpotential of 400 mV, a turn over number of 17 and faradaic efficiency of 92%. Interestingly the hydroxyl in (**1.12b**) was incorporated to increase water solubility and doesnot appear to have a major effect on rate or overpotential.

Reisner and co-workers<sup>53,54</sup> described a cobaloxime based complex (**1.14**) which they found to selectively reduce protons to hydrogen under neutral pH in the presence of atmospheric concentration of oxygen. The phosphonic acid group allows water solubility and also immobilisation on to metal oxide surfaces. In the presence (21%  $\text{O}_2$ ) and absence of oxygen (under nitrogen) the complex gave a catalytic current at -0.55 V vs NHE at a glassy carbon working electrode in an aqueous solution of triethanolamine (TEOA) and  $\text{Na}_2\text{SO}_4$  (0.1 M) at pH 7 and 25 °C. No additional waves from the reduction of oxygen were seen, and only a small increase in catalytic current (-25 to -30  $\mu\text{A}$ ), was observed in chronoamperometric studies. There are very few molecular hydrogen evolution catalysts which are known at present to selectively reduce hydrogen in the presence of oxygen. Notably only an expensive ruthenium-based complex based on Wilkinson's catalyst<sup>55</sup> or a cobalt corrole complex.<sup>56</sup>

## 1.7 Proton coupled electron transfer, proton relays and thermodynamics of protonation

As shown in **section 1.4.1**, efficient catalytic hydrogen evolution requires the coupling of electron transfer (ET) and proton transfer (PT) in proton-coupled electron transfer (PCET) reactions. In the absence of PCET, reaction intermediates possess excessively large equilibrium potentials and a kinetic barrier of 2.3 V.<sup>8</sup> PCET, however, shifts the equilibrium potentials of the intermediate redox steps to a narrower potential range, minimising the overpotential to sustain catalysis at a desired turn-over rate.<sup>57,58</sup> PCET reactions may be classified into stepwise and concerted pathways. In concerted proton coupled electron transfers (PCET), the electron and the proton go through a common transition state, whereas in stepwise PCET, ET is followed by PT (ETPT), or PT followed by ET (PTET). Concerted pathways avoid thermodynamically energetic intermediates (high activation energies), however, they may experience kinetic losses associated with proton tunnelling.<sup>59,60</sup>

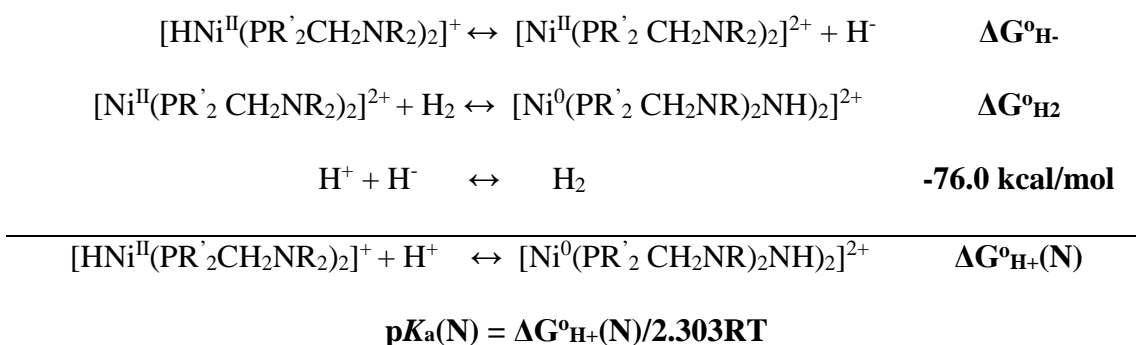
Proton relays are pendant bases or acids within the secondary coordination sphere of an active catalytic centre which can facilitate the transfer of protons between the solution and the catalytic centre.<sup>61</sup> The incorporation of these proton relays into the secondary coordination sphere of catalysts facilitates the transfer of protons, and therefore can give a route for the coupling of proton and electron transfer (PCET) for hydrogen evolution and other such multi-electron proton reactions. For example, in nature; the presence of an amine in the secondary coordination sphere of the di-iron hydrogenase enzymes active site (**1.20**) contributes to the high catalytic activity; as the pendant amine assists in the heterolytic cleavage of H<sub>2</sub> and bond formation by facilitating proton transfer and coupling PCET reactions.<sup>62,61</sup>

It is known that, in comparison to an organic basic site, a metal centre can be slow to protonate. The intrinsic barrier to proton transfers to and from metals (the formation and breaking of M-H bonds) is substantially larger than the barrier to proton transfer to amine bases, for example. Proton self-exchange between amine bases (e.g. aniline/anilinium) typically occurs at diffusion-controlled rates ( $k > 10^9 \text{ M}^{-1} \text{ s}^{-1}$ ), while proton transfer self-exchange from  $\text{HW}(\text{CO})_3\text{Cp}$  to its conjugate base  $[\text{WCO}_3\text{Cp}]^-$ , occurs with a second-order rate constant of  $650 \text{ M}^{-1} \text{ s}^{-1}$  at 298 K in MeCN.<sup>63</sup> A basic site close to the catalytic metal

centre ideally positioned to relay protons to the metal, therefore, can promote the formation of a metal hydride, a key intermediate in hydrogen evolution and oxidation. This has been found to be essential for the reversible oxidation of hydrogen.<sup>64</sup>

An understanding of how a basic site can influence the free energy of the reaction of heterolytic cleavage and therefore formation of hydrogen can be obtained from thermodynamic data of the individual reactions, the sum of their free energies equates to the free energy of the overall reaction ( $\Delta G^\circ$ ).<sup>61</sup> To avoid the formation of high energy intermediates during the oxidation or production of H<sub>2</sub> via a heterolytic route, it is important to match the hydride acceptor ability of the metal with the proton acceptor ability of the base. If the protonated base shows a pK<sub>a</sub> that will complement the hydride acceptor ability of the metal centre ( $\Delta G^\circ_{\text{H-}}$ ), the overall free energy of the reaction ( $\Delta G^\circ$ ) can then be close to zero.<sup>65-67</sup> The thermodynamic cycle to determine the pK<sub>a</sub> values of the protonated pendant amines of DuBois type nickel phosphine systems (explained in detail in **section 1. 8**), is illustrated in **Table 1.3**

**Table 1.3** Thermodynamic cycle for the determining pK<sub>a</sub> values of protonated pendant amines<sup>67</sup>



## 1.8 Proton reduction catalysts with organic ligands incorporating proton relays in the secondary coordination sphere

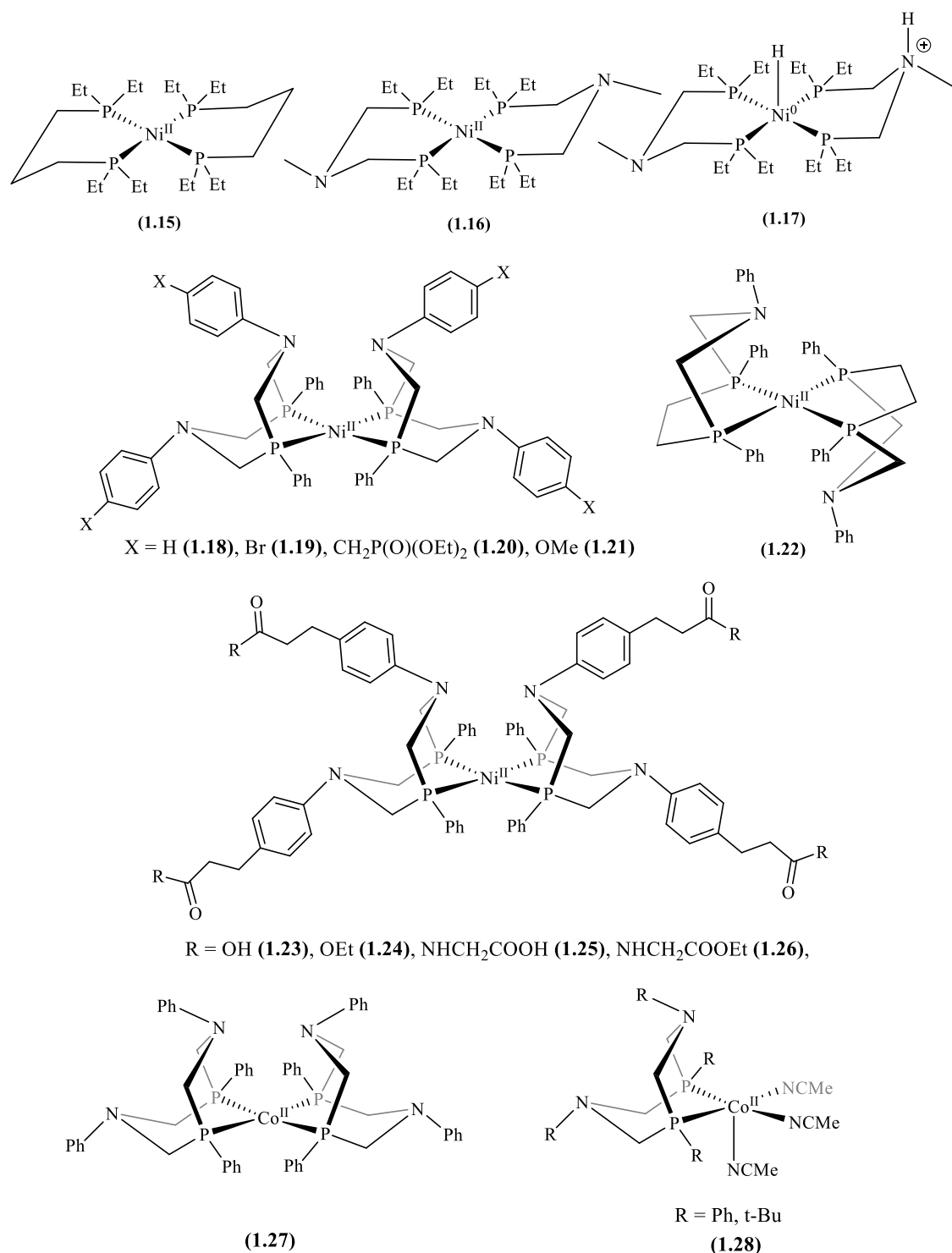


**Figure 1.3** DuBois type proton reduction catalysts with proton relays in their secondary coordination sphere.<sup>69-84</sup>

DuBois and co-workers,<sup>68</sup> taking inspiration from the active site of the [FeFe] hydrogenase enzymes containing a dinuclear iron complex with a bridging azadithiolate ligand, recently developed a series of nickel-based molecular catalysts, in which each



ligand contains two phosphine coordination sites and two non-coordinating amine sites, for electrocatalytic hydrogen production. Although the nature of the dithiolate backbone had not been definitively established at the time of the initial research, subsequent studies found an azadithiolate bridge promotes the shuttling of protons and heterolytic cleavage of dihydrogen.<sup>69-71</sup>

In previous work of the DuBois group investigated the catalytic and thermodynamic properties of some simple diphosphine nickel complexes in acetonitrile.<sup>72-75</sup> It was found that the 1,3-bis(diethylphosphino)propane nickel complex **1.15** slowly oxidises hydrogen at a potential of *ca.* 0.8 V (*vs* the Fc/Fc<sup>+</sup> couple) in the presence of an external base. Furthermore, when a nitrogen base was incorporated into the backbone as in **1.16**, it can readily add hydrogen to give compound **1.17** and improved electrocatalysis with an overpotential of *ca.* 150 mV, and turnover rate of between 0.01 and 0.5 s<sup>-1</sup>. For the electrochemical oxidation of hydrogen at low overpotentials (less than 0.15 V), the enhanced reactivity of (**1.15**) as compared to **1.16** is attributed to facile inter- and intramolecular proton/hydride exchange. X-ray studies of **1.22** found that chair conformation of the six-membered chelate ring is the most stable conformation.<sup>76</sup> However, to allow simultaneous interaction of the nickel and the pendant base with dihydrogen, the ligand must adopt the less stable boat conformation. Therefore, to further optimise the position of the pendant bases in the complex, a cyclic diphosphine ligand was used to force the pendant ligand into the boat conformation such as in **1.18**.

Complex **1.18** also shows a catalytic wave for the reduction of protons at -0.86 V *vs* the Fc/Fc<sup>+</sup> couple in acetonitrile. Bulk electrolysis at -0.94 V *vs* Fc/Fc<sup>+</sup> in acetonitrile solution with triflic acid, gave a faradaic efficiency of 99 % for hydrogen production, and a turn over frequency of 130 moles s<sup>-1</sup> per mole of catalyst. Hydrogen oxidation from an acetonitrile solution purged with 0.8 atm of hydrogen and triethylamine as an external base, exhibited a catalytic wave from the oxidation of hydrogen with a half-wave potential of -0.73 V *vs* Fc/Fc<sup>+</sup> at a rate of 10 s<sup>-1</sup>.<sup>77</sup>

Considerable research into these systems has focused on the variation of the pendant amines as biomimetic proton relays. Recently a group of complexes have been found to have enhanced catalytic activity for proton reduction from acetonitrile solution spiked with water. For example, compound (**1.20**) has found to have a TOF of 500 s<sup>-1</sup> and

overpotential of 320 mV in pure acetonitrile. Spiking the solution with water leads to an increased TOF of  $1850\text{ s}^{-1}$  at an over potential of 370 mV. Compound (**1.21**) was found to reduce protons in acidic ionic liquid water solutions with a TOF of  $> 4 \times 10^4\text{ s}^{-1}$  at an overpotential of 400 mV.<sup>78</sup> The addition of 1.2 M of water to acetonitrile solutions of compound (**1.22**) with only one pendant amine per ligand, held in the right conformation by the seven membered ring, increases the TOF from  $33,000\text{ s}^{-1}$  to  $106,000\text{ s}^{-1}$  at -490 mV vs SHE using protonated dimethylformamide as the acid source.<sup>79</sup>

### **1.9 Homogenous proton reduction catalysts with organic ligands incorporating proton relays in the outer coordination sphere.**

Shaw and co-workers,<sup>80,81</sup> have recently described a series of DuBois catalysts featuring unnatural amino acid (3-(4-aminophenyl)-propionic acid) appendages in their outer coordination spheres as hydrogenase mimics. Preliminary studies focused on amino acid 3-(4-aminophenyl) propionic cyclic diphosphine complex (**1.23**) and its ethyl ester (**1.24**), followed by the incorporation of the simplest amino acid glycine (**1.25**), ethyl ester (**1.26**) and its dipeptide (**1.19**). Results showed a strong dependence on the addition of water and the acid type as shown for other catalysts of the DuBois type.<sup>82</sup> For example, when using *p*-cyanoanilinium as the acid, rates for the peptide catalysts are  $14\text{--}25\text{ s}^{-1}$ . These rates increase an order of magnitude or more when using  $\text{DMFH}^+$ , where the observed rates are  $140\text{--}1000\text{ s}^{-1}$ . Catalytic rates are also observed to show significant enhancement (1.4–7 times faster) when water is added to the acidic solution, protonation of secondary coordination sphere carboxylic acid and amine groups plays an important role in catalytic  $\text{H}_2$  production, possibly by facilitating proton transfer to the active site or increasing proton concentration near the active site. Rates were shown to be faster for larger complexes demonstrating that activity is not hindered by steric effects. This may be due to stabilising effects.

DuBois and co-workers<sup>83,84</sup> have also described the analogous cobalt complex (**1.27**) and its relative with a single cyclic diphosphine ligand (**1.28**). Compound (**1.27**) is not catalytically active towards hydrogen evolution; this is presumably an electronic problem, as cobalt is harder to protonate than nickel, with strong backbonding to the phosphine ligands withdrawing electron density from the metal centres and reducing their basicity.

However, compound (**1.28**) is electrocatalytically active for the production of hydrogen with a TOF of  $90\text{ s}^{-1}$  and overpotential of *ca.* 285 mV, when (R = Ph). This improves to a turnover frequency of  $160\text{ s}^{-1}$  and an overpotential of 160 mV, when R = *t*-Bu, using bromoanilinium tetrafluoroborate as the acid in acetonitrile.

### 1.10 Hangman Cobalt and Nickel Porphyrins

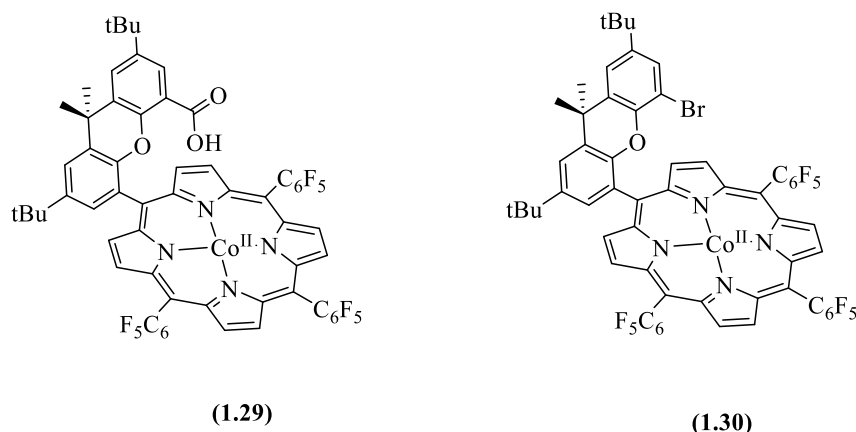


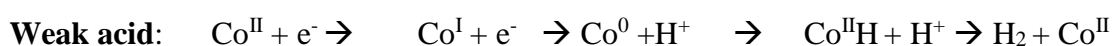
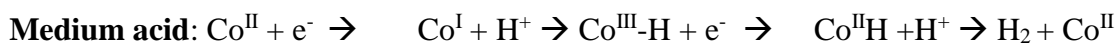
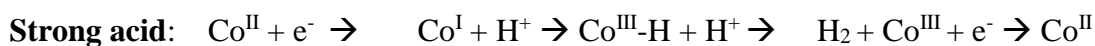
**Figure 1.5** Nocera and co-workers “hangman” porphyrin complexes.

Nocera and co-workers<sup>85</sup> have described a number of “hangman” porphyrins which incorporate a carboxylic acid functionality proximate to the metal centre, competent for hydrogen evolution. In the presence of excess benzoic acid, the complexes (**1.30**) and (**1.29**) have overpotentials of *ca.* 800 mV and *ca.* 680 mV, and faradaic efficiencies of 85 and 80% respectively. The proximal carboxylate allows for a mechanistic evaluation through the stoichiometric control of proton concentration. The acid-base hangman/pendant group permits the facile transfer of a single proton to or from a substrate bound to the metal centre, which gives a *ca.* 200 mV positive shift in potential for the  $\text{Co}^{\text{I}/0}$  couple of (**1.29**) compared to (**1.30**), termed the “hangman” effect. This is where the one electron reduction of  $\text{Co}^{\text{I}}$  in (**1.29**) is followed immediately by proton transfer from the hanging/pendant group to produce  $\text{Co}^{\text{II}}\text{H}$ . In the presence of excess benzoic acid ( $\text{pK}_\text{a} = 20.7$  in acetonitrile), (**1.29**) and (**1.30**) both exhibit catalytic cathodic waves. Analysis showed that  $\text{Co}^{\text{III/I}}$  reduction is not affected by the presence of acid, but the  $\text{Co}^{\text{I}/0}$  reduction which gives a catalytic current. Therefore, it is shown that benzoic acid is too weak to protonate the  $\text{Co}^{\text{I}}$  centre, and therefore catalytic  $\text{H}_2$  production is only observed on further reduction to  $\text{Co}^0$ . The pendant group gives a decrease in overpotential for (**1.29**) of 120 mV compared to (**1.30**) at 3 mM acid concentration. For (**1.29**) the potential of the  $\text{Co}^{\text{I}/0}$

wave is the same in the presence and absence of acid, but shifts by 80 mV negative for (1.30) on increasing acid concentration. In (1.29), proton transfer is not rate-determining for catalysis, whereas in (1.30), the proton transfer is a determinant of the mechanism, for either case, H<sub>2</sub> catalysis is initiated from the Co<sup>II</sup>H state. In the presence of the stronger tosic acid (pK<sub>a</sub> = 8.3 in acetonitrile), both (1.29) and (1.30) exhibit catalytic cathodic waves at *c.a.* -1.5 V, giving almost identical overpotential and catalytic current. This showed that the stronger acid overwhelms the chemistry of the system and the hangman effect is obviated. Unlike for benzoic acid, the Co<sup>II/I</sup> wave becomes irreversible in the stronger tosic acid for both (1.29) and (1.30). This indicates that Co<sup>I</sup> is protonated by the tosic acid. Electrocatalysis for (1.29) and (1.30) occurs at potentials negative of the Co<sup>II/I</sup> couple, indicating that a Co<sup>III</sup>H species formed needs to be further reduced to Co<sup>II</sup>H for H<sub>2</sub> evolution.

Artero and co-workers<sup>86</sup> showed a similar acid dependence on mechanistic redox pathway on the [Co(dmgBF<sub>2</sub>)<sub>2</sub>L] (1.10) where L is DMF or MeCN.

**Table 1.4** Mechanism of hydrogen evolution from [Co(dmgBF<sub>2</sub>)<sub>2</sub>L] (1.15) depending on the acid strength used



The three pathways begin with the reduction of Co<sup>II</sup> to Co<sup>I</sup>, this is owing to the low basicity of the Co<sup>II</sup> complex which would require a very strong acid to protonate. The strong acid *p*-cyanoanilinium tetrafluoroborate (pK<sub>a</sub> = 7.6 in MeCN) causes the appearance of a large irreversible catalytic wave at potentials close to the Co<sup>II/I</sup> redox couple. This shows that it is strong enough to protonate both Co<sup>II</sup> and Co<sup>III</sup>-H. With addition of medium strength acids such as CF<sub>3</sub>COOH in MeCN (pK<sub>a</sub> = 12.7 in MeCN), catalytic behaviour at the Co<sup>II/I</sup> couple is observed, with the introduction of a new cathodic irreversible wave at -1.00 V vs Ag/AgCl which increases with increasing acid concentration corresponding to the reduction of Co<sup>III</sup>-H to Co<sup>II</sup>-H from which hydrogen evolves through reaction of the metal hydride with protons. With the addition of a weak acid such as Et<sub>3</sub>NHCl (pK<sub>a</sub> = 18.7 in MeCN) catalytic current occurs at more negative

potential of -1.43 V vs Ag/AgCl, because only the  $\text{Co}^0$  state is basic enough to be protonated by the weak acid.

### 1.11 The Coordination Complexes of 1,3,5-substituted Cyclohexanes and their Catalytic Properties

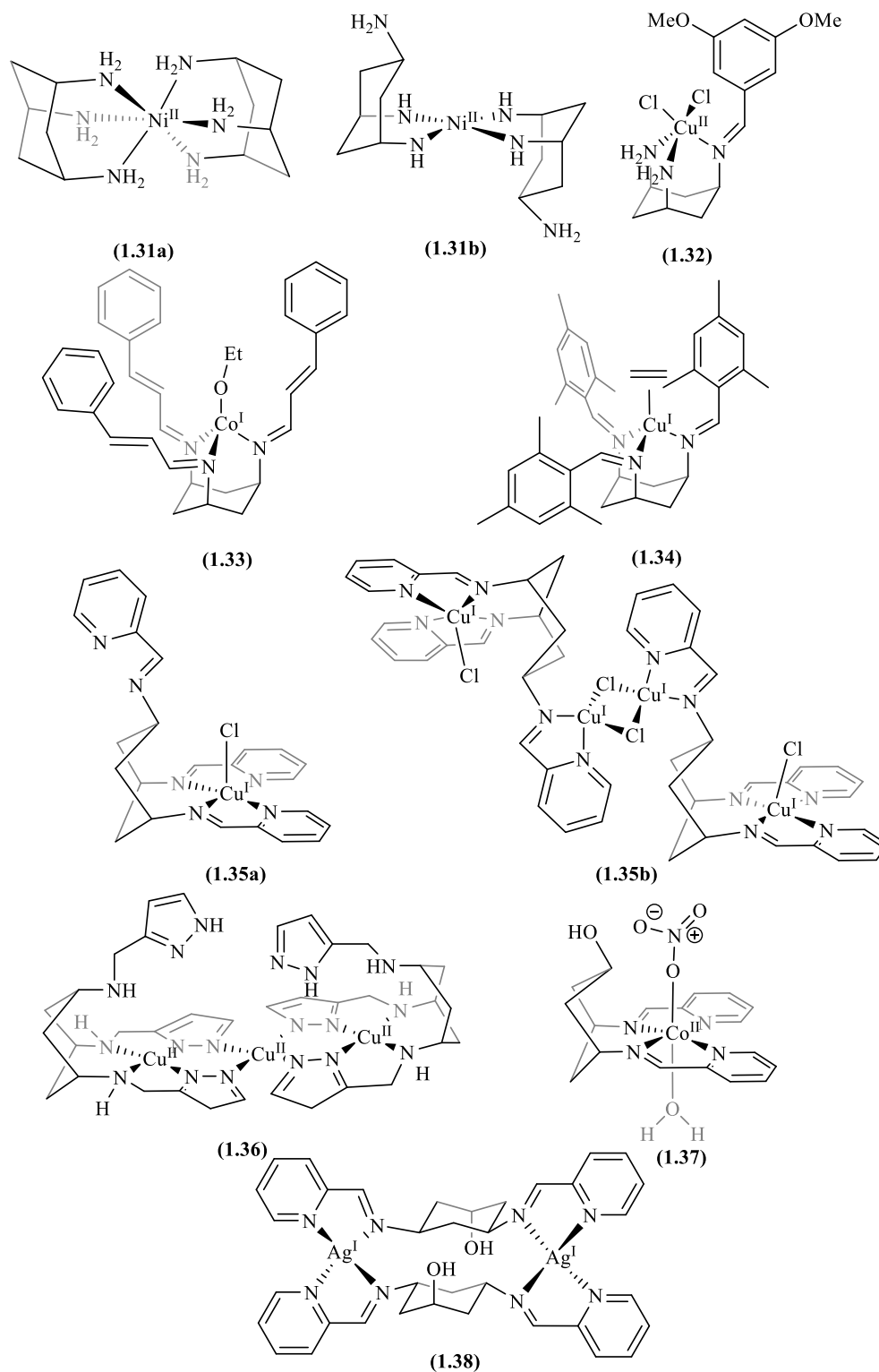


**Figure 1.5** Coordination Complexes of 1,3,5-substituted cyclohexanes

The coordination chemistry of 1,3,5-trisubstituted cyclohexanes and their properties are introduced, as it is an important feature in the work presented, as the cyclohexane backbone allows control of the stereochemistry of substituents, important in governing geometry of the complexes and consequently catalysis.

1,3,5-Substituted cyclohexanes undergo rapid conformational exchange, but if it behaves as a polydentate ligand, can become conformationally locked into a rigid framework upon coordination to a metal centre. These have been shown to give a wide variety of coordination modes, including working models of metalloenzymes, mimicking the secondary coordination sphere of enzyme active sites.

Some of the first 1,3,5 – substituted cyclohexane based ligands were *cis,cis*-1,3,5 – triaminocyclohexane (*cis*-TACH) and *cis,trans*-1,3,5–triaminocyclohexane (*trans*-TACH) illustrated in **(1.31a)** and **(1.31b)** respectively. Which on coordination with nickel(II) salts give two differing homoleptic complexes. In which, *cis*-TACH caps both faces of the nickel's octahedral coordination sphere, whereas the *trans*-TACH complex of nickel, gives a square planar geometry with the non-coordinating '*trans*' pendant amines positioned alternately to eliminate steric interactions between the two cyclohexane rings.<sup>87,88</sup>

*cis* and *trans*-TACH are easily N-functionalised through condensation reaction with a number of aldehydes to give imines.<sup>89</sup> Walton and co-workers,<sup>90</sup> have prepared a number of N-functionalised *cis*-TACH derivatives from benzaldehydes. However, on complexation of the triimine cyclohexane ligands with the copper(II) salts of nitrate, acetate and chloride, monoimine complexes were obtained, where two of the imine groups were selectively hydrolysed. This is illustrated by the imine diamine complex **(1.32)** formed from the complexation of CuCl<sub>2</sub>•2H<sub>2</sub>O with the triimido cyclohexane synthesised from *cis*-TACH and 3,5-dimethoxybenzaldehyde. This selective hydrolysis is presumably owing to the elimination of strain in the intermediate complexes formed. The use of cinnamaldehydes to N- functionalise *cis*-TACH instead of benzaldehydes, conversely, results in complexes resistant to hydrolysis on coordination. These complexes were used as secondary coordination sphere models of metalloenzymes.<sup>91,92</sup> Complex **(1.33)**, for example, is a structural model of the active site of carbonic anhydrase and able to catalytically decompose dimethyl pyrocarbonate (dmpc) [dimethyl-oxo-

bis(dioxocarbonate)] and diethyl pyrocarbonate (depc) to dimethyl and diethyl carbonate respectively along with the evolution of carbon dioxide.<sup>93</sup>

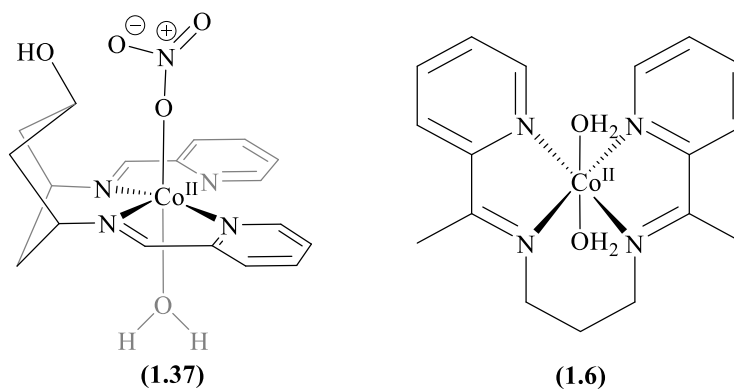
Interestingly Wass and co-workers<sup>94</sup> recently reported some *cis*-TACH based ligand systems prepared by the N-functionalisation with benzaldehydes similar to Walton and co-workers, where the imine arms remain intact on coordination. However, they use metal salts with non-coordinating anions for their complexations, such as [Cu(NCMe)<sub>4</sub>][PF<sub>6</sub>]. The lower oxidation state of the copper may be significant in this, as there should be less polarisation of the imines and therefore less vulnerability to hydrolysis. The complexes made, such as (**1.34**), were shown to bind reversibly with CO and ethylene, giving possible application in olefin separation and extraction.

1,3,5 – Substituted cyclohexanes can also provide frameworks for mixed metal complexes and coordination polymers. For example, the ligand made from the imination of *trans*-TACH with 2-pyridinecarboxaldehyde gives 3 sets of bidentate moieties. In the ring flipped conformation this gives two *axial* bidentate donor sets providing a tetradentate chelating pocket able to coordinate to the same metal, while maintaining the equatorial bidentate site free for further coordination. The stability difference between the tetradentate and bidentate coordination ensures that the metal coordination occurs in two successive steps. The reaction with the ligand with one equivalent of copper(II) chloride has been shown to give the mononuclear complex (**1.35a**), where the copper centre sits in the tetradentate coordination pocket, with the equatorial bidentate site free. The reaction of 1.5 or 2 equivalents of copper(II) chloride, however, both give the 2:1 metal to ligand complex with  $\mu_2$ -chloro bridged copper(II) dimer (**1.35b**).<sup>95</sup>

Gajda and co-workers<sup>96</sup> recently showed that a bridged tricopper complex using a *cis*-TACH based ligand from the imination with 1-H-pyrazole-5-carboxaldehyde (**1.36**) can act as an oxidase enzyme mimic. The cyclohexane provides a fixed organised tripodal scaffold and the pyrazole allows for metal bridging, these features allowed for the controlled formation of an oligometallic core. The triply deprotonated trinuclear complex was shown to be an efficient functional catechol oxidase mimic, with a low optimum pH of *ca.* pH = 5.6.

Cronin and co-workers<sup>97-99</sup> made a number of ligands based on *cis*-3,5-diamino-*trans*-hydroxycyclohexane (*cis,trans*-DAHC) synthesized from the mono protection, tosylation, deprotection and azide inversion and reduction of *cis,cis*-1,3,5-cyclohexanetriol. This 1,3,5 – substituted cyclohexane ligand gives a wide array of mononuclear and supramolecular complexes. Imination with 2-pyridinecarboxyaldehyde of (*cis,trans*-DAHC) gives the bis(imidopyridine) tetra-dentate ligand DDOP. On complexation with copper(II), cobalt(II), cadmium(II), and zinc(II), this forms mononuclear, ring-flipped complexes with the imino pyridine functionalities of the ligand encapsulating the metal centre in a chelating N<sub>4</sub> coordination pocket, fixing the non-coordinating hydroxyl in the equatorial position, as shown in the cobalt complex (**1.37**). However, on coordination with silver(I) leads to the formation of a four-coordinate dinuclear mesocate structures as shown in (**1.38**). It was postulated that the mononuclear, octahedral complexes, for example, in the case of the d<sup>10</sup> zinc(II) and cadmium(II) result from the energetic stabilisation gained through two extra coordinate bonds, while in the case of silver(I) the lower tendency of the metal centre for six-coordination give the energetically preferred dinucleating mesocate conformation.<sup>44</sup>

### 1.12 Outline and Aims of Thesis



This thesis takes inspiration from a cobalt based electrocatalyst (**1.6**) reported by Gray and Peters,<sup>44</sup> and shown to give hydrogen at ambient pH in water, and together with work by Cronin and co-workers,<sup>100-102</sup> on cyclohexane based ligands for coordination chemistry, illustrated in (**1.37**).



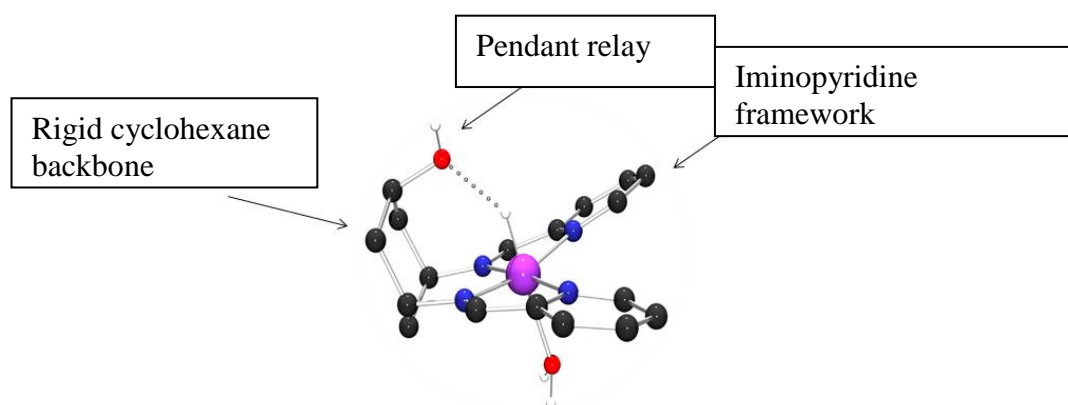


**Figure 1.6** DFT structure of proposed catalyst

The precedent from Gray and Peters indicates that using an iminopyridine macrocyclic framework for a cobalt centre should give hydrogen evolution from weakly acidic conditions with a low over potential. The relative ease of Schiff base chemistry would then allow for tuneable electronics and the rigid cyclohexane backbone give the ability to enforce a proton relaying group in a defined orientation around the metal second coordination sphere. A hydroxyl relay was chosen as an initial starting point for its relative ease of synthesis, enabling access to analogues may with the hydroxyl positioned proximal or distal to the metal centre. Hydroxyls are not perhaps the best proton relays due to their relatively low basicity, however, they have been shown to give an enhancement in other systems, such as work by Rauchfuss on di-iron hydrogenase models.<sup>103</sup> The synthesis of ligands incorporating likely more effective nitrogen-based proton relay groups was then explored.

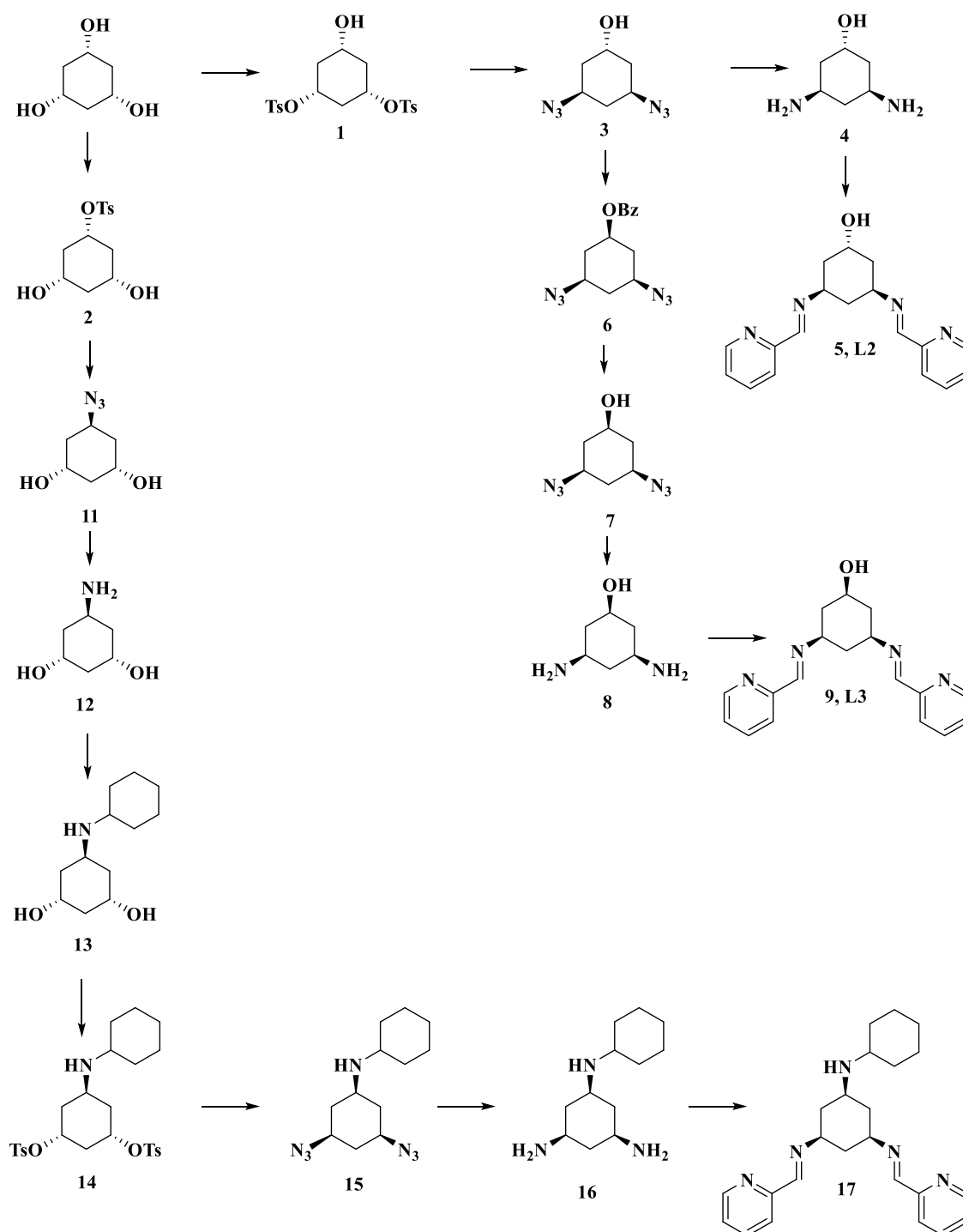
# **Chapter 2.0**

*Ligand synthesis and characterisation*

## 2.1 Synthesis

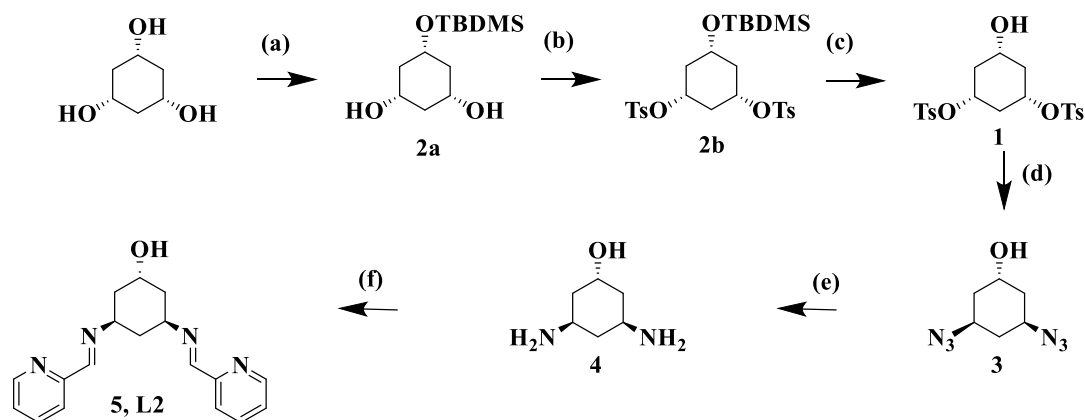
### 2.1.1 Overview of ligand synthesis

This chapter covers the synthesis and characterisation of the 1, 3, 5 – trisubstituted cyclohexane based ligands explored within this thesis, with an overview of the synthetic schemes to the ligands shown in **Scheme 2.1**.



**Scheme 2.1** Overview of ligands synthesis

### 2.1.2 Synthesis of **5**, **L2**



**Scheme 2.2** Cronin and co-workers<sup>104</sup> synthesis of **5**, **L2** ; reagents, conditions and yields: (a) TBDMSCl, NEt<sub>3</sub>, NaH, THF, 40°C, 20 hr, 97%; (b) TsCl, pyridine, 0 °C, 48 hr, 90%; (c); HF, CH<sub>3</sub>CN, 45 °C, 18 hr, 92% (d) NaN<sub>3</sub>, DMF, 70°C, 24 hr, 79%; (e) H<sub>2</sub>, Pd/C, EtOH, rt, 18 hr, 90%; (f) 2-pyridine carboxylaldehyde, NEt<sub>3</sub>, MeOH, reflux, 20 hr, 92%.

The cyclohexane-based ligand, **5**, **L2**, was initially synthesised by Cronin and co-workers,<sup>104</sup> (illustrated in **Scheme 2.2**). The synthesis starts from *cis*-1,3,5-cyclohexanetriol with a highly selective and high yielding mono TBDMS silylation (**a**), using one equivalent of sodium hydride, TEA and TBDMSCl in THF. This selectivity presumably comes from stabilisation of the anion formed by hydrogen bonding interactions when all the hydroxyls are in the axial conformation, as illustrated in **figure 2.1**. This added stabilisation of the negative charge in this conformation means further deprotonations of the same molecule are thermodynamically less favourable. Tosylation of the mono-protected product in pyridine using tosyl chloride after two days at 0 °C, gives the ditosylated derivative (**b**). Desilylation using hydrofluoric acid in acetonitrile solution then gives the ditosylate **2**.

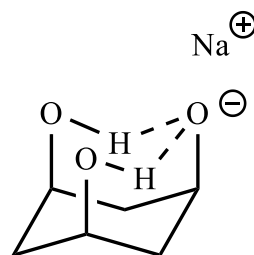
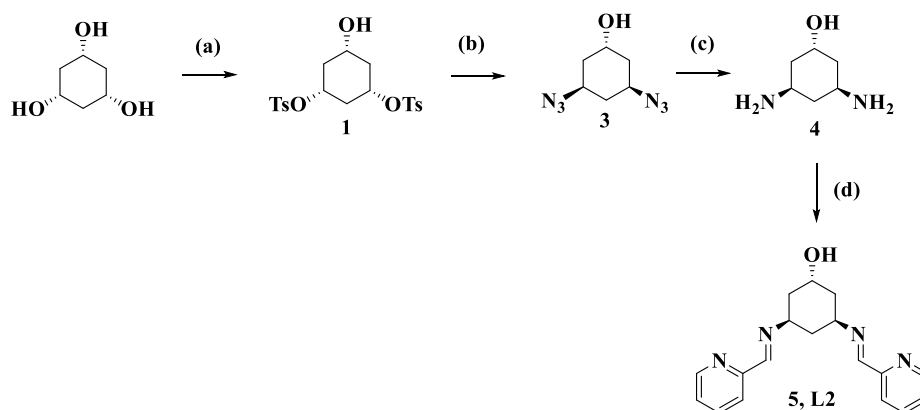


**Figure 2.1** Proposed cause of selectivity in the mono silylation

We decided however to change the synthetic route and directly tosylate *cis*-1,3,5-cyclohexanetriol, eliminating the protection/de-protection steps in the interest of shortening the synthetic procedure and stopping the use of highly toxic HF, as shown in **Scheme 2.3**.



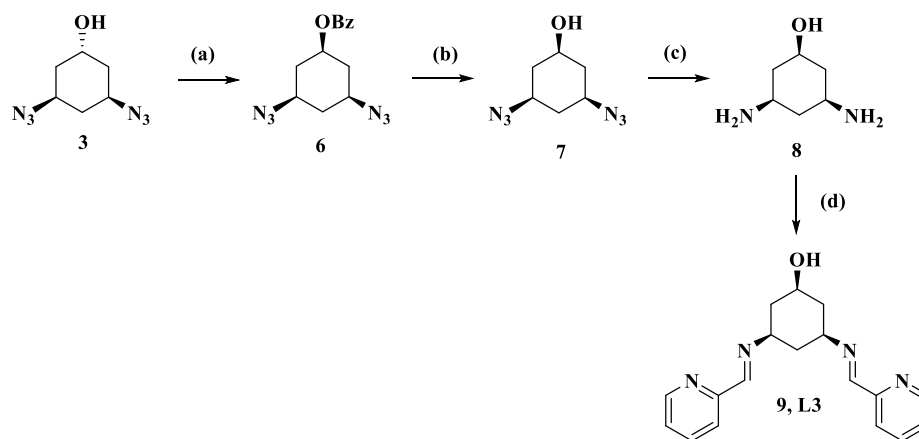
**Scheme 2.3** Direct tosylation to **5, L2**; reagents, conditions and yields: (a) TsCl, pyridine, 0°C, 18 hr, 57%, (mono 25%); (b) NaN<sub>3</sub>, DMF, 70°C, 24 hr, 68%; (c) H<sub>2</sub>, Pd/C, EtOH, rt, 18 hr, 92%; (d) 2-pyridinecarboxaldehyde, NEt<sub>3</sub>, MeOH, reflux, 20 hr, 92%.

Direct tosylation of *cis*-1,3,5-cyclohexanetriol was carried out at 0 °C under anhydrous conditions in pyridine with 2.1 eq of tosyl chloride. The reaction was found to be very sensitive to water and the volume of pyridine used, but gives the ditosylated product **1** in 57% yield, with the useful mono-tosylated by-product **2** being obtained in a yield of 25%. Stereochemical inversion of the ditosylate using sodium azide in large excess in DMF gave the *cis,trans* diazide **3** after chromatographic separation. Reduction of the azide using Pd/C under a high pressure (620 kPa) of hydrogen gave the diamino alcohol *cis,trans*-DAHC **4**, which was then reacted with 2-carboxaldehyde to form Schiff base derivatives in methanol using 0.5 equivalents of triethylamine catalyst giving the *bis*-pyridyl imine ligand **5, L2**. The identity of all compounds was confirmed by NMR spectroscopy (<sup>1</sup>H, <sup>13</sup>C), mass spectrometry, infra-red spectroscopy and elemental analysis. The <sup>1</sup>H-NMR spectrum of **4** is discussed in **section 2.4** to confirm its stereochemistry.

### 2.1.3 Synthesis of **9, L3**

A number of synthetic routes were attempted to give the inverted alcohol *cis,cis*-DAHC **8**, and amine derivatives. For example, tosylation or triflation of the diazide **2** and inversion through acylation, however, these gave either starting materials or a

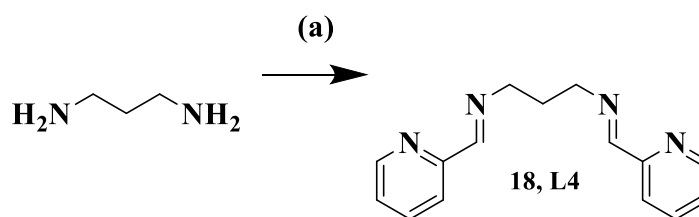
complicated mixture of products in low yields, with the largest component being the elimination product. These routes were motivated by a concern that the conditions for the Mitsunobu reaction conventionally used to invert alcohols would be incompatible with the azide functionality.<sup>105, 106</sup>



**Scheme 2.4** Hydroxyl inversion chemistry to give **9, L3**; reagents, conditions and yields: (a) DEAD, PPh<sub>3</sub>, BzOH, THF, 3 hr, -50 °C 62%; (b) NaOMe, MeOH, 4 hr, 79%; (c) H<sub>2</sub>, Pd/C, EtOH, rt, 18 hr, 94%; (d) 2-pyridine carboxaldehyde, NEt<sub>3</sub>, MeOH, reflux, 20 hr, 86%.

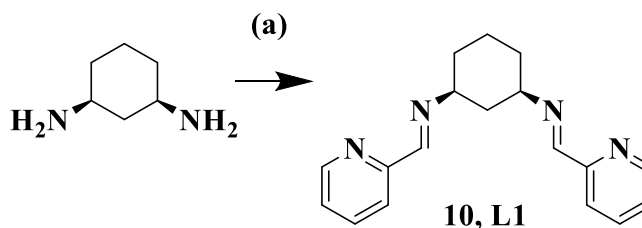
However, it was found subsequently that a route developed by Elchert and co-workers<sup>104</sup> of Mitsunobu inversion of the azidoalcohol **2** followed by hydrolysis of the ester, gave the all *cis* diazido alcohol which could then be reduced to the desired product as shown in **scheme 2.4**. The Mitsunobu reaction of diazide **2** using PPh<sub>3</sub>, DEAD and benzoic acid in THF at -50 °C proceeds to give the inverted benzoate ester **6** in 62% yield, under anhydrous conditions. Presumably reaction of triphenylphosphine with the alcohol is thermodynamically and kinetically more favourable than the formation of the phosphazide at -50 °C. After chromatographic separation the benzoate was hydrolysed using sodium methoxide and protonated with the use of Amberlite IR-120 (plus) resin to give the all *cis* diazido-alcohol **7**. Reduction of this over palladium on carbon with hydrogen at high pressure (620 kPa) gave the *cis,cis*-DAHC **8** product. This was then reacted with 2-pyridinecarboxaldehyde to form the Schiff base ligand in methanol using 0.5 equivalents of triethylamine catalyst to give the *bis*-pyridylimine ligand **9, L3**. All compounds were identified by NMR spectroscopy (<sup>1</sup>H, <sup>13</sup>C), mass spectrometry, infrared spectroscopy and elemental analysis. The <sup>1</sup>H-NMR spectrum of **8** discussed in **Section 2.4** to confirm its stereochemistry.

#### 2.1.4. Synthesis of 18, L4 and 10, L1



**Scheme 2.5.** Imination of 1,3-diaminopropane to give **18, L4**; reagents, conditions and yields: (a) 2-pyridine carboxylaldehyde, EtOH, reflux, 17 hr, 82%.

The commercially obtained 1,3-diaminopropane was stirred with 2-pyridinecarboxaldehyde ethanolic solution under reflux to form the Schiff base ligand **18, L4** shown in **scheme 2.5**.



**Scheme 2.6** Imination reaction; reagents, conditions and yields: (a) 2-pyridine carboxylaldehyde,  $\text{NEt}_3$ , MeOH, reflux, 20 hr, 80 %.

Cyclohexane analogue **10, L1** was synthesised in an analogous fashion to **18, L4**, starting from the commercially obtained *cis,cis*-1,3-diaminocyclohexane and stirring in methanolic solution of 2-pyridinecarboxaldehyde under reflux to form the Schiff base ligand shown in **scheme 2.6**.

## 2.2 Ligands Based on a *cis,cis*-triaminocyclohexane Core: Demonstration of Synthetic Feasibility

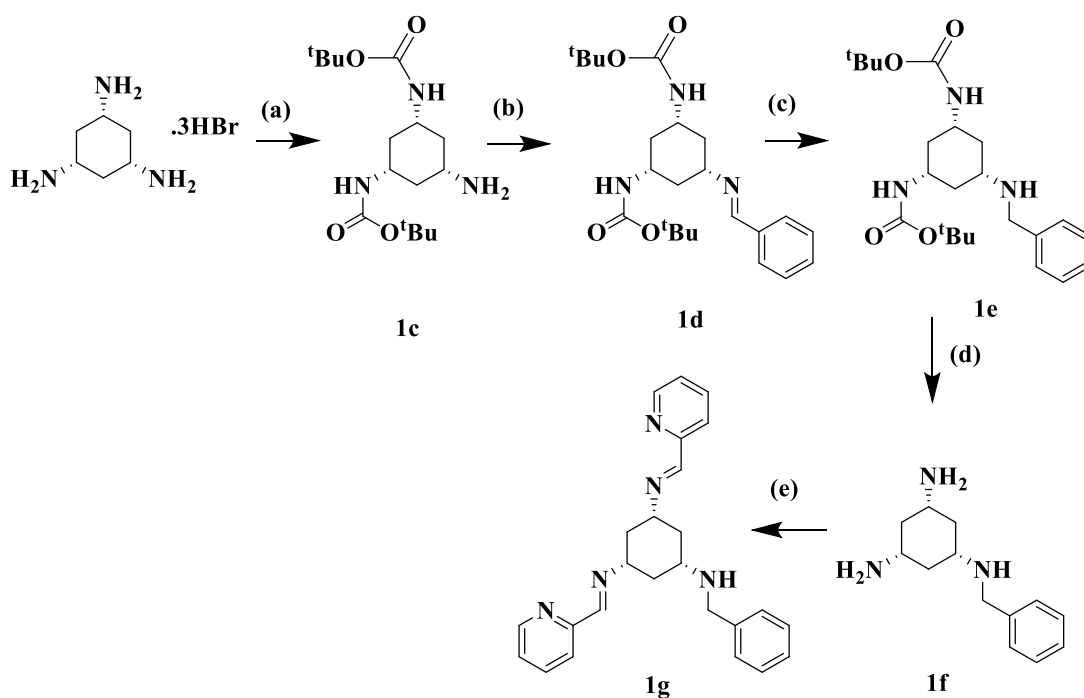
Replacing the -OH functionality in **L2** and **L3** with an amine group is a desirable goal, because the higher pK<sub>a</sub> of the amine makes it a much better proton acceptor, and the most encouraging results with proton relay groups have been obtained using amines.<sup>68</sup> However, obtaining *bis*-pyridyl imine ligands with the desired heterofunctionalised *cis,cis*-triaminocyclohexane (*cis*-TACH) cores is a synthetic challenge, requiring control over stereochemistry and derivatisation of three primary amine groups.

### 2.2.1. Route 1: Protection of *cis*-TACH

The first attempt at obtaining the desired class of ligands was carried out using chemistry developed by, and performed during a secondment with the research group of Professor Paul Walton at the University of York.

As shown in **scheme 2.7**, the synthetic route begins with the di-*tert*-butoxycarbonyl (Boc) protection of *cis*-TACH. DiBoc carbonate was added very slowly to a solution of *cis*-TACH at a rate of 10-12 drops per second over 18 hours. This reaction is very sensitive to scaling; the Walton group have found that 200 mg was the optimum quantity of starting triamine to give the highest yield of the diprotected product, giving up to 53% yield. The diBoc protected *cis*-TACH **1c** was reacted in a chloroform methanol mixture with benzaldehyde to form the Schiff base imine product **1d**. Compound **1d** was then reduced with sodium borohydride to the benzyl product **1e**. This was followed by a Boc de-protection step with concentrated hydrochloric acid in methanol at 0 °C, to give the benzylTACH **1f**. This step suffered from low yields most likely from protonation and removal of the benzyl group as is shown to be possible under highly acidic conditions, even though low temperature helps to disfavour this to the diBoc deprotection.<sup>107</sup> The benzylTACH **1f** obtained was reacted with 2-carboxaldehyde in toluene using Dean-Stark apparatus to form the Schiff base product **1g**. The resulting *bis*-iminopyridine ligand **1g** was added dropwise as a dilute methanol solution to an equimolar concentrated solution of cobalt(II) nitrate, resulting in a colour change from a pink cobalt solution to a dark brown indicating a change in ligand environment around the cobalt centre. Under these conditions no crystal suitable for x-ray diffraction was obtained.



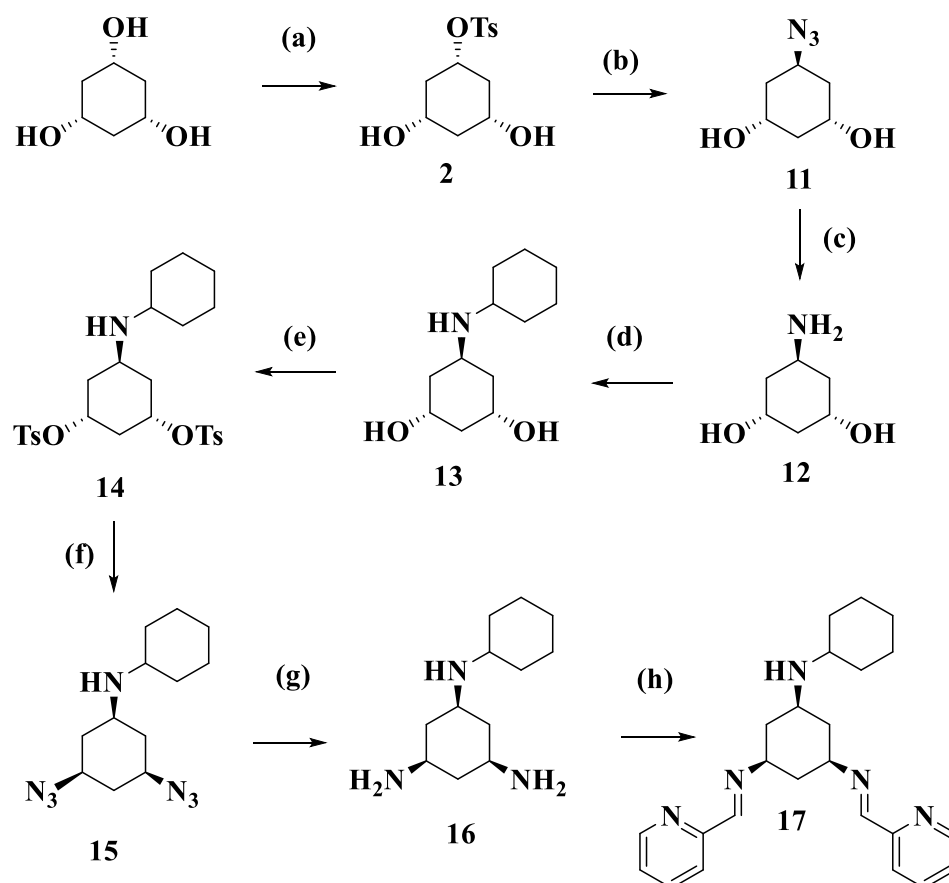


**Scheme 2.7.** Walton group Boc protection of TACH chemistry; reagents, conditions and yields: (a) TMA, diBoc carbonate, MeOH, RT, 18.5 hr, 53%; (b) benzaldehyde, MeOH/CHCl<sub>3</sub>, RT, 24 hr, 105% (excess benzaldehyde); (c) NaBH<sub>4</sub>, MeOH, rt, 18 hr, 85%; (d) Conc HCl, MeOH/CHCl<sub>3</sub>, 0 °C, 1 hr, 37%; (e) 2-pyridine carboxaldehyde, NEt<sub>3</sub>, MeOH, reflux, 20 hr, 62%.

This route was abandoned for a number of reasons. The small scale needed to get reasonable yield of the diBoc protected *cis*-TACH **1c**, would require a number of repetitions to give any appreciable quantity of product. <sup>1</sup>H-NMR of nearly all synthetic intermediates gave very broad overlapping signals, thought to be caused by micelle formation due to the surfactant nature of the molecules. NMR signals are broadened in micelles as the tumbling rate is decreased with respect to the timescale of the experiment.<sup>108</sup> Due to the poorly resolved <sup>1</sup>H NMR, the synthetic route relies heavily on mass spectrometry technique to characterise the intermediates involved: our dependence on the EPSRC national service for mass spectral characterisation make this too slow. Deprotection of the diBoc groups with concentrated acid gave low yields, (37%), due to conditions that also cleave the benzyl to give *cis*-TACH starting material. This deprotection step could possibly be improved through the use of a group more stable under highly acidic conditions than a benzyl. For example, use of cyclohexanone instead of benzaldehyde leads to an enamine, which on reduction to the amine is stable to highly acidic conditions.<sup>109</sup>

### 2.2.2. Route 2: Via *cis*-1,3-dihydroxy-*trans*-5-amino cyclohexane

DiBoc protection of *cis*-TACH did not seem to be a good option (see above), and attempts to introduce an amine *via* tosylation or triflation of the diazide **3** and reaction with primary amine nucleophiles were also unpromising. It was therefore decided that a route to a ligand with a proximal amine group might be feasible starting from monotosylate **2** obtained as by-product from the tosylation of *cis,cis*-1,3,5-cyclohexanetriol, *via* the known *cis*-1,3-dihydroxy-*trans*-5-azidocyclohexane **11** and *cis*-1,3-dihydroxy-*trans*-5-aminocyclohexane **12**, as is illustrated in **scheme 2.7**.



**Scheme 2.9** Proximal cyclohexane amine relay ligand synthesis; reagents, conditions and yields: (a) TsCl, pyridine, 0 °C, 18 hr, 25%, (bis-product **1** 57%); (b) NaN<sub>3</sub>, DMF, 70 °C, 16 hr, 80%; (c) H<sub>2</sub>, Pd/C, EtOH, rt, 18 hr, 94%; (d) cyclohexanone, ammonium formate, MeOH/toluene, Dean-Stark, reflux, 16 hr, 66%; (e) TsCl, pyridine, 0 °C, 3 days, 40%; (f) NaN<sub>3</sub>, DMF, 70 °C, 2 days, 50%; (g) H<sub>2</sub>, Pd/C, EtOH, rt, 18 hr, 82%; (h) 2-pyridine carboxaldehyde, NEt<sub>3</sub>, MeOH, reflux, 20 hr, 90%.

The synthesis begins with the stereochemical inversion, via an  $S_N2$  azide reaction of the monotoyslate **2** using sodium azide in large excess in DMF at 70 °C for 16 hours, to give the monoazide **11** after chromatographic separation. Reduction of the monoazide using Pd on carbon under high pressure (620 kPa) of hydrogen gave the monoaminediol, *trans*-5-aminocyclohexane **12** in high yield. Next, the direct reductive amination of **12** was carried out by a Leuckart type reaction using an adapted method from Saba and co-workers,<sup>110</sup> yielding **13**. Initial attempts to do this failed, however, resulting only in isolation of the starting materials. This is likely to have been due to solubility problems, as the original method uses toluene as the solvent; **12** is very polar and the ammonium formate reductant may worsen this by protonating it. Therefore, in the successful procedure **12** was initially refluxed with cyclohexanone in methanol for 16 hours to give the intermediate enamine, toluene and the ammonium formate reductant were then added along with additional cyclohexanone and refluxed in a Dean-stark apparatus to give the desired product **13** in 66% yield. Tosylation with 10 eq of tosyl chloride at 0 °C in pyridine gave **14** as a brown precipitate on pouring the reaction mixture into ice.

Due to time constraints and lack of material, optimisation of reaction conditions and full characterisation for the subsequent steps described below was not achieved. Products were characterised as far as possible with the available material, and the small quantities have precluded use of destructive techniques such as elemental analysis. Nonetheless, the data obtained is sufficient to demonstrate the feasibility of this synthetic route for future use – yields for the tosylation and azide reaction could very likely be substantially improved with further work – and the results have been included in the thesis for this reason.

Stereo-chemical inversion of **14** was achieved via an  $S_N2$  azide reaction in the presence of sodium azide in large excess in DMF at 70 °C for 2 days to give **15** at 50% yield, after chromatographic separation. Reduction of the diazide **15** using Pd on carbon at 620 kPa pressure of hydrogen gave the amine product **16**. The amine product **16** was refluxed overnight with 2-pyridinecarboxaldehyde to form the Schiff base ligand in methanol using 0.5 equivalents of triethylamine to give the *bis*-iminiopyridine ligand **17**. As found in the synthesis of all the other Schiff base ligands, **L1**, **L2** and **L3** small quantities of unreacted 2-pyridinecarboxyaldehyde are always present in the products even after precipitation or crystallisation. Purification by column chromatography or distillation was

not possible as the conditions result in the hydrolysis of the imine groups, and the small quantity of product obtained could not conveniently be reprecipitated from diethyl ether/hexane as done for the other imine derivatives. Purification with larger quantities of the ligands, through the dissolution of the product in a small volume of diethyl ether and precipitation with hexane for most ligands, results in a cleaner product with *ca.* 5 % 2-pyridinecarboxaldehyde.

Complexation of **17** with cobalt(II) nitrate was attempted, by adding a dilute solution in methanol to an equimolar quantity of the metal salt in methanol. A colour change from pink to brown was observed on the addition, however, analysis revealed that under these conditions a mixture of unreacted **17** and cobalt nitrate were the main result. The paramagnetic NMR of the material obtained showed a large number of peaks in the range from 80 to -80 ppm, with small peak heights, consistent with formation of complexes similar to those of Co(II) with **L2** and **L3**. However, much larger peaks were observed in the region from 8 to 0 ppm indicative of broadened ligand peaks. Crystals were obtained on diethyl ether diffusion into concentrated methanolic mother liquor from the reaction, however, these were shown to be cobalt nitrate. These results indicated that the conditions were not right for the formation of the desired cobalt complex of **17**, this may be due to the increase steric demands of the ligand compared to the other ligands synthesised. Walton and co-workers have also observed previously that complexations of sterically bulky cyclohexane based ligands with imine ligands with certain metal salts can result in the hydrolysis of one or two of the imine groups.<sup>90</sup>

## 2.3 NMR of Cyclohexanes

Over the subsequent sections, there follows discussion of the identification and stereochemical assignment of the series of cyclohexane-based products synthesized. This has been achieved primarily by  $^1\text{H}$ -NMR, which can give lots of information on cyclohexane conformation and substitution, from coupling constants, sterics and chemical shifts. The rigidity of cyclohexanes means that groups are held in fixed positions. The relative positions of the protons on the cyclohexane ring will have different influences on each other as described by coupling constants, steric compression, and substituents. For this reason, a brief introduction to  $^1\text{H}$ -NMR in cyclohexanes is provided below.

### 2.3.1 Coupling constants

Coupling constants in cyclohexanes can be explained by the Karplus equation. The Karplus equation is an expression (derived from observations and theoretical calculations) that relates the NMR coupling constant ( $^3J_{\text{H-H}}$  values) with dihedral angle between vicinal protons. It shows that couplings will be maximum at dihedral angles of  $180^\circ$  and  $0^\circ$  (anti or eclipsed) as found in cyclohexane axial-axial interactions, approach zero at dihedral angles of  $90^\circ$ , and still be very small at the *ca.*  $60^\circ$  dihedral angle observed for cyclohexane equatorial-equatorial (and equatorial-axial) interactions. This relationship although is strictly applied to unstrained hydrocarbon systems, and electronegative substituents may cause perturbations from this.<sup>111,112</sup> This phenomenon is due to strong hyper-conjugative interactions increasing the communication between the proton spins at dihedral angles of  $180^\circ$  and  $0^\circ$  (anti or eclipsed), these are minimised at  $90^\circ$  and still small at  $60^\circ$  because there is little or no orbital overlap.<sup>113</sup>

Karplus Equation

$$3J(\varphi) = A \cos^2(\varphi) + B \cos(\varphi) + C$$

Where (A,B, and C) are parameters for a particular molecule.

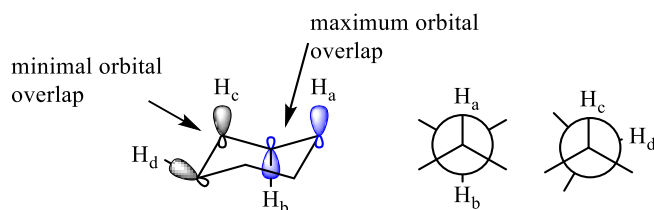


**Figure 2.3** Cyclohexane in the chair conformation (*left*) with corresponding Newman projection (*right*). Maximum orbital overlap is seen between anti-periplanar protons  $H_a$  and  $H_b$ , and minimal orbital overlap between  $H_c$  and  $H_d$ .

### 2.3.2 Steric compression

Steric compressions occur when molecular structure cause a proton to be forced close to other protons, or to various functional groups, the proton will in general be deshielded as a result of dispersion interactions. Shifts of this type are hard to distinguish from magnetic anisotropy interactions and are especially large in highly compressed compounds like "birdcage" molecules. The inside proton in the "out" alcohol **A** at  $\delta$  4.48 is downfield by 0.96 ppm from the model **B**, as illustrated in **figure 2.4**.<sup>114</sup>

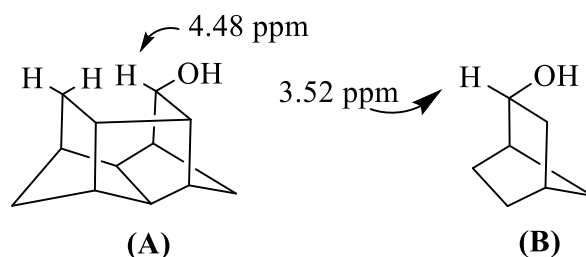


**Figure 2.4** Illustration of steric compression on birdcage molecule (**A**) compared to (**B**) without steric compression.

### 2.3.3 Axial and equatorial cyclohexane shifts

In cyclohexane itself, as well as in most substituted and heterocyclic 6-membered rings the axial protons are upfield of the equatorial ones. There are, however, a few exceptions and so these chemical shift effects must be used with caution. The  $\delta_e - \delta_a$  values below show the difference between equatorial ( $\delta_e$ ) and axial ( $\delta_a$ ) chemical shifts:<sup>115</sup>

X	$\delta_e - \delta_a$		
	$\alpha$	$\beta$	$\gamma$
CH <sub>2</sub>	0.52	0.52	0.52
NH	0.48	0.12	0.45
NH <sub>2</sub> <sup>+</sup>	0.47	0.16	0.34
O	0.5	-0.07	0.32
S	-0.19	0.38	0.5
SO <sub>2</sub>	<0.10	0.17	0.45

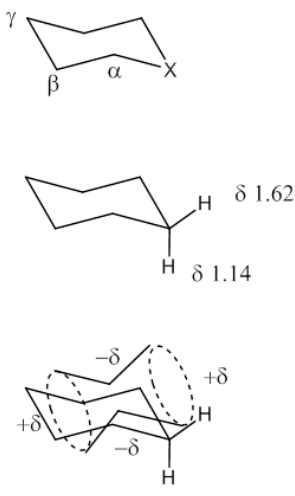


**Figure 2.5** Axial and equatorial cyclohexane shifts.<sup>116</sup>

One explanation for this shift effect is based on the anisotropy cones shown in **figure 2.5** (*right*), where the equatorial protons reside in the deshielding (+ $\delta$ ) region of the C-C anisotropy, and the axial in the - $\delta$  region. The variation in  $^1J_{CH}$  has also been interpreted in these terms.

## 2.4 <sup>1</sup>H-NMR Spectroscopy and characterisation of L4

Compound **18**, **L4** shows infrared and mass spectra consistent with its proposed structure. The IR spectrum shows a strong peak at 1650 cm<sup>-1</sup>, corresponding to the C=N imine stretch. The mass spectrometry shows a molecular peak at 253.15 M/Z, corresponding to the protonated molecular ion.

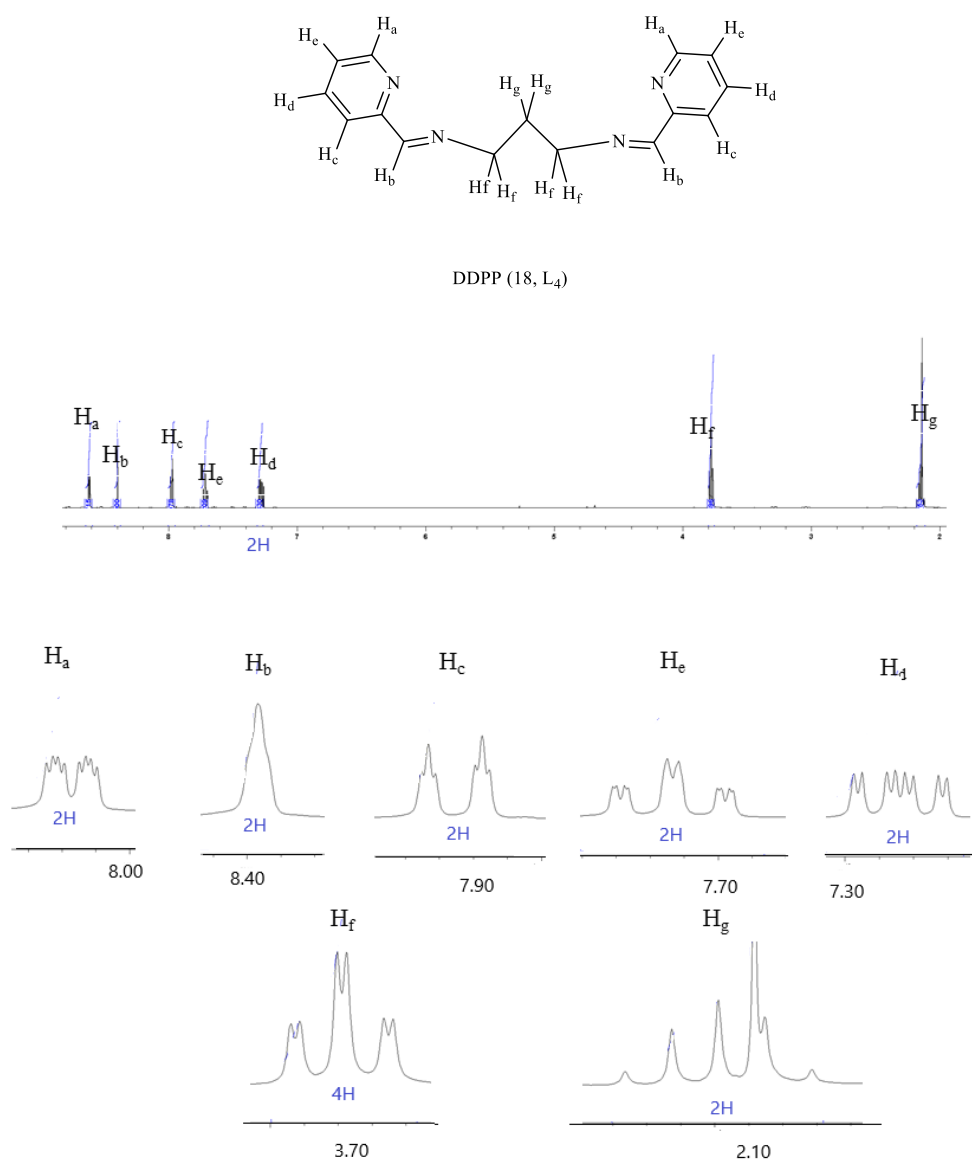


**Figure 2.6**  $^1\text{H}$ -NMR (500 MHz,  $\text{D}_2\text{O}$ ) spectra of DDPP (**18**, **L4**). With expansion of the spectrum of show integrals and fine structure (*bottom*).

The assignment of the  $^1\text{H}$ -NMR spectrum of DDPP (**18**, **L4**) is shown in **figure 2.6**. The most deshielded protons are  $\text{H}_a$  ( $\delta = 8.57$  ppm) on the pyridine ring, which displays a doublet of doublets of doublets splitting pattern. This multiplicity is a result of strong  $^2J_{ortho}$  coupling with  $\text{H}_e$  and weaker  $^3J_{meta}$  &  $^3J_{para}$  coupling with  $\text{H}_d$  and  $\text{H}_c$  respectively. The next most deshielded protons are  $\text{H}_b$  ( $\delta = 8.35$  ppm) from the imine protons displaying a broadened singlet. The next signal downfield is from the  $\text{H}_c$  ( $\delta = 7.93$  ppm) protons of the pyridine ring displaying a doublet of triplets. This is a result of strong  $^2J_{ortho}$  coupling with  $\text{H}_d$  and weaker  $^3J_{meta}$  with  $\text{H}_e$ . The next signal downfield is from the  $\text{H}_e$  ( $\delta = 7.66$  ppm) protons of the pyridine ring displaying a triplet of doublets, from the strong  $^2J_{ortho}$



coupling with  $H_a$  and  $H_d$  and weaker  $^3J_{meta}$  with  $H_c$ . The next signal downfield is from the  $H_d$  ( $\delta = 7.24$  ppm) protons of the pyridine ring displaying a doublet of doublets of doublets, from the strong  $^2J_{ortho}$  coupling with  $H_e$  and  $H_c$  and weaker  $^3J_{meta}$  with  $H_a$ . The next signal downfield is from the  $H_g$  ( $\delta = 3.73$  ppm) protons of the propane displaying a pentet from strong  $^3J_{HH}$  coupling from the four  $H_f$  protons. The most upfield signal being from the  $H_f$  ( $\delta = 2.10$  ppm) from the propane, displaying a triplet of doublets from strong  $^3J_{HH}$  coupling from the two  $H_g$  protons and weak  $^4J_{HH}$  coupling from  $H_b$ .

## 2.5 $^1H$ -NMR spectroscopy of cyclohexane based ligands

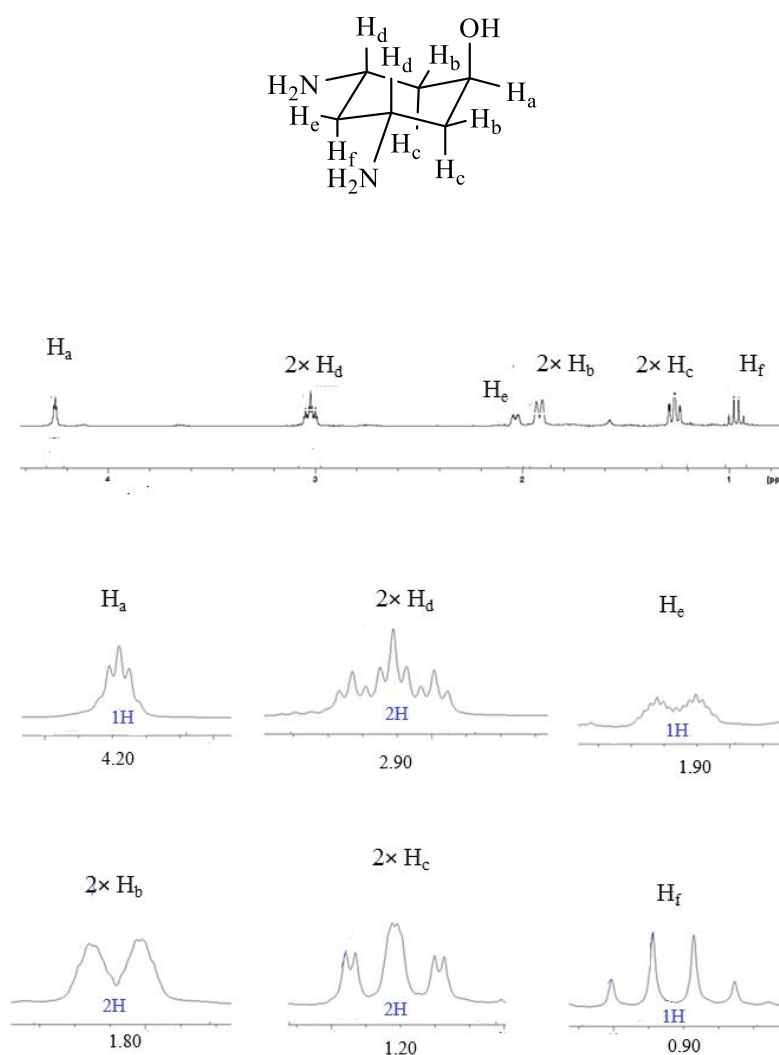


**Figure 2.7**  $^1H$ -NMR (500 MHz,  $D_2O$ ) spectra of *cis,trans*-DAHC **4**. With expansion of the spectrum of DAHC to show integrals and fine structure (*bottom*).

The  $^1\text{H}$ -NMR spectral assignment of *cis,trans*-DAHC **4** and *cis,cis*-DAHC **8**, as shown in **figure 2.7** and **2.8**, show the differences in the shifts and multiplicities seen when the alcohol group has been inverted via the Mitsunobu reaction.

The assignment of the  $^1\text{H}$ -NMR spectrum of *cis,trans*-DAHC **4** is shown in **figure 2.7**. The most deshielded environment is the methine proton  $\text{H}_a$  ( $\delta = 4.17$ ) geminal to the oxygen, which displays a *pseudo*-pentet splitting pattern. This multiplicity is a result of weak  $^3J_{HH}$  equatorial-equatorial and  $^3J_{HH}$  equatorial-axial couplings by the Karplus equation, with the two  $\text{H}_b$  and two  $\text{H}_c$  protons. Next most deshielded are the two methine protons  $\text{H}_d$  ( $\delta = 2.93$ ), which have a less negative value of  $\delta$  as a consequence of nitrogen's weaker electron withdrawing effect and their axial location. In this case the multiplicity observed is a *pseudo*-triplet of *pseudo*-triplets due to strong  $^3J_{HH}$  axial-axial couplings to the anti-periplanar  $\text{H}_c$  and  $\text{H}_f$ , and weak  $^3J_{HH}$  axial-equatorial couplings to  $\text{H}_b$  and  $\text{H}_e$ . Equatorial methylene protons  $\text{H}_e$  ( $\delta = 1.95$ ) and the two  $\text{H}_b$  ( $\delta = 1.83$ ) display similar multiplets but are easily distinguished from each other by their integrals. In both cases a doublet splitting resulting from strong  $^2J_{HH}$  geminal coupling to  $\text{H}_c$  and  $\text{H}_f$  respectively is broadened by weak  $^3J_{HH}$  equatorial-equatorial and  $^3J_{HH}$  equatorial-axial couplings to  $\text{H}_a$  and  $\text{H}_d$  for  $\text{H}_b$ , and the two  $\text{H}_d$  for  $\text{H}_e$ . The axial methylene protons  $\text{H}_c$  and  $\text{H}_f$  can be identified both by their integrals and multiplicities. The  $\text{H}_c$  protons ( $\delta = 1.18$ ) give a *pseudo* triplet of doublets, as a consequence of strong  $^2J_{HH}$  geminal and  $^3J_{HH}$  axial-axial couplings with similar magnitudes, to  $\text{H}_b$  and  $\text{H}_d$  respectively, to give a triplet pattern, and a weaker doublet splitting from  $^3J_{HH}$  axial-equatorial coupling to  $\text{H}_a$ . Meanwhile  $\text{H}_f$  ( $\delta = 0.88$ ) displays a *pseudo*-quartet as a result of strong,  $^2J_{HH}$  geminal ( $\text{H}_e$ ) and  $^3J_{HH}$  axial-axial ( $\text{H}_d$ ) couplings.

The assignment of the  $^1\text{H}$ -NMR spectrum of *cis,cis*-DAHC **8** is shown in **figure 2.8**. This compound has six proton chemical environments, excluding the amines and hydroxyl proton which are affected by H/D exchange and/or quadrupolar broadening. The most deshielded is the methine proton  $\text{H}_a$  ( $\delta = 3.72$ ) geminal to the oxygen, found to be axial in  $\text{D}_2\text{O}$ , as the hydroxyl and amine groups are in the equatorial position. This gives an observed multiplicity of a triplet of triplets due to strong  $^3J_{HH}$  axial-axial couplings to the two anti-periplanar  $\text{H}_c$  protons, and weak  $^3J_{HH}$  axial-equatorial couplings to the two  $\text{H}_b$  protons. Next most deshielded are the two methine protons  $\text{H}_d$  ( $\delta = 2.83$ ), which have a less negative value of  $\delta$  as a consequence of nitrogen's weaker electron withdrawing

effect and their axial location. The multiplicity observed is also a *pseudo*-triplet of *pseudo*-triplets due to strong  $^3J_{HH}$  axial-axial (Karplus, dihedral angle,  $\Phi = 180^\circ$ ) couplings to the anti-periplanar  $H_c$  and  $H_f$ , and weak  $^3J_{HH}$  axial-equatorial couplings to  $H_b$  and  $H_e$ .

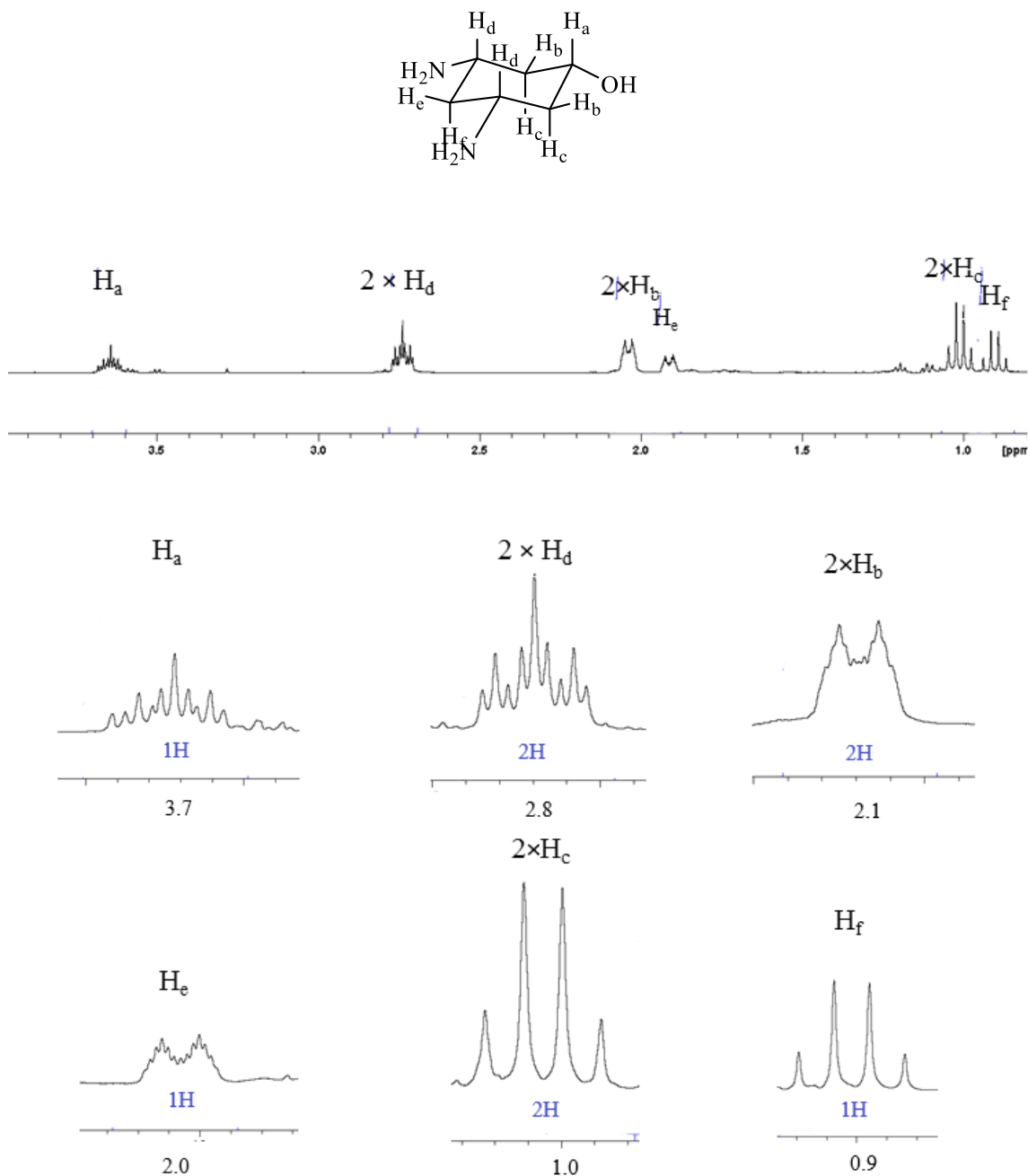


**Figure 2.8**  $^1\text{H}$ -NMR (500 MHz,  $\text{D}_2\text{O}$ ) spectra of *cis,cis*-DAHC **8**. With expansion of the spectrum of DAHC to show integrals and fine structure (*bottom*).

Equatorial methylene protons the two  $H_b$  ( $\delta = 2.12$ ) and  $H_e$  ( $\delta = 1.99$ ) display similar multiplets but are easily distinguished from each other by their integrals. In both cases a

doublet splitting resulting from strong  $^2J_{HH}$ , geminal coupling to H<sub>c</sub> and H<sub>f</sub> respectively is broadened by weak equatorial-axial couplings to H<sub>a</sub> and H<sub>d</sub> for H<sub>b</sub>, and the two H<sub>d</sub> for H<sub>e</sub>. The axial methylene protons 2 x H<sub>c</sub> and H<sub>f</sub> can also be identified both by their integrals and multiplicities. The H<sub>c</sub> protons ( $\delta = 1.09$ ) gives a *pseudo*-quartet as a result of strong,  $^2J_{HH}$  geminal to H<sub>b</sub> and strong  $^3J_{HH}$  axial-axial couplings to H<sub>a</sub> and H<sub>d</sub>. Lastly, H<sub>f</sub> ( $\delta = 0.98$ ) displays a *pseudo*-quartet as a result of strong,  $^2J_{HH}$  geminal (H<sub>e</sub>) and  $^3J_{HH}$  axial-axial (H<sub>d</sub>) couplings.

There is a shift upfield of 0.45 ppm for H<sub>a</sub> in going from *cis,trans*-DAHC **4** to *cis,cis*-DAHC **8**, this is expected as axial protons in cyclohexanes are usually upfield with respect to an equivalent equatorial proton ( $\delta_{eq} > \delta_{ax}$ ). This is usually explained by arguing that a C-H bond is a stronger  $\sigma$  donor than a C-C bond, leading to increased electron density in the axial protons (anti to two C-H's).<sup>115</sup> There is a shift upfield of 0.11 ppm for H<sub>d</sub> in going from *cis,trans*-DAHC **4** to *cis,cis*-DAHC **8**, this is can probably be explained in terms of steric compression from the axial hydroxyl to the H<sub>d</sub> protons in *cis,cis*-DAHC **8**.<sup>117</sup> There is a reversal of shifts for the two equatorial methylene protons on going from *cis,trans*-DAHC **4** to *cis,cis*-DAHC **8**, H<sub>b</sub> appears more downfield than H<sub>e</sub>, There is a 0.29 ppm shift downfield for the H<sub>b</sub> protons, and a 0.04 ppm shift downfield for the H<sub>e</sub> proton. This reflects that the highly electronegative oxygen of the hydroxyl group in the equatorial position, having a larger influence on the equatorial H<sub>b</sub> protons, shifts them further downfield than the nitrogens on proton H<sub>e</sub>. There is also a shift 0.16 ppm upfield in the axial H<sub>c</sub> and a 0.03 ppm downfield in the H<sub>f</sub> protons on going from *cis,trans*-DAHC **4** to *cis,cis*-DAHC **8**, also suggesting that having the hydroxyl group in the equatorial position has a greater influence on the axial protons of the cyclohexane.

## 2.6 <sup>1</sup>H-NMR Spectroscopy of *cis*-TACH based products and precursors

The <sup>1</sup>H-NMR of **13** to **17** is shown below in **figures 2.9** and **2.10**. As addition of the second cyclohexane group leads to a number of signals becoming fairly poorly resolved multiplets, the shifts in signals given are by arrows. These assignments have been confirmed by analysis of <sup>1</sup>H-COSY spectra.

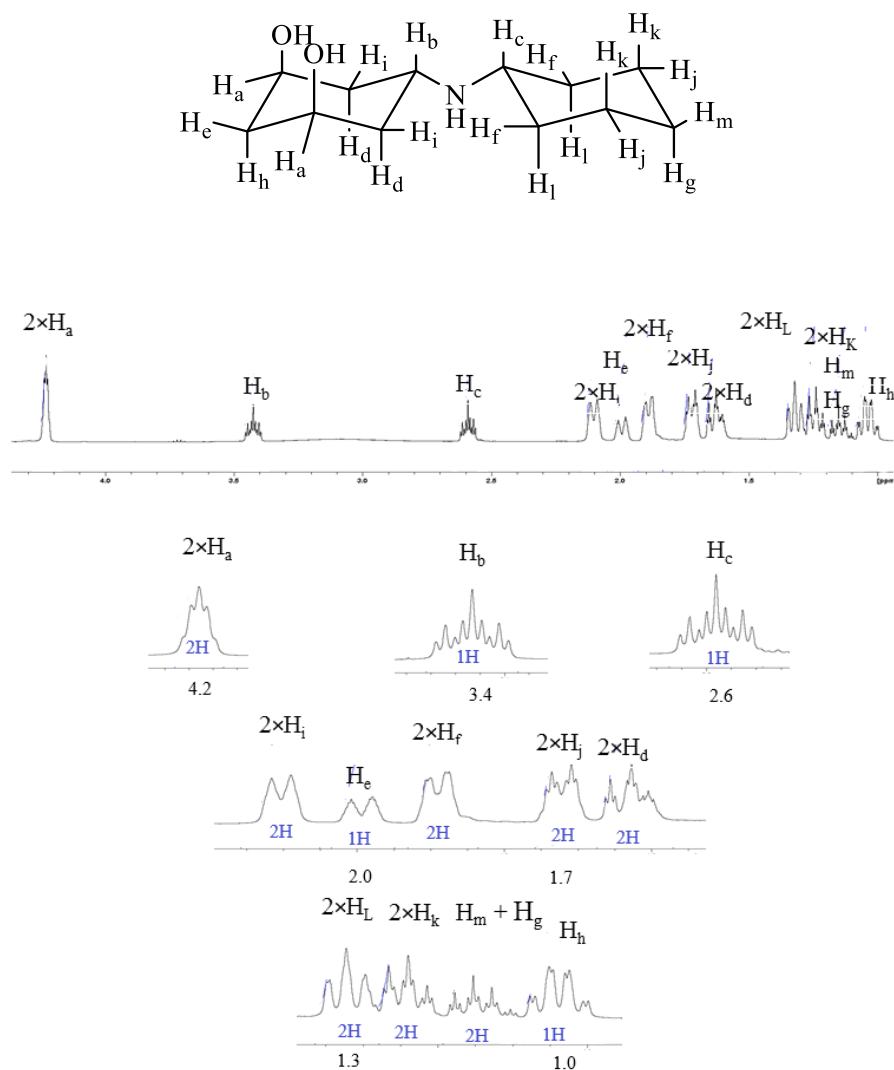


**Figure 2.9** <sup>1</sup>H-NMR assignment of **13**, with expansion of the spectrum to show integrals and fine structure (*bottom*)

The bulky cyclohexamine group of **13** is locked in the equatorial position in chloroform solution, and therefore the two alcohols are held in the axial position. In the <sup>1</sup>H-NMR the electronegativity of the oxygens of the two axial alcohols mean that the two equatorial methine protons H<sub>a</sub> ( $\delta = 4.23$  ppm) have the most downfield chemical shift. Their signal appears as a *pseudo*-pentet as a result of weak equatorial-equatorial coupling to the two H<sub>i</sub> and H<sub>e</sub> and weak equatorial-axial coupling to the two H<sub>d</sub> and H<sub>h</sub>. The next most downshifted is the proton geminal to the equatorial amine H<sub>b</sub> ( $\delta = 3.43$  ppm) on the cyclohexane ring containing the two hydroxyl groups, whose signal is a merged *pseudo*-triplet of *pseudo*-triplets, results from strong axial-axial couplings to the two H<sub>d</sub> and weak axial-equatorial couplings with the two H<sub>i</sub>. Next most downfield is the axial methine proton H<sub>c</sub> ( $\delta = 2.59$  ppm), on the second cyclohexane, which shows as similar signal to

H<sub>b</sub>, resulting from strong axial-axial couplings to the two H<sub>i</sub> and weak axial-equatorial couplings with the two H<sub>f</sub>. As the other signals are badly resolved multiplets, unambiguous assignment is a lot harder.

However, from the <sup>1</sup>H-NMR of simpler 1,3,5-*tris*-substituted cyclohexanes and knowledge of the Karplus equation,<sup>118,111</sup> it is known that the doublet type signals found at ( $\delta$  = 2.10, 1.99 and 1.89 ppm), originate from equatorial methylene protons, due to the strong, <sup>2</sup>*J*<sub>HH</sub>, geminal coupling with the geminal axial protons giving the large peak separation, and then weaker, <sup>3</sup>*J*<sub>HH</sub> equatorial-equatorial coupling, which broadens the signal and can sometimes resolve into *pseudo*-doublets of triplets.

The *pseudo*-quartet type signal found at ( $\delta$  = 1.04 ppm), originates from axial methylene protons, with two protons anti-periplanar to them as in the case for H<sub>g</sub>. This is due to the strong, <sup>2</sup>*J*<sub>HH</sub> geminal coupling with the geminal equatorial proton giving the large peak separation, and then strong <sup>3</sup>*J*<sub>HH</sub>, axial-axial coupling with the two anti-periplanar protons also giving a large peak separation. As the magnitude of the <sup>2</sup>*J*<sub>geminal</sub> and <sup>3</sup>*J*<sub>axial-axial</sub> values for each are similar, this has the effect of behaving as three equivalent proton environments, therefore splitting the signal into a *pseudo*-quartet.

The *pseudo*-triplet type signals found at ( $\delta$  = 1.72, 1.63, 1.32, 1.24 and 1.15 ppm) originate from axial methylene protons, with one proton anti-periplanar to them. This is due to the strong, <sup>2</sup>*J*<sub>HH</sub>, geminal coupling with the geminal equatorial proton giving the large peak separation, and then strong <sup>3</sup>*J*<sub>HH</sub>, axial-axial coupling with the anti-periplanar proton. As the magnitude of the <sup>2</sup>*J*<sub>geminal</sub> and <sup>3</sup>*J*<sub>axial-axial</sub> values for each are similar, this has the effect of behaving as two equivalent proton environments, therefore splitting the signal into a *pseudo*-triplet. This can then be split further by weak, <sup>3</sup>*J*<sub>HH</sub>, equatorial-equatorial coupling.

For **13** to **17**, the three most downfield peaks in the <sup>1</sup>H-NMR of each compound describe the changes in the molecules in each subsequent reaction, and are the peaks from protons geminal to the functionality in the 1, 3 and 5 positions of the cyclohexane rings. Their shifts up or downfield depend on the nature of the substituent and the splitting of the peaks gives conformational information about the cyclohexane, *i.e.* whether the functionality is equatorial or axial.

On the tosylation of **13** to give **14** the increased electron withdrawing effect of the tosyl groups shifts the peak corresponding to the methine protons geminal to them further downfield to ( $\delta$  = 4.89 ppm). There is also a slight shift for the proton geminal to the equatorial amine of the tri-substituted cyclohexane to ( $\delta$  = 3.60 ppm), and the proton geminal to the equatorial amine of the other cyclohexane ( $\delta$  = 2.81 ppm). Although the signals have broadened, the overall shape and width of the multiplets are the same as that found in **13**, suggesting that the most downfield peak is still *pseudo*-pentet in nature and the other two peaks *pseudo*-triplet of *pseudo*-triplets. This indicates there is no change in conformation on tosylation of the hydroxyls. This is most probably caused by steric factors which make it more thermodynamically favourable to have the cyclohexane substituted amine in the equatorial position. Even though tosyl groups have large steric bulk, they occupy less volume than a cyclohexane and there is more distance between the bulky aromatic rings and the cyclohexane core (because of the  $-\text{SO}_2-$  linkage).

In **15**  $\text{S}_{\text{N}}2$  inversion of the tosyl groups with azides gives a large change in shift for the most downfield peak. The peak corresponding to the two methine protons geminal to the azides shifts to ( $\delta$  = 3.31 ppm), due to the decrease in inductive effect from the less electron withdrawing nitrogen of the azide groups. There is also a change in multiplicity from a *pseudo*-pentet in **14** to a merged *pseudo*-triplet of *pseudo*-triplets. This reflects a change in stereochemistry of the two geminal protons to the azides to equatorial, resulting in strong axial-axial couplings to the two axial anti-periplanar proton environments and weak axial-equatorial couplings with the two equatorial proton environments in the  $^1\text{H}$ -NMR. There is also a shift in the other two most down field peaks from the other two geminal protons to ( $\delta$  = 2.74 ppm) and ( $\delta$  = 2.63 ppm), also reflecting the decrease in inductive effect from the more electropositive azide groups, but the peaks remain with the same *pseudo*-triplet of *pseudo*-triplets character. This is because the cyclohexane substituted amine locks the other cyclohexane in the chair conformation, with the substituted amine in the equatorial position.

In **16** the azides are reduced to the corresponding amines, this gives a large shift in the peak corresponding to the two methine protons geminal to the primary amines to ( $\delta$  = 2.74 ppm), reflecting the decrease in inductive effect from the more electropositive amine groups. The peaks from the other two geminal protons shift only a by a small amount to

( $\delta$  = 2.69 ppm) and ( $\delta$  = 2.63) ppm. This reflects the electron-withdrawing and inductive effect of the different amine environments on the two cyclohexane rings. As the environment around the geminal proton on the monosubstituted cyclohexane doesn't change between the azide and amine the peak remains in the same place at the lowest shift as it only has one nitrogen group withdrawing electron density from it. However, for the proton on the *tris*-substituted cyclohexane geminal to the secondary amine, it is influenced by all three nitrogens and therefore now has the highest shift downfield. The peak for the other two protons geminal to the primary amines is in between the two, giving what appears as a merged *pseudo*-triplet of *pseudo*-triplet of *pseudo*-triplets.

In **17** the amines have undergone a Schiff base reaction with 2-pyridinecarboxylaldehyde to the corresponding imines. This gives a large shift in the peak downfield corresponding to the two methine protons geminal to the imine groups ( $\delta$  = 3.53 ppm), reflecting the strong electron withdrawing character of the imine groups. There is no change in multiplicity as all the substituents of the cyclohexane are in the equatorial positions and therefore the geminal protons are in the axial positions. There is also a shift in the second peak from the geminal proton to the secondary amine to ( $\delta$  = 2.97 ppm) with the peak corresponding to the proton geminal to the amine on the mono-substituted amine remaining almost the same.

Mass spectrometry (electrospray) for amine derivatives **13** to **17** supports the  $^1\text{H}$ -NMR characterisation data, by giving peaks corresponding to the monoprotonated molecular ions of each target molecule as follows; **13**  $m/z$  (ESI $^+$ ): 214.18 [M + H] $^+$ , **14**  $m/z$  (ESI $^+$ ): 522.2 [M+H], **15**  $m/z$  (ESI $^+$ ): 264.19 [M+H] $^+$ . **16**  $m/z$  (ESI $^+$ ): 212.21 [M+H] $^+$ , and **17**  $m/z$  (ESI $^+$ ): 390.26 [M+H] $^+$ . Formation of the desired targets is also supported by infrared spectroscopy. For **13** this gives peaks at 2927 and 2852  $\text{cm}^{-1}$  from C-H stretches of the cyclohexane rings and a very broad peak at 3267  $\text{cm}^{-1}$  suggesting the O-H and N-H peak of the secondary amine are overlapping in the same area. On tosylation of the hydroxyl groups to give **14**, the O-H is lost to give a broad peak at 3417  $\text{cm}^{-1}$  from the N-H stretch of the secondary amine. On reaction with sodium azide, to give **15**, there is the appearance of a strong sharp peak at 2079  $\text{cm}^{-1}$  indicative of the N=N stretch in an azide group, but the secondary amine NH peak remains constant. On reduction of **15** the peak corresponding to the azide group at 2079  $\text{cm}^{-1}$  is lost, and large broad peaks at 3310 and 3270  $\text{cm}^{-1}$  are seen from the N-H stretches of the primary amines. On forming the Schiff



base **17** with 2-pyridinecarboxaldehyde a peak at  $3056\text{ cm}^{-1}$  is seen from the N-H of the secondary amine and a new sharp peak at  $1645\text{ cm}^{-1}$  is seen from the C=N stretch of the imine groups. There is however a small peak at  $1715\text{ cm}^{-1}$  as seen with some of the other Schiff base ligands, indicating the presence of unreacted 2-pyridinecarboxaldehyde.

# **Chapter 3**

## *Coordination Chemistry*

### 3.1 Synthesis of metal complexes

To support the development of molecular hydrogen evolution catalysts, the coordination chemistry of the ligand sets developed was explored with a range of first row transition metals.

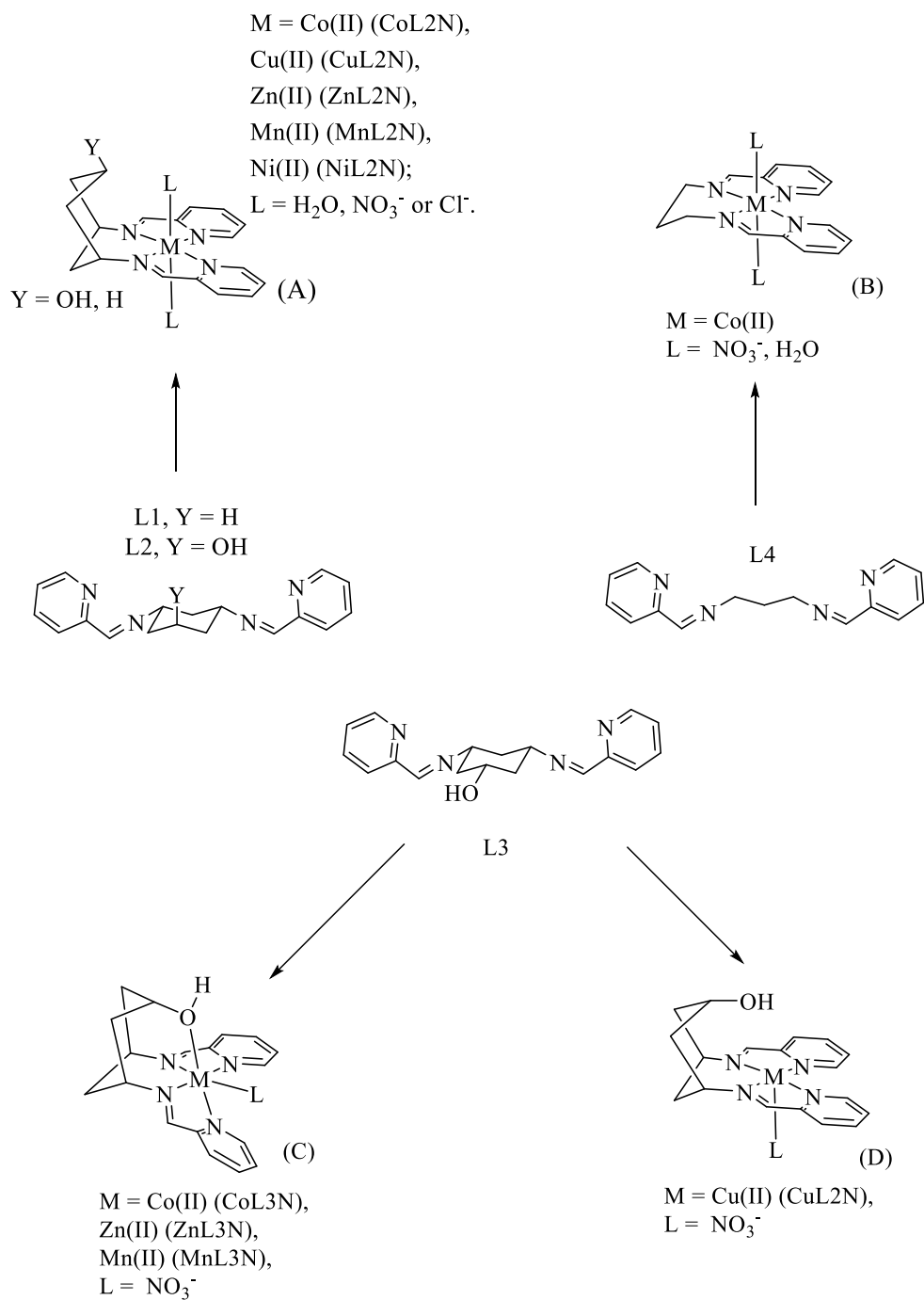


**Figure 3.1** Overview of possible coordination modes of L1, L2, L3 and L4, first row transition metal complexes.

An overview of the coordination chemistry of ligands **L1**, **L2**, **L3** and **L4** with first row transition metal complexes can be seen in **figure 3.1**. The chelating tetradentate imine ligands **L1**, **L2**, **L3**, and **L4**, all form mononuclear complexes with copper(II), cobalt(II), manganese(II), and zinc(II). The imino pyridine functionalities of the ligand encapsulate the metal centre in a chelating N<sub>4</sub> coordination pocket. This causes the cyclohexane backbone to ring-flip from the conformation with the 3,5-iminopyridines in the equatorial position (favoured in the absence of metal coordination), to a conformation with axial iminopyridine groups. This also conformationally locks the cyclohexane backbone, forcing the hydroxyl group present in **L2** and **L3** in the 1-position, to be either distal, out of the primary coordination sphere of the metal as in **L2**, or proximal, in the primary coordination sphere of the metal as in **L3**.

All complexes synthesised gave moderate yields by reaction of the ligand, **L1**, **L2**, and **L3** and **L4** with the appropriate metal salt at room temperature in methanol. Crystallisation of all the complexes was achieved by diffusion of ether into the concentrated metholic solution. The copper, cobalt and zinc and manganese complexes crystallised with the metal nitrate. However, in the case of nickel crystals were obtained with **L2** using nickel(II) chloride, and not the nitrate. In both the **L2** and **L1** complexes where the hydroxyl group is *trans* to the iminopyridines groups or absent, the *bis*-chelating N<sub>4</sub> coordination pockets are almost perfectly planar, with the *bis*-chelating iminopyridines occupying the equatorial coordination sites on the octahedral metal centre, and the counterion and/or water ligands *trans* to one another, as shown in (A) in **figure 3.1**. However, in the case of **L3**, where the hydroxyl group is *cis* to the iminopyridines groups two coordination mode were found. The hydroxyl group is either bound to the metal *cis* to the counterion, giving a trigonal prismatic geometry, which in turn means the *bis*-chelating coordination pocket is no longer planar as in the cobalt(II), manganese(II), and zinc(II) complexes, as illustrated in (C) in **figure 3.1**. Or where the hydroxyl is not bound, and the *bis*-chelating N<sub>4</sub> coordination pocket is almost perfectly planar as in the copper(II) complex, like in the **L2** and **L1** complexes, but giving a square pyramidal geometry due to the absence of a sixth ligand, as shown in **CuL3N**. With late transition metals such as silver(I), **L2**, has been shown to give dinuclear complexes, but is beyond the scope of this thesis.<sup>97,98</sup>

### 3.1.1 cobalt complexes

Over the course of this research cobalt complexes with ligand **L4**, (with a propane backbone) were also synthesised to help understand electrochemical properties of the systems, and answer questions relating to the effect of the sterics, electronics and flexibility or rigidity of the ligands.

The chelating tetradentate imine ligand **L4**, forms a mononuclear complex with cobalt(II) salts under highly dilute conditions, with the imino pyridine functionalities encapsulating the metal centre. This is illustrated in **(B)** in **figure 3.1**. The cobalt nitrate complex **CoL4N**, was prepared in 50% yield by the addition of **L4** as a 0.01 M solution in methanol to a solution of cobalt (II) nitrate also in methanol. Crystallisation attempts by vapour diffusion of diethyl ether into a concentrated methanolic solution resulted in microcrystals that were unsuitable for characterisation by x-ray diffraction. However, other data supports the formation of the product. Elemental analysis shows matches for the percentages of carbon, nitrogen and hydrogen expected for **CoL4N**. IR spectroscopy of the complex gives a sharp peak at  $1650\text{ cm}^{-1}$  consistent with a coordinated imine stretch as found in other imino pyridine complexes. Mass spectrometry gives a molecular ion peak at  $310.06\text{ m/z}$  and a fragmentation profile consistent with  $[\text{M}-2\text{NO}_3\text{H}]^+$ . In addition to this characterisation is provided by paramagnetic  $^1\text{H-NMR}$ , this is described in greater detail in **section 3.3.4**. X-ray structural data for the cobalt(II) perchlorate salt of this ligand has been shown previously and used to represent the mononuclear binding mode of this ligand for cobalt, presented in **figure 3.5**.

### 3.1.2 Non- coordinating anion – BF<sub>4</sub>

During the course of this work questions were raised as to the effect of nitrate on the electrochemistry of the cobalt system synthesised. Therefore, it was decided that the cobalt complexes of the ligand sets developed with non-coordinating anion BF<sub>4</sub><sup>-</sup> would also be synthesised and studied.

For the synthesis of these cobalt complexes with non-coordinating BF<sub>4</sub><sup>-</sup> anions, it was necessary either to carry out anion exchange metathesis from another salt, or to use the metal salt of the non-coordinating anion. Preliminary exploration of anion exchange metathesis of BF<sub>4</sub><sup>-</sup> salts, such as KBF<sub>4</sub>, NaBF<sub>4</sub> and NH<sub>4</sub>BF<sub>4</sub> with the nitrate salt of the cobalt complexes gave only partial exchange of one of the nitrates or a mixture, which due to their similarities in solubility make their purification difficult. For example, anion metathesis in methanol of **CoL3N** with KBF<sub>4</sub> results in precipitation of what is presumably (**CoL3NB**) due to its paramagnetic <sup>1</sup>H-NMR being intermediate between **CoL3N** and **CoL3B**, but in low yield. Therefore, it was decided to approach the tetrafluoroborates *via* a metal salt of the non-coordinating anion, [Co(NCMe)<sub>6</sub>](BF<sub>4</sub>)<sub>2</sub>.<sup>119</sup> The paramagnetic NMR of the three salts **CoL3N**, **CoL3NB**, and **CoL3B** are shown in **figure 3.23**.

Attempts to synthesise complexes using the hexaaqua tetrafluoroborate cobalt(II), [Co(H<sub>2</sub>O)<sub>6</sub>](BF<sub>4</sub>)<sub>2</sub>, failed due to the limited solubility of this salt in many common organic solvents including acetonitrile, THF, DCM, ethyl acetate and DMSO, which is essential for complex formation.

Therefore, the synthesis of Co(MeCN)<sub>6</sub>(BF<sub>4</sub>)<sub>2</sub> was investigated, by extended reflux of the [Co(H<sub>2</sub>O)<sub>6</sub>](BF<sub>4</sub>)<sub>2</sub> under an atmosphere of nitrogen. A Soxhlet extractor was fitted to the top of the reaction vessel containing molecular sieves to help dehydrate the salt, as shown in the literature.<sup>120</sup> Infrared spectroscopy of the product indicates the presence of nitrile functionalities, giving sharp stretching frequencies at 2316 and 2288 cm<sup>-1</sup>. Signals at 3006 and 2944 cm<sup>-1</sup> were attributed to methyl groups of the acetonitrile ligands. A broad stretch at 3396 cm<sup>-1</sup>, however, would suggest the presence of an O-H group, indicating that complete dehydration had not been achieved. Elemental analysis also showed that composition of the compound is consistent with a dimer, with hydroxyl groups bridging

two cobalt centres as shown in **figure 3.3**. This may, however, be due to drying *in vacuo*, where MeCN may be lost and any adventitious water would coordinate to the cobalt. The hydroxyl bridging groups are formed due to the highly electropositive metal centre polarising the bound aquo ligands making them highly acidic, facilitating proton loss to give the hydroxyl.

It should also be understood that in solution a dynamic equilibrium will exist. Water and acetonitrile are both labile for cobalt(II) and therefore, there will be a large mixture of different structures present in solution which at high dilution in acetonitrile, should be pushed to the monomeric and dimeric forms.

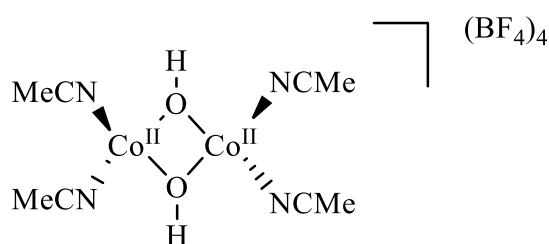


**Figure 3.3** Proposed structure of acetonitrile soluble Co(II)(BF<sub>4</sub>)<sub>2</sub> salt.

Despite the uncertainty as to its exact composition, the solubility of the product in acetonitrile made it an attractive material for the synthesis of the complexes and used to give complexes non-coordinating BF<sub>4</sub><sup>-</sup> salt of three of the ligand sets.

### 3.1.3 Characterisation and synthesis of cobalt(II) tetrafluoroborate complexes

The complexes **CoL4B**, **CoL3B** and **CoL1B** were prepared by stirring **L4**, **L3**, and **L1** with the acetonitrile soluble **CoB**, respectively under highly diluted conditions, in degassed acetonitrile for approximately 45 minutes at room temperature and under an inert atmosphere of nitrogen, **figure 3.4**.

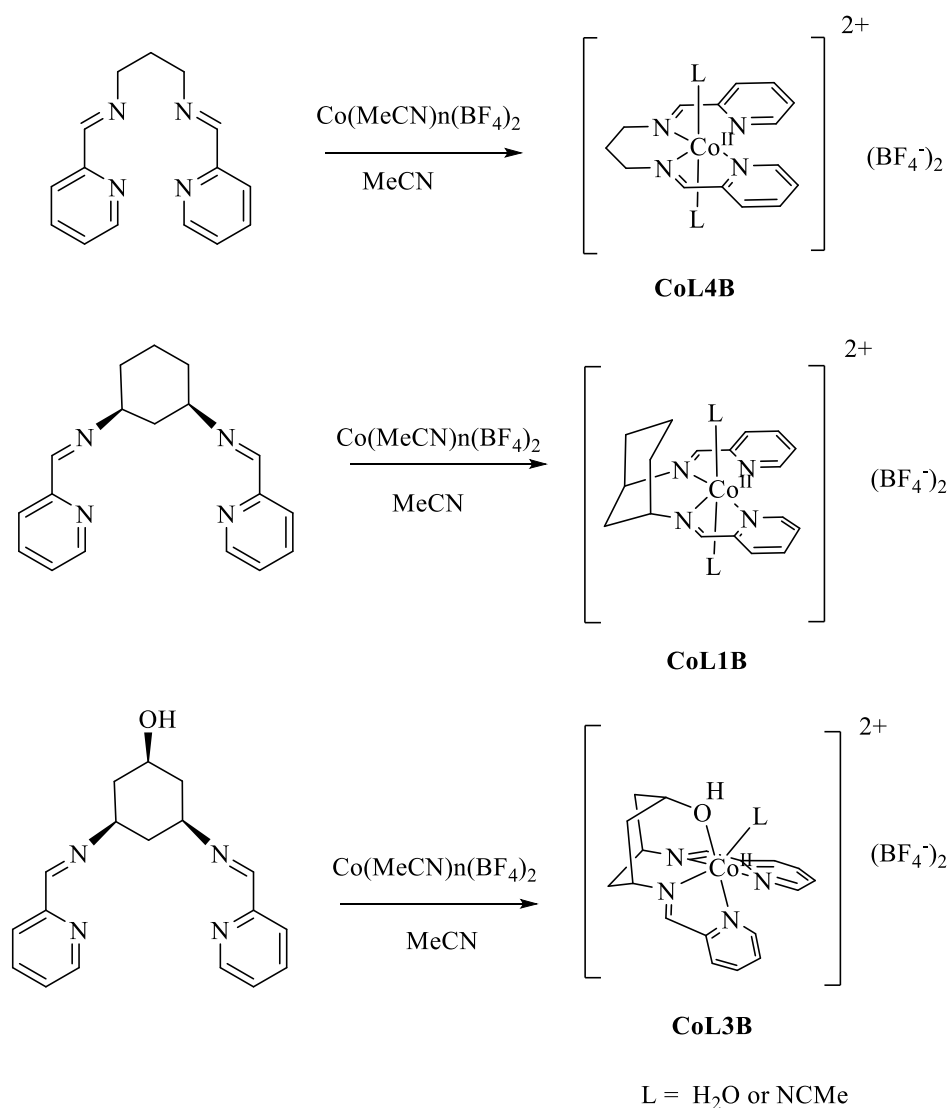


**Figure 3.4** Synthesis of cobalt(II) bis(iminopyridine) tetrafluoroborate complexes

The difficulty in driving complete formation of  $\text{Co}(\text{MeCN})_6(\text{BF}_4)_2$  suggests they are likely to be aqua ligands. However, whether aqua or acetonitrile, these ligands should be labile in solution.

All attempts at growing X-ray quality crystals for the three  $\text{BF}_4^-$  salts failed. Other characterisation data, however, shows that the complexes were formed. Solution phase IR in acetonitrile for **CoL4B** gives peaks at 3637, 1529 and  $1635\text{ cm}^{-1}$ . The band at  $3637\text{ cm}^{-1}$  can be assigned to an O-H stretch, mostly likely from water axially bound to the cobalt metal centre. The peak at  $1529\text{ cm}^{-1}$ , can be attributed to aromatic C=C, and the peak at  $1635\text{ cm}^{-1}$  characteristic of C=N stretches of the imine group. Similarly, **CoL1B** shows signals for C-H and C=N stretches at 2879 and  $1636\text{ cm}^{-1}$  respectively. Also



observed, however, is a peak at  $1714\text{ cm}^{-1}$ , which is characteristic of the presence of an aldehyde and suggests some imine hydrolysis. **CoL3B** has the same C-H and imine signals, with an additional weak but broad signal at  $3308\text{ cm}^{-1}$ , corresponding to the cyclohexane hydroxy group.

The mass spectrum of **CoL4B** shows a peak at  $m/z$  174.05 with a molecular profile corresponding to  $[M+\text{MeCN}]^{2+}$ . Mass spectrometry of **CoL1B** gives a molecular peak at  $m/z$  438.10 with a molecular profile corresponding to  $[M+2\text{MeCN}]^{2+}$ . The mass spectrometry of **CoL3B** gives a molecular peak at  $m/z$  183.55 with a molecular profile corresponding to a  $[M+\text{MeCN}]^{2+}$ . Mass spectroscopy of all three compounds was undertaken in acetonitrile.

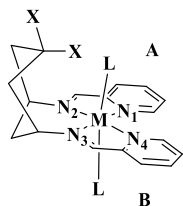
The electrochemical profiles of the tetrafluoroborate complexes **CoL4B**, **CoL1B**, and **CoL3B** are also comparable to their nitrate based counterparts, **CoL4N**, **CoL1N**, and **CoL3N**, as shown in **figure 4.37**. Which as the fundamental electronics of the *bis*-imino pyridine ligand frameworks are the same can be expected, and therefore act as further confirmation that the complexes were formed.

### 3.2 Crystal structures

**Table 3.1** Bond lengths in the coordination sphere of the metals for Co(II), Cu(II), Mn(II) and Zn(II) complexes of DDP (**10**, **L1**), DDOP (**5**, **L2**), and DDOPi (**9**, **L3**).

Compound	Iminopyridine arm (1) Length/Å		Iminopyridine arm (2) Length/Å		$R_{M-O}$ /Å				
	M - N(1) Py	M - N(2) Im	M - N(3) Py	M - N(4) Im	Water	(axial) Nitrate (B)	(axial) Nitrate (A)	(cis) Nitrate*	hydroxyl relay distance
<b>CoL4P</b>	2.142(6)	2.099(7)	2.091(7)	2.148(7)	2.084(7) 2.093(7)				
<b>CoL1N</b>	2.118(1)	2.123(3)	2.103(3)	2.194(1)	2.085(1) <sup>1</sup>	-	-	-	-
<b>CoL2N</b>	2.137(6)	2.112(7)	2.094(6)	2.144(7)	2.153(6)	-	2.138(6)	-	5.109
<b>CoL3N</b>	2.176(4)	2.142(14)	2.116(5)	2.205(4)	-	-	-	2.117(3)	2.075(2)
<b>CuL1N</b>	2.033(3)	2.008(3)	1.989(3)	2.043(3)	-	2.399(3)	2.399(3)	-	-
<b>CuL2N</b>	2.055(5)	2.015(6)	1.994(5)	2.063(6)	2.366(6)	-	2.515(5)	-	5.087
<b>CuL3N</b>	2.039(5)	1.985(5)	1.979(5)	2.042(5)	-	2.398(4)	-	-	2.752
<b>MnL1N</b>	2.510(9)	2.254(5)	2.510(9)	2.254(5)	2.154(2)	-	-	-	-
<b>MnL2N</b>	2.270(5)	2.286(5)	2.250(5)	2.288(5)	-	2.257(5)	2.216(5)	-	5.186
<b>MnL3N</b>	2.307(1)	2.255(1)	2.255(1)	2.272(1)	-	-	-	2.140(9)	2.176(9)
<b>ZnL2N</b>	2.137(2)	2.110(2)	2.136(2)	2.126(9)	2.173(2)	-	2.280(2)	-	5.152
<b>ZnL3N</b>	2.232(3)	2.112(4)	2.189(3)	2.187(4)	-	-	-	2.085(2)	2.123(1)

<sup>1</sup>1-X,+Y,1/2-Z (symmetry generated), \* Bond lengths for *cis* nitrate ligands found in the trigonal prismatic complexes of **L3**.  
Planes (A/B) and labelled nitrogen atoms are given in the figure to the below.



L = H<sub>2</sub>O, NO<sub>3</sub><sup>-</sup>

X = H, OH

Crystal structures for metal complexes **CoL4P** is from reference 118. **CoL2N**, **CuL2N**, and **ZnL2N** are from reference 121.

### 3.2.1 X-ray crystal structures of cobalt complexes

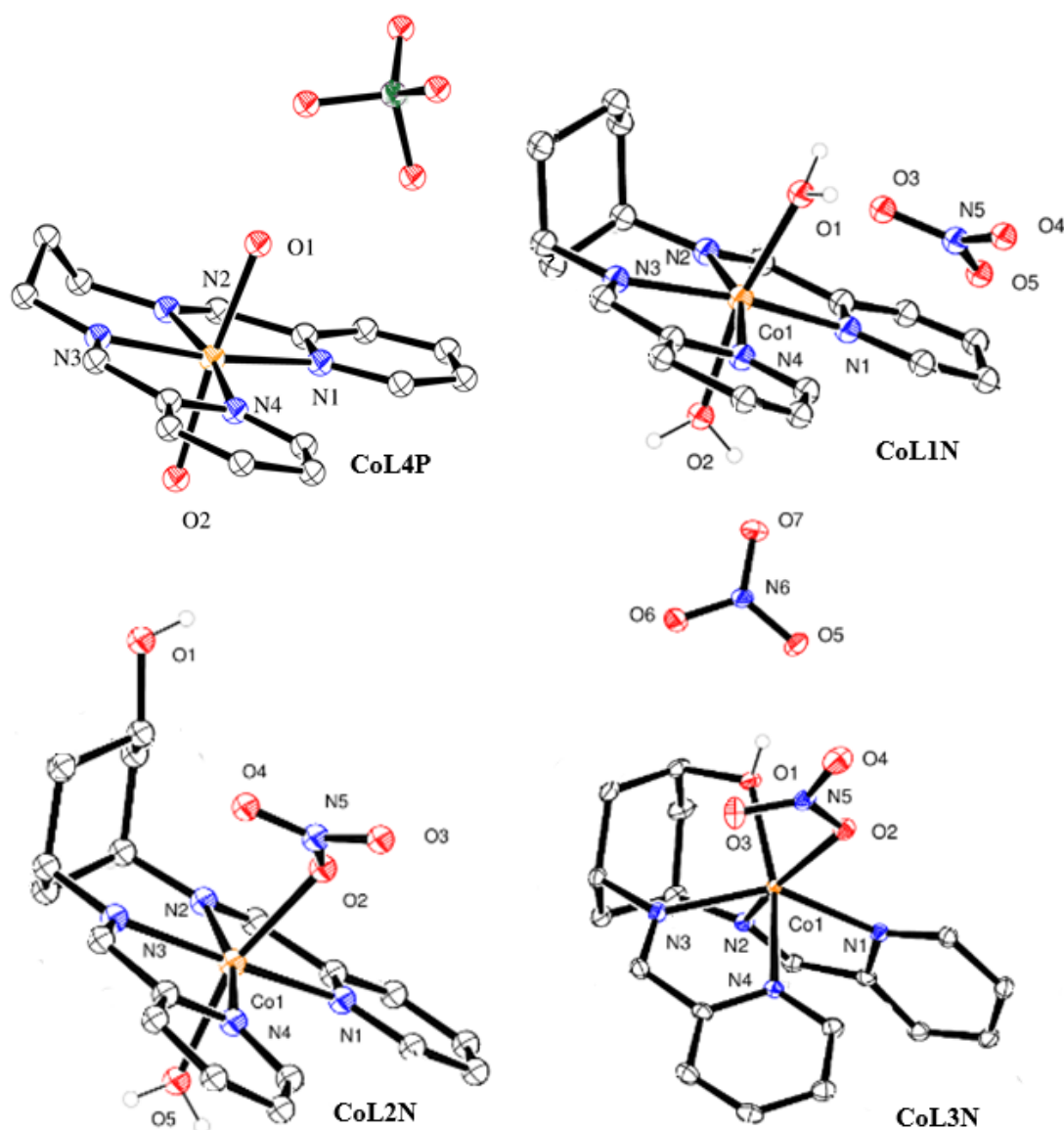


**Figure 3.5** ORTEP-3 representation of the complex cation in **CoL4P** (from ref 102) (*top left*), **CoL1N** (*top right*), **CoL2N** (*bottom left*), and **CoL3N** (*bottom right*), thermal ellipsoids at 30% probability; carbon atoms are unlabelled.

As previously stated X-ray structural data could not be obtained for the cobalt(II) nitrate salt, **CoL4N**, and therefore, data is shown for the cobalt(II) perchlorate salt **CoL4P** of this ligand, from the literature, this is presented in **figure 3.5** along with the other cobalt based structures.<sup>102</sup>

Both **CoL4P** and **CoL1N** show nearly identical octahedral coordination geometries. The two imino pyridine arms of the chelate lie in the equatorial plane of the octahedra, with

two axially bound aqua ligands filling the other two sites; these are themselves hydrogen bonded to the counter perchlorate and nitrate anions. As the counterions are not bound directly to the cobalt centre, their effect on the electronics and therefore bonding around the cobalt centre should be minimal. Any influence the counterions have will be in the form of cumulative hydrogen bonding interactions through the crystal lattice. If in effect, these influences are most likely to affect the bonding interactions of the hydrogen bonding aqua ligands.<sup>121</sup> The cyclohexane ring seems to have minimal effect on the bonding of the imino pyridine chelate, being the same within experimental error for the average Co-N(py) and Co-N(imine) bonding distances in **CoL4P** as found in the cyclohexane complex **CoL1N**.

**CoL2N** shows analogous octahedral coordination to **CoL4P** and **CoL1N**, however, instead of having two axially bound water molecules, the axial coordination site closest to the cyclohexane is occupied by one of the nitrate counterions. As the only difference in ligand structure from **CoL1N** is the distal hydroxyl group on the cyclohexane, it might be surmised that this is a consequence of hydrogen bonding from the hydroxyl group to the nitrate stabilising decreasing its lability and exchange with aqua ligands. However, in the solid state it is most likely an intermolecular solid-state effect, not an intramolecular one, as the closest intramolecular O...O distance is *ca.* 3.953 Å, and O-H...O hydrogen bonding requires O...O distances of no more than around 3 Å. The H atom (crystallographically located) is also pointing away from the nitrate on the same molecular ion. **CoL3N**, however, shows completely different coordination behaviour to the other cobalt complexes, as the DDOPi (**9**, **L3**) ligand enforces a trigonal prismatic geometry. The proximal hydroxyl group effectively pulls the cobalt metal centre from the planar N<sub>4</sub> pocket of the octahedron, resulting in the imino pyridine arms twisting. A nitrate counterion then fills the position *cis* to the proximal hydroxyl group to give the trigonal prismatic geometry.

Cobalt(II) sits on the borderline in between hard and soft acids in HSAB theory, and so binds strongly to the pyridine and imine N-donors which themselves sit on the borderline of hard and soft bases. The Co-O distance to the axially bound waters in **CoL1N** are 3.3% shorter than found in **CoL2N**, 2.085(1) Å in **CoL1N** compared to 2.153(2) Å in **CoL2**. The smaller Co-O distance in axial ligand in **CoL1N** compared to that of **CoL2N** is probably a consequence of electronics, as the cobalt centre in **CoL1N** should be more

electropositive than in **CoL2N** due to the weakly coordinating, less electron rich nitrate being bound in **CoL2N** and therefore resulting in a stronger bond with the aqua ligands in **CoL1N**, resulting in a difference of less than 0.03 Å between the average Co-N and Co-O bond lengths.

**CoL1N** and **CoL2N** both form 2-dimensional hydrogen bonded networks which run in layers parallel to the crystallographic *ab* plane, this is due to the ability of **CoL1N** to donate two hydrogen bonds via the two aqua ligands to the two nitrate groups, which in turn hydrogen bond to another molecule via the bound aqua ligands and so forth. This creates chains of cations, linked through hydrogen bonds. In **CoL2N** this is also the case, however, there are hydrogen bonding interactions between the distal hydroxyl group, nitrate and aqua ligand, as shown in **figure 3.6**.<sup>122,102</sup> In comparison, however, **CoL3N** does not form a 2-dimensional hydrogen bonding network, having no hydrogen bonding interactions in the crystal structure linking cations. Although, there is an internal hydrogen bond between the proximal hydroxyl group and the unbound nitrate of *ca.* 2.67 Å. Interestingly in **CoL3N**, there is a strong interaction between the oxygen of the bound nitrate anion and the nitrogen atom of the imine group, with a nitrogen oxygen distance of *ca.* 3.05 Å.

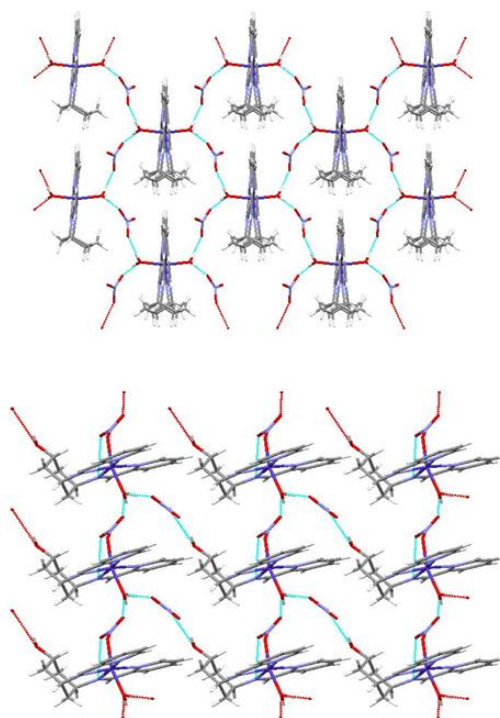


**Figure 3.6** Mercury crystal packing diagrams showing hydrogen bonding networks for:  
**CoL1N** *ac* plane (*top*), **CoL2N** *ac* plane (*bottom*)

### 3.2.2 X-ray crystal structures of copper complexes

The copper complexes of DDOP (**5**, **L2**), DDOPi (**9**, **L3**), and DDP (**10**, **L1**), have the shortest Cu-N equatorial distances, but the longest Cu-O distance for the axial ligands, and show a procession from 6 to 5 coordinate from **CuL1N**, **CuL2N** to **CuL3N**. In the case of **CuL1N** the equatorial Cu-N distance averages *ca.* 2.018 Å, and the two nitrates have Cu-O bonding distances of 2.399(3) Å. In **CuL2N** the equatorial Cu-N average distance is 2.032 Å. A weakly bound water is bound to the copper on the bottom **B** face of the N<sub>4</sub> -plane and a very weakly bound nitrate NO<sub>3</sub><sup>-</sup> **A** on the top face (see **section 3.2**), the Cu-O distances are 2.364(2) Å to the water and 2.515(2) Å to the nitrate. In this case the copper centre can be viewed as being almost 5-coordinate. **CuL3N**, however, appears to be fully 5-coordinate with the equatorial Cu-N average distances of 2.011 Å, and a weakly bound nitrate on the bottom face of the N<sub>4</sub> -plane NO<sub>3</sub><sup>-</sup> **B** with Cu-O distance of 2.399(3) Å, akin to that of the nitrates found in **Cu1N**. There may, however be a weak interaction with the ligand hydroxyl group whose oxygen is situated *ca.* 2.75 Å from Cu. In this way, the behaviour of **CuL3N** is completely different to that found in the other complexes of DDOPi (**9** **L3**). In the zinc(II), cobalt(II) and manganese(II) complexes, the DDOPi (**9**, **L3**) ligand enforces trigonal prismatic geometry as it is favourable for the proximal hydroxyl group to ligate to the metal centres.

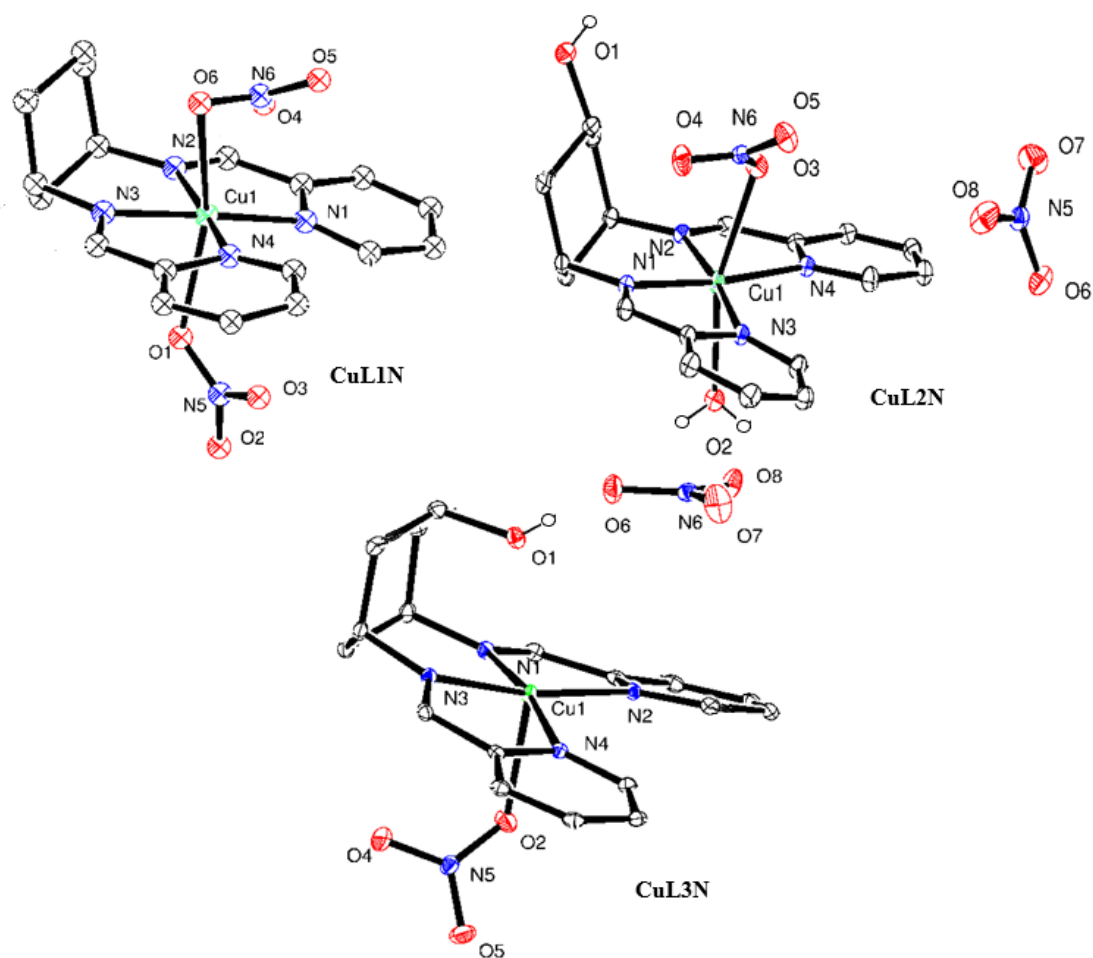


**Figure 3.7** ORTEP-3 representation of the complex cation in **CuL1N** (left), **CuL2N** (right) and **CuL3N** (bottom) thermal ellipsoids at 30% probability; carbon atoms are unlabelled.

As the three ligand substituents are all *cis* in the 1,3,5 positions of the cyclohexane ring this means that ligation of two of these groups, (the two imine nitrogen atoms, **N2** and **N3**), to a metal centre puts the cyclohexane group into the chair conformation with two groups in the axial positions. As there is rotational freedom around the cyclohexane-N-imine bonds, coordination of the third functionality (the proximal hydroxyl) also in the axial position, governs the coordination mode, and therefore the geometry of the metal complex formed. If the third group strongly ligates the metal centre, the metal is affectively pulled out of the planar **N4** equatorial pocket, with the cy-N-bonds twisting to allow steric relaxation, reducing the overall free energy of the system. This gives the trigonal prismatic geometry found in **CoL3N**, **MnL3N**, and **ZnL3N**. In **CuL3N**, however, the rigidity and conformational demands of the ligand; the hydroxyl can only bind properly if the imine arms twist and produce a trigonal prismatic geometry. However, in copper(II) the energetic gain of forming an extra coordinate bond from the

hydroxyl to the metal is not great enough to compensate for the penalty of twisting the imines giving the trigonal prismatic geometry. This leads to little or no bonding interaction of the proximal hydroxyl. This therefore, means that the N<sub>4</sub> equatorial pocket remains almost planar like that found in **CuL2N** and **CuL1N** and other complexes of **L2**, and **L1** with the proximal hydroxyl **O1** hanging freely over the copper centre, with a Cu–O<sub>1</sub> distance of *ca.* 2.75 Å. **CuL3N** has almost perfectly square-pyramidal geometry with an index for  $\tau_5$  of 0.05116.<sup>123,124</sup>

### 3.2.3 X-ray crystal structures of zinc complexes

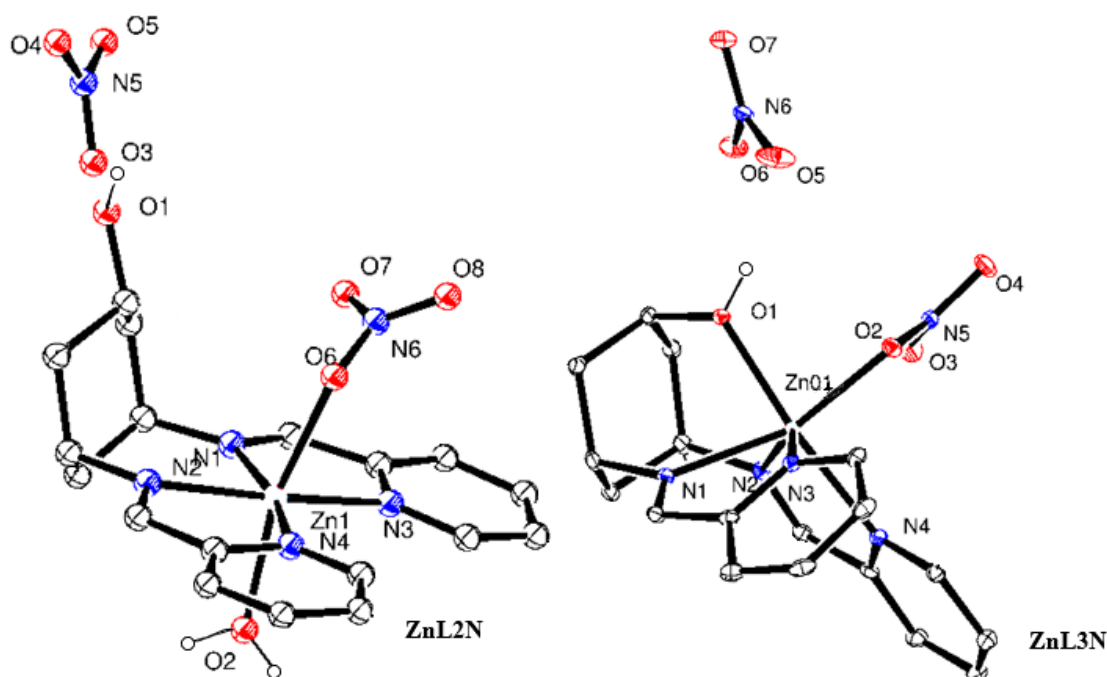


**Figure 3.9** ORTEP-3 representation of the **ZnL2N** (left) and **ZnL3N** (right) thermal ellipsoids at 30% probability; carbon atoms are unlabelled.

Unfortunately X-ray crystallographic data for **ZnL1N** obtained highly disordered preventing the resolving of a reasonable X-ray structure. However, **ZnL2N** shows the same octahedral coordination geometry and coordination as found in **CoL2N**, **CuL2N**, **NiL2C**, and **MnL2N**.<sup>98,102</sup> The zinc(II) complex of **L3**, **ZnL3N**, also shows the same trigonal prismatic geometry as found in **CoL3N**, **CuL3N** and **MnL3N**.

Zinc(II) also sits on the borderline between hard and soft acids, and therefore binds more strongly to the pyridine and imine N-donors than the harder O-donors. As seen in **ZnL2N** the average equatorial Zn–N distances is *ca.* 2.127 Å, in the aqua ligand the Zn–O bond is



2.173(3) Å, and the weaker bound nitrate Zn-O bond at 2.280(2) Å. Interestingly in **ZnL3N** there is a deviation in this behaviour. It is found that the shortest bond is to the nitrate, with a Zn-O bond length of 2.085(1) Å, and then that of hydroxyl with a Zn-O bond length of 2.223(1) Å, which should be a harder base than the iminopyridine N donors. This may be caused by the interaction between one of the oxygen's of the bound nitrate and the nitrogen of the imine group, which in **ZnL3N**, has a distance of *ca.* 3.072 Å. The average Zn-N bonding distances though are *ca.* 2.18 Å, 4.4% longer than in **ZnL2N**. The variation in distances may reflect steric constraints imposed on the metal by the ligand environment, due to the enforcement of geometry from the cyclohexane ring, the hydroxyl affectively pulls the zinc out of the N<sup>4</sup> macrocyclic plane. There are no Jahn-Teller distortions and no ligand field stabilisation energy, as Zn<sup>2+</sup> has a set of completely filled d orbitals.

### 3.2.4 X-ray crystal structures of manganese complexes

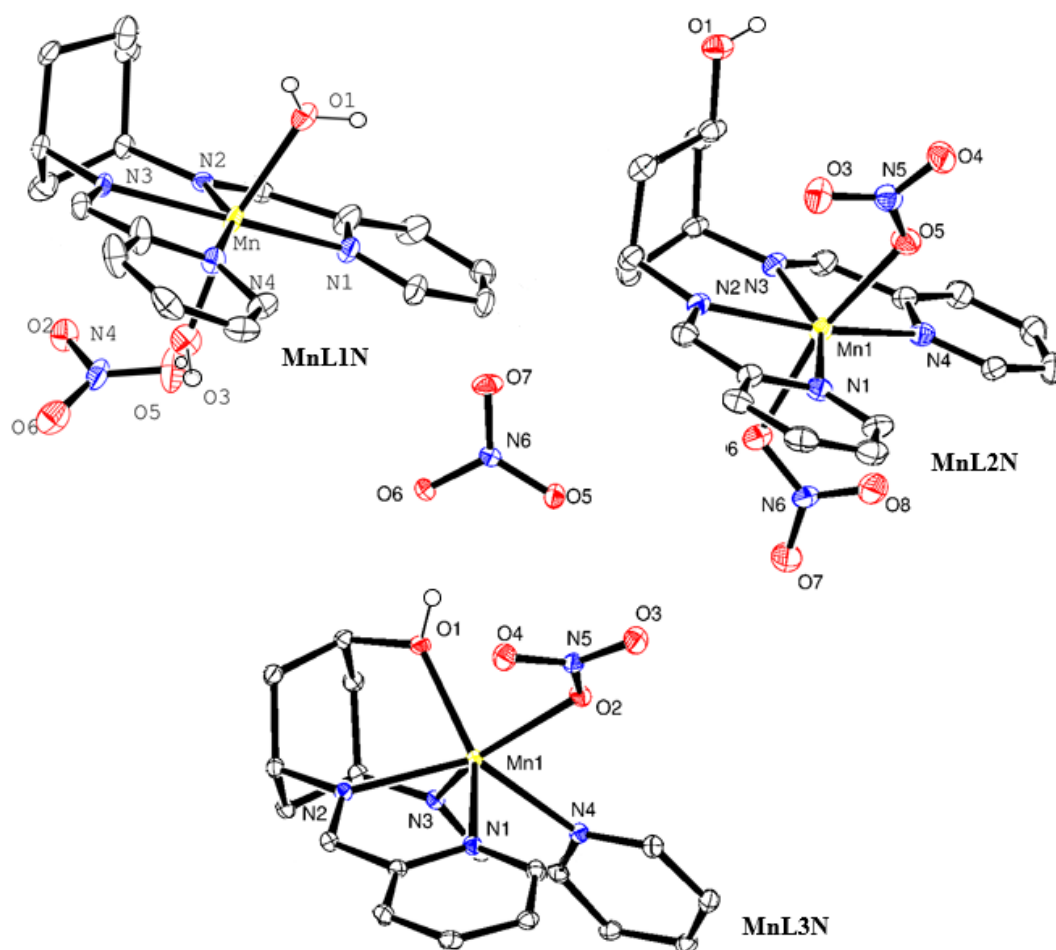


**Figure 3.10** ORTEP-3 representation of the complexes **MnL1N** (*left*), **MnL2N** (*right*), and **MnL3N** (*bottom*), thermal ellipsoids at 30% probability; carbon atoms are unlabelled.

**MnL1N** shows the same octahedral coordination geometry and the two axial aqua ligands as found in **CoL1N**. **MnL2N** shows the same octahedral coordination geometry and co-ligands as found in **CoL2N**, **CuL2N**, **NiL2C** and **ZnL2N**. The manganese(II) complex of DDOPi (**9, L3**), **MnL3N**, also shows the same trigonal prismatic geometry as found in **CoL3N** and **ZnL3N**.

$\text{Mn}^{2+}$  is classed as a hard acid in HSAB theory due to its small size and therefore binds most strongly to the harder oxygen based ligands. In **MnL1N** the average equatorial Mn-N distance is 2.385 Å, with the Mn-O distance for the aqua ligands being 2.154 Å. In **MnL2N** the average equatorial Mn-N distance is ca. 2.274 Å. A difference in the Mn-O distances for the two axially bound nitrates is observed, where the Mn-O distance for **NO<sub>3</sub><sup>-</sup> B** is 1.9% longer at 2.257(5) Å than **NO<sub>3</sub><sup>-</sup> A** at 2.216(5) Å. This may be due to the lattice structure interactions as illustrated in **figure 3.11**, as it is seen that there is a strong H-bond between an oxygen of **NO<sub>3</sub><sup>-</sup> B** and the hydroxyl group of another complex, O-O (H-Bond) distance of 2.919 Å, which may cause an elongation of the Mn-O bond.

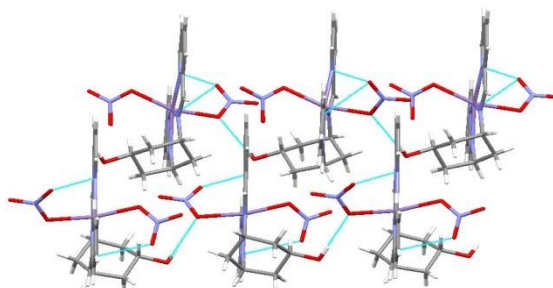


**Figure 3.11** Mercury representation of H-bonding in **MnL2N**, shown along the *bc* plane.

Like **CoL3N**, **MnL3N** does not form a 2-dimensional hydrogen bonding network, having no hydrogen bonding interactions in the crystal structure linking cations. Although, there is, as in **CoL3N**, an internal hydrogen bond between the proximal hydroxyl group and the unbound nitrate of ca. 2.64 Å. In **MnL3N**, there is also an interaction between the oxygen of the bound nitrate anion and the nitrogen atom of the imine group, with a nitrogen oxygen distance of ca. 3.98 Å, however this is weaker than found in **CoL3N**.

### 3.2.5 X-ray crystal structures of nickel complexes

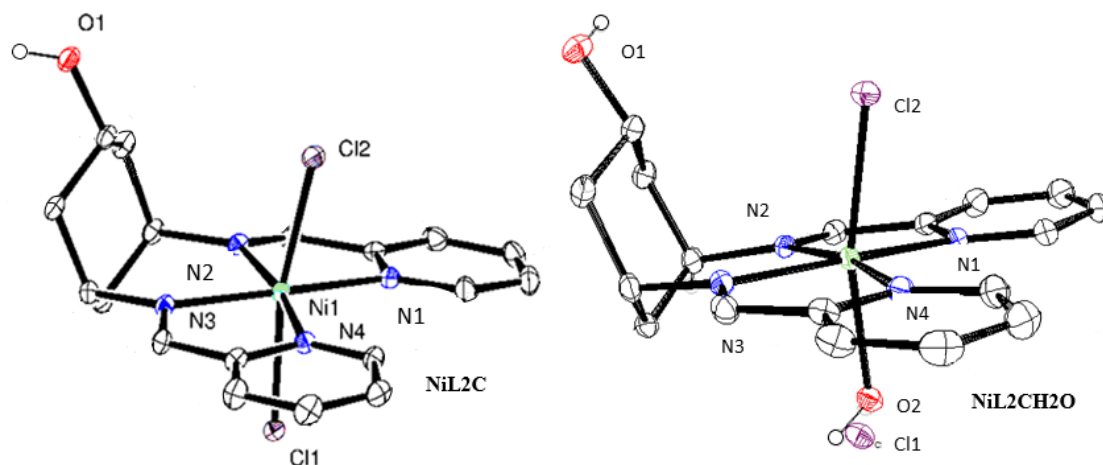


**Figure 3.12** ORTEP-3 representation of the complex cation in **NiL2C** (left) and **NiL2CH2O** (right) thermal ellipsoids at 30% probability; carbon and hydrogen atoms are unlabelled.

Under the conditions attempted, only pure material and x-ray quality crystals of one nickel(II) complex was achieved with the **L2** ligand set giving **NiL2C**. **NiL2C** gives the same geometry found with the other 1<sup>st</sup> row transition metals used with the **L2** ligand, but with two axially bound chloride ligands. This complex had previously been synthesised using **L2** under the same highly dilute methanolic conditions, but gave (**NiL2CH2O**), with an aqua ligand on the **B** face, however, instead of a chloride ligand found in this work. This suggests that the axial ligands are highly labile, specifically on the **B** face, (shown in the diagram of **table 3.1**). The only cause for this could be extra water in either the methanol or the starting materials. The Ni-N bonds remain constant between the two complexes.

**Table 3.2** Bond lengths in the coordination sphere of the metals for Ni(II) DDOP (**5**, **L2**) complexes.

Compound	Iminopyridine arm (1) Length/Å		Iminopyridine arm (2) Length/Å		$R_{M-L}$ /Å	
	M - N(1)	M - N(2)	M - N(3)	M - N(4)	(axial) chloride (A face)	(axial) chloride or water (B face)
	Py	Im	Py	Im		
<b>NiL2C</b>	2.118(3)	2.048(3)	2.078(2)	2.104(3)	2.430(8)	2.449(8)
<b>NiL2CH2O</b>	2.119 (9)	2.067(8)	2.070(9)	2.127(9)	2.401(6)	2.121(7)

*Crystal structures for metal complexes **NiL2CH2O** is from reference 102, 98*

### 3.3 Octahedral versus trigonal prismatic geometry

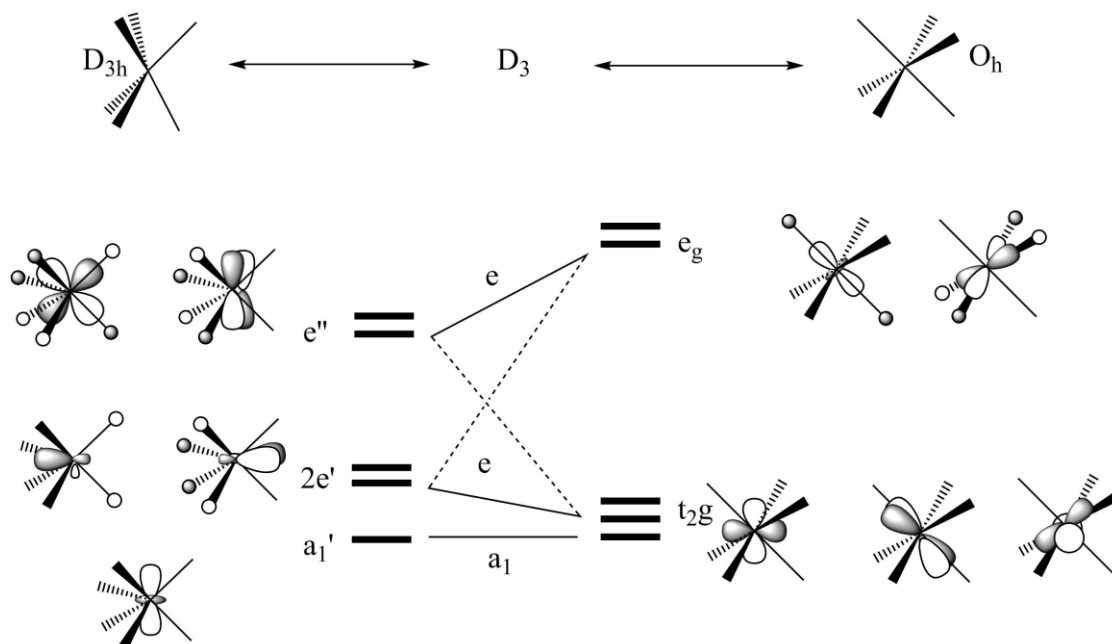


**Figure 3.13** Correlation diagram for the d orbitals between the trigonal prism (*left*) and the octahedron (*right*).

The preference for trigonal prismatic geometry *vs* octahedral geometry has been studied in depth by Alvarez and co-workers,<sup>125</sup> using a Jahn-Teller approach they showed that in the trigonal prismatic geometry the d orbitals are split into three sets (figure 8). While the  $a_1'$  orbital is strictly non-bonding (disregarding  $\pi$  interactions), the  $2e'$  and  $e''$  sets have different degrees of  $\sigma$ -antibonding character. The antibonding character of the  $2e'$  set, however, is reduced by the mixing with high lying orbitals of the same symmetry involving the empty metal  $3e'$  ( $p_x, p_y$ ). At the same time mixing of  $1e'$  and  $2e'$  enhance the bonding character of the former. Mixing of  $1e'$  and  $2e'$  is forbidden in octahedral geometry because they have different symmetries ( $T_{1a}$  and  $T_{2g}$ , respectively). As a consequence,  $1e'$  has less metal character in octahedral than in trigonal prismatic geometry. This results in a preference for the trigonal prismatic geometry for complexes with  $d^0$ ,  $d^1$ , and low spin  $d^2$  electronic configuration.

**Table 3.3** Preference for octahedral or trigonal prismatic geometry for different ‘d’ electron electronic configurations, classified according to the difference in occupation between the 2e’ and e’’ orbital sets in the trigonal-prismatic geometry from 125.

Trigonal Prismatic			Octahedral	
←-----→				
d <sup>0</sup> ,d <sup>1</sup>				
(LS) d <sup>2</sup>	(HS) d <sup>2</sup>			
	(LS) d <sup>3</sup>	(HS) d <sup>3</sup>		
	(HS) d <sup>4</sup>	(LS) d <sup>4</sup>		
(HS) d <sup>5</sup>			(LS) d <sup>5</sup>	
(HS) d <sup>6</sup>				(LS) d <sup>6</sup>
	(HS) d <sup>7</sup>		(LS) d <sup>7</sup>	
		d <sup>8</sup>		
	d <sup>9</sup>			
d <sup>10</sup>				
(HS) - high spin; (LS) - low spin				

For electron configurations other than that of d<sup>0</sup>, d<sup>1</sup>, and low spin d<sup>2</sup>, the twist of the trigonal prism towards the octahedron can be explained as a second-order Jahn-Teller (SOJT) effect. This effect produces a stabilisation of the molecule through mixing of nearby occupied and empty orbitals that become of the same symmetry upon distortion. This mixing is governed by the symmetry rules of first and second order Jahn-Teller effects. The stabilisation resulting from the SOJT distortion which converts the trigonal prism into an octahedron is dependent on the populations of the 2e’ and e’’ orbitals. All d<sup>n</sup> configurations in trigonal prismatic coordination can be classified by the difference in occupation of those two orbital sets. The trigonal prismatic geometry is easily attainable for electronic configurations d<sup>0</sup>, d<sup>1</sup>, and low spin d<sup>2</sup>, high spin d<sup>5</sup> or d<sup>6</sup> and d<sup>10</sup>. In contrast, a strong drive is found towards octahedral geometry for complexes of high spins d<sup>3</sup>, low-spin d<sup>6</sup> or d<sup>8</sup> configurations. The preference for trigonal prismatic or octahedral geometry of different electronic configurations is summarised in **table 3.3**.<sup>125</sup>

**Table 3.4** Calculated energy difference between the found the free energy of the optimised trigonal prismatic geometries and the free energies of the optimised octahedral geometry structures with the hydroxyl *trans* to the counterion and the iminopyridine rings for **L3** metal complexes.

Complex	Added stability of trigonal prismatic geometry kJ/mol
<b>ZnL3N</b>	70
<b>MnL3N</b>	63
<b>CuL3N</b>	28
<b>CoL3N</b>	30

The DDOPi (**9 L3**) ligand has preference for trigonal prismatic geometry for the zinc(II), manganese(II) and cobalt(II) complexes. This coordination mode has been seen previously in cyclohexane based ligands in tach complexes of the form  $M(\text{Py-TACH})_3^{2+}$  with three imino pyridine arms, as shown in **figure 3.14**.<sup>126</sup> DDOPi (**9 L3**) however, gives the open square-pyramidal geometry for **CuL3N** due to  $d^9$  Jahn-Teller distortions. All the complexes synthesised should be high spin, as the imino pyridines only have a moderate ligand field strength (strong  $\sigma$  donor, weak  $\pi$  acceptor) and the co-ligands (water, nitrate, hydroxyl) are weak field. **ZnL3N**, **MnL3N** and **CoL3N** which have  $d^{10}$ ,  $d^5$  (HS) and  $d^7$  (HS) electronic configurations, respectively, have trigonal prismatic geometry which is consistent with that shown in **table 3.3**.

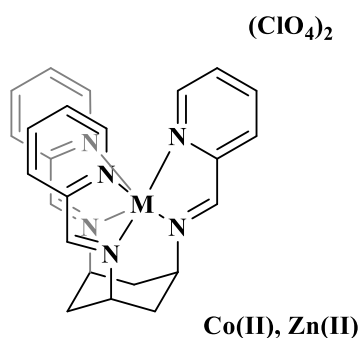
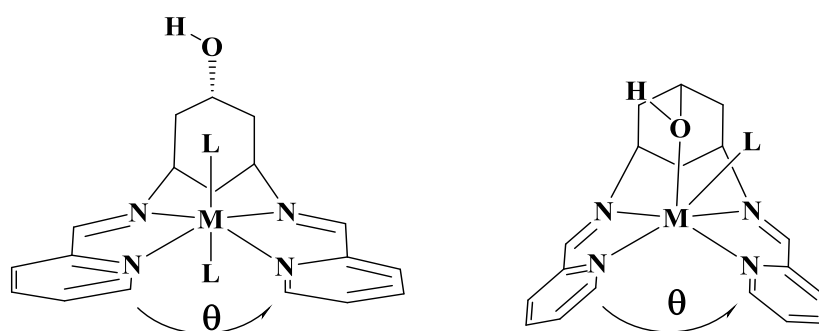


**Figure 3.14** TACH complexes  $M(\text{Py-TACH})_3^{2+}$  with three imino pyridine arms.<sup>126</sup>

DFT calculations of the octahedral and trigonal geometries for each of the DDOPi (**9, L3**) complexes were completed to show the difference in free energy between the different geometries for each metal as show in **table 3.4**. For example, calculations showed that **CoL3N** in the trigonal prismatic geometry, compared to the octahedral geometry, with

the hydroxyl *trans* to the counterion and the iminopyridine rings almost planar, is 30 kJ mol<sup>-1</sup> more stable. The two largest energy gains of *ca.* 65 – 70 kJ mol<sup>-1</sup>, being for **ZnL3N** and **MnL3N** which is consistent with their higher preference for trigonal prismatic geometry as shown in the work by Alvarez.<sup>125</sup> **CuL3N** modelled in the trigonal prismatic geometry has the lowest free energy gain out of all the complexes modelled, compared to the octahedral geometry. This is consistent with results found. However, there are additional Jahn-Teller distortions leading to a square-pyramidal geometry, instead of octahedral.

**Table 3.4** The angle between pyridine rings calculated in shelex-86 using MPLA, with planes defined as the atoms of the pyridine rings for trigonal prismatic structure and octahedral structures.



	Angle in between py rings/ °		Angle in between py rings/ °
<b>CuL2N</b>	11.787 (0.08)	<b>CuL3N</b>	18.879 (0.09)
<b>CoL2N</b>	8.032 (0.08)	<b>CoL3N</b>	84.736 (0.05)
<b>ZnL2N</b>	7.864 (0.11)	<b>ZnL3N</b>	85.323 (0.05)
<b>MnL2N</b>	7.257 (8.20)	<b>MnL3N</b>	74.338 (0.04)

**Table 3.4** shows the calculated angles between pyridine rings for selected **L2** and **L3** metal complexes. The small difference in angles found for **CoL3N**, **ZnL3N** and **MnL3N** show that the trigonal prismatic geometry for each is similar, although there is a slight deviation in **MnL3N**. The main cause of this may be the longer Mn-N bonds which allow for a slightly smaller angle between the pyridine rings. For the **L2** complexes the angle

between pyridine rings is almost planar, and consistent at *ca.* 7-8°, apart from **CuL2N**, where the angle reaches almost 12°. This is most likely caused by the Jahn-Teller effect, which shortens of the Cu-N bonds and thus may require an increased angle to relieve sterics between the pyridyl ring protons. The larger angle found in **CuL3N** can be accounted for also by the shortened Cu-N bonds, but mostly from the bonding interaction of the proximal hydroxyl group with the copper(II) centre.

### 3.4 <sup>1</sup>H-NMR of diamagnetic zinc complexes

#### 3.4.1 <sup>1</sup>H- NMR of diamagnetic zinc complexes: aliphatic region

As zinc(II) has a 3d<sup>10</sup> electronic configuration it is diamagnetic, making it possible to obtain diagnostic <sup>1</sup>H-NMR spectra for all the zinc(II) complexes, **ZnL1N**, **ZnL2N**, and **ZnL3N**. This allows us to see the complexes structure in solution as well as that found in the solid state from x-ray crystal structures. The effect on the ligand conformation on complexation can be seen by comparing the <sup>1</sup>H-NMR of the ligand with that of its zinc(II) complex. As shown previously from the crystal structures, complexation induces a ring-flip in the cyclohexane backbone which can be clearly seen in the signals of two particular chemical environments, protons H<sub>a</sub> and H<sub>d</sub> in **ZnL2N** and **ZnL3N**, and just H<sub>d</sub> in **ZnL1N**.

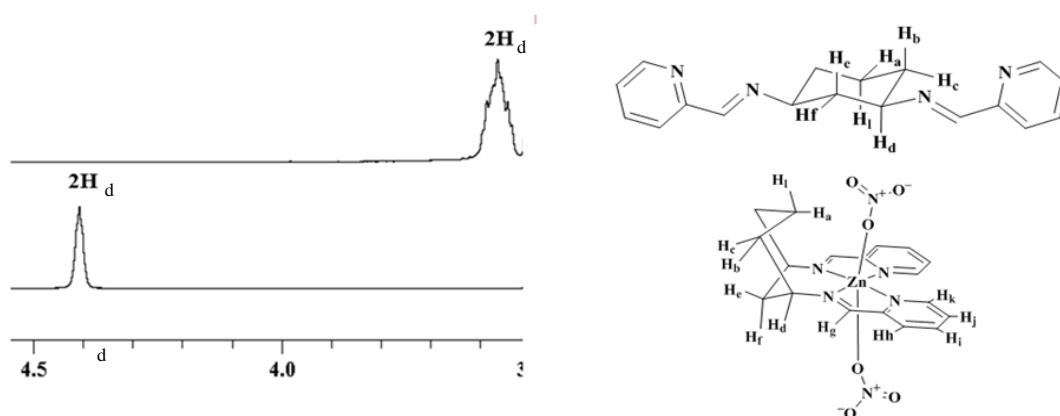


**Figure 3.15** <sup>1</sup>H-NMR spectra and structures of **DDP (10, L1)** (top) and **ZnL1N** (bottom).

As shown in **figure 3.15**, in uncomplexed **DDP (10, L1)**, where the iminopyridine groups are in the equatorial position, the H<sub>d</sub> protons ( $\delta = 3.56$  ppm), display a poorly resolved *pseudo*-triplet of *pseudo*-triplets multiplicity due to strong <sup>3</sup>J<sub>HH</sub> axial-axial couplings to



the anti-periplanar  $H_c$  and  $H_f$ , and weak  $^3J_{HH}$  axial-equatorial couplings to  $H_b$  and  $H_e$ , with an integral of two. On complexation with zinc(II) (to give **ZnL1N**) a ring-flip occurs, this is where the iminopyridine groups are in axial positions. The signal resulting from the two  $H_d$  protons would be predicted to change to a *pseudo*-pentet splitting pattern, this is a result of a change in conformation giving weak  $^3J_{HH}$  equatorial-equatorial coupling with  $H_b$  and  $H_e$  and  $^3J_{HH}$  equatorial-axial couplings with  $H_f$  and  $H_c$  protons, with an integral of two. The observed signal is not well resolved but the narrower signal is consistent with the weaker coupling to  $H_b$  and  $H_e$  which is expected in the ring-flipped conformation. The electron withdrawing effect of the metal centre and the change to an equatorial environment shifts the signal downfield to  $\delta = 4.41$  ppm.

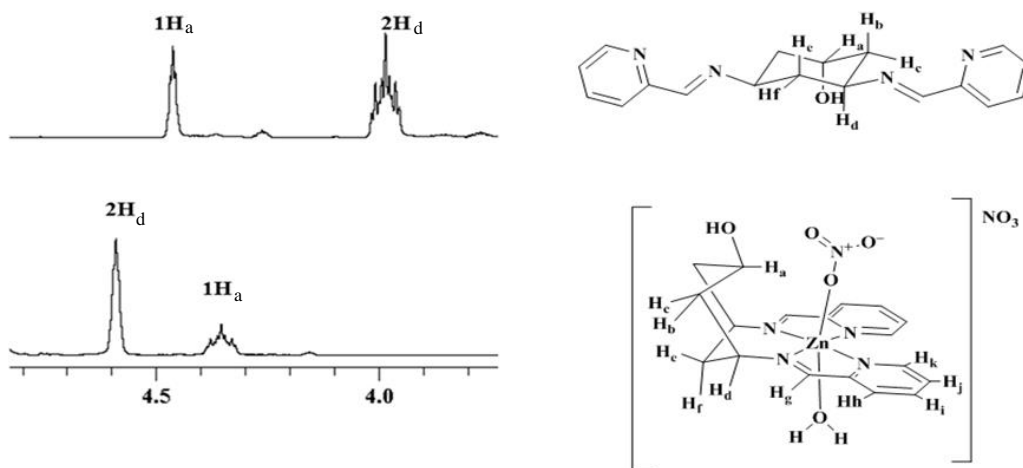


**Figure 3.16**  $^1\text{H}$ -NMR spectra and structures of DDOP (**5**, **L2**) (top) and **ZnL2N** (bottom).

As shown in **figure 3.16**, in uncomplexed **DDOP (5, L2)**, where the iminopyridine groups are in the equatorial position,  $H_a$  ( $\delta = 4.40$  ppm) displays a *pseudo*-pentet splitting pattern, this is a result of weak  $^3J_{HH}$  equatorial-equatorial and  $^3J_{HH}$  equatorial-axial couplings by the Karplus equation, with the two  $H_b$  and two  $H_c$  protons, with an integral of one. The  $H_d$  protons ( $\delta = 3.90$  ppm), display a *pseudo*-triplet of *pseudo*-triplets multiplicity due to strong  $^3J_{HH}$  axial-axial couplings to the anti-periplanar  $H_c$  and  $H_f$ , and weak  $^3J_{HH}$  axial-equatorial couplings to  $H_b$  and  $H_e$ , with an integral of two. On complexation with zinc(II) giving **ZnL2N**, a ring-flip occurs, this is puts the iminopyridine groups in the axial positions. In this case,  $H_a$  couples much more strongly with two  $H_c$  protons due to the  $^3J_{HH}$  axial-axial couplings due to their anti-periplanar conformation. With the addition of weaker  $^3J_{HH}$  equatorial-axial couplings with the two

H<sub>d</sub> protons results in a *pseudo*-triplet of *pseudo*-triplets with an integral of one and is shifted to ( $\delta = 4.35$  ppm). The signal resulting from the two H<sub>d</sub>, protons is predicted to display a *pseudo*-pentet splitting pattern, as a result of weak  $^3J_{HH}$  equatorial-equatorial coupling with H<sub>b</sub> and H<sub>e</sub> and  $^3J_{HH}$  equatorial-axial couplings with H<sub>f</sub> and H<sub>c</sub> protons, with an integral of two. However, the observed signal is not well resolved, but the narrower signal is consistent with the weaker coupling to H<sub>b</sub> and H<sub>e</sub> which is expected in the ring-flipped conformation. The electron withdrawing effect of the metal centre and the change to an equatorial environment shifts the signal downfield, beyond H<sub>a</sub>, to  $\delta = 4.59$  ppm.

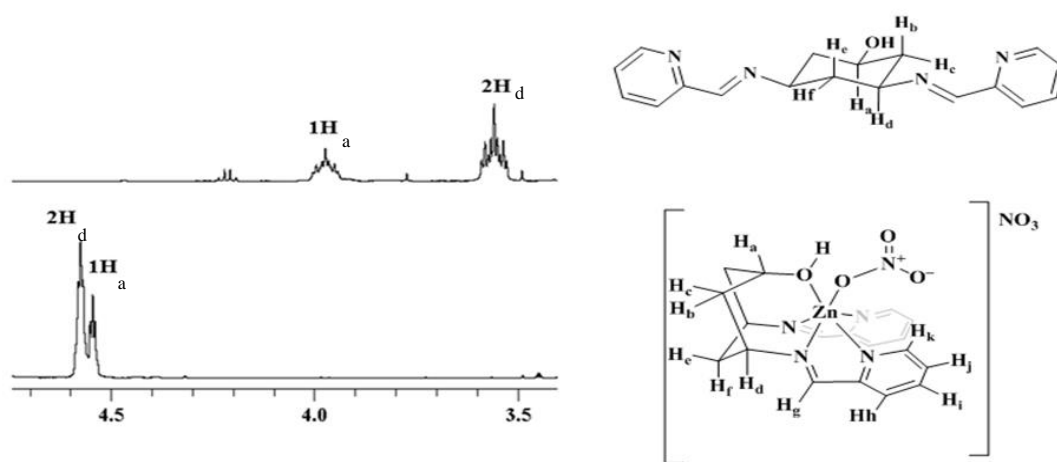


**Figure 3.17**  $^1\text{H}$ -NMR spectra and chemdraw of DDOPi (**9**, **L3**) (top) and **ZnL3N** (bottom).

As shown in **figure 3.17**, in uncomplexed DDOPi (**9**, **L3**), where the iminopyridine groups are in the equatorial position, H<sub>a</sub> ( $\delta = 3.97$  ppm), displays a *pseudo*-triplet of *pseudo*-triplets multiplicity due to strong  $^3J_{HH}$  axial-axial couplings to the anti-periplanar H<sub>c</sub> and weak  $^3J_{HH}$  axial-equatorial couplings to H<sub>b</sub>, with an integral of one. The H<sub>d</sub> protons ( $\delta = 3.56$  ppm), display a *pseudo*-triplet of *pseudo*-triplets multiplicity due to strong  $^3J_{HH}$  axial-axial couplings to the anti-periplanar H<sub>c</sub> and H<sub>f</sub>, and weak  $^3J_{HH}$  axial-equatorial couplings to H<sub>b</sub> and H<sub>e</sub>, with an integral of two. On complexation with zinc(II) giving **ZnL3N**, a ring-flip occurs, this is where the iminopyridine groups are in axial positions, also enforcing the hydroxyl group in to the axial position. In this case, H<sub>a</sub> shifts downfield to ( $\delta = 4.55$  ppm) due to the electron withdrawing effect of the metal centre and the change to an equatorial environment, and displays a *pseudo*-pentet splitting pattern (integral = 1H), as a result of weak  $^3J_{HH}$  equatorial-equatorial and  $^3J_{HH}$  equatorial-axial couplings with the two H<sub>b</sub> and two H<sub>c</sub> protons. The signal resulting from the two H<sub>d</sub>, protons displays a *pseudo*-pentet splitting pattern, this is a result of weak  $^3J_{HH}$  equatorial-

equatorial coupling with H<sub>b</sub> and H<sub>e</sub> and  $^3J_{HH}$  equatorial-axial couplings with the H<sub>f</sub> and H<sub>c</sub> protons, with an integral of two. The electron withdrawing effect of the metal centre and the change to an equatorial environment shifts the signal downfield, beyond H<sub>a</sub>, to  $\delta = 4.57$  ppm.

### 3.4.2 $^1\text{H}$ - NMR of diamagnetic zinc complexes: aromatic region

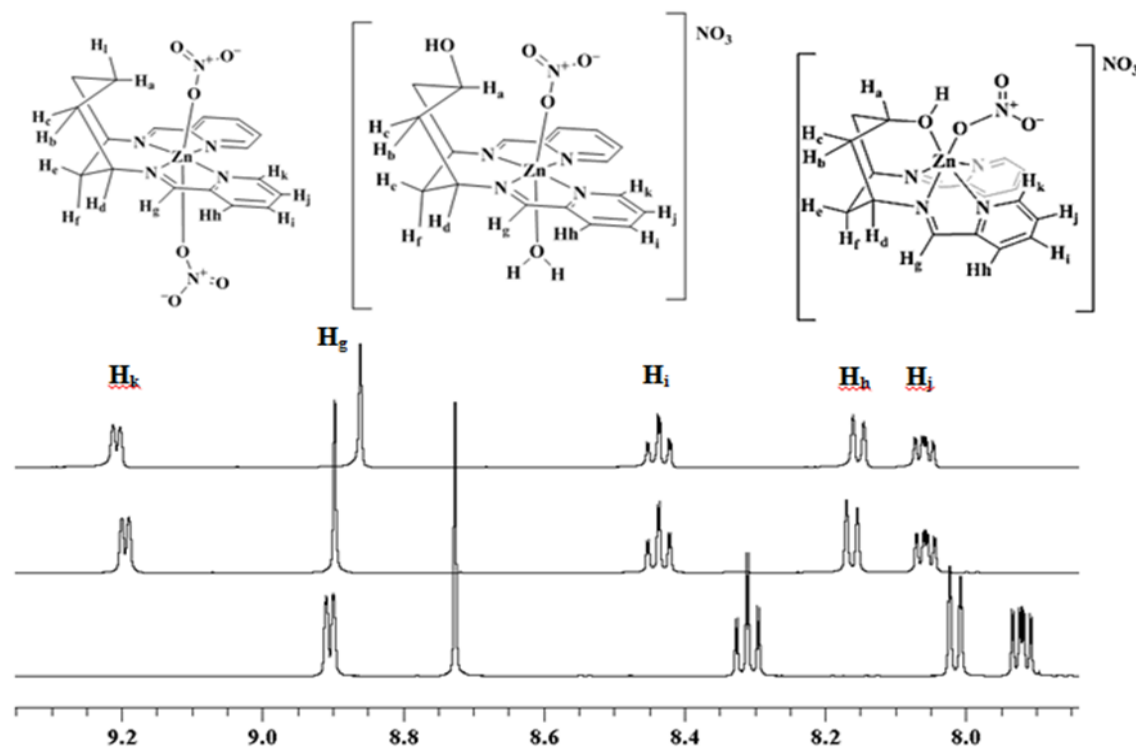


**Figure 3.18** Aromatic region of the  $^1\text{H}$ -NMR of **ZnL1N** (left + top spectrum), **ZnL2N** (centre + centre spectrum), and **ZnL3N** (right + bottom spectrum).

All three ligands contain the same imino-pyridine functionality, which in the free ligand state gives virtually identical  $^1\text{H}$ -NMR spectra in the aromatic region. On complexation with zinc(II), however, large differences in  $\delta$  emerge for this region in **ZnL3N** compared to **ZnL1N** and **ZnL2N**, as shown in **figure 3.18**. The peak corresponding to the aromatic pyridine protons H<sub>j</sub>, H<sub>i</sub>, H<sub>h</sub> and the imine proton H<sub>g</sub>, shift by *ca.* 0.15 ppm upfield in **ZnL3N** compared to **ZnL1N** and **ZnL2N**. This may be explained in terms of the differences in electron density caused by the coordination of the electron donating hydroxyl group to the zinc complex, thus making the zinc centre less electropositive and thus less electron withdrawing. It may also be due to the change in coordination geometry from octahedral in **ZnL1N** and **ZnL2N**, to trigonal prismatic in **ZnL3N** as in the two

geometries the ligand orbitals overlap to a different degree with the d-orbitals of the metal centre, and are consequently influenced by the metal to a different extent. The peak corresponding to the aromatic pyridine protons,  $H_k$ , is shifted even further by *ca.* 0.30 ppm upfield in **ZnL3N** compared to **ZnL1N** and **ZnL2N**. This may be explained by a combination of the effects previously described in addition to shielding by the adjacent pyridine's ring currents, as found in the  $^1\text{H}$ -NMR of  $\text{Ru}(\text{bpy})_3^{2+}$  complexes, as the trigonal prismatic geometry brings the pyridines into an orientation where this may occur.<sup>127</sup>

It can be concluded that the zinc(II) solution structures of all of the complexes are principally the same as the solid state on the timescale of the  $^1\text{H}$ -NMR experiment. It is therefore, reasonable to assume that the solution geometries of the complexes of the other metals remain very similar to the geometries observed in the solid state.

### 3.5 Paramagnetic NMR

#### 3.5.1 Introduction to paramagnetic NMR

Nuclear magnetic resonance (NMR) has been previously used as a tool to study the ligand environments of paramagnetic metal complexes. These paramagnetic effects can be used to determine information on structural, thermodynamic and dynamic properties.<sup>128-130</sup>

Paramagnetic materials are those with positive magnetic susceptibility associated with unpaired electrons. These unpaired electron spins have a profound influence on the NMR spectra, notably enhancing the rates of nuclear spin relaxation, in turn leading to line broadening and isotropically shifted proton resonances within the ligand frameworks, provided the relevant electron spin-nuclear spin interaction has a non-zero average. An isotropic shift is the difference between the chemical shift of a given nucleus in a diamagnetic *vs* that of a paramagnetic environment. Isotropic shifts result from two mechanisms: contact shifts and pseudo-contact shifts. Both effects happen simultaneously but one or the other term can be dominant. Contact shifts result from spin polarisation conveyed through the molecular orbitals of the molecule (dipole). Pseudo-contact shifts result from magnetic field from the paramagnetic centre (scalar term). This means contact shifts are directional and depend on the whole molecular electronic structure. Whereas

pseudo-contact shifts are non-directional and depend only on the magnetic properties of spin centre and the distance from it.<sup>131,132</sup>

Pseudo-contact shifts follow  $1/r^3$  dependence and tend to be smaller, often within the normal 1-10 ppm range for  $^1\text{H}$ -NMR.<sup>133</sup> The contact term arises from transfer of spin polarization to the observed nucleus. Spin polarization is a consequence of the very strong electron-nuclear interaction (hyperfine coupling). This is on the order of MHz vs a few Hz found for J coupling observed in normal diamagnetic NMR spectra, reflecting the very large magnetic moment of an electron ( $-1.0 \mu\text{B}$ ), compared to any nuclear magnetic moment ( $1.52 \times 10^{-3} \mu\text{B}$ ). Owing to rapid spin relaxation, electron-nuclear coupling is not observed in the NMR spectrum. The affected nuclear resonance appears as the average of the two coupled energy states (weighed with their spin populations). As the magnitude of the coupling is so large the Boltzmann distribution between spin states is uneven (not close to 1:1), thus leading to net spin polarization on the affected nucleus and large contact shifts.<sup>134,135</sup>

Paramagnetic complexes may contain exchangeable ligands, which give intrinsic relaxation, shift and splitting properties, contributing to the line-shapes observed. Paramagnetic species lead to significant broadening of nuclear resonances – a direct indication that the distribution of local magnetic fields within the sample is spread sizably because of the large perturbation by the unpaired electrons of the paramagnetic species. The degree of broadening reflects the extent and duration of the interaction between the unpaired electrons and the nucleus in question. Thus paramagnetic line broadening yields information on structure and bonding with the addition of kinetic information.

### 3.5.2 Paramagnetic NMR assignment

$^1\text{H}$ -NMR was recorded for all the cobalt(II) complexes synthesised giving rise to well resolved  $^1\text{H}$  paramagnetic NMR spectra. This relatively high resolution is due to the rapid electron relaxation of the high spin  $d^7$  systems and therefore giving relatively sharp resonances, as expected.<sup>136-142</sup>

The theory of unpaired electron-nucleus interaction and its consequences for NMR spectroscopy has been developed over the past decades and summarised

comprehensively.<sup>136-144</sup> In diamagnetic molecules the orbital shift ( $\delta_{orb}$ ) provides the principal contribution to the observed chemical shifts. In paramagnetic samples the hyperfine shift ( $\delta_{hf}$ ) which has temperature dependence adds to the orbital shift, leading to the observed chemical shift:

$$\delta_{obs} = \delta_{orb} + \delta_{hf} \quad \text{eq 1}$$

The hyperfine shift itself may be expressed as in **eq 2**, where  $S$  is the total electron spin,  $\beta_e$  the Bohr magneton,  $\gamma_N$  the nuclear gyromagnetic ratio, and then  $g$  and  $A$  are the  $g$ - and  $A$ - hyperfine tensors.

$$\delta_{hf} = \frac{S(S+1)\beta_e}{3kT\gamma_N} gA \quad \text{eq 2}$$

For an arbitrary number of unpaired electrons a general expression of the NMR shielding tensor  $gA$ , has been developed only recently. Although there are several isotropic and anisotropic contributions to  $\delta_{hf}$ , it is possible to analyse paramagnetic NMR spectra in solution by considering only three contributions, the orbital shift,  $\delta_{orb}$ , the Fermi contact shift  $\delta_{con}$ , and the pseudocontact shift,  $\delta_{pc}$ . Consequently equation one becomes **eq 3**.

$$\delta_{obs} = \delta_{orb} + \delta_{hf} \cong \delta_{orb} + \delta_{con} + \delta_{pc} \quad \text{eq 3}$$

The Fermi contact shift ( $\delta_{con}$ ) is caused by coupling of the unpaired electrons with the atomic nuclei and is transmitted through chemical bonds, it is proportional to the residual spin density of the atom centre,  $\rho_{\alpha\beta}$ . The latter can be extracted from DFT calculations so that  $\delta_{con}$ , can be obtained using **eq 4**.

$$\delta_{con} = \frac{\mu_0 \mu_B^2 g_e^2 (S+1)}{9kT} \rho_{\alpha\beta} \quad \text{eq 4}$$

The pseudo-contact shift arises from a dipolar through-space interaction between the magnetic moment of the unpaired electron and the magnetic moments of the unpaired electrons and the magnetic moments of the nuclei. It is strongly dependent on the distance of the nucleus of interest to the paramagnetic centre and may be of little influence to the chemical shift of nuclei distant from the metal core. Thus the Fermi contact is presumed to dominate the chemical shifts of covalently bound ligands in 3d metal complexes.<sup>145-148</sup>

Using this approximation (Fermi contacts dominate the chemical shifts of covalently bound ligands) Fermi contacts were calculated from DFT calculations, using 6-311g(d,p)

basis set for CHNO and TZVP basis set for the cobalt centre. Their magnitude is used as a guide to assign the  $^1\text{H}$ -NMR shifts of the ligands, as the most highly shifted will be those most greatly affected by the paramagnetic centre.<sup>149,132</sup>

As the Fermi contacts obtained from DFT are effectively solid state static calculations, the Fermi contacts for magnetically and chemically equivalent protons were averaged to give values which should be representative in solution. It should be understood that the assignment and modelling of paramagnetic NMR spectra is highly complex and has lots of contributing factors, requiring intensive study modelling power and time, with whole books written on the subject. This method, therefore, is just a guide to allow educated assignment of the protons.

Assignments for the three main cobalt(II) complexes, **CoL1N**, **CoL2N** and **CoL3N** are given below in **figure 3.18**, **figures 3.19**, and **figures 3.20**.

### 3.5.3 Paramagnetic $^1\text{H}$ -NMR of CoL3N, CoL2N, and CoL1N.

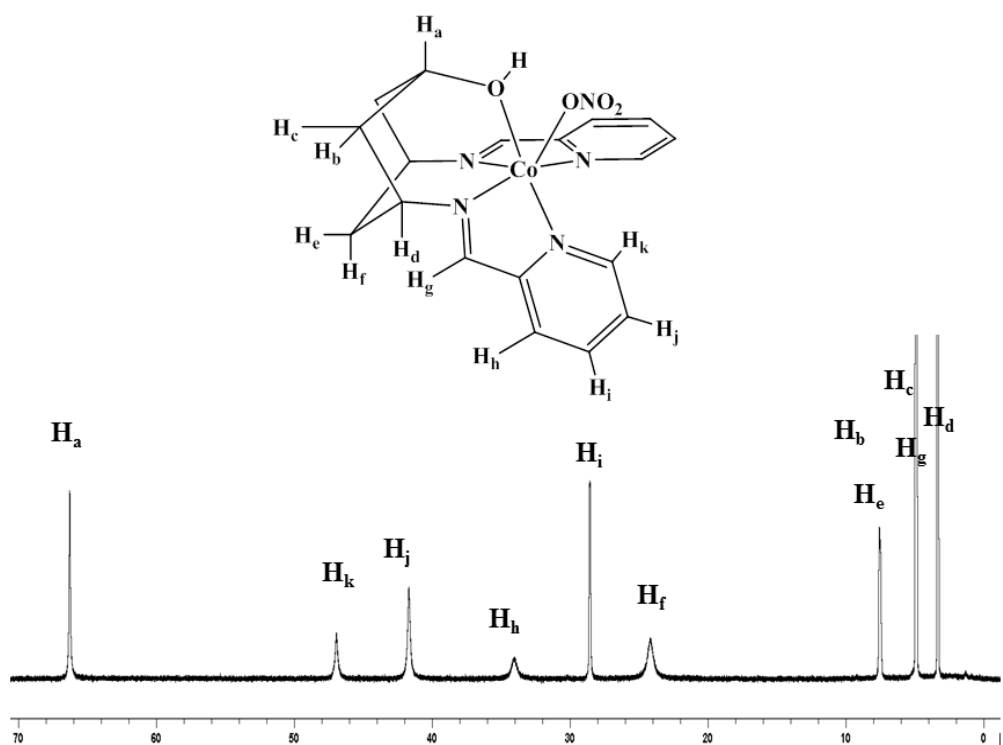
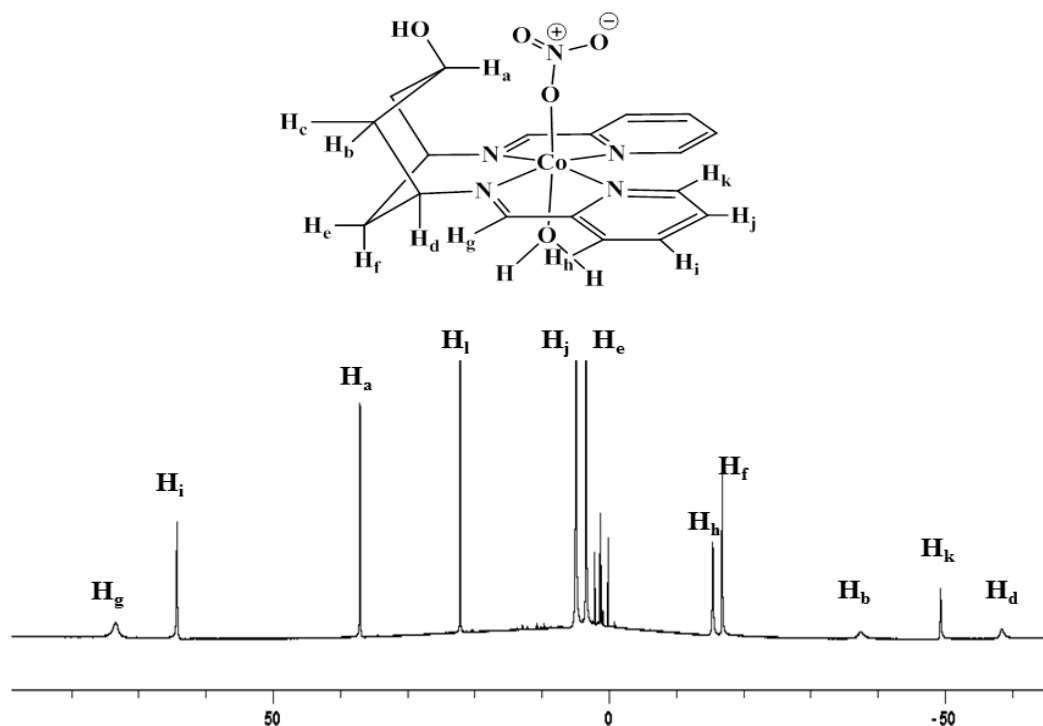


Figure 3.18 Paramagnetic  $^1\text{H}$ -NMR spectra of CoL3N.

**Table 3.5** Average Fermi contacts from DFT calculations and the corresponding proton assignments and experimental shifts found for CoL3N.

Average Fermi contacts from DFT Calculations/ a.u.	Proton assignment	Experimental data/ppm
9.385	H <sub>a</sub>	66.36
2.572	H <sub>k</sub>	46.95
0.960	H <sub>j</sub>	41.68
0.793	H <sub>h</sub>	34.12
0.215	H <sub>i</sub>	28.57
-0.025	H <sub>f</sub>	24.22
-0.065	H <sub>b</sub>	7.57
-0.105	H <sub>e</sub>	7.49
-0.146	H <sub>c</sub>	4.94
-0.429	H <sub>g</sub>	4.88
-0.978	H <sub>d</sub>	3.37





**Figure 3.19** Paramagnetic  $^1\text{H}$ -NMR spectra of **CoL2N**.

**Table 3.6** Average Fermi contacts from DFT calculations and the corresponding proton assignments and experimental shifts found for **CoL2N**.

Average Fermi contacts from DFT Calculations/ a.u.	Proton assignment	Experimental data/ppm
0.61704	H <sub>g</sub>	73.34
0.279905	H <sub>i</sub>	64.19
0.19138	H <sub>a</sub>	37.00
0.187895	H <sub>c</sub>	22.07
0.13444	H <sub>j</sub>	4.87
0.04973	H <sub>e</sub>	2.08
-0.00402	H <sub>b</sub>	-15.45
-0.00996	H <sub>f</sub>	-16.93
-0.02896	H <sub>b</sub>	-37.52
-0.16471	H <sub>k</sub>	-49.4
-2.70341	H <sub>d</sub>	-58.53

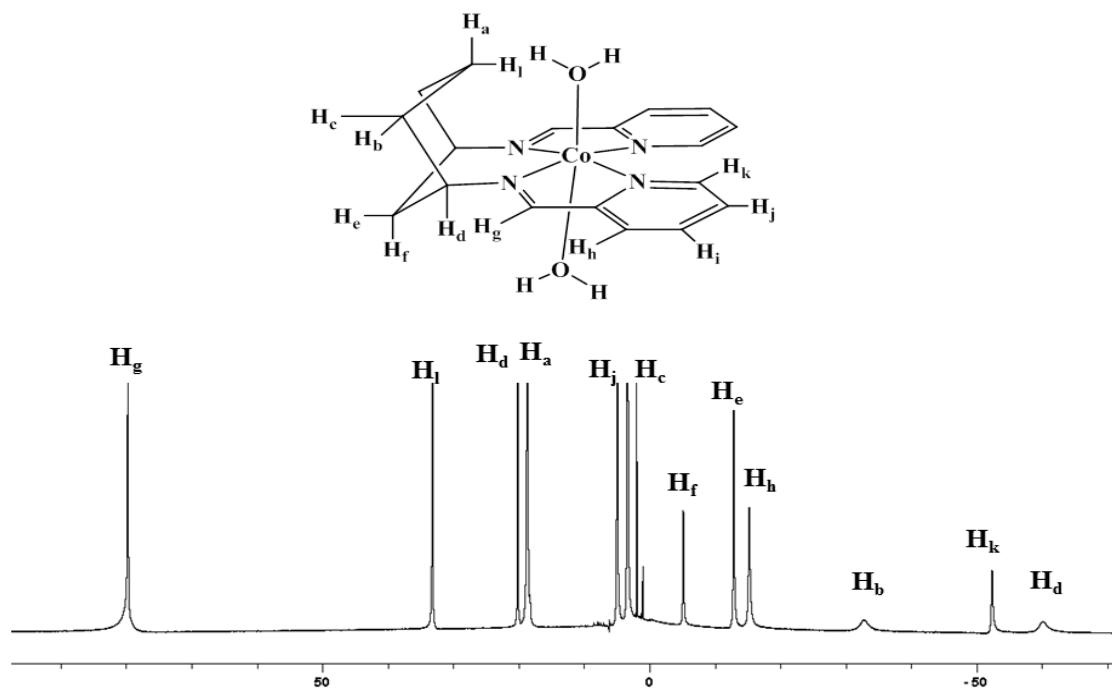


**Figure 3.20** Paramagnetic  $^1\text{H}$ -NMR spectra of **CoL1N**.

**Table 3.7** Average Fermi contacts from DFT calculations and the corresponding proton assignments and experimental shifts found for **CoL1N**.

Average Fermi contacts from DFT calculations	Proton assignment	Experimental data/ppm
0.72125	H <sub>g</sub>	79.66
0.49338	H <sub>i</sub>	33.13
0.290355	H <sub>i</sub>	20.07
0.25598	H <sub>a</sub>	18.64
0.14175	H <sub>j</sub>	4.88
0.052525	H <sub>c</sub>	1.96
0.01354	H <sub>f</sub>	-5.21
0.012	H <sub>e</sub>	-12.92
0.006645	H <sub>h</sub>	-15.29
0.000125	H <sub>b</sub>	-32.84
-0.19834	H <sub>k</sub>	-52.39
-2.2898	H <sub>d</sub>	-60.26

The  $^1\text{H}$ -NMR of all the cobalt (II) complexes, as illustrated by **figures 3.18 – 3.20** gave resonances for all of the proton environments. It can also be seen that there is large and clear difference seen in the  $^1\text{H}$ -NMR of the trigonal prismatic geometry and the octahedral geometries. This reaffirms the conclusion that solution structures for the cobalt(II) state of all of the complexes are principally the same as the solid state. Unlike in the  $^1\text{H}$ -NMR of **ZnL3N** where  $\text{H}_b$  ( $\delta = 8.90$  ppm) is the most downfield peak, the Fermi contacts from the DFT studies of **CoL3N** shown in **table 3.5** that  $\text{H}_a$  ( $\delta = 66.36$  ppm) has the highest Fermi contact, and is therefore the most influenced by the paramagnetic cobalt centre. On the other hand,  $\text{H}_d$  ( $\delta = 4.57$  ppm), in the diamagnetic  $^1\text{H}$ -NMR of **ZnL3N** is the second most downfield signal of the aliphatic cyclohexane, but in the paramagnetic  $^1\text{H}$ -NMR,  $\text{H}_g$  ( $\delta = 3.37$  ppm), is the least influenced by the paramagnetic centre, which reflects the differences in the effect of a paramagnetic metal centre on the  $^1\text{H}$ -NMR. In the paramagnetic  $^1\text{H}$ -NMR of **CoL2N**,  $\text{H}_g$  ( $\delta = 73.34$  ppm) is the most downfield peak followed by  $\text{H}_i$  ( $\delta = 64.19$  ppm) and  $\text{H}_a$  ( $\delta = 37.00$  ppm). As with **CoL3N** the most upfield peak is from  $\text{H}_d$ , but unlike **CoL3N** this has a large negative shift of  $-58.53$  ppm compared to TMS. The paramagnetic  $^1\text{H}$ -NMR of **CoL1N**, also shows  $\text{H}_g$  ( $\delta = 79.66$  ppm) as the most downfield peak followed by  $\text{H}_i$  ( $\delta = 33.13$  ppm),  $\text{H}_i$  ( $\delta = 20.07$  ppm) and  $\text{H}_a$  ( $\delta = 18.64$  ppm). The most up-field peak is from  $\text{H}_d$ , as in the other two complexes and also has a large negative shift of  $-60.26$  ppm compared to TMS, similar to that found in **CoL2N**.

Some patterns can be observed from the Fermi contact based assignment of the cobalt(II) paramagnetic  $^1\text{H}$ -NMR spectra. In the octahedral coordination sphere found in **CoL1N** and **CoL2N** (assumed to be maintained in solution as shown from diamagnetic  $^1\text{H}$ -NMR studies of the Zn(II) complexes), protons found in the  $xy$ ,  $zy$  or  $zx$  planes as shown in **figure 3.21** of the paramagnetic cobalt (II) centre aligned with the  $x$ ,  $y$ , or  $z$  axis are found to have the highest isotropic shifts, in order of distance from the paramagnetic centre. For example, as shown in **figure 3.21** in **CoL2N**,  $\text{H}_g$  lies on the  $xy$  plane, is aligned with the  $x$  axis and is the closest to the paramagnetic centre, and has the highest isotropic shift. This is followed by  $\text{H}_i$ , which is also on the  $xy$  plane, and is aligned with the  $y$  axis, but further from the paramagnetic centre. Protons found on one of the planes but positioned in between the  $x$ ,  $y$  or  $z$  axes (such that a *ca.*  $45^\circ$  angle is defined by either axis and a line from the origin to the proton) have the next highest isotropic shifts in order of distance

from the paramagnetic centre. For example  $H_a$ , which is on a plane  $45^\circ$  to the  $x$  and  $y$  axes and closest to the paramagnetic centre. This is followed by protons  $120^\circ$  to the  $x$ ,  $y$ , or on the  $z$  axis, in order of distance from the paramagnetic centre, as in  $H_j$  and  $H_f$  respectively. In an octahedral geometry the isotropic shifts of all the other protons become negative in value. Protons at other angles to the axis in order of distance from the paramagnetic centre, such as  $H_k$  and  $H_d$  are the most negatively isotropically shifted protons. In **CoL3N** with trigonal prismatic geometry, however, there is not a clear pattern, other than proton,  $H_a$  has the largest isotropic shift as it lies on the  $z$  axis of the paramagnetic centre, followed by the protons of the aromatic pyridine ring closest to the paramagnetic centre. Generally those with large negative or positive Fermi contacts are separated from Co by only a few bonds, or by conjugated systems. All the isotropic shifts are positive in **CoL3N**, however, compared to TMS.

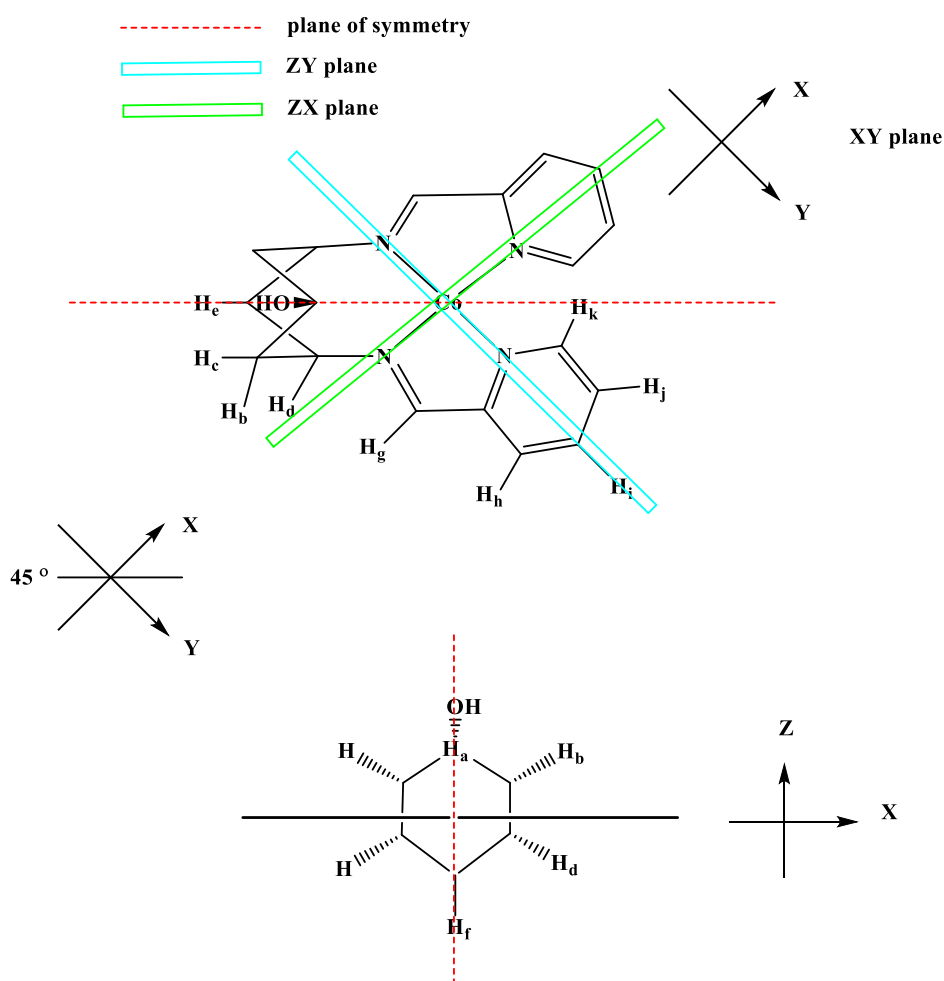


**Figure 3.21**  $xy$  plane (top)  $zx$  plane (bottom) of **CoL2N**.

The appearance of peaks negatively shifted compared to TMS in **CoL1N** and **CoL2N**, but not in **CoL3N**, may be due to the different orientation of the relevant protons to the paramagnetic current of the cobalt(II) centre. This difference in orientation could result in an induced magnetic field that opposes the applied magnetic field in the vicinity of the protons, effectively providing the shielding that would account for the large negative values of  $\delta$ . This effect is seen in the  $^1\text{H}$ -NMR of organometallic metal hydrides, where the paramagnetic current induces an induced field in around the hydride which opposes the applied field in the region acting to shield the proton, giving it a negative shift in comparison to TMS, as illustrated in **figure 3.22**.<sup>150,151</sup>

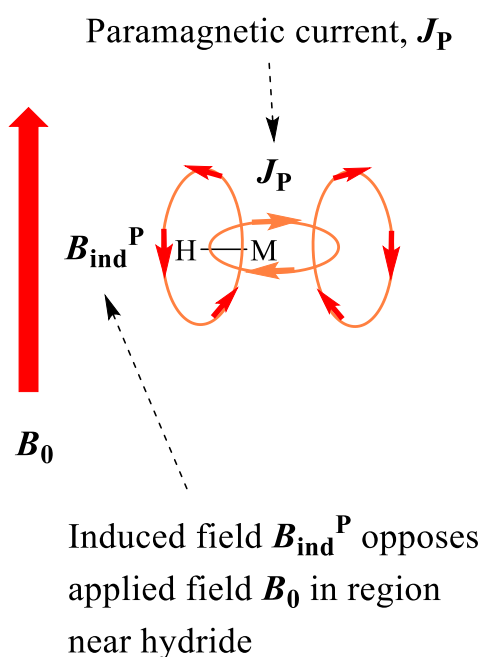


**Figure 3.22** Negative shifts in transition metal hydrides from fields induced from paramagnetic centres.<sup>150,151</sup>

### 3.5.4 Comparison of paramagnetic NMR of nitrate and tetrafluoroborate complexes

From **figure 3.23**, the paramagnetic  $^1\text{H}$ -NMR of **CoL1N** and **CoL1B** both give the expected 12 proton environments as previously shown for **CoL1N** in **figure 3.20**, however, there are some shifts up and down-field of different peaks. For example, there is a shift downfield of *ca.* 31 ppm in **CoL1B** compared to **CoL1N** for the most downfield peak.

From **figure 3.24** the paramagnetic  $^1\text{H}$ -NMR of **CoL3N** (*top*), **CoL3NB** (*centre*) and **CoL3B** (*bottom*), all give the expected 11 proton environments as previously shown for **CoL3N** in **figure 3.18**. There are however, some differences in shift up and downfield of some peaks. These shifts, however, are smaller than found in the paramagnetic NMR of the other complexes. With the largest shift of *ca.* 13 ppm, this is likely to be due to the dependence on the anion, as five of the coordination sites on the metal are taken up by the ligand, this leaves only one labile coordination site, compared to the two found in the complexes of **L4**, **L1**, and **L2**. In the case of **CoL3N** and **CoL3BN** it is most likely taken by a nitrate anion but may also be replaced by a solvent ligand.

From **figure 3.25**, the paramagnetic  $^1\text{H}$ -NMR of **CoL4N** and **CoL4B** both give the expected 9 proton environments, however, there are some shifts up and down-field of different peaks. For example, there is a shift downfield of *ca.* 34 ppm in **CoL4B** compared to **CoL4N** for the most downfield peak. Even though **CoL4N** and **CoL4B** have increased degrees of freedom compared to the other complexes synthesised, due to the flexibility of the propane back bond; from the crystal structure of **CoL4P** it may be assumed that the complexes will have a octahedral geometry with the imino pyridine chelate lying on the equatorial plane of the octahedron and two aqua ligands or solvent molecules in the axial sites. However, the paramagnetic  $^1\text{H}$ -NMR suggests that this might not be the case. If **CoL4N** and **CoL4B** were octahedral and thus had the same form as **CoL1N** and **CoL2N** there should be more than one peak negatively shifted compared to TMS, as the  $\text{H}_g$ ,  $\text{H}_b$  and  $\text{H}_c$  protons in **CoL1N** and **CoL2N** are negatively shifted. But as there is one negatively shifted peak, it can be also gathered that the structure is also not trigonal prismatic. It could be then be postulated that in solution **CoL4N** and **CoL4B** either have an intermediate geometry between octahedral and trigonal prismatic, or that conformational exchange is occurring on the NMR timescale.

From this study, the key conclusions for subsequent chapters is that the nitrate anions are not just spectating in solution, but are interacting strongly with the cobalt centres, and that complexes of **L4** are likely to be conformationally mobile.

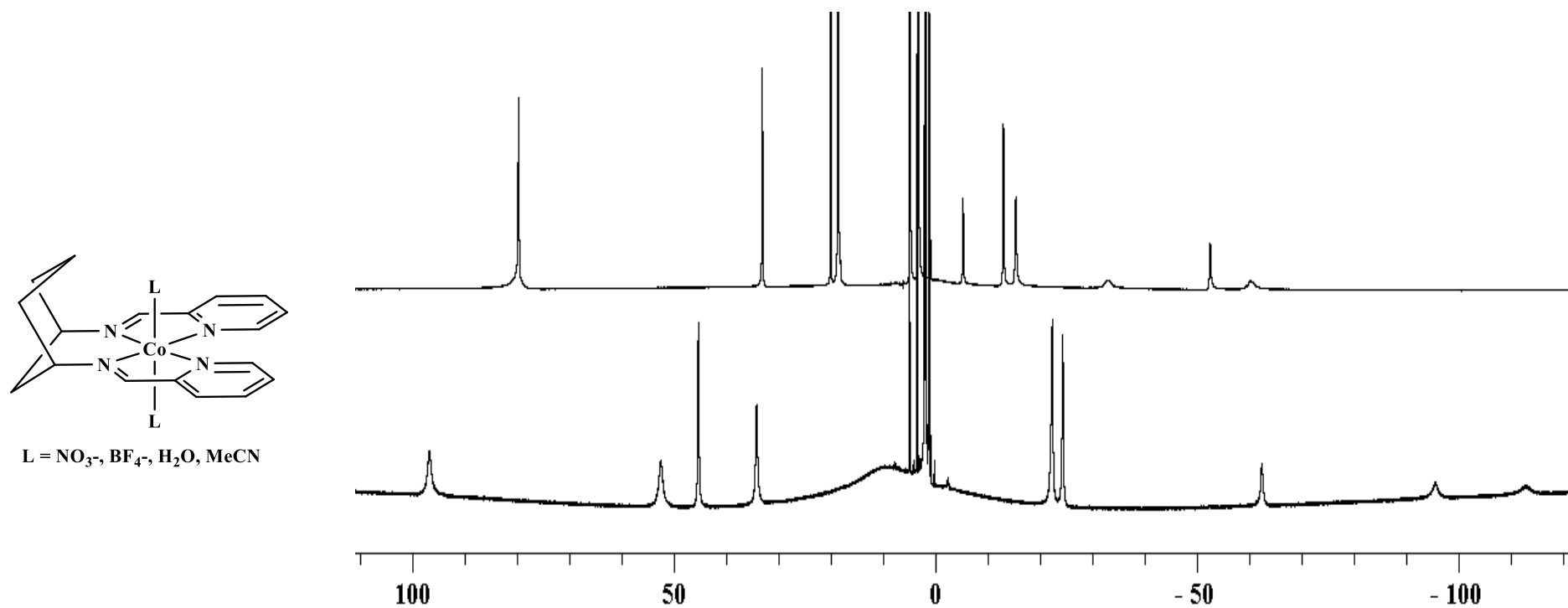
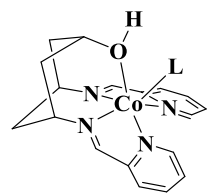


**Figure 3.23** Paramagnetic  $^1\text{H}$ -NMR **CoL1N**) (*top*) and **CoL1B**) (*bottom*).



$L = \text{NO}_3^-, \text{BF}_4^-, \text{H}_2\text{O}, \text{MeCN}$

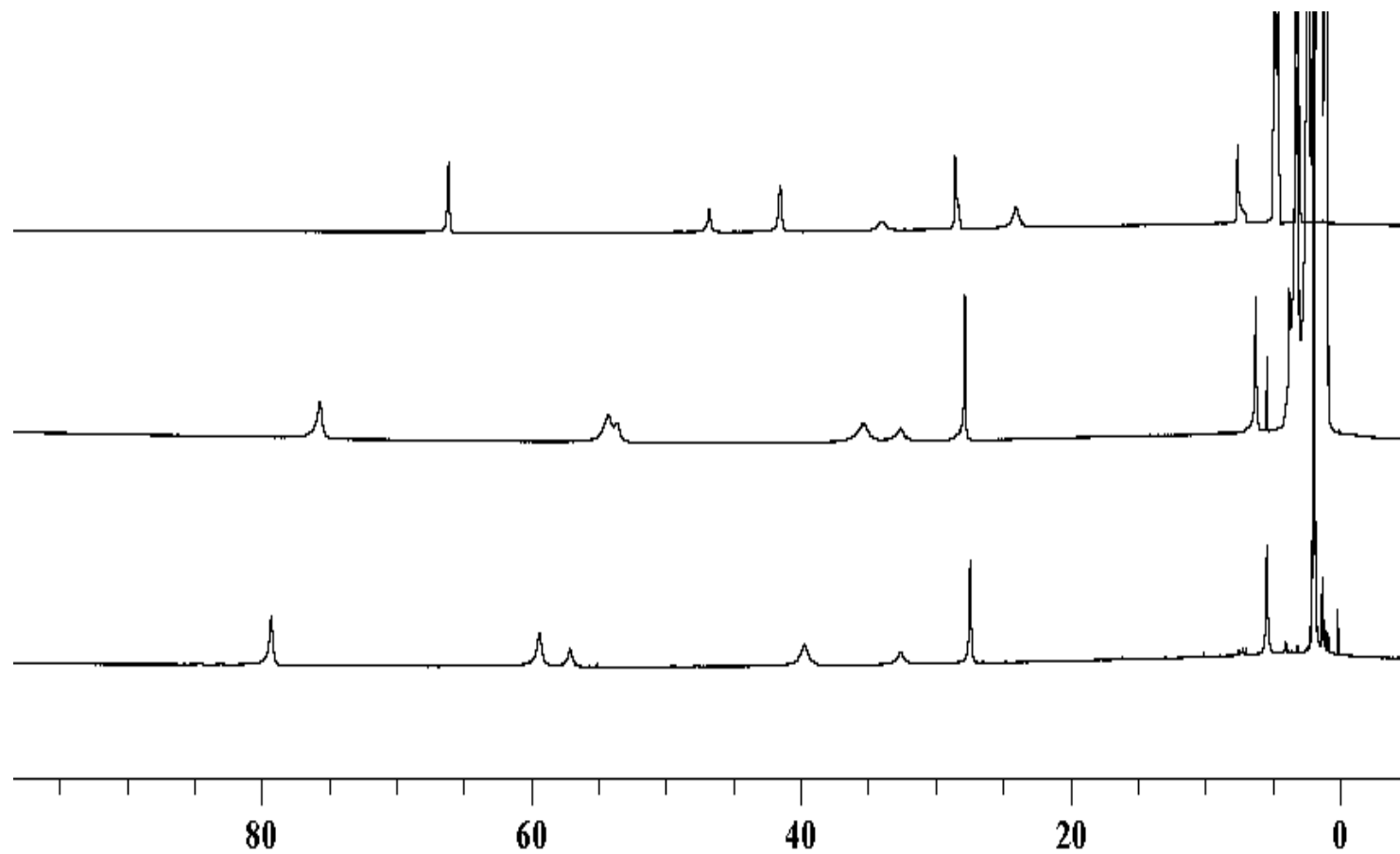
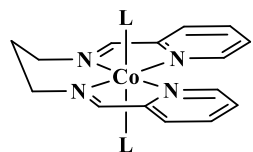


**Figure 3.24** Paramagnetic  $^1\text{H}$ -NMR **CoL3N** (*top*), **CoL3NB** (*centre*) and **CoL3B** (*bottom*).





$L = \text{NO}_3^-, \text{BF}_4^-, \text{H}_2\text{O}, \text{MeCN}$

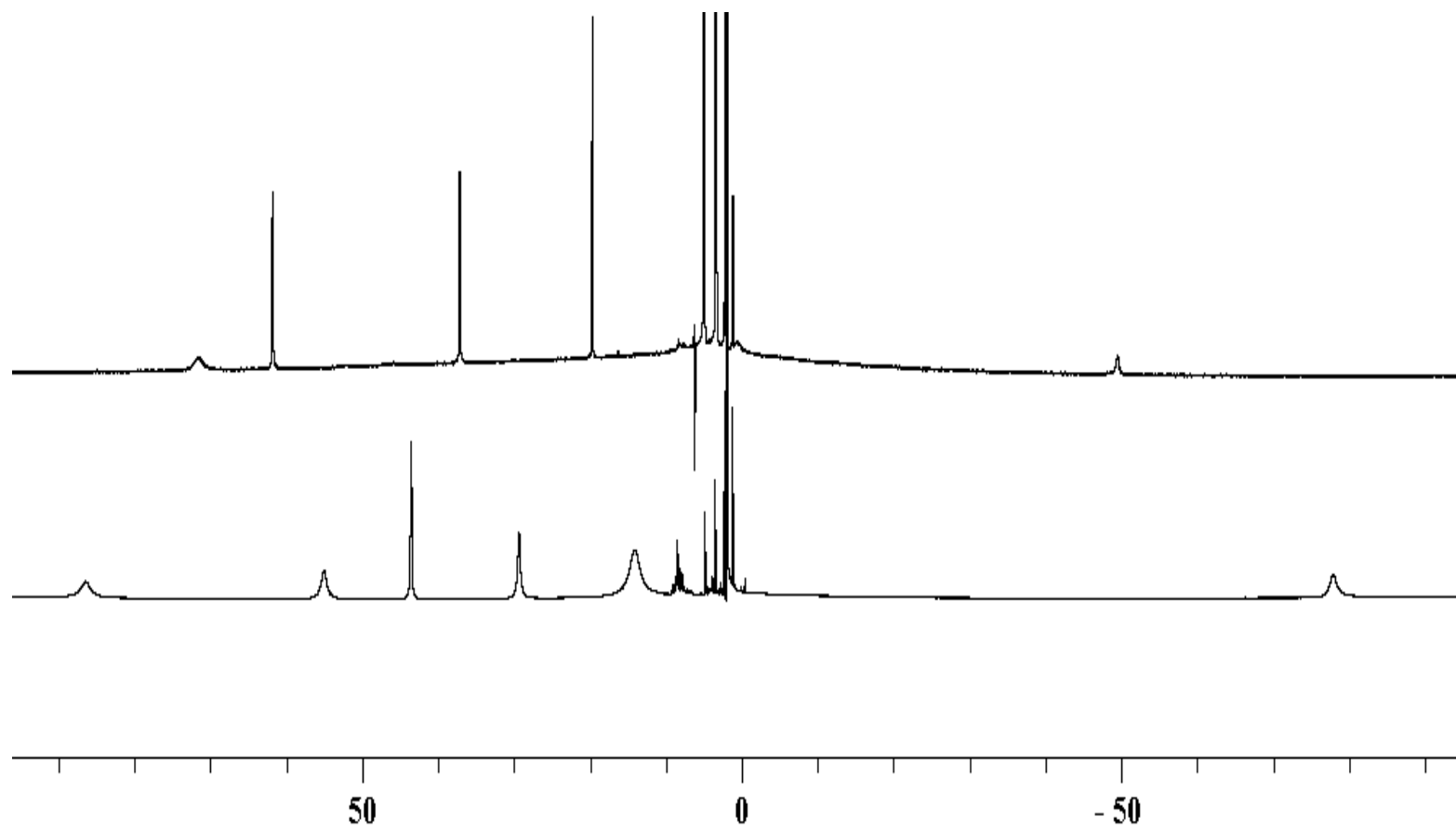


**Figure 3.25** paramagnetic  $^1\text{H}$ -NMR  $\text{CoL4N}$  (*top*) and  $\text{CoL4B}$  (*bottom*).

# **Chapter 4**

## ***Electrochemistry of Coordination Complexes***

#### 4.1.1 Electrochemistry introduction – General aspects of electrochemistry

##### Cyclic voltammetry

Cyclic voltammetry is one of the most used techniques to explore electrochemical behaviour, allowing the rapid determination of thermodynamic and kinetic properties of the species under investigation. The distinct redox potentials of the species give detailed information about the thermodynamics of the redox processes involved, with reduction and oxidation potentials dependant on the LUMO and HOMO of the species respectively.<sup>151-153</sup> Information on the kinetics of the process can be obtained from the magnitude of heterogeneous electron-transfer, and also the reversibility of the process.<sup>153,154</sup>

Cyclic voltammetry with macroelectrodes is usually conducted in a three-component cell consisting of a working electrode, reference electrode and counter electrode. Potentials are applied to the working electrode relative to the fixed potential the reference electrodes. The three electrode set up minimises cell resistance between the working and reference electrode, using a counter electrode with large relative surface area for the current to flow through, and limiting current flow through the reference electrode. In a cyclic voltammetry experiment, the potential of the working electrode is swept linearly over time using a triangular potential wave form. The potential is swept from  $E_1$  to  $E_2$  and then back to  $E_1$  to complete the scan. The rate at which this is done is known as the scan rate (gradient of the potential time graph,  $E$  vs  $t$ ), shown on the right of **figure 4.1**. The plot of current ( $i$ ) vs potential ( $V$ ) is known as cyclic voltammogram (CV). A cyclic voltammogram (CV) is complex and dependent on time and physical and chemical properties.

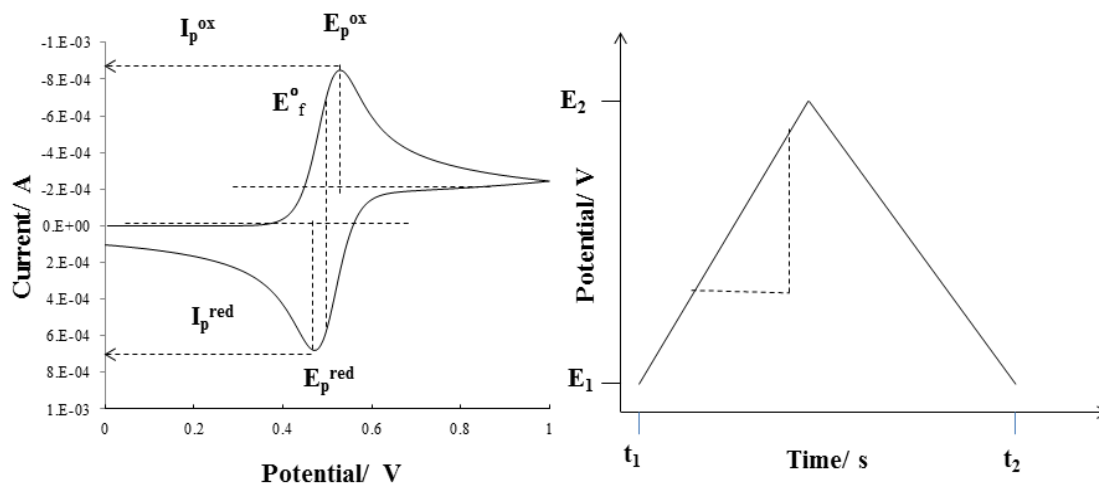


**Figure 4.1** A typical reversible cyclic voltammetric curve (CV) for a simple reversible process. Characteristics of the voltammogram are the peak height ( $I_p$ ), the potential at which the peak occurs ( $E_p$ ) and scan rate ( $V.s^{-1}$ ). In this work the IUPAC convention is used where positive potentials are plotted in the positive 'x' direction, and thus anodic currents (due to oxidations) are positive.

Different heterogeneous electron transfer rates give rise to different CV profiles; classed as reversible, quasi-reversible and irreversible, as show in **figure 4.2**

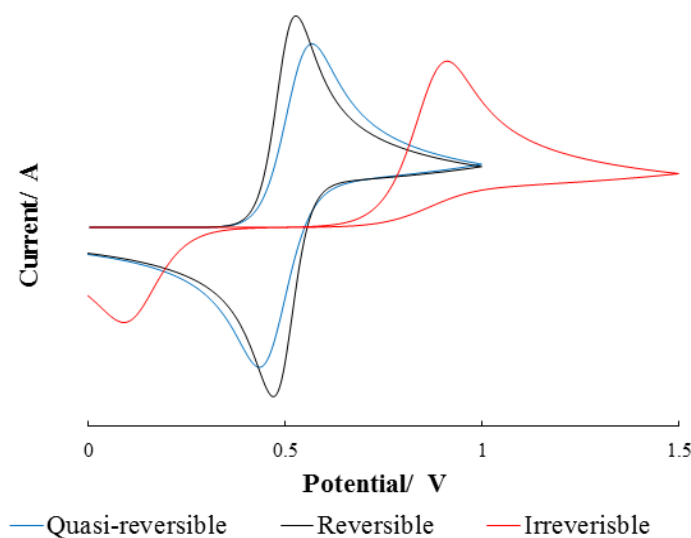
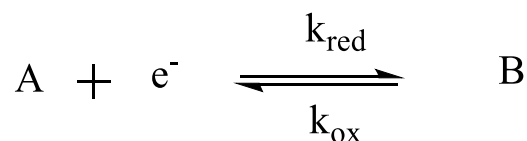


**Figure 4.2** Cyclic voltammogram (CV) profiles for reversible, quasi-reversible and irreversible behaviour.

The physical processes responsible for the ‘reversible’ voltammogram, for a process;



Are based on Fick’s Law of diffusion, **eq 4.1**;

$$\frac{\partial[A]}{\partial t} = D \frac{\partial^2[A]}{\partial x^2} \quad \text{eq 4.1}$$

And the Nernst equation, **eq 4.2**;

$$E = E_f^0 \left( \frac{A}{B} \right) + \frac{RT}{F} \ln \frac{[B]_0}{[A]_0} \quad \text{eq 4.2}$$

The exponential form of the Nernst law, **eq 4.3**;

$$\frac{[B]_0}{[A]_0} = e^{\frac{nF\eta}{RT}} \quad \text{eq 4.3}$$

Where; D = diffusion coefficient, R = molar gas coefficient, F = Faraday’s constant, T = temperature, E = the potential,  $E_f^0 \left( \frac{A}{B} \right)$  = the formal potential for the couple.

The exponential form of the Nernst law, where ( $\eta = E - E_f^0$ ), helps in the consideration of the diffusion layer at each point in the CV, by describing the concentrations of species A and B, which in turn gives rise to the peak shape observed. In the ‘reversible’ case the heterogeneous electron transfer rate,  $k^0$ , is large and fast, relative to the rate of mass transport, and therefore a Nernstian equilibrium is attained at the electrode surface throughout the CV with concentrations of A and B at the electrode surface given by the Nernst equation. E is the applied potential defining the ratio of the surface concentrations of [A]<sub>0</sub> and [B]<sub>0</sub> once  $E_f^0 \left( \frac{A}{B} \right)$  is given.

### 4.1.2 Explanation of a cyclic voltammogram

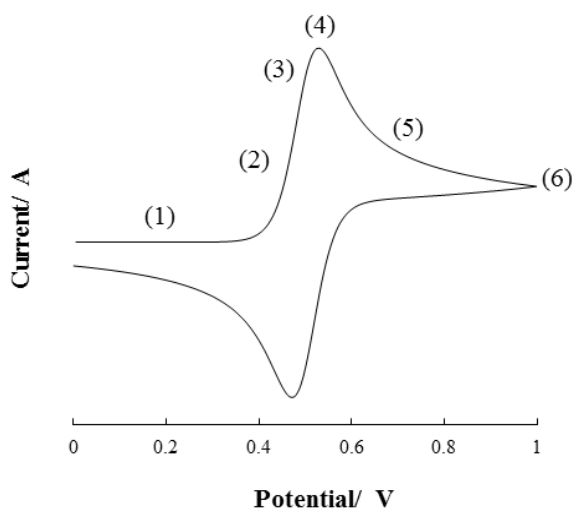


**Figure 4.3** A typical reversible cyclic voltammogram (CV) for a simple reversible process, numbered with points of interest.

**Figure 4.3** shows a reversible cyclic voltammogram, labelled with points 1 to 6, each of which will be discussed in turn. At point (1), the potential is not sufficient to drive electrolysis, at point (2) as  $E$  approaches  $E^0_f$  ( $E = E^0_f$ , given by point (3) on the graph), the current increases as electrolysis in which the oxidation of A to B occurs, this current is governed by heterogeneous electron transfer,  $k^0$ , (Butler-Volmer kinetics, discussed in **section 4.1.3**), as A diffuses to the electrode surface, (diffusion layer *ca.* 10  $\mu\text{m}$ ). Following the exponential Nernst law the current would be expected to rise exponentially, but A becomes depleted at the electrode surface and therefore requires more A to diffuse from the bulk solution (which is slow relative to electron transfer). With no stirring, current thus becomes mass transport limited (governed by Fick's laws), giving the peak at point (4). At point (5) the current is decreasing with increasing potential as the concentration of A at the surface approaches zero, therefore this part of the CV is controlled by mass transport, and the diffusion layer thickness is *ca.* 40  $\mu\text{m}$ . At point (6), the potential is reversed. As  $E$  approaches  $E^0_f$  the current increases as electrolysis occurs, with the reduction of B back to A, which is also governed by heterogeneous electron transfer,  $k^0$ . The current increase follows the exponential Nernst law until B is depleted at the electrode surface, and requires the diffusion of B from the bulk solution, giving the reverse peak on the CV. This current decreases to zero as the diffusion layer of B increases to the point that there is almost zero B at the electrode surface, completing the CV.

### 4.1.3 Electrochemical reversibility

Electrode processes have two limiting behaviours - reversible and irreversible. These correspond to the rate of electron transfer; large (fast) or small (slow) values of the heterogeneous electron transfer coefficient,  $k^0$ , relative to mass transport kinetics, governed by the mass transport coefficient,  $k_{mt}$ .

$$\begin{aligned} k^0 &\gg k_{mt} && \text{electrochemical reversibility} \\ k^0 &\ll k_{mt} && \text{electrochemical irreversibility} \end{aligned}$$

In reversible processes,  $k^0 \approx 1 \text{ cm s}^{-1}$ , irreversible processes,  $k^0 \approx 10^{-5} \text{ cm s}^{-1}$ , and for the intermediate case,  $k^0$ , lies between this range.

Electron transfer follows Butler-Volmer kinetics as given by the following equations **eq 4.4** to **4.7**;

$$k_{red} = k_{red}^0 e^{\left(\frac{-\alpha F}{RT} \eta\right)} \quad \text{eq 4.4}$$

$$k_{ox} = k_{ox}^0 e^{\left(\frac{(1-\alpha)F}{RT} \eta\right)} \quad \text{eq 4.5}$$

$$i_0 = F A k^0 [R]_{bulk}^\alpha [O]_{bulk}^{1-\alpha} \quad \text{eq 4.6}$$

$$i = i_0 \left( \frac{[R]_0}{[R]_{bulk}} e^{\left\{\frac{(1-\alpha)F}{RT} \eta\right\}} - \frac{[O]_0}{[O]_{bulk}} e^{\left\{\frac{-\alpha F}{RT} \eta\right\}} \right) \quad \text{eq 4.7}$$

Where,  $A$  is the area of the electrode,  $i_0$ , is the standard exchange current,  $\alpha$  is the transfer coefficient of the species under investigation which reflects the symmetry of the transition state, for the process presented  $[R]$  = species B,  $[O]$  = species A, and  $\eta$  is the overpotential; the difference between the formal potential for the A/B couple and the overpotential is given by **eq 4.8**:

$$\eta = E - E_{A/B}^{0'} \quad \text{eq 4.8}$$

As electrolysis of A progresses, all the A at the electrode is consumed resulting in the depletion of A near the electrode surface, in turn giving a concentration gradient which fresh A must diffuse to give further electrolysis, given by **eq 4.10**. The depletion zone is known as the diffusion layer,  $\delta$ , the thickness of which increases as a function of time,  $t$ , in one dimension giving, given by **eq 4.9**:

$$\delta = \sqrt{2Dt} \quad \text{eq 4.9}$$

$$k_{mt} = \sqrt{\frac{DFv}{RT}} \quad \text{eq 4.10}$$

In reversible reactions the electron transfer rate is, at all potentials, greater than the rate of mass transport and the peak potential is independent of the applied scan rate. In the case of quasi-reversible the rate of electron transfer becomes comparable to the rate of mass transport and the peak potentials increase with increasing scan rate. For the irreversible case electron transfer rates are smaller than the rate of mass transport.<sup>155</sup>

#### 4.1.4 Effect of scan rate

At slow scan rates, the diffusion layer is very thick, while at faster scan rate the diffusion layer is thinner, and therefore, greater diffusional flux to the electrode ( $k_{mt}$  also increases) is seen at faster scan rates giving a larger peak current. Since the reversibility or otherwise of an electrochemical process reflects the competition between electron transfer kinetics and mass transport kinetics, faster scan rates will encourage greater electrochemical irreversibility. Unless the irreversibility is caused by a chemical reaction, in which case, reversibility may emerge at higher scan rates.



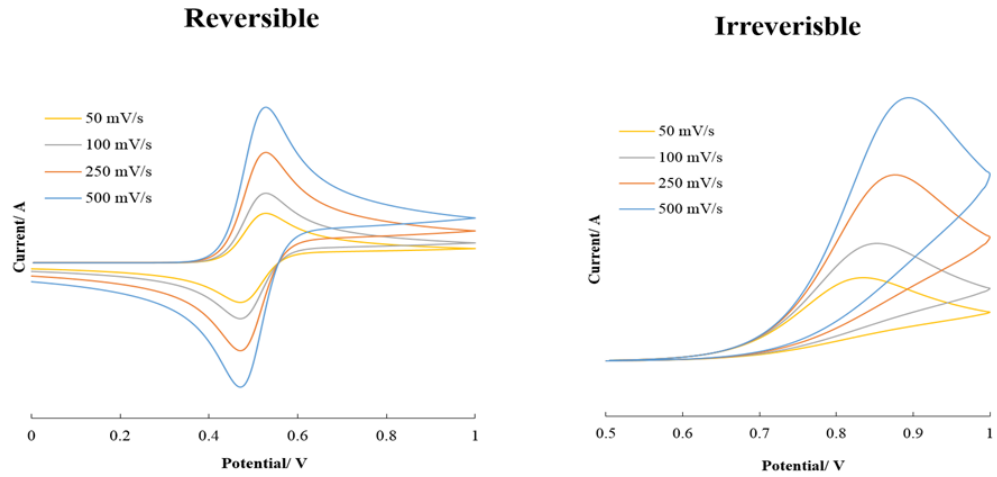


**Figure 4.4** Scan rate dependent cyclic voltammograms of a typical reversible (*left*) and irreversible (*right*) process.

#### 4.1.5 Diagnostic criteria of reversible and irreversible systems

Below are given the diagnostic criteria of cyclic voltammograms (CV) used to describe the reversibility, quasi-reversibility and irreversibility of different systems.

##### For a reversible process

- $\Delta E_p = (E_p^{ox} - E_p^{red}) = \text{constant}$ , with increasing scan rate
- $\left| E_p - E_{\frac{1}{2}} \right| = 2.218 \frac{RT}{F}$
- $i_p \propto \sqrt{v}$
- $i_p = 0.466 F A C_{bulk} \sqrt{\frac{F D v}{RT}}$
- $i_p = 2.69 \times 10^5 A C_{bulk} \sqrt{D v}$  (Randles –Sevcik equation), plot of  $i_p$  vs  $\sqrt{v}$  leads to D or A
- $\left| \frac{i_{p,ox}}{i_{p,red}} \right| = 1.0$

### For an irreversible process

- $E_p$  increases with increasing scan rate, and  $\Delta E_p = (E_p^{ox} - E_p^{red})$  increases if reverse peak is present
- $\left| E_p - E_{\frac{1}{2}} \right| = 1.857 \frac{RT}{\alpha F}$ , for reduction
- $\left| E_p - E_{\frac{1}{2}} \right| = 1.857 \frac{RT}{(1-\alpha)F}$ , for oxidation
- $i_p \propto \sqrt{v}$ , but the peak current is smaller
- $\left| \frac{i_{p, forward}}{i_{p, backward}} \right| > 1.0$ , if back wave is present at all

### For a quasireversible process

- $\Delta E_p = (E_p^{ox} - E_p^{red})$  = increases with increasing scan rate
- $i_p$  not necessarily proportional to  $\sqrt{v}$ , but the peak current is smaller than in reversible case
- Simulation is required to extrapolate kinetic and diffusion values

#### 4.1.6 Temperature dependence

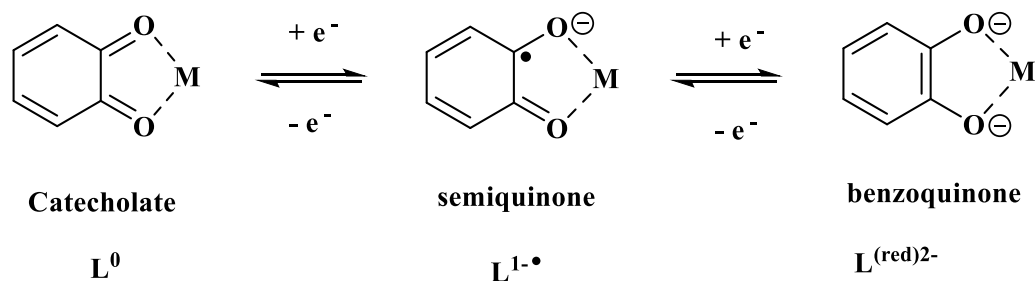
Cyclic voltammograms at different temperatures are current normalised by dividing by the square root of the diffusion coefficient,  $\sqrt{D}$  by the current  $i_p$ , at the different temperatures. Plots of  $\sqrt{D}/i_p$  vs  $V$  give temperature dependent behaviour of the cyclic voltammetry (CV) on a comparable scale. (Assuming the diffusion coefficients of all the reduced and oxidised species in the coordination complex are comparable and show the same dependence on temperature. In addition, the magnitude of the current is proportional to  $\sqrt{D}$  and therefore, minor differences in the diffusion coefficients are reduced when square rooted).<sup>156,157</sup>

## 4.2 Electrochemistry of metal complexes with redox non-innocent ligands

Before discussing the results obtained for the complexes studied in this thesis, there first follows a summary of relevant background literature.

### 4.2.1 Redox non-innocent ligands - $\alpha$ -iminopyridines

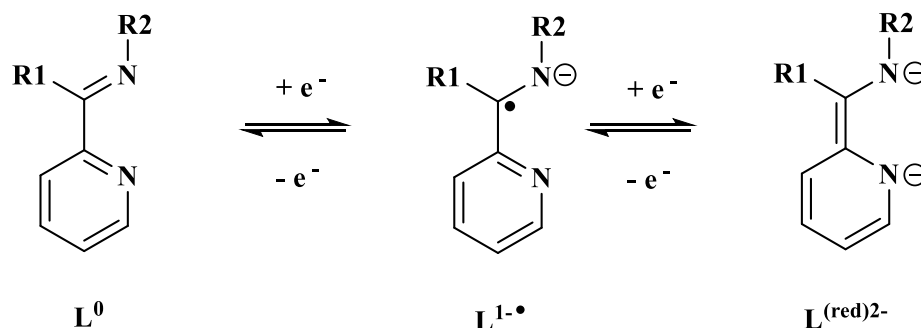
The term “non-innocent”, was introduced in 1966 by Jørgensen, who explained that “ligands are innocent when they allow oxidation states of the central atom to be defined”.<sup>158</sup> One of the first ligand sets to show “non-innocent” behaviour are the nickel dithiolene complexes, in which assignment of metal oxidation state is problematic. Analysis of electronic structure and calculation of frontier orbitals of the compounds has shown that electron transfer to and from the complexes is largely ligand-based rather than metal-based.<sup>159,160</sup> Ligands capable of behaving in this way, such as open-shell ligand radicals, are found throughout the coordination chemistry of transition metals. Examples include catechols,<sup>161-162</sup> *o*-phenylenediamines,<sup>163</sup> *o*-benzene-1,2-dithiolates and mixed analogues.<sup>164</sup>



**Scheme 4.1** Redox behaviour of catechol (benzene-1,2-diol) ligands.

These ligands are typically found as closed-shell dianions, but their electron-rich  $\pi$ -systems can be oxidized in one-electron steps to produce first the benzosemiquinone radical and then oxidised further to the benzoquinone. For example, catechol (benzene-1,2-diol) as shown in **scheme 4.1**, can coordinate to metal centres in the dianionic catecholato (benzoquinone) mode. Such ligands are non-innocent because there is an ambiguity as to how electrons will be delocalised between them and the metal, this will depend on the degree of mixing between appropriate metal and ligand orbitals. Catechols, semiquinones and quinones themselves are members of a redox rich series, and therefore

catechol complexes also show this rich electrochemistry in addition to that of the metal. The electrochemistry may involve the catechol ligand, the metal or both; and thus makes it difficult to disentangle these.<sup>165</sup>



**Scheme 4.2** Redox behaviour of  $\alpha$ -iminopyridine ligands

Ligands with electron-accepting  $\pi$ -systems, such as  $\alpha$ -diimines,  $\alpha$ -iminoketones, and  $\alpha$ -diketones are also redox non-innocent.<sup>166</sup> With structures resembling benzoquinone, having functionality in the 1,2-positions of a conjugated system, they can be reduced by one electron to generate the monoanionic-radical equivalent of the benzosemiquinone.<sup>167</sup> It has also been previously shown that iminopyridine ligands are redox non-innocent. With their extensive  $\pi$ -system, iminopyridines have been shown to exist in the neutral closed shell form, a monoanionic and as dianionic  $\pi$ -radical(s) within coordination complexes.  $\alpha$ -Iminopyridines can have three different redox states akin to that of catechol, shown in **scheme 4.2**.<sup>168</sup> The neutral  $\alpha$ -iminopyridine ( $L^0$ ) is the most commonly found. The open shell monoanion ( $L^{\cdot-}$ ) which has only been structurally characterised in two manganese complexes,<sup>169</sup> and the doubly reduced anion ( $L_{red}^{2-}$ ), which as of yet has not been structurally characterised.

#### 4.2.2 Series of comparable *bis*( $\alpha$ -iminopyridine)metal complexes

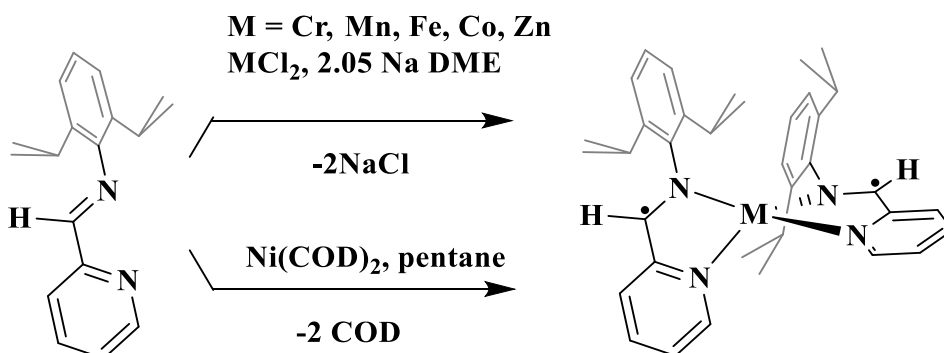
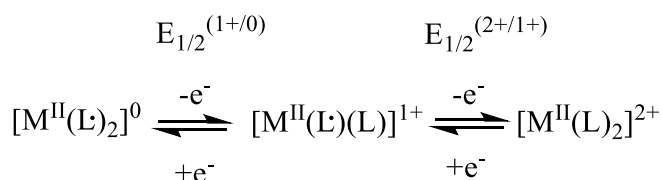


**Figure 4.5** A series of *bis*( $\alpha$ -iminopyridine) metal complexes.

Wieghardt and co-workers<sup>168</sup> previously synthesized a series of *bis*( $\alpha$ -iminopyridine)metal complexes featuring the first-row transition ions (Cr, Mn, Fe, Co, Ni, and Zn) as illustrated in **figure 4.5**. They showed that the iminopyridine ligands are redox non-innocent and their paramagnetic  $\pi$  radical monoanionic forms can exist in coordination complexes. Based on spectroscopic and structural characterizations, the neutral complexes were described as possessing a divalent metal centre and two monoanionic  $\alpha$ -iminopyridine  $\pi$  radicals. The neutral  $M(L^\bullet)_2$  compounds undergo ligand-centred, one-electron oxidations generating a second series,  $[(L^x)_2M(\text{THF})][B(\text{ArF})_4]$  [where  $L^x$  represents either the neutral  $\alpha$ -iminopyridine  $(L)^0$  and/or its reduced  $\pi$  radical anion  $(L^\bullet)^-$ ]. The cationic series comprise mostly mixed-valent complexes, wherein the two ligands have formally different redox states,  $(L)^0$  and  $(L^\bullet)^-$ , and the two ligands may be electronically linked by the bridging metal atom. Experimentally, the cationic Fe and Co complexes exhibited Robin-Day Class III behaviour (fully delocalized), whereas the cationic Zn, Cr, and Mn complexes belong to Class I (localized), see **section 4.6.1**.

Electrochemistry of all of the complexes demonstrated comparable electron transfer properties, with an irreversible ligand centred wave occurring at *ca.*  $-2.2 \text{ V vs Fc/Fc}^+$ . Also, each complex was shown to exhibit two reversible or quasi-reversible waves, which were assigned to the discrete one-electron oxidations of the ligand radicals.

**Table 4.1** Reduction potentials found for the *bis*( $\alpha$ -iminopyridine) metal complexes of Wieghardt and co-workers, *vs*  $\text{Fc/Fc}^+$ .



<b>M =</b>	<b>E<sub>1/2</sub><sup>(1+/0)</sup> /V</b>	<b>E<sub>1/2</sub><sup>(2+/1+)</sup> /V</b>	<b>ΔE<sub>1/2</sub> / mV</b>
<b>Cr</b>	-1.17	-0.9	270
<b>Mn</b>	-1.4	-1.14 (α)	260
<b>Fe</b>	-1.35	-1 (α)	350
<b>Co</b>	-1.26	-0.76	500
<b>Ni</b>	-1.2	-0.56	630
<b>Zn</b>	-1.33	-1.16	170

α = quasi-reversible

The separation between the potential of the two processes was shown to steadily increase moving across the period from Cr to Ni, however the smallest separation was seen for Zn (**table 4.1**). The increasing ΔE<sub>1/2</sub> was proposed to reflect the growing electronic interaction between the ligands across the period from Cr to Co, which is also interpreted as an increasing metal character in the predominately ligand-centred oxidations. The E<sub>1/2</sub><sup>(2+/1+)</sup> event for nickel was found to be almost completely metal-centred. The Co complex was shown to have an additional quasi-reversible event at -1.96 V which was assigned to the metal-centred reduction Co<sup>II+</sup> + e<sup>-</sup> → Co<sup>I+</sup>. An analogous feature was shown to also be present for the earlier transition metals Cr, Mn and Fe but completely irreversible, and absent in the later transition metals Ni, and Zn.

### 4.3 Understanding electrochemistry through computation: Density Functional Theory (DFT)

During the course of this research DFT studies of some of the complexes under investigation were undertaken by Mr. Christopher Prior of the Oganeyan research group, to try to understand processes occurring on reduction and oxidation.

DFT calculations were performed on the three main cobalt complexes **CoL1N**, **CoL2N**, and **CoL3N** for the four reduced states (from an overall complex charge of 2+ to -1) to further the understanding of their electrochemical and electrocatalytic behaviour. Additional calculations were performed on other systems of interest to help explain certain points: specifically the rich oxidation chemistry of **MnL3N** and the two isomers of **ZnL3N**. It should be understood that these DFT calculations may not account for all possible variables such as other potential conformation and that in solution there will be interaction with solvent molecules (the energy of such is accounted for), and primarily serve to help support a *qualitative* interpretation of experimental data.

#### 4.4.1 Electrochemistry of iminopyridine ligands

To help understand the electrochemistry of the metal complexes, the electrochemical behaviour of the *bis*-iminopyridine ligand **5**, **L2** is described below, as a representative of the entire series of similar ligands described in Chapter 2. These all have identical iminopyridine functionality.<sup>170</sup>

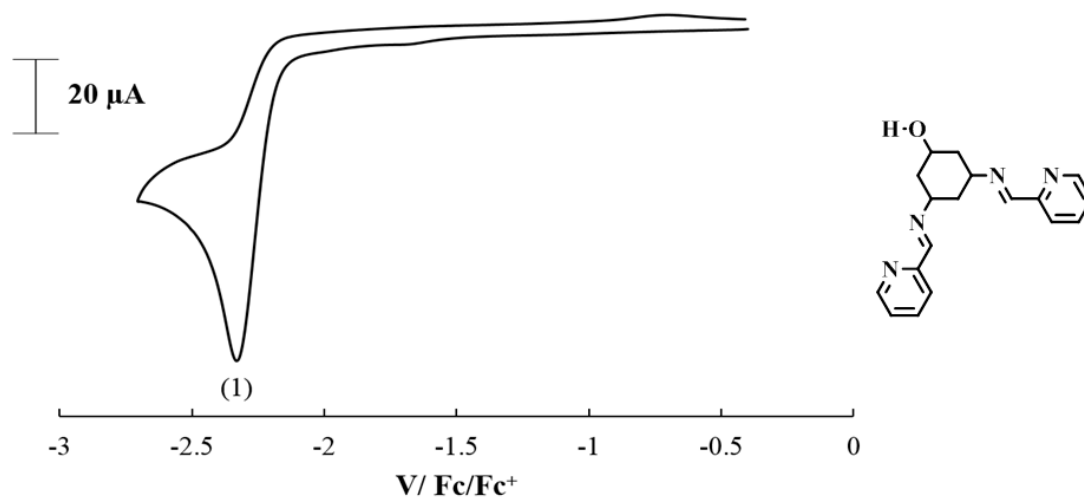


**Figure 4.6** Cyclic voltammogram of 1 mM **5**, **L2** at GCE at 100 mV/s in acetonitrile. RE = Ag/AgCl (internal Fc/Fc<sup>+</sup> ref). CE = Pt. 0.1 M TBABF<sub>4</sub> supporting electrolyte

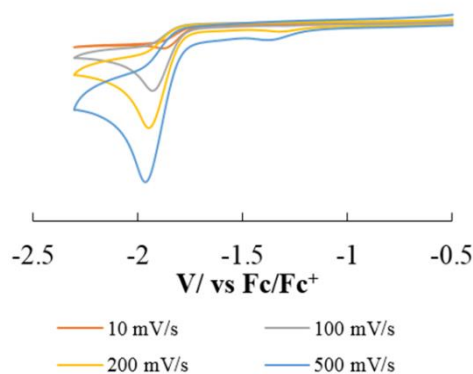


**Figure 4.7** Scan rate dependence for 1 mM **5**, **L2** at GCE

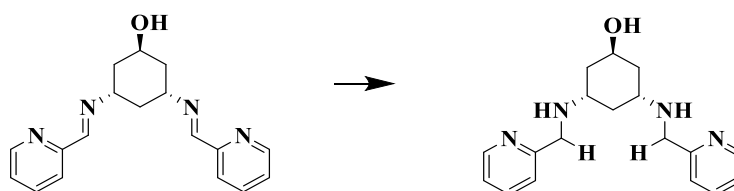


**Figure 4.8** Reduction of imine groups of **5**, **L2** to corresponding amine.

The cyclic voltammetry of **5**, **L2** gives a large peak at  $E_p = -2.32$  V vs Fc/Fc<sup>+</sup> (at 100 mV/s). This wave shifts to a more negative potential with increasing scan rate, indicating irreversible electron transfer. The peak is significantly positively shifted from that of pyridine (*ca.*  $-3.5$  V vs Fc/Fc<sup>+</sup> on GCE),<sup>171-173</sup> or 4,4-bipyridine ( $-2.65$  V, and reversible). Therefore, this reduction must be attributed to the reduction of the imines to the saturated amines as shown in **figure 4.8**. This behaviour has been shown previously by Andrieux and Saveant, that in MeCN, most Schiff bases give a single two-electron wave leading to the saturated amine. These radical anions of the imines are more basic than the corresponding ketyl anions and can abstract a proton from residual water present in the acetonitrile solvent.<sup>174</sup>



#### 4.4.2 Electrochemistry of Zinc complexes – ZnL1N, ZnL2N and ZnL3N

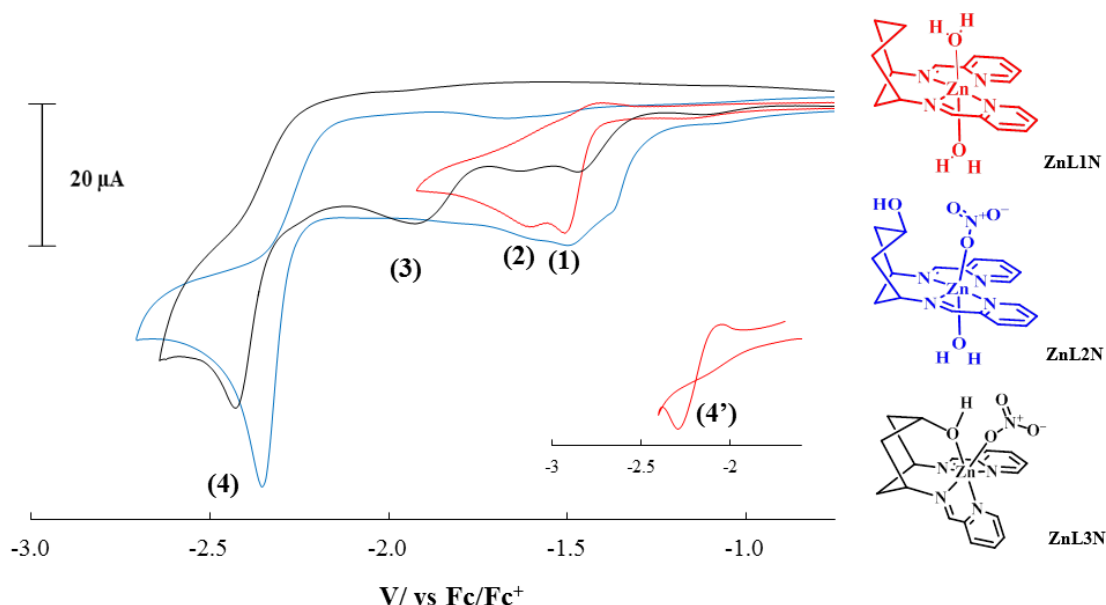


**Figure 4.9** Cyclic voltammetry of 1 mM **ZnL1N**, **ZnL2N** and **ZnL3N** at GCE at 100 mV/s in acetonitrile. RE = Ag/AgCl (internal Fc/Fc<sup>+</sup> reference). CE = Pt. 0.1 M TBABF<sub>4</sub> supporting electrolyte.

**Table 4.2** Peak potentials E<sub>P</sub> of **ZnL1N**, **ZnL2N** and **ZnL3N** in MeCN at GCE vs Fc/Fc<sup>+</sup> /V

Complex	E <sub>P</sub> (1)	E <sub>P</sub> (2)	E <sub>P</sub> (3)	E <sub>P</sub> (4)
<b>ZnL2N</b>	-1.38	-1.49	-	-2.36
<b>ZnL3N</b>	-1.46	-1.62	-1.95	-2.43
<b>ZnL1N</b>	-1.5	-1.59	-	‘-2.6’

Zinc(II) has a 3d<sup>10</sup> electronic configuration and thus access to higher energy metal based orbitals is not energetically feasible. Zn<sup>II</sup> itself is therefore, redox inactive over the working potential range (solvent window, -3.0 to +2.0 vs Fc/Fc<sup>+</sup>). However, as shown by Wieghardt and co-workers,<sup>168</sup> α-iminopyridine ligands are themselves redox active. Therefore, the zinc complex allows investigation of the redox properties of the ligand in the coordination environment of a redox silent metal and can provide information that helps interpret electrochemistry of other metal complexes.

#### Electrochemistry of ZnL2N and ZnL1N

The cyclic voltammogram of **ZnL2N** shows 3 irreversible peaks at E<sub>P</sub> = - 1.38, -1.49 and -2.36 V vs Fc/Fc<sup>+</sup> (at 100 mV/s). Scan rate dependence shows these waves to shift

more negative with increasing scan rate indicative of irreversible electron transfer. The waves at at  $-1.38$  and  $-1.49$  V can be attributed to one electron processes and the wave at  $-2.36$  V attributed to a 2 electron irreversible reduction having twice the peak current of the other two processes. The cyclic voltammetry of **ZnL1N** gives 2 irreversible peaks at  $E_p = -1.5$  and  $-1.59$  V vs  $\text{Fc}/\text{Fc}^+$  (at  $100$  mV/s). Scan rate dependence shows these waves to a shift more negative with increasing scan rate indicative of irreversible electron transfer. On scanning to even more negative potentials a 3<sup>rd</sup> wave is also seen, however this suffers from cross-over, shown on the insert of **figure 4.9**. This is characteristic of nucleation and growth processes on the electrode surface.<sup>175</sup> This therefore indicates that **ZnL1N** deposits on the electrode surface at these highly reducing potentials.

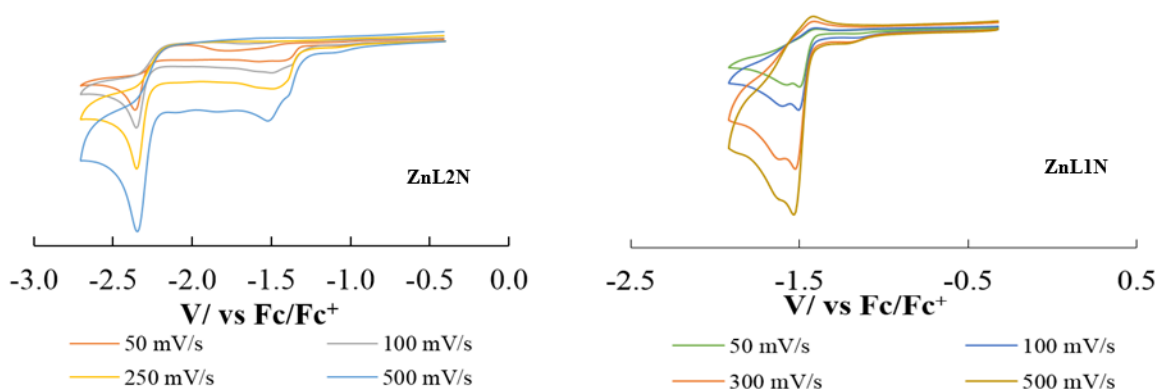
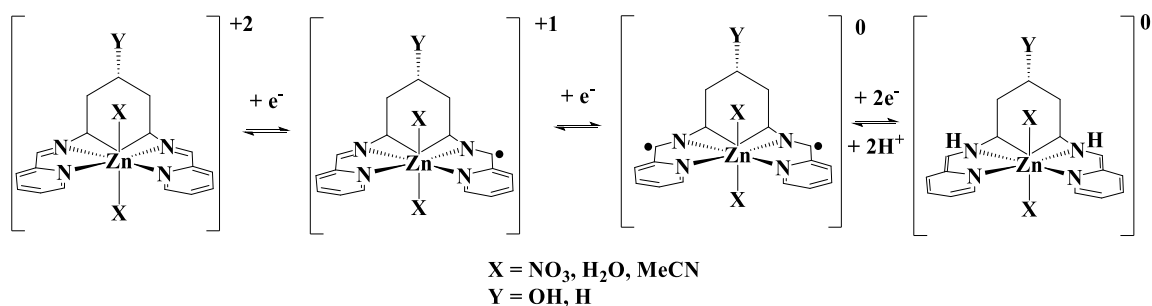
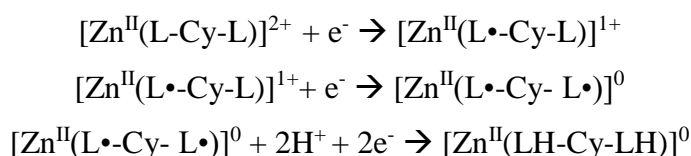


**Figure 4.10** Scan rate dependence for 1 mM **ZnL2N** (left) and **ZnL1N** (right) at GCE

The first two reductions of **ZnL2N** and **ZnL1N**, at  $-1.38$ ,  $-1.49$ , and  $-1.5$ ,  $-1.59$  V respectively can be assigned to successive independent reductions of the two iminopyridine “arms” of the ligands, resulting in two monoanionic arms (an overall dianion-diradical ligand) as shown in Wieghardt’s work. As the peak at  $-2.36$  V for **ZnL2N** has twice the peak current of the other two processes, and a peak at similar potential ( $-2.2$  V) was shown to be solely ligand based in Wieghardt’s work, it can be postulated that peak is from the two electron two proton reduction of the ligand to the diamine, as shown in **scheme 4.3** with protons coming from the solvent.



**Scheme 4.3** Proposed reductions of **ZnL1N** and **ZnL2N**.



### Electrochemistry of **ZnL3N**

The cyclic voltammetry of **ZnL3N** is more complex than that of the other zinc complexes, with emergence of an additional peak resulting in a total of 4 peaks at  $-1.46$ ,  $-1.62$ ,  $-1.95$  and  $-2.43$  V vs  $\text{Fc}/\text{Fc}^+$  (at  $100 \text{ mV s}^{-1}$ ). As **ZnL3N** introduces no additional redox active groups vs the other zinc complexes (**ZnL1N** and **ZnL2N**), this behaviour is tentatively ascribed to molecular motion involving interconversion between two isomers (**A** and **B**, **figure 4.14**). **A** has the crystallographically observed trigonal prismatic geometry, and **B** has a similar geometry to  $\text{Cu}^{\text{II}}$  analogue (**CuL3N**) with the Zn-O bond broken, or greatly elongated and the imino-pyridines occupying the equatorial plane. Thus, de-coordination of the hydroxyl in **B** yields a similar Zn-iminopyridine geometry to **ZnL2N** and **ZnL1N**. (Illustrated in **figure 4.14**)

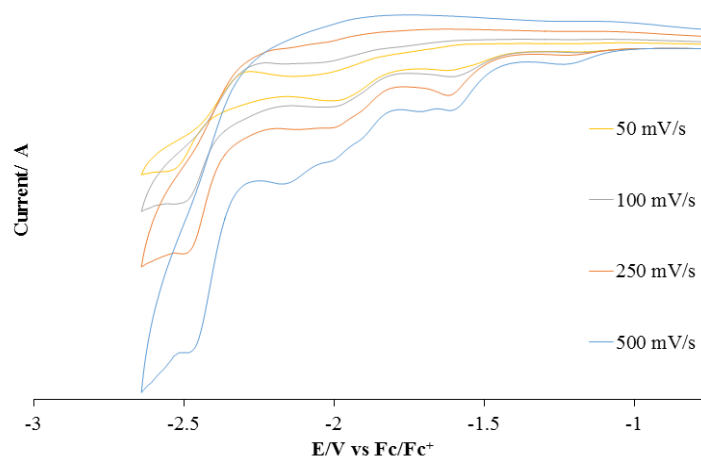


**Figure 4.11** Scan rate dependence for 1 mM **ZnL3N** at 5 °C.

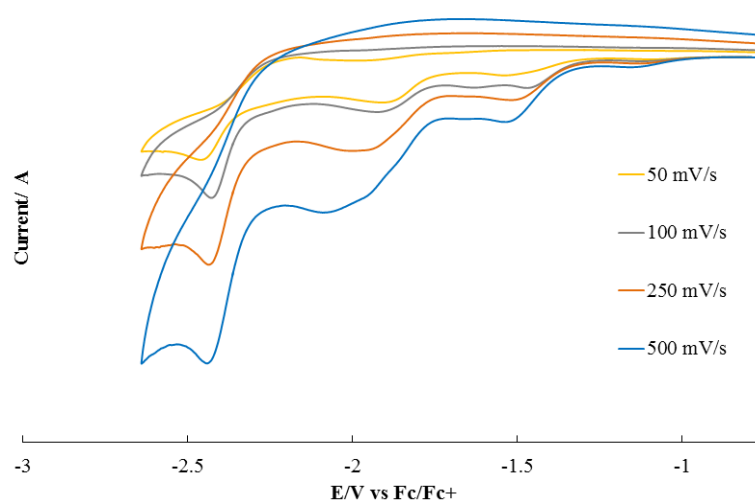


**Figure 4.12** Scan rate dependence for 1 mM **ZnL3N** at room temperature.

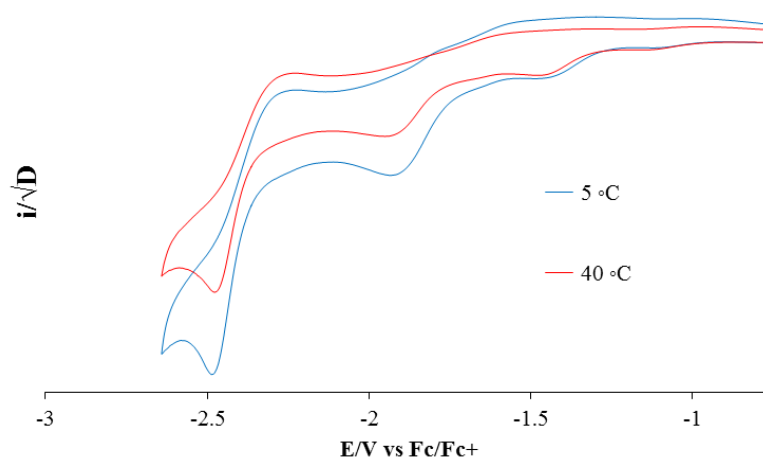


**Figure 4.13.** Current normalised temperature dependence **ZnL3N** at 100 mV/s. (Current normalised through division of the square root of the diffusion coefficient, found at room temperature from Randles-Sevcik analysis).

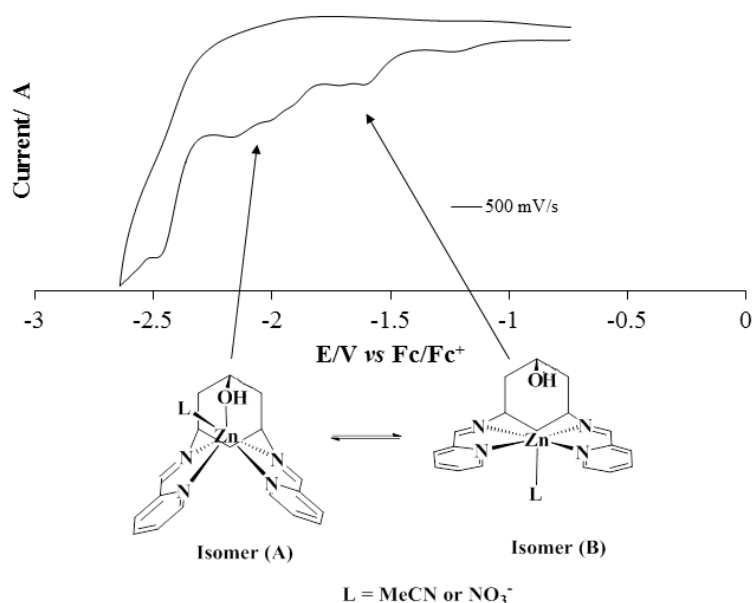


**Figure 4.14.** Proposed explanation for behaviour seen by cyclic voltammetry.

**Table 4.3** Average metal –oxygen bond dissociation energies <sup>175-178</sup>

Bond	KJ/mol
Zn-O	284
Cu-O	343
Co-O	368
Mn-O	402

Several lines of evidence support this hypothesis. Firstly, high scan rate data at 5 °C (**figure 4.11**), show the waves at *ca.* –2 and –1.6 V *vs* Fc/Fc<sup>+</sup>, resolving into two processes, –1.60 and –1.69 V for the first process, and –1.99 and –2.15 V for the second process (at 500 mV s<sup>–1</sup>). The reductions at –1.60 and –1.69 V can be assigned to that of isomer (**B**), as they occur at similar potential to **ZnL2N** and **ZnL1N**. Those at –1.99 and –2.15 V are assigned to isomer (**A**). The two processes for each isomer correspond to independent reductions of the two iminopyridine arms, as described for the other zinc complexes. Isomer (**A**) has reductions at more positive potential than (**B**) as the hydroxyl present in (**A**) donates electron density to the metal centre and therefore making it less electro-positive, therefore the zinc withdraws less electron density from the ligands, and thus the iminopyridine ligands become harder to reduce. There may also be an effect from the change in geometry on the energy of the ligand centred LUMO.

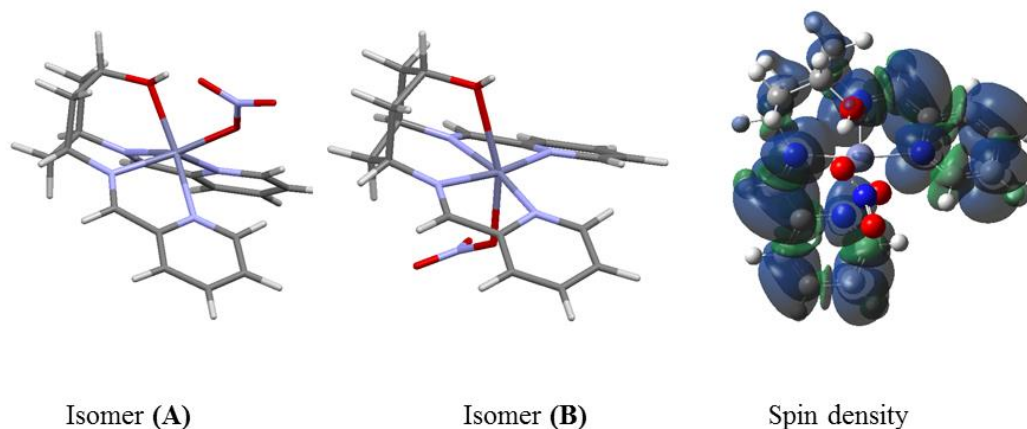
Scan rate dependence for **ZnL3N** at room temperature shown in **figure 4.12**, shows a fairly constant ratio of the peak currents for the two isomers at the various scan rates, and hence a fairly constant ratio of their concentrations. This suggests one of two limiting cases; that the kinetics of interconversion between the two is relatively slow: too slow to be observed over the range of scan rates studied. Or interconversion is fast enough in both directions that within the range of scan rates covered, there is no difference to what is observed through changing the scan rate

At low temperatures (5 °C) there is a larger percentage of isomer (**A**), shown from the larger ' $i_p$ ' in the peaks centred at  $-1.95\text{ V vs Fc/Fc}^+$ , compared to that seen at higher temperatures. This is in accordance with expectations. At low temperatures there is a smaller amount of thermal energy to break the Zn-O bond, so at 5 °C the Boltzmann population of isomer (**B**) is smaller than at 40 °C where there is more energy to break/elongate the Zn-O bond and give isomer (**B**).

The average Zn-O bond dissociation energy is  $284\text{ kJ mol}^{-1}$  (**table 4.3**), the weakest of the average metal-oxygen bonds of the four metal complexes made with the **L3** ligand, even though copper(II)  $3d^9$ , undergoes Jahn-Teller distortions and therefore has elongated and weakened axial bonds. In the crystal structure of **CuL3N** is shown to give a square based pyramidal geometry with full de-coordination of the proximal hydroxyl. As the average Cu-O bond dissociation energy is  $343\text{ kJ mol}^{-1}$ ,  $59\text{ kJ mol}^{-1}$  more than that of zinc it can be assumed that this is also possible for zinc. In addition, as zinc(II) is  $3d^{10}$  the d orbitals have full occupancy and therefore there is no ligand field stabilisation energy present. Ligand coordination therefore should not be dictated by d orbital energies.

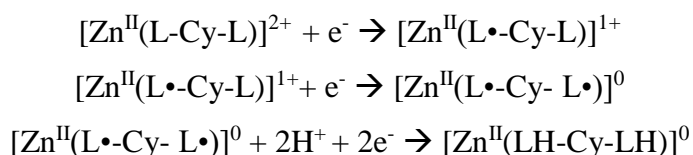
The energy difference between the LUMOs of the two isomers can be estimated from the CV, using their reduction potentials (a measure of the energy of the LUMO). This difference of 425 mV translates to  $41.0\text{ kJ mol}^{-1}$  (from  $\Delta G = -nFE$ , where  $n$  = number of electrons,  $F$  = Faraday's constant,  $E$  = difference in potential between peaks). This is reasonably consistent with a DFT estimated difference of LUMO energies between the isomers of  $20\text{ kJ mol}^{-1}$ . The difference in these energies may be caused by solvent affects or geometry changes not accounted for in the calculations. DFT also calculates an elongation of the Zn-O bond from 2.16 to 2.55 Å. Electron density for each of the reduced

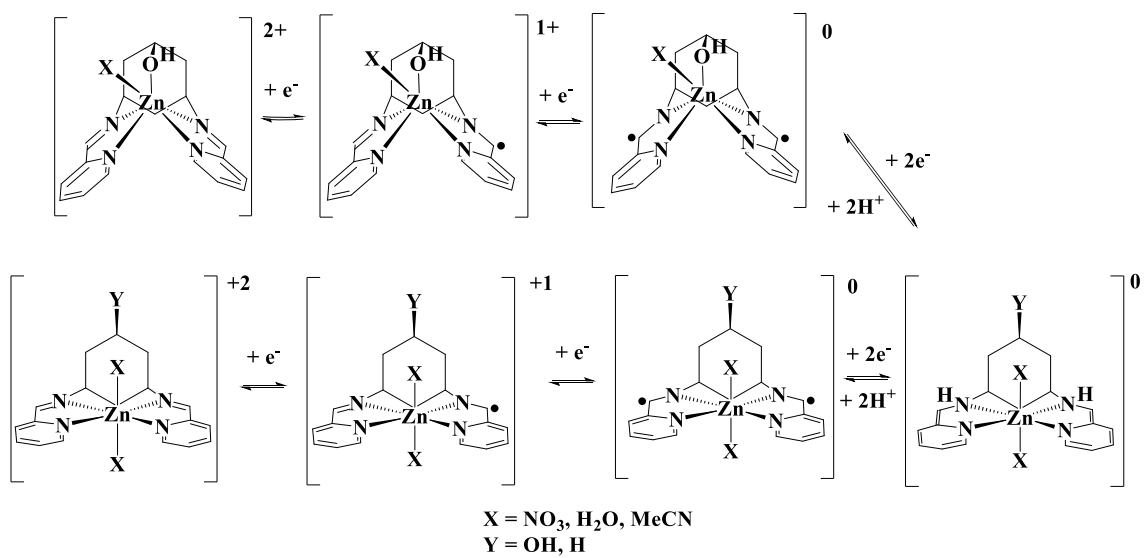
structures is focused on the iminopyridine ligands as expected for zinc, as shown in **figure 4.15**.



**Figure 4.15** DFT structures of proposed isomers for **ZnL3N** and spin density for **ZnL3N<sup>-1</sup>**.

The wave at  $-2.46\text{ V vs Fc/Fc}^+$  remains constant for both isomers, suggesting the same electronic environment and perhaps the same geometry, as this peak comes at roughly the same potential as the DDOP (**5**, **L2**) ligand which is itself an isomer of the DDOPi (**9**, **L3**) with the same iminopyridine redox active functionality. This suggests that after reduction only isomer **B** is present and therefore, this wave can therefore be assigned to a ligand based two electron two proton reduction process from from the decoordinated form (isomer **B**) for reduction of the imine to the amine as shown for **ZnL1N** and **ZnL2N**.





**Scheme 4.4** Proposed reduction of the two isomers of **ZnL3N**



#### 4.4.3 Electrochemistry of Manganese complexes – MnL1N, MnL2N and MnL3N

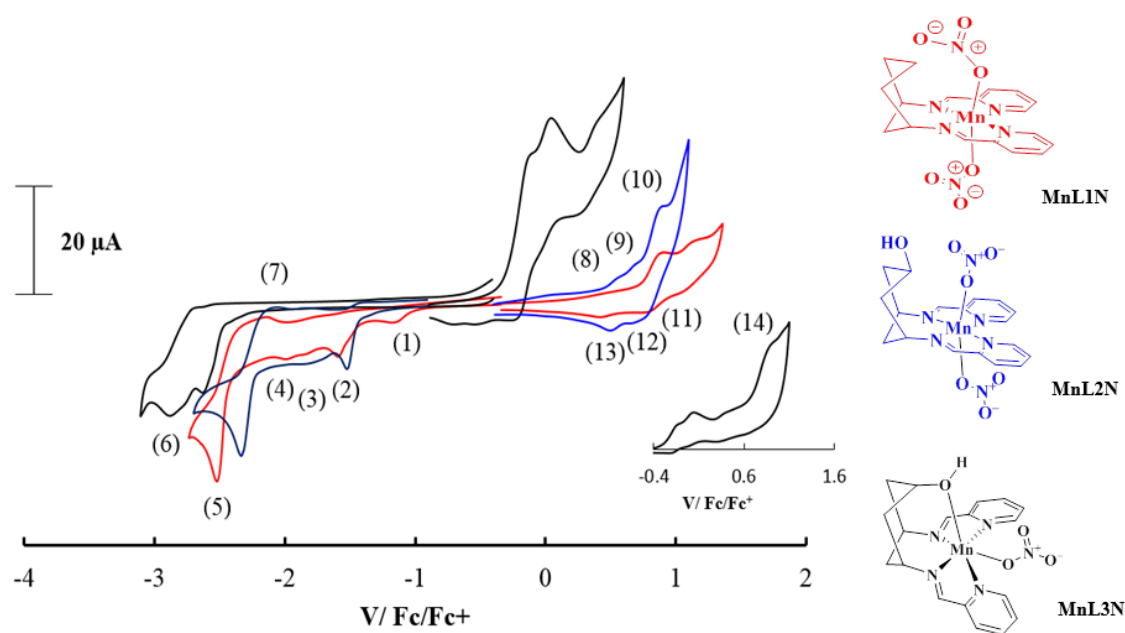


**Figure 4.16** Cyclic voltammetry of 1 mM **MnL1N**, **MnL2N** and **MnL3N** at GCE at 100 mV/s in acetonitrile. RE = Ag/AgCl (internal Fc/ Fc<sup>+</sup> reference). CE = Pt. 0.1 M TBABF<sub>4</sub> supporting electrolyte.

**Table 4.4** Peak potentials  $E_P$  of **MnL1N**, **MnL2N** and **MnL3N** in MeCN at GCE vs Fc/Fc<sup>+</sup>/V

Reductive							
Complex	$E_P$ (1)	$E_P$ (2)	$E_P$ (3)	$E_P$ (4)	$E_P$ (5)	$E_P$ (6)	$E_P$ (7)
<b>MnL2N</b>	-1.34	-1.51	-1.86	-	-2.34	-	-2.05
<b>MnL3N</b>	-	-	-	-2.66	-2.81	-2.87	-
<b>MnL1N</b>	-1.15	-1.55	-1.8	-1.98	-2.53	-	-2.15
Oxidative							
Complex	$E_P$ (8)	$E_P$ (9)	$E_P$ (10)	$E_P$ (11)	$E_P$ (12)	$E_P$ (13)	$E_P$ (14)
<b>MnL2N</b>	0.53	0.66	0.85	-	0.69	0.52	
<b>MnL3N</b>	-0.1	0.06	0.4	-	0.28	-	0.95
<b>MnL1N</b>	0.89	1.02	-	1.08	0.80	0.48	

## Electrochemistry of MnL2N

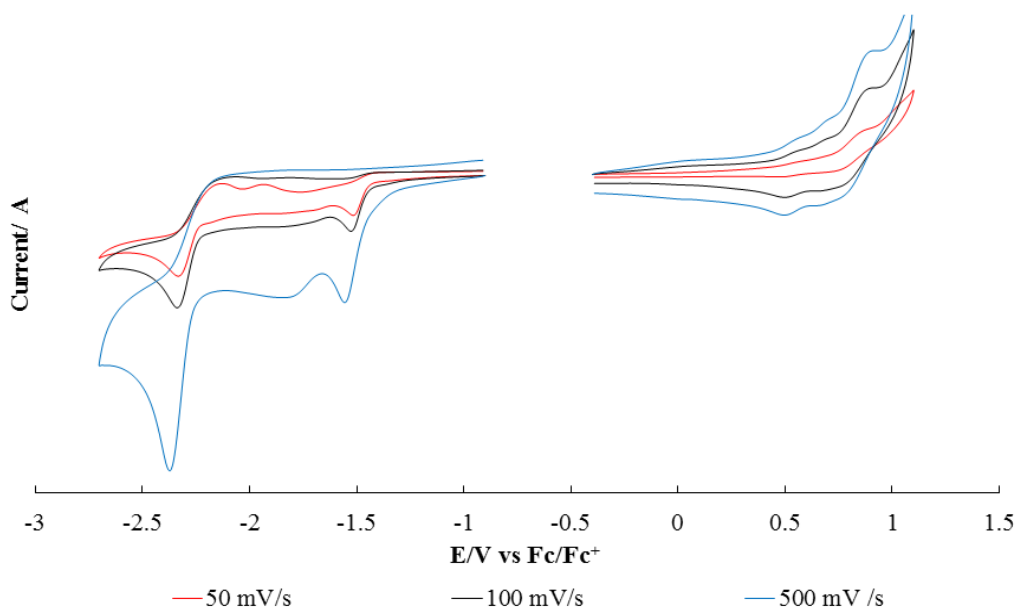
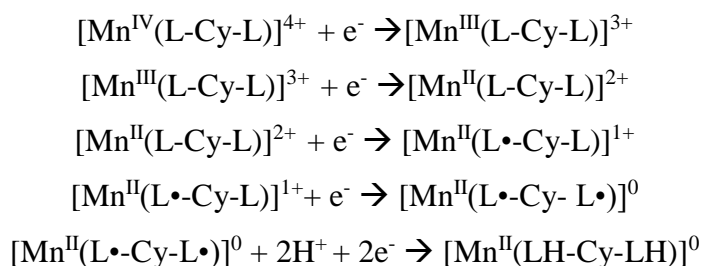


**Figure 4.17** Scan rate dependence for 1 mM **MnL2N**

On sweeping the potential negatively the cyclic voltammetry of **MnL2N** gives 3 main largely irreversible peaks at  $E_P = -1.51, -1.86,$  and  $-2.34$  V vs  $\text{Fc/Fc}^+$  (at 100 mV/s). Scan rate dependence shows these waves to shift more negative with increasing scan rate indicative of irreversible electron transfer. The waves at  $-1.51$  and  $-1.86$  V can be attributed to one electron processes and the wave at  $-2.34$  V assigned to a 2 electron irreversible reduction having twice the peak current of the other two processes. Reduction of  $\text{Mn}^{\text{II}}$  to  $\text{Mn}^{\text{I}}$  over the potential range is unfavourable due to pairing energy associated; therefore the reductions seen are likely to have large ligand character as shown by Wieghardt and co-workers for their iminopyridine manganese complex.<sup>179</sup> On sweeping to positive potentials the cyclic voltammetry of **MnL2N** gives 3 quasi-reversible oxidations with  $E_P = 0.53, 0.66,$  and  $0.85$  V vs  $\text{Fc/Fc}^+$  (at 100 mV/s). These waves increase linearly with the square root of scan rate indicating a freely diffusing species. These must be metal based oxidations, as the ligand has no oxidations over the range given, shown by the electrochemistry of the free ligand and the zinc complexes. The current of the initial two waves at 0.53 and 0.66 V are around half of that for the one electron reductions, and is therefore consistent with transfer of “half” an electron. This is postulated to be due to disproportionation of  $\text{Mn}^{3+}$  into  $\text{Mn}^{2+}$  and  $\text{Mn}^{4+}$ .  $\text{Mn}^{3+}$  is commonly found to be highly unstable and disproportionates.<sup>179</sup>



### The electrochemistry of MnL3N

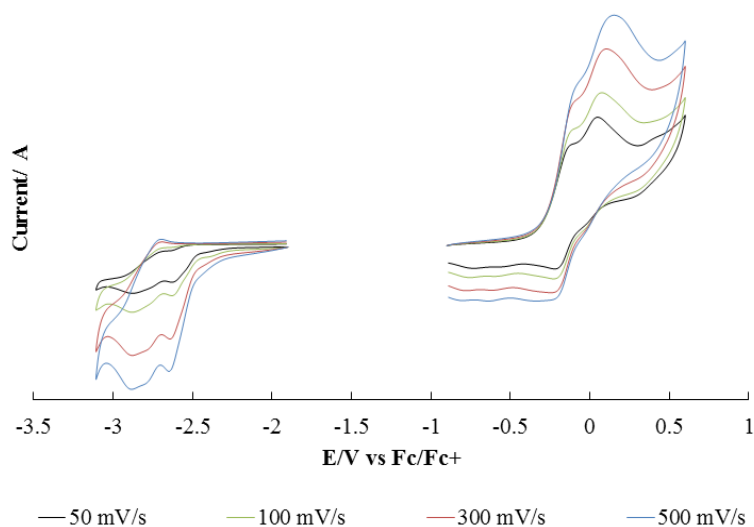


**Figure 4.17** Scan rate dependence for 1 mM **MnL3N**

On sweeping the potential negatively the cyclic voltammetry of **MnL3N** gives 3 main irreversible peaks at  $E_p = -2.66, -2.81$  and  $-2.87$  V vs  $\text{Fc}/\text{Fc}^+$  (at 100 mV/s), which increase linearly with the square-root of scan rate, indicating a freely diffusing species. The waves at  $-2.66$  and  $-2.81$  V although overlapping can be attributed to one electron processes and the wave at  $-2.87$  V assigned to a two-electron irreversible reduction having twice the peak current of the other two processes. From the DFT of **MnL3N** it is shown that on reduction to the 1+ state there is a lengthening of the Mn-O bond from 2.052 to 2.091 Å, with a slight change in geometry toward a more perfect trigonal pyramidal geometry as shown in **figure 4.18**. From the LUMO diagram of the 2+ state it can be seen that this process has a mixed ligand metal based reduction with a significant contribution from the metal. On further reduction to the 0 state there is a further elongation of the Mn-O bond to 2.127 Å, and a change in geometry to a distorted square based pyramidal. From the LUMO of the 1+ state it can be seen that this process is a mixed ligand metal based reduction with a significant contribution from the metal. This change in geometry may be

caused by the donation of electron density into the  $e'$  orbitals of the trigonal prismatic 'd' orbitals, which is shown to disfavour the trigonal prismatic geometry and to favour that of octahedral geometry,<sup>180</sup> as shown in **figure 3.13** and **table 3.4**. This effect may also favour square based pyramidal geometry as seen in the DFT, which gives a larger ligand field splitting than octahedral. The reductions are shifted more much more negative than in **MnL2N**, this can be attributed to the electron rich hydroxyl donating electron density to the metal centre, and thus withdrawing less electron density from the ligands, raising the LUMO in energy and making the reductions harder. The difference in LUMO energy for **MnL3N** compared to **MnL2N** from DFT studies is *ca.* 35 kJ mol<sup>-1</sup>, (*ca.* 363 mV). This negative shift in reduction potential is also seen with **ZnL3N** with a *ca.* 425 mV shift found in the isomer **A** with the hydroxyl bound compared to isomer **B**.

The first two reductions of **MnL3N**, -2.66, -2.81, can be assigned to independent reductions of the two iminopyridine ligands giving two mono-anionic ( $L\bullet^-$ ) iminopyridine ligand arms, as found in the zinc complexes. With the peak at -2.87 V *vs* Fc/Fc<sup>+</sup> which was shown to be solely ligand based in Wieghardt's work, occurring at a potential 500 mV more negative than reduction of the free ligand. It can be postulated that this is from the proton coupled electron reduction of the ligand with protons coming from the solvent.

On sweeping the potential positively the cyclic voltammetry of **MnL3N** gives 4 main peaks, with the first two showing quasi-reversible behaviour and the latter two irreversible behaviour at  $E_p = -0.1, 0.06, 0.4$  and  $0.95$  V *vs* Fc/Fc<sup>+</sup> (at 100 mV/s) ( $E_p$  for the oxidations are given for quasi-reversible waves, as the return reduction waves are small and less defined). These are shown to increase linearly with the square-root of scan rate indicative of a freely diffusing species. The peak at -0.1 V has a peak current consistent with a two electron process, which is consistent with metal based oxidation from DFT studies and electrochemistry of the zinc complex. Therefore this process can be assigned to a two electron metal based oxidation, from Mn<sup>2+</sup> to Mn<sup>4+</sup>. Mn<sup>3+</sup> complexes have been shown to be unstable and susceptible to disproportionation reactions, and therefore this behaviour may be a consequence of this.<sup>181</sup> The oxidation at 0.06 V can be attributed to the one electron oxidation of Mn<sup>4+</sup> to Mn<sup>5+</sup>. The oxidation at 0.4 V can also be assigned to a one electron oxidation from Mn<sup>5+</sup> to Mn<sup>6+</sup>. The process at 0.95 V gives a large enhancement of peak current corresponding to that of nine electrons, this is indicative of a catalytic process. There are several possible explanations for this catalytic

response; either the complex is catalytically oxidising residual water present in the solution to oxygen, the complex may be catalysing the oxidative destruction of acetonitrile, or the complex is catalysing its own oxidative destruction, or a combination of all three processes is occurring. The further investigation required to delineate these possible contributions is beyond the scope of this thesis.

## Electrochemistry of MnL1N

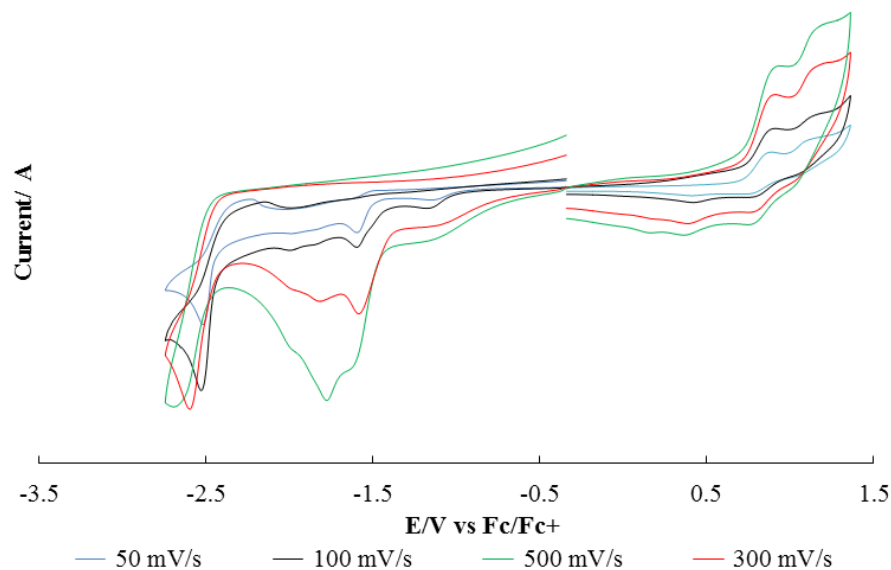


**Figure 4.21** Scan rate dependence for 1 mM **MnL1N**.

On sweeping the potential negatively the cyclic voltammetry of **MnL1N** gives 4 main irreversible peaks at  $E_P = -1.55, -1.8, -1.98$  and  $-2.53$  V vs  $\text{Fc/Fc}^+$  (at 100 mV/s). At low scan rates ( $<100$  mV/s), it shows similar electrochemical behaviour to **MnL2N** and **ZnL2N**, but a more complex response at faster scan rates suggests an additional process is occurring to those seen for the DDOP (**5**, **L2**) complexes. The reductions at  $-1.55$  and  $-1.98$  V increase steadily in current with square-root of scan rate and shift to more negative potentials. However, the relative current for the reduction at  $-1.8$  V grows significantly from 100 to 300 and 500  $\text{mV s}^{-1}$ , and shifts to more positive potential. The reduction at  $-2.53$  V, however, behaves in the opposite fashion, declining in current relative to the other processes between 100 and 500  $\text{mV s}^{-1}$ , and shifting to more negative potential. As it is seen that the zinc(II), DDP (**10**, **L1**) complex, **ZnL1N** is unstable at highly reducing potentials, it is quite probable that the manganese complex of the same ligand suffers from the same problem: both Mn(II) ( $d^5$ ) and Zn(II) ( $d^{10}$ ) complexes have

no ligand field stabilisation. There should also be less back-bonding in manganese than zinc as the metal d-orbitals have fewer electrons. This suggests that the complicated behaviour may be due to the formation of a decomposition product which is also redox active but highly reactive, therefore, only seen at faster scan rates before it has had a chance to react on.

On sweeping the potential positively the cyclic voltammetry of **MnL1N** gives two peaks at 0.89 and 1.02 V *vs* Fc/Fc<sup>+</sup> (at 100 mV/s), but also gives three small reverse reduction peaks at 1.08, 0.80, and 0.48 V *vs* Fc/Fc<sup>+</sup> (at 100 mV/s). This suggests that either the oxidations are multi electron processes which give a change in the complex on oxidation leading to different re-reduction of the species formed. Or there is a decomposition product formed with a different potential. The oxidative peak currents increase linearly with increase in the square-root of scan rate indicating a freely diffusing species. These could be postulated to be metal based oxidations, as the ligand has no oxidations over the range given. The currents of the initial two waves at 0.89 and 1.02 V are consistent with transfer of one electron, and are therefore are postulated Mn<sup>2+</sup> to Mn<sup>3+</sup>, and the oxidation of Mn<sup>3+</sup> to Mn<sup>4+</sup>.

#### 4.4.4 Electrochemistry of Nickel complex - NiL2C

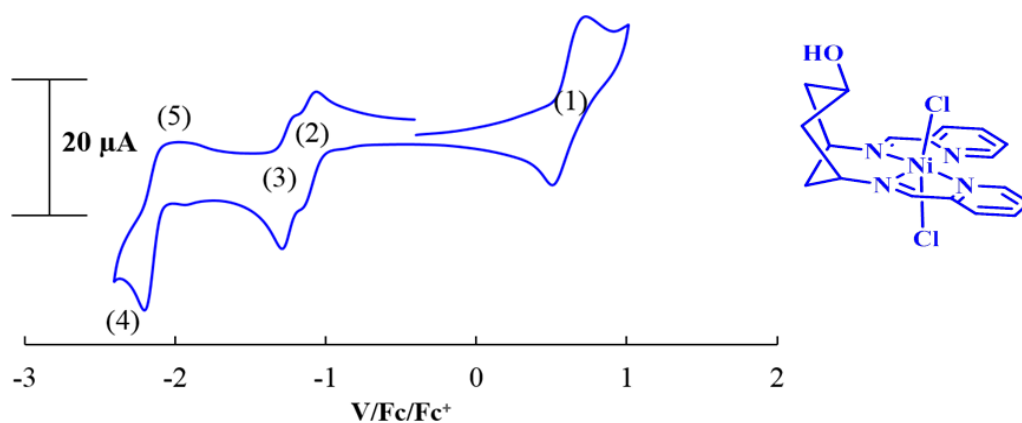


**Figure 4.22** Cyclic voltammetry of 1 mM **NiL2C** at GCE at 100 mV/s in acetonitrile. RE = Ag/AgCl (internal Fc/Fc<sup>+</sup> reference). CE = Pt. 0.1 M TBABF<sub>4</sub> supporting electrolyte.

**Table 4.5** Reduction potentials  $E_p$  and  $E_{1/2}$  of **NiL2C** in MeCN at GCE vs Fc/Fc<sup>+</sup>/V

Complex	$E_{1/2}$ (1)	$E_{1/2}$ (3)	$E_{1/2}$ (4)	$E_p$ (5)	$E_p$ (6)
<b>NiL2C</b>	0.67	-1.08	-1.26	-1.89	-2.2

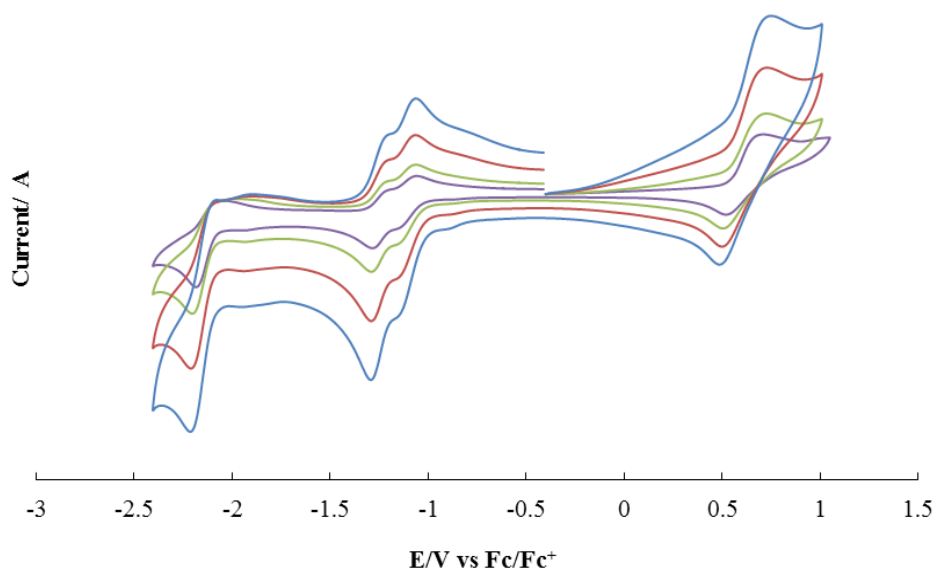
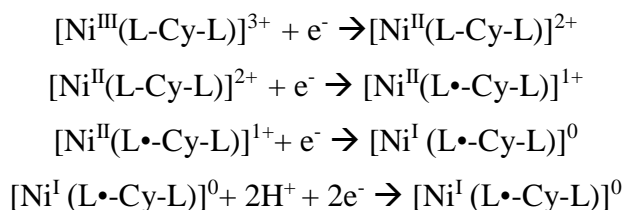


**Figure 4.23** Scan rate dependence for 1 mM **NiL2C**.

The cyclic voltammetry of **NiL2C** gives a quasi-reversible oxidation and two reversible reductions followed by an irreversible reduction at  $E_{1/2} = 0.67, -1.08, -1.26$  and  $E_p = -2.2$  V vs Fc/Fc<sup>+</sup> (at 100 mV/s). Scan rate dependence shows the reversible waves to increase linearly with the square root of scan rate indicative a freely diffusing species. The processes at 0.67 V can be attributed to metal based reversible oxidation of Ni<sup>2+</sup> to Ni<sup>3+</sup>. The assignment of the reversible reductions at 0.67, -1.08 V is challenging as for redox active Ni<sup>2+</sup> Wieghardt and co-workers showed that in their related iminopyridine complexes the redox active electrons aren't localised on the ligands but are delocalised over the whole complex. However, in Wieghardt's work due to steric constraints of the ligand their complexes give tetrahedral geometry, and a more conjugated aryl iminopyridine ligand, which would both act to lower the energy of the ligand LUMO orbitals in comparison to the iminopyridine ligands in this work, and thus shift the redox potentials to more positive potentials compared to that found in **NiL2C**.





#### 4.4.5 Electrochemistry of Copper complexes – CuL1N, CuL2N and CuL3N

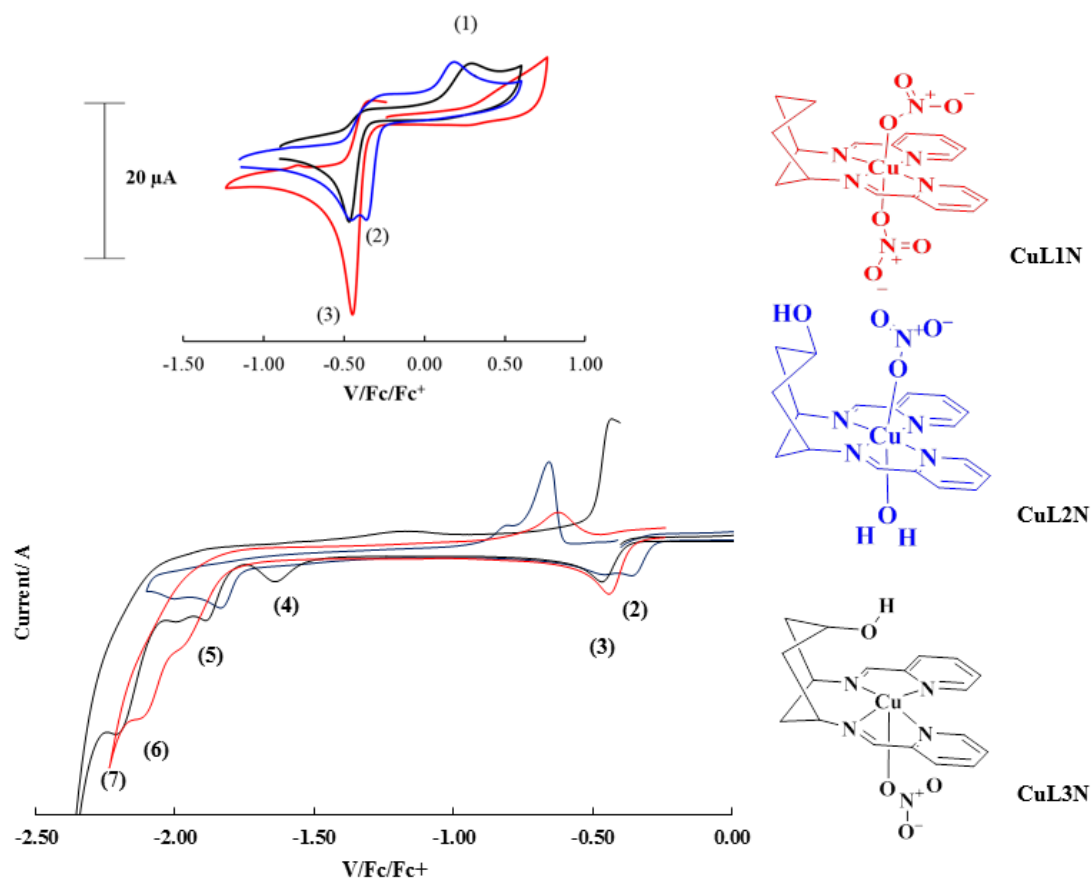


**Figure 4.24** Cyclic voltammetry of 1 mM CuL1N, CuL2N and CuL3N at GCE at 100 mV/s in acetonitrile. RE = Ag/AgCl (internal Fc/Fc<sup>+</sup> reference). CE = Pt. 0.1 M TBABF<sub>4</sub> supporting electrolyte.

**Table 4.6** Reduction potentials  $E_{1/2}$  of CuL1N, CuL2N and CuL3N at 100 mV/s in MeCN at GCE vs Fc/Fc<sup>+</sup>.

Complex	$E_P$ (1)	$E_P$ (2)	$E_P$ (3)	$E_P$ (4)	$E_P$ (5)	$E_P$ (6)	$E_P$ (7)
CuL2N	0.20	-0.35	-0.46	-	-1.85	-2.01	-
CuL3N	0.32	-	-0.46	-1.65	-1.91	-2.0	-2.21
CuL1N	0.60	-	-0.44	-	-1.98	-	-2.11

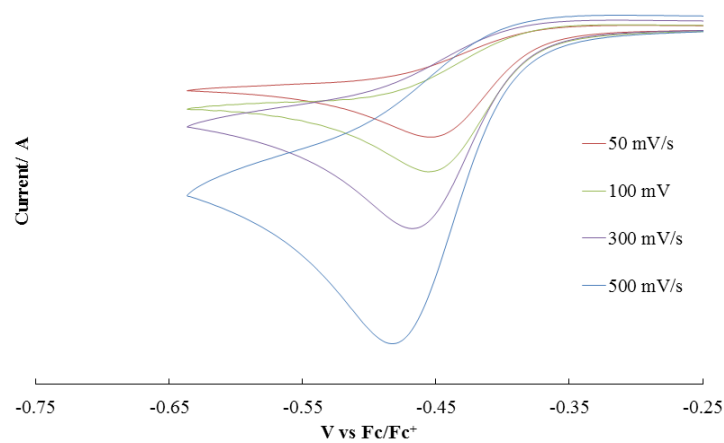


**Figure 4.25** Scan rate dependence for 1 mM CuL1N.

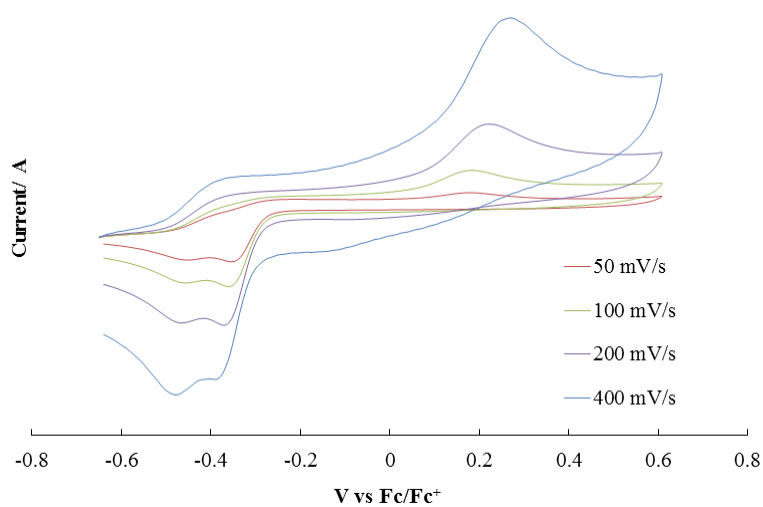


**Figure 4.26** Scan rate dependence for 1 mM CuL2N.

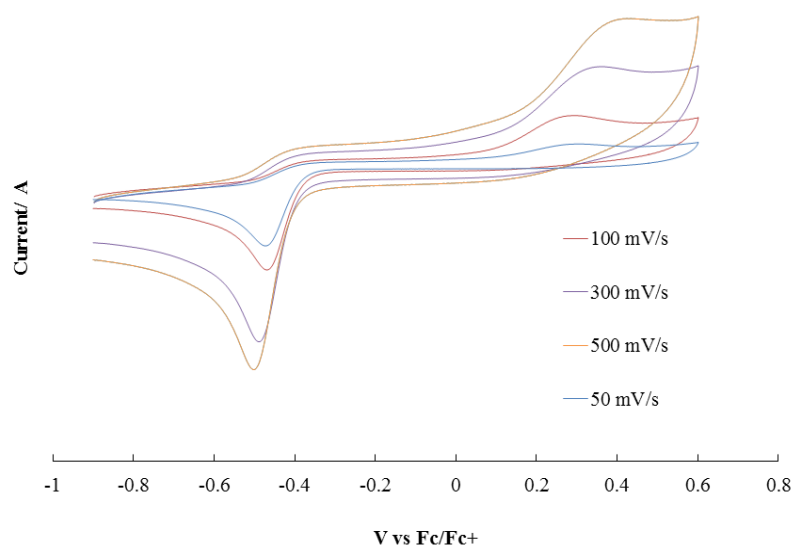


**Figure 4.27** Scan rate dependence for 1 mM CuL3N.

The cyclic voltammetry of **CuL1N** gives 4 peaks at  $E_p = 0.60, -0.44, -1.98$  and  $-2.11$  V vs  $Fc/Fc^+$  (at  $100 \text{ mV s}^{-1}$ ). The first reduction shows a linear dependence of current on the square-root of scan rate, indicating a freely diffusing species, as shown in **figure 4.25**. The cyclic voltammetry of **CuL2N** gives 5 peaks at  $E_p = 0.20, -0.35, -0.46$  and  $-1.85$  and  $-2.01$  V vs  $Fc/Fc^+$  (at  $100 \text{ mV/s}$ ). Scan rate dependence for the first reduction is shown to increase linearly with the square-root of scan rate indicative a freely diffusing species, as shown in **figure 4.26**. The cyclic voltammetry of **CuL3N** gives 6 peaks at  $E_p = 0.32, -0.46$  and  $-1.65$  and  $-1.91, -2.0$ , and  $-2.21$  V vs  $Fc/Fc^+$  (at  $100 \text{ mV/s}$ ). Scan rate dependence for the first reduction is shown to increase linearly with the square-root of scan rate indicative a freely diffusing species, as shown in **figure 4.27**. Reverse oxidation peaks are excluded from analysis as it was shown that at highly reducing potential that the copper complexes deposit on to the electrode surface.

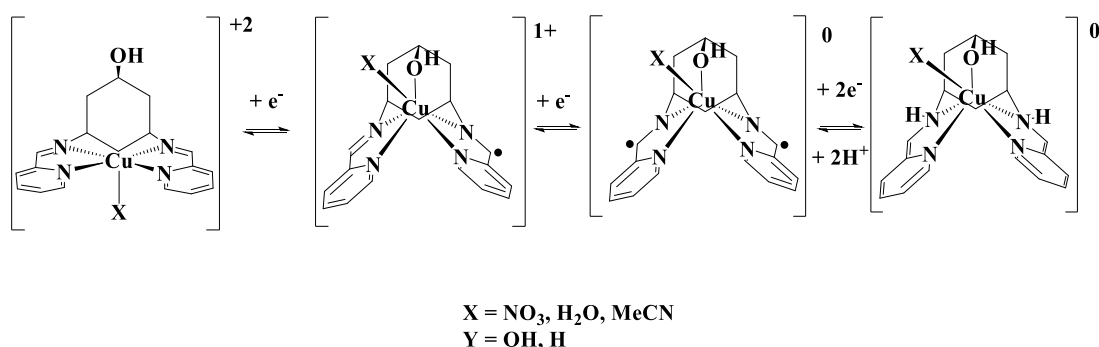
The peaks at  $0.2, 0.32$  and  $0.6$  V for each of the complexes vs  $Fc/Fc^+$  can be assigned to the  $Cu^{3+/2+}$ , as the ligand has no oxidations near this range and the open circuit potential for the three complexes is *ca.*  $0$  V vs  $Fc/Fc^+$ .

On the reductive sweep, it seems likely that the peak at  $-0.46$  V vs  $Fc/Fc^+$  present in the CV of all three complexes is from the  $Cu^{2+/1+}$  reduction event. In the case of **CuL1N**, this reduction at  $-0.46$  V vs  $Fc/Fc^+$ , may also overlap with the imine ligand reduction event, to give a two electron process, as it has an  $i_p$  twice as large as that for the one electron reductions of the other compounds. The peak at  $-0.35$  V vs  $Fc/Fc^+$  in **CuL2N** can also be assigned to the imine ligand reduction.

The second reduction in **CuL3N**, however, is  $1210 \text{ mV}$  more negative in potential compared to the imine based reduction of **CuL2N**. This is most likely caused by a change in geometry from square based pyramidal found in the crystal structure of **CuL3N**, to trigonal prismatic geometry with the proximal hydroxyl bound more strongly to the copper centre on reduction, as  $Cu^{1+}$  gives a  $d^{10}$  electronic configuration which is isoelectronic with **ZnL3N** (which has the trigonal prismatic geometry as shown in **figure 3.9**). The reduction found at  $-1.65$  V vs  $Fc/Fc^+$  therefore, can also be attributed to a imine ligand based reduction, with the proximal hydroxyl donating electron density to the  $Cu^{1+}$  metal centre, decreasing its electro-positivity and thus its ability to withdraw electron

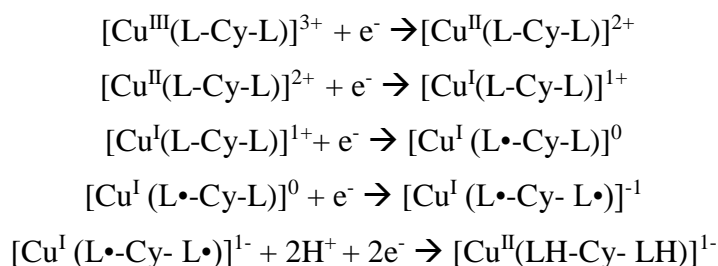
density from the iminopyridine ligands. This in turn makes it harder to reduce the imine groups of the iminopyridine ligand, causing the shift to more negative potential.

The shift in reduction potential of 1190 mV for imine reduction in **CuL3N** on change in geometry is larger than that found in **ZnL3N** (425 mV), this is most likely due to electronic communication between the radical anions formed. In **ZnL3N** there is a smaller difference in reductions as there is little interaction between radical anions formed as the 3d<sup>10</sup> zinc(II) metal centre acts as an insulator between imino pyridine ligands. However, in **CuL3N**, it seems that the radical anion formed can be delocalised through the copper centre. This electronic communication between redox centres is expanded in **section 4.6.1**.



**Scheme 4.5** Proposed change in geometry on reduction of **CuL3N**.

The next reduction event in all three complexes at -1.85, -1.91 and -1.98 vs Fc/Fc is also tentatively assigned to the next ligand reduction as the reduction to Cu<sup>0</sup> is unlikely, as has been shown by others on Cu salen complexes.<sup>182</sup> The last reduction event seen for **CuL1N** and **CuL3N**, with twice the peak current (**CuL2N** appears to be more prone to deposition at less reducing potential than the others), can be postulated to the 2 electron and proton coupled reduction of the ligand to the amine.



#### 4.5.1 Spin cross-over in cobalt complexes

Spin cross-over is introduced here as it is used in proceeding sections to describe electrochemical behaviour of the  $\text{Co}^{3+/2+}$  couples in cobalt complexes described.

Spin cross-over is a common phenomenon in cobalt complexes on going from  $\text{Co}^{2+}$  to  $\text{Co}^{3+}$ . Spin cross-over occurs in cases where the high-spin state and low spin state of a complex are separated by small energy barrier, roughly equivalent to the thermal energy at room temperature. The magnetic properties of the complexes therefore, change anomalously (differing from Curie behaviour). The origin of spin cross-over can be expressed in the form of ligand field theory by the magnitude of  $d$  orbital splitting and the spin-pairing energy,  $P$ . Where the  $d$  orbital splitting energy and the spin pairing energy are almost equal, the high spin and low spin states will have very similar energies.<sup>183</sup> The magneto-chemical analysis of the  $\text{Co}^{2+}$  complex **CoL2N** has been previously reported, showing that in the weak octahedral ligand field from the iminopyridine and water/nitrato co-ligands gives the  $\text{Co}^{2+}$  ( $3d^7$ ) octahedral high-spin.<sup>102</sup> A number of  $\text{Co}^{2+}$  imine complexes have been shown previously to show spin cross-over behaviour.<sup>184</sup> This behaviour may therefore be seen in the cobalt complexes presented, and will be reflected in the electrochemical behaviour of the  $\text{Co}^{3+/2+}$  couples, as the oxidation of high spin (HS)  $\text{Co}^{2+}$  to low spin (LS)  $\text{Co}^{3+}$  is a well-known example of redox coupled-spin crossover (RCSCO).<sup>185</sup> The switch from high spin to low spin is caused by  $\text{Co}^{3+}$  complexes having larger octahedral crystal splitting energy,  $\Delta_o$ , than  $\text{Co}^{2+}$  complexes with the same ligand due to the increase in charge, reflecting the electrostatic nature of the crystal field splitting. This gives irreversible or quasi-reversible behaviour in cyclic voltammetry because the oxidation/reduction is accompanied by an electronic (and sometimes structural) rearrangement.

Previous studies on cobalt imine complexes suggests that oxidation of the high spin (HS)  $3d^7 \text{Co}^{2+}$  complexes initially produces a high spin (HS) ( $3d^6$ )  $\text{Co}^{3+}$  intermediate which can be re-reduced close to the oxidation peak. The high spin (HS) ( $3d^6$ )  $\text{Co}^{3+}$  intermediate rapidly undergoes spin crossover to the more stable low spin (LS) ( $3d^6$ )  $\text{Co}^{3+}$  state which is reduced at significantly more negative potential, resulting in the wide separation between the oxidation and the its reverse reduction peak. The absence of a corresponding peak for the low spin ( $3d^7$ )  $\text{Co}^{2+}$  intermediate was thought to be due to rapid spin cross

over in the studies undertaken. The concerted pathway directly from high spin (HS)  $\text{Co}^{2+}$  to low spin (LS)  $\text{Co}^{3+}$  is also possible and consistent with the data.<sup>186-191</sup>

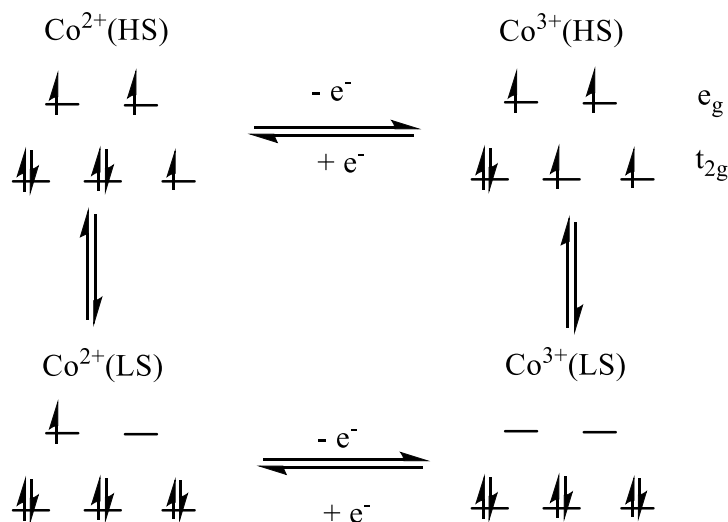


**Figure 4.28** Redox coupled spin crossover square scheme for an octahedral .

#### 4.5.2 Electrochemistry of Cobalt complexes

During this work on the development of molecular catalysts for electrocatalytic hydrogen evolution, it became apparent that the cobalt complexes of the ligand sets developed were the best in terms of stability under reducing conditions and their response to a proton source. Therefore, the cobalt complexes were studied in greater depth. In addition, related cobalt complexes based on the iminopyridine framework with a propane backbone were also synthesized. Within this study questions were also raised as to the influence of the nitrate anion on activity to a proton source, in this light cobalt complexes of some of the ligand sets were synthesized and analysed with non-coordinating tetrafluoroborate anions.

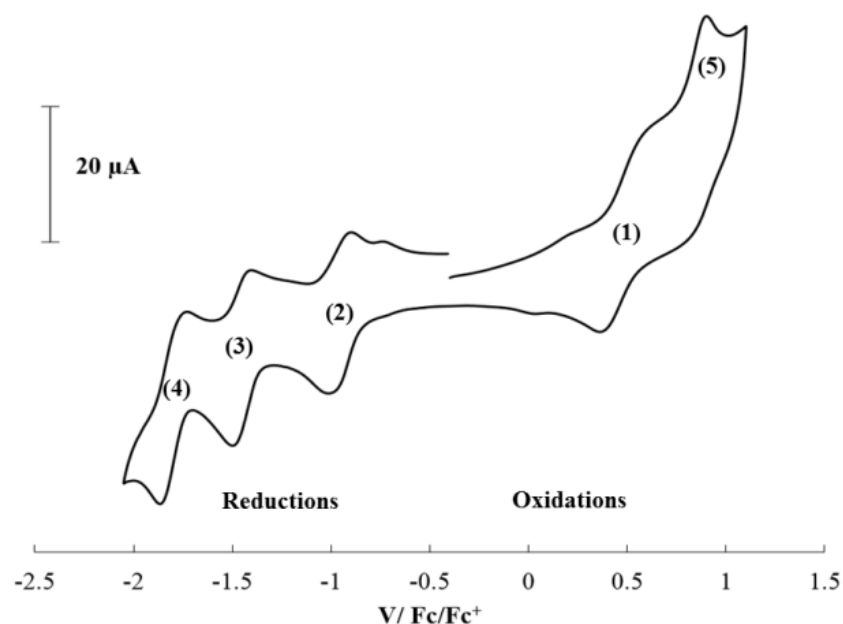
The cyclic voltammograms of all the cobalt complexes synthesized gave one quasi-reversible oxidation (couple marked **(1)** in **table 4.7**) and three largely reversible or quasi-reversible reductive couples (reductive couples marked **2** to **4** in **table 4.7**), with the exception **CoL2N** which also shows an additional irreversible oxidation (marked **(5)** in **table 4.7**). The potentials and peak separations,  $\Delta E$ , of all the cobalt complexes are summarized in **table 4.7**, with the cyclic voltammetry at 100 mV/s and their scan rate

dependence shown in **figures 4.29 to 4.32**. The effect of a hydroxyl group distal and proximal to the metal centre, the effect of the anion and the effect of the rigidity of the backbone framework on the electrochemistry is explored.

**Table 4.7** Reduction potentials  $E_p$  and  $E_{1/2}$  for 1 mM **CoL2N**, **CoL4N**, **CoL4B**, **CoL1N**, **CoL1B**, **CoL3N** and **CoL3B** in MeCN at GCE vs Fc/Fc<sup>+</sup>/V, with peak separation,  $\Delta E$ , for each couple given in brackets .

Below is a labelled CV of **CoL2N** relating the table to each CV, with oxidations labelled **1** and **5** and reductions labelled **2** to **4**.

Complex	(4) $E_{1/2}$ ( $\Delta E$ )	(3) $E_{1/2}$ ( $\Delta E$ )	(2) $E_{1/2}$ ( $\Delta E$ )	(1) $E_{1/2}$ ( $\Delta E$ )	(5) $E_p$
<b>CoL2N</b>	-1.81 (121)	-1.45 (110)	-0.94 (121)	0.46 (232)	0.9
<b>CoL4N</b>	-1.88 (171)	-1.44 (81)	-1.00 (141)	0.41 (272)	
<b>CoL4B</b>	-1.85 (188)	-1.49 (60)	-0.93 (80)	0.80 (413)	
<b>CoL1N</b>	-1.77 (60)	-1.37 (70)	-0.85 (80)	0.53 (130)	
<b>CoL1B</b>	-1.86 (76)	-1.50 (81)	-0.92 (88)	0.60 (330)	
<b>CoL3N</b>	-1.80 (201)	-1.40 (81)	-1.16 (91)	0.43 (393)	
<b>CoL3B</b>	-1.79 (103)	-1.39 (95)	-1.16 (63)	0.56 (547)	



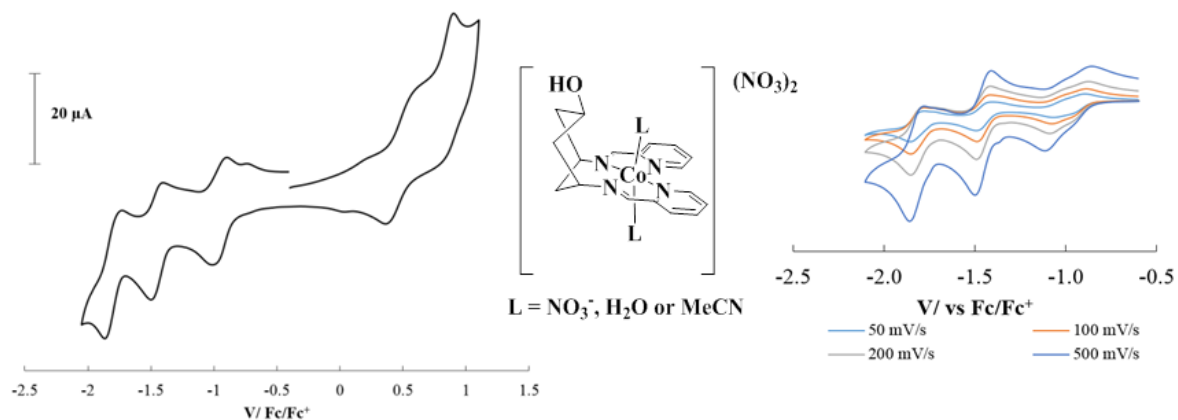


**Figure 4.29** Cyclic voltammogram of 1 mM **CoL2N** at GCE in acetonitrile, at 100 mV/s (*left*) and scan rate dependence (*right*). RE = Ag/AgCl (internal Fc/Fc<sup>+</sup> reference), CE = Pt. 0.1 M TBABF<sub>4</sub> supporting electrolyte.

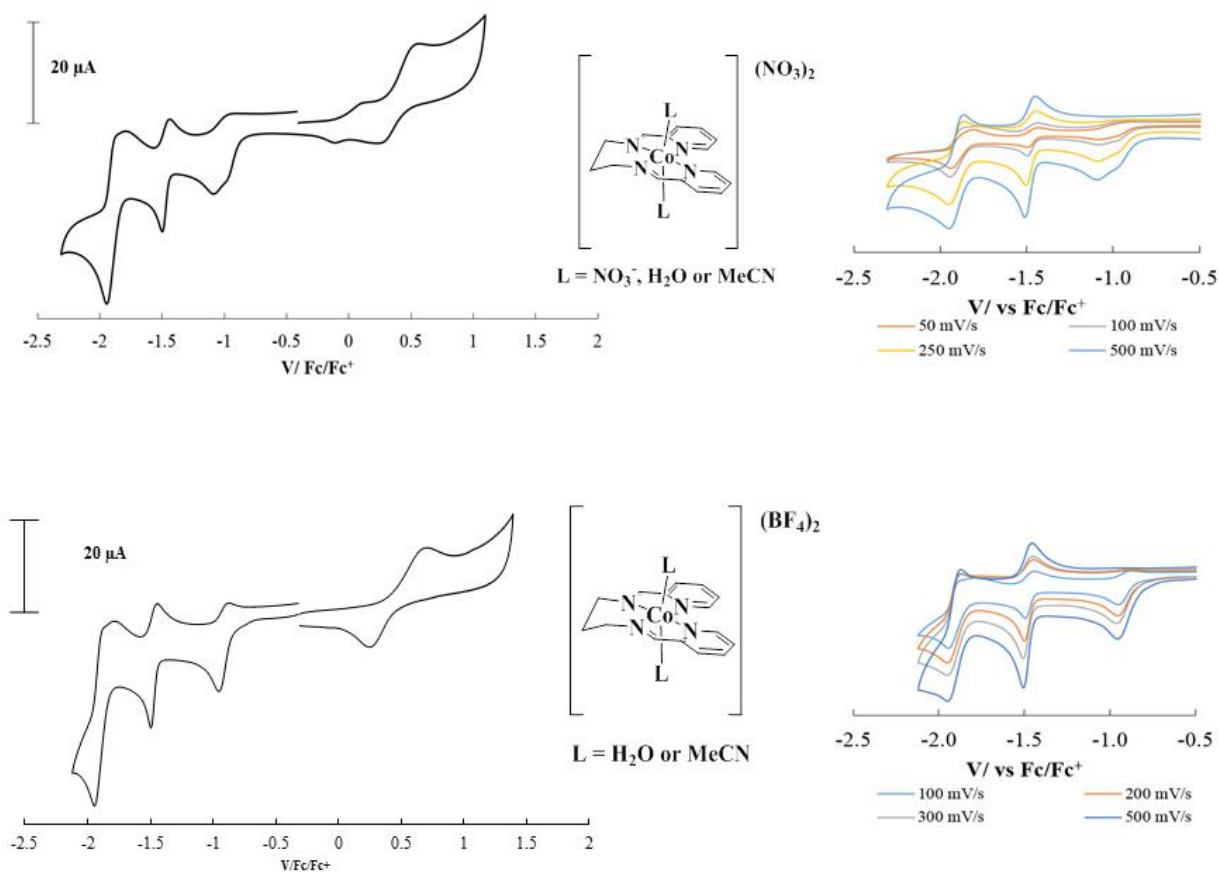


**Figure 4.30** Cyclic voltammogram of 1 mM **CoL4N** (*top*) and **CoL4B** (*bottom*) at GCE in acetonitrile, at 100 mV/s (*left*) and scan rate dependence (*right*). RE = Ag/AgCl (internal Fc/Fc<sup>+</sup> reference), CE = Pt. 0.1 M TBABF<sub>4</sub> supporting electrolyte.



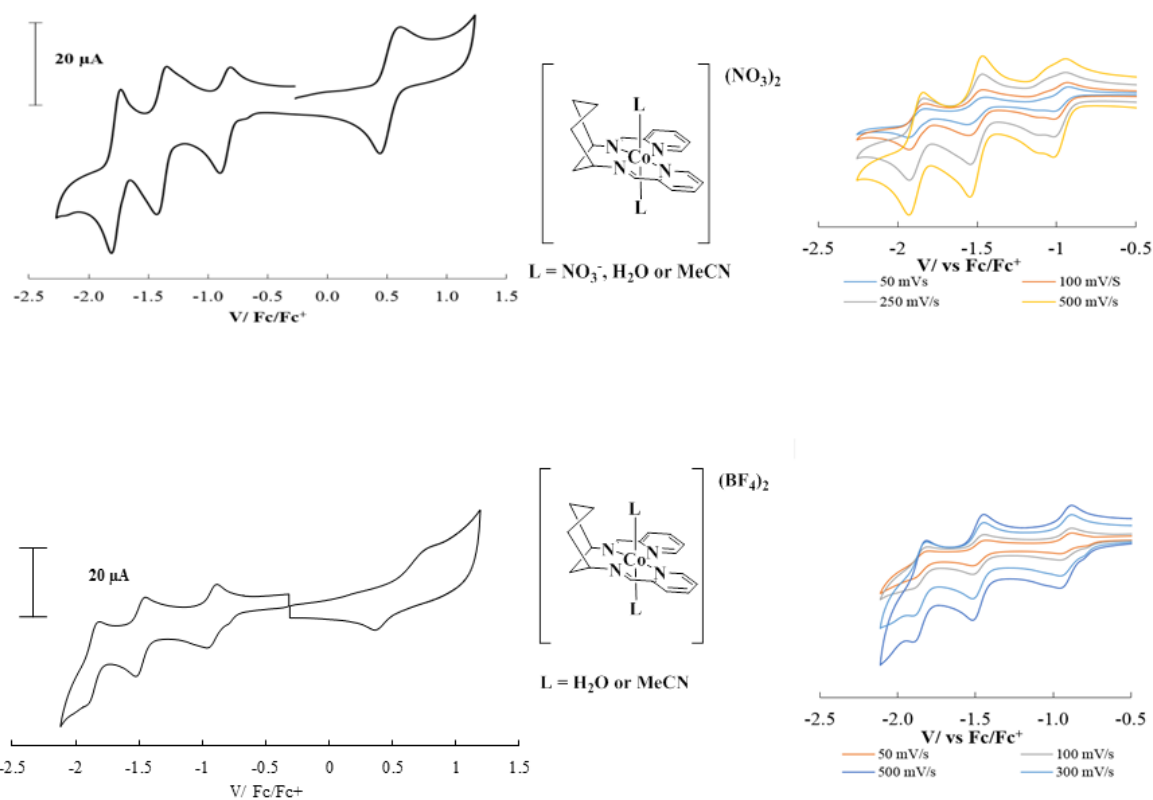


**Figure 4.31** Cyclic voltammogram of 1 mM CoL1N (top) and CoL1B (bottom) at GCE in acetonitrile, at 100 mV/s (left) and scan rate dependence (right). RE = Ag/AgCl (internal Fc/Fc<sup>+</sup> reference), CE = Pt. 0.1 M TBABF<sub>4</sub> supporting electrolyte.

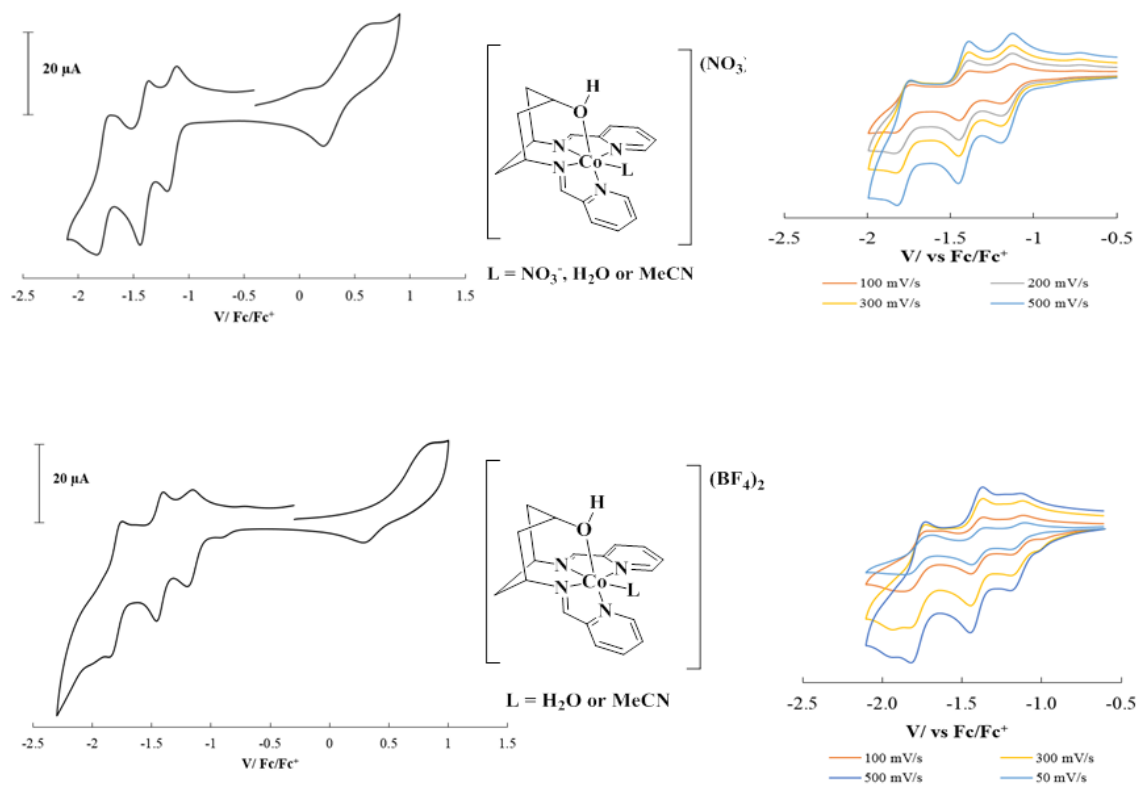


**Figure 4.32** Cyclic voltammogram of 1 mM CoL3N (top) and CoL3B (bottom) at GCE in acetonitrile, at 100 mV/s (left) and scan rate dependence (right). RE = Ag/AgCl (internal Fc/Fc<sup>+</sup> reference), CE = Pt. 0.1 M TBABF<sub>4</sub> supporting electrolyte.

### 4.5.3 Effect of adding distal hydroxyl ‘proton relay’ to the cyclohexane backbone

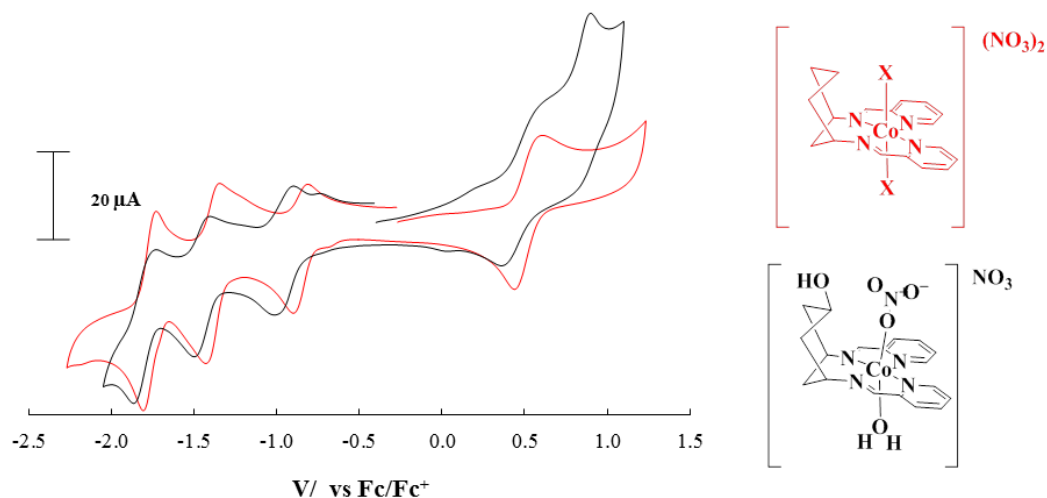


**Figure 4.33** Cyclic voltammetry of 1 mM **CoL1N** (red) and **CoL2N** (black) at GCE in acetonitrile, at 100 mV/s. RE = Ag/AgCl (internal  $\text{Fc}/\text{Fc}^+$  reference), CE = Pt. 0.1 M TBABF<sub>4</sub> supporting electrolyte.

Going from the simple cyclohexane backbone of **CoL1N** to the cyclohexane backbone with distal hydroxyl group of **CoL2N**, there is a 70 mV shift more negative in the oxidation  $\text{Co}^{3+/2+}$  couple from 0.53 V, and becomes much more irreversible in character. Another oxidation event is also present in **CoL2N** at 0.9 V vs  $\text{Fc}/\text{Fc}^+$ , only seen for this cobalt complex. This oxidation is most likely a metal based oxidation,  $\text{Co}^{4+/3+}$ . This behaviour could tentatively be attributed to stabilisation of the  $\text{Co}^{4+}$  state by the hydrogen bonded nitrate ligand. The presence of  $\text{Co}^{4+}$  in the electrochemistry and EPR of complexes has been seen previously but is quite rare.<sup>192,193</sup>

The first reduction, shifts 90 mV more negative from -0.85 V, and becomes more irreversible going from the simple cyclohexane (**CoL1N**) to the cyclohexane with distal hydroxyl (**CoL2N**). The second reduction shifts 80 mV more negative from -1.34 V. The reduction at -1.77 V is also shifted more negative by 40 mV. The shift negative for the three reductions can be attributed to donation of electron density from the negatively charged nitrate, which is presumably held in place by hydrogen bonding interactions in solution on the distal hydroxyl and therefore making the metal centre harder to reduce.

#### 4.5.4 Effect of adding proximal hydroxyl ‘proton relay’ to the cyclohexane backbone

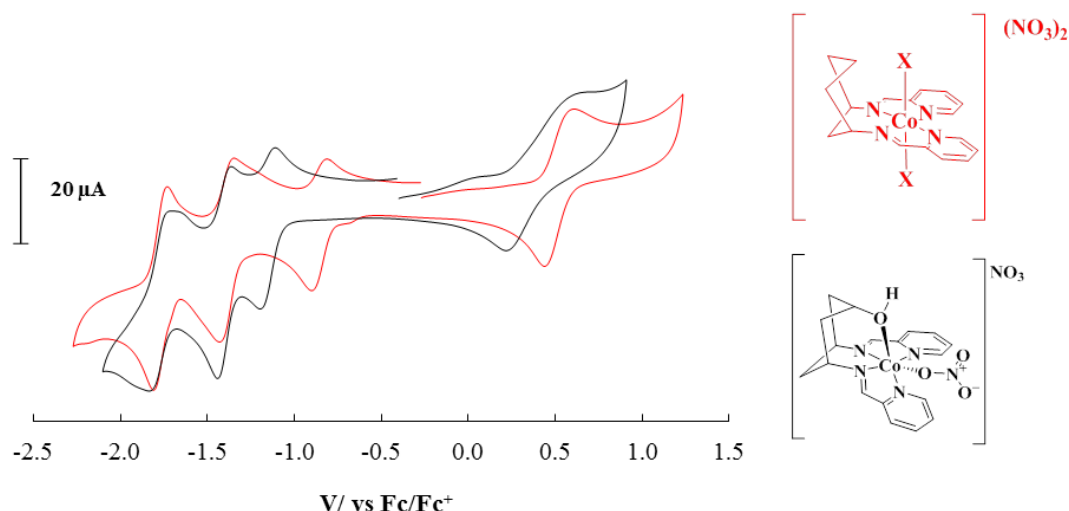


**Figure 4.34** Cyclic voltammetry of 1 mM **CoL1N** (red) and **CoL3N** (black) at GCE in acetonitrile, at 100 mV/s. RE = Ag/AgCl (internal Fc/Fc<sup>+</sup> reference), CE = Pt. 0.1 M TBABF<sub>4</sub> supporting electrolyte.

Going from the simple cyclohexane backbone of **CoL1N** to the cyclohexane backbone with the coordinating proximal hydroxyl group of **CoL3N**, there is a 140 mV shift more negative in the oxidation (Co<sup>3+/2+</sup> couple) from 0.53 V, and this also becomes much more irreversible in character. The first reduction shifts more negative by 310 mV and becomes slightly less reversible ( $\Delta E$  from 80 to 91 mV). The second and third reductions also shift more negative by 30 and 20 mV respectively, there is a slight decrease in reversibility ( $\Delta E$  from 70 to 81 mV) in the second reduction and a large decrease in reversibility of the third reduction ( $\Delta E$  from 60 to 103 mV). As shown from the DFT studies in **section 4**, the 1+ structure of **CoL3N** (proximal hydroxyl) has similar 5-coordinate, distorted square pyramidal geometry to that of **CoL1N**, which therefore would account for the fairly similar second reduction potentials ( $\Delta E_{1/2} = 30$  mV). The third reductions are also similar ( $\Delta E_{1/2} = 20$  mV). However, **CoL3N** has a slightly different geometry in the neutral state compared to the simple cyclohexane complex **CoL1N**, this last reduction is shown to be largely ligand based with some metal character and therefore, may not be so dependent on the geometry changes. Or that the lability of the Co-O bond in the neutral complex is such that it is mostly de-coordinated and therefore the geometry of the neutral complex more closely resembles that of **CoL1N**. The decrease in reversibility of the couples in the proximal complex supports that there are more re-organisation processes occurring.

#### 4.5.5 Effect of going from non-coordinating BF<sub>4</sub> to coordinating nitrate

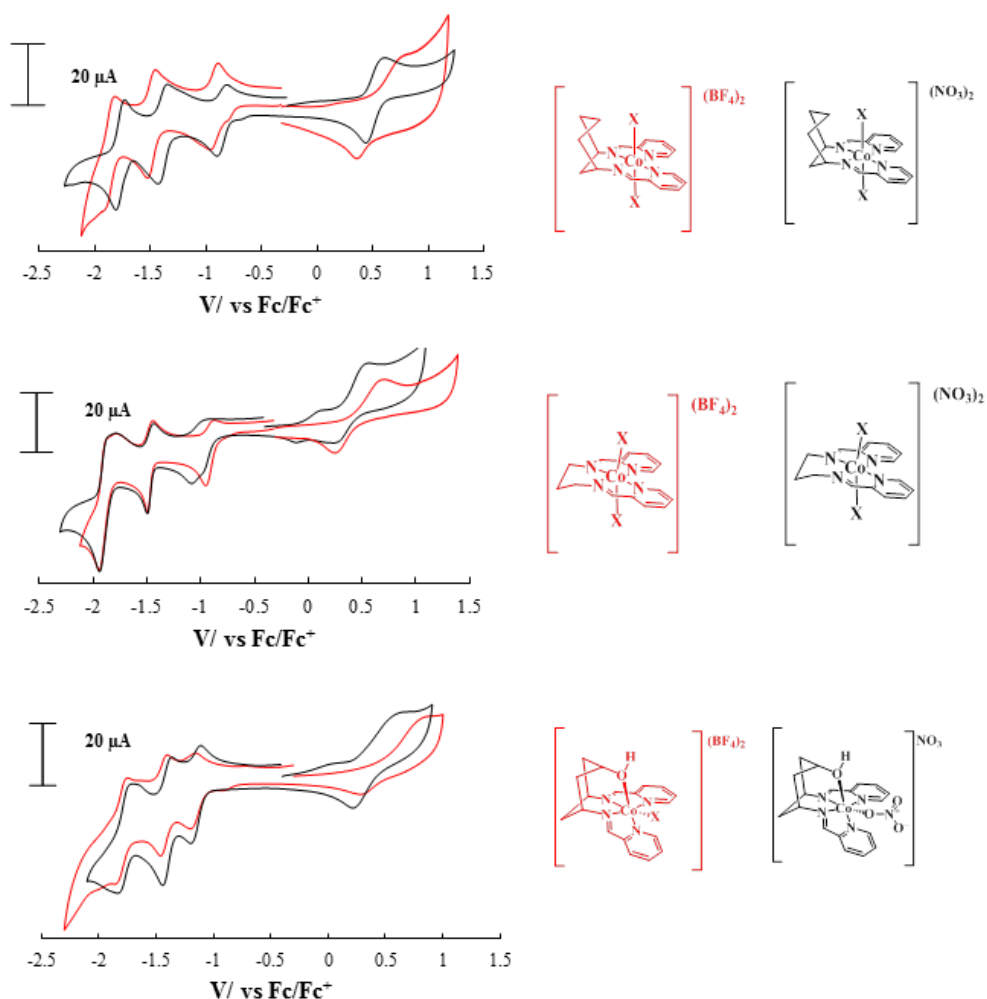


**Figure 4.37** Cyclic voltammetry of 1 mM (**CoL1B** (red) and **CoL1N** (black) (top)), (**CoL4B** (red) and **CoL4N** (black) (top)), and (**CoL3B** (red) and **CoL3N** (black) (top)) at GCE in acetonitrile, at 100 mV/s. RE = Ag/AgCl (internal Fc/Fc<sup>+</sup> reference), CE = Pt. 0.1 M TBABF<sub>4</sub> supporting electrolyte.

*Spectrochemical series for ligands involved: NO<sub>3</sub><sup>-</sup> > H<sub>2</sub>O > CH<sub>3</sub>CN*

In the simple cyclohexane complexes, of the DDP (**10**, **L1**) ligand, going from the non-coordinating anion BF<sub>4</sub> to the weakly coordinating anion nitrate, the Co<sup>3+/2+</sup> couple shifts more negative by 60 mV from 0.60 V vs Fc/Fc<sup>+</sup>, and becomes much more reversible ( $\Delta E$  from 330 to 130 mV). All the reductions shift more positive, by 90 to 130 mV, with the peak separations  $\Delta E$  remaining constant. In the acetonitrile solution of the electrochemical experiment, in the case with the non-coordinating BF<sub>4</sub> anion of **CoL1B**, acetonitrile will be bound in the two axial positions of the complex (NMR evidence of

structure of DDP ligand is the same in both complexes, **section 3.5.4**), however, in the case where nitrate is the anion, in **CoL1N**, nitrate (or water seen in the crystal structure) will be bound in the axial positions of the complex. Acetonitrile is a strong field ligand in the spectrochemical series, whereas nitrate is a weak field ligand. Therefore, as both complexes should have the same octahedral geometry, there will be a larger  $\Delta_{\text{oct}}$  in the case with the acetonitrile bound and smaller with the nitrate bound. This therefore means the rate of spin cross-over from high spin  $\text{Co}^{3+}$  to low spin  $\text{Co}^{3+}$  should be faster in the case of the nitrate bound complex with small ligand splitting energy, compared to the acetonitrile bound complex. This reflects the large increase in reversibility of the  $\text{Co}^{3+/2+}$  couple in the nitrate complex. The positive shift in potential can be attributed to the exchange of the more electron donating acetonitrile, for the more electron withdrawing nitrate.

In the propyl complexes, of the DDPP (**18, L4**) ligand, going from the non-coordinating anion  $\text{BF}_4$  (**CoL4B**) to the coordinating anion nitrate (**CoL4N**), the  $\text{Co}^{3+/2+}$  couple shifts more negative by 40 mV from 0.44 V *vs*  $\text{Fc}/\text{Fc}^+$ , and remains irreversible). The first reduction shifts 70 mV more negative, but also has a minor shoulder peak at roughly the same potential as the  $\text{BF}_4$  complex. The second and third reductions remain roughly constant. The change in the  $\text{Co}^{3+/2+}$  couple is the same as that seen in the DDP complexes. The difference in behaviour of the first reduction of the two complexes could be attributed to a change in geometry or mixed coordination modes which are accommodated by the flexible propyl based ligand, with the two waves showing the interconversion between the two. This wave may also be involved in the electrochemical hydrogenation of the imine ligand, which may account for the lack of reversibility of the couple, as has been described for systems with a similar ligand set.<sup>194</sup>

In the proximal hydroxyl complexes, of the DDOPi (**9, L3**) ligand, going from the non-coordinating anion  $\text{BF}_4$  of **CoL3B** to the coordinating anion nitrate, **CoL3N**, the  $\text{Co}^{3+/2+}$  couple shifts more negative by 130 mV from 0.56 V *vs*  $\text{Fc}/\text{Fc}^+$ , and becomes more reversible ( $\Delta E$  from 547 to 393 mV). There is almost no change in potential of any of the three reductions; however, there is a slight increase in reversibility for the first reduction and decrease in reversibility for the second and third couples.

Paramagnetic NMR's of the two cobalt DDOPi (**9**, **L3**) complexes are almost identical; suggesting the trigonal prismatic geometry found in **CoL3N** is also maintained in **CoL3B**. The highly irreversible behaviour of the  $\text{Co}^{3+/2+}$  couples of the cobalt DDOPi (**9**, **L3**) complexes compared to the other cobalt complexes presented can be attributed both to redox coupled-spin crossover (RCSCO), the oxidation of high spin (HS)  $\text{Co}^{2+}$  to low spin (LS)  $\text{Co}^{3+}$ .<sup>186</sup> But also to a change in geometry from trigonal prismatic geometry to octahedral, shown to be favoured for low spin  $d^6$ , which is the case for  $\text{Co}^{3+}$ . The 130 mV shift more negative of the couple for **CoL3N** compared to the **CoL3B**, suggests an increase in stabilisation of these processes and of the  $\text{Co}^{3+}$  state in the nitrate complex.

#### 4.5.6 Effect of rigidity going from propane to cyclohexane backbone

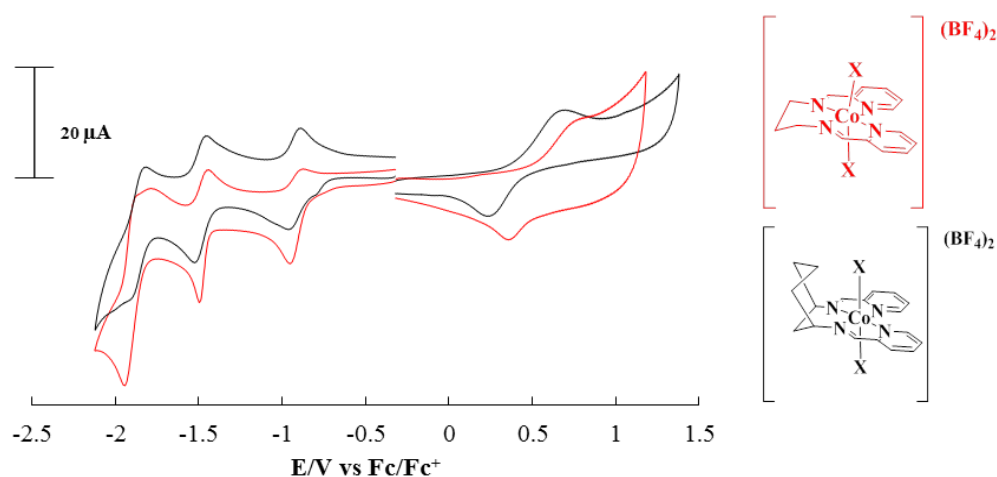


**Figure 4.36** Cyclic voltammetry of 1 mM **CoL4B** (red) and **CoL1B** (black) at GCE in acetonitrile, at 100 mV/s. RE = Ag/AgCl (internal  $\text{Fc}/\text{Fc}^+$  reference), CE = Pt. 0.1 M TBABF<sub>4</sub> supporting electrolyte.

Going from the flexible propane (**CoL4B**) to the rigid cyclohexane backbone (**CoL1B**), there is a 200 mV shift more positive in the oxidation ( $\text{Co}^{3+/2+}$  couple) from 0.80 V, which also becomes slightly more reversible in character ( $\Delta E$  from 413 to 330 mV). The potentials for the three reductions remain almost constant, however, and become more reversible with the increase in rigidity. The behaviour seen for the first reduction in **CoL4B**, suspected to be due to imine reduction,<sup>194</sup> is absent in **CoL1B**, suggesting an increase in stability, which may be expected on increasing steric bulk, limiting accessibility and thus reactivity of the imine groups. The positive shift in  $\text{Co}^{3+/2+}$  potential shows that the increased rigidity of the cyclohexane backbone (**CoL1B**) appears to increase the thermodynamic stability of the  $\text{Co}^{3+}$  state. Interestingly larger  $\Delta E$ 's are

usually seen for the  $\text{Co}^{3+/2+}$  couple with more sterically bulky ligands, due to a reduction of the rate of electron transfer.<sup>195,196</sup> However, an increase in reversibility (413 to 330 mV) is seen on increasing the rigidity to **CoL1B**. This suggests that the extra rigidity of the system may increase the rate of spin crossover either by a concerted pathway directly from high spin  $\text{Co}^{2+}$  to low spin  $\text{Co}^{3+}$ , or from the high spin  $3d^6$   $\text{Co}^{3+}$  intermediate to the more stable low spin  $3d^6$   $\text{Co}^{3+}$  state, and that any reductions in electron transfer rate from the increased steric bulk are compensated for this. Another reason may be the increased rigidity of the cyclohexane, forcing the geometries of the oxidised and reduced states to be more similar, and therefore decreasing the reorganisation energy.

#### 4.5.7 DFT and cyclic voltammetry of CoL1N

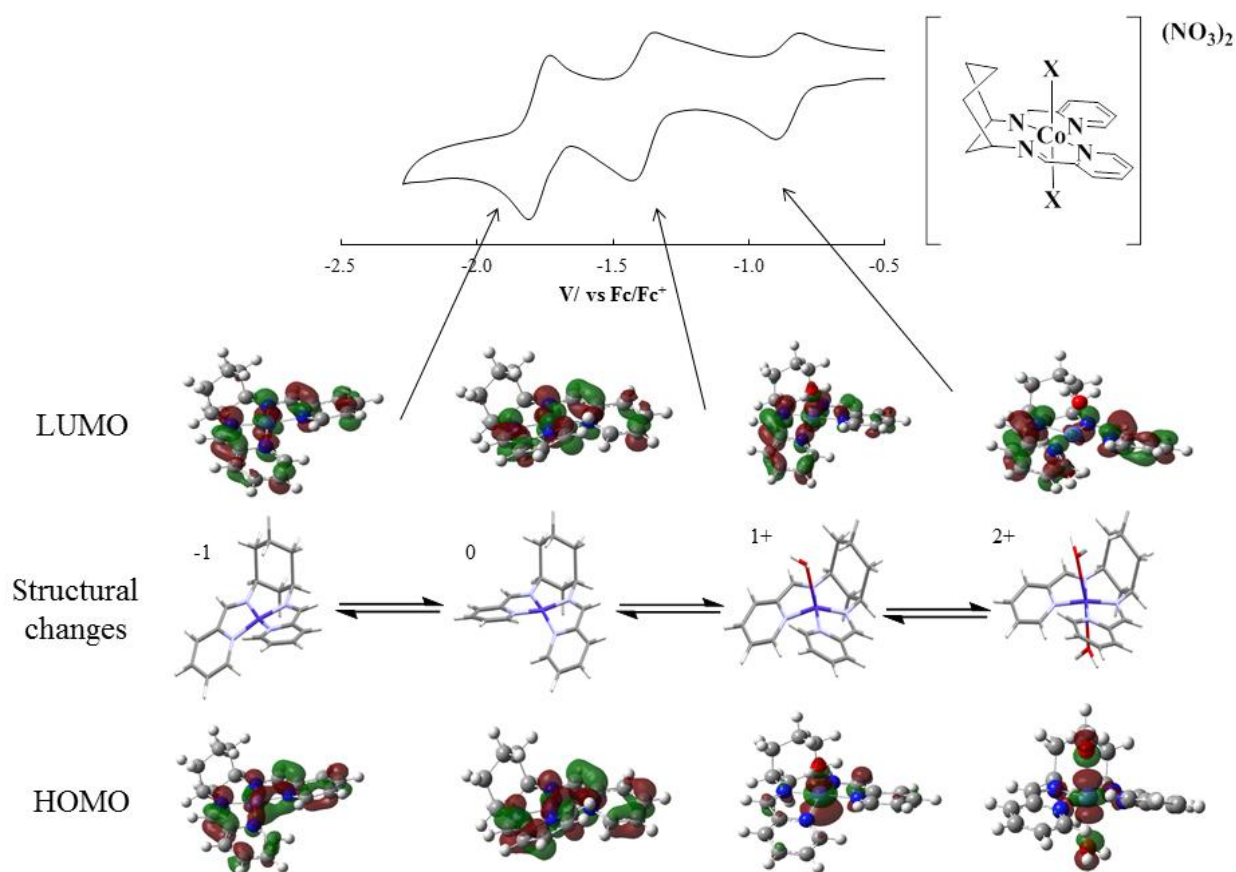


**Figure 4.37** Cyclic voltammetry of 1 mM **CoL1N** at GCE in acetonitrile at 100 mV/s. Corresponding DFT computed structures (*middle*), LUMO (*top*) and HOMO (*bottom*) are shown below with arrows indicating the couples. Overall charge on the complex is given by the number to the top left of each structure.

From the DFT of **CoL1N**, it is shown that on reduction to the 1+ state there is de-coordination/bond elongation of one of the axial aqua ligands, giving a 5-coordinate

complex. On further reduction to the 0 state, there is further loss/bond elongation of the other axially bound aqua ligand giving a 4-coordinate square planar complex. Further reduction to the -1 state shows little change in geometry from the 0 state. Overall the geometry of the iminopyridine chelate remains almost constant throughout the reduction events.

For **CoL1N** in the 2+ state, the LUMO is shown to be mainly focused on the ligand, and thus the first reduction is mostly influenced by the ligand electronics. For the 1+ state the LUMO is shown to have largely mixed iminopyridine ligand/ metal character, with a large contribution from the metal centre, therefore the couple associated with this is assigned to the  $\text{Co}^{2+/1+}$ . It is therefore likely that the second reduction is affected by axially bound ligands. For the 0 and -1 states the LUMO also has mixed metal ligand character.

#### 4.5.8 DFT and cyclic voltammetry of CoL2N

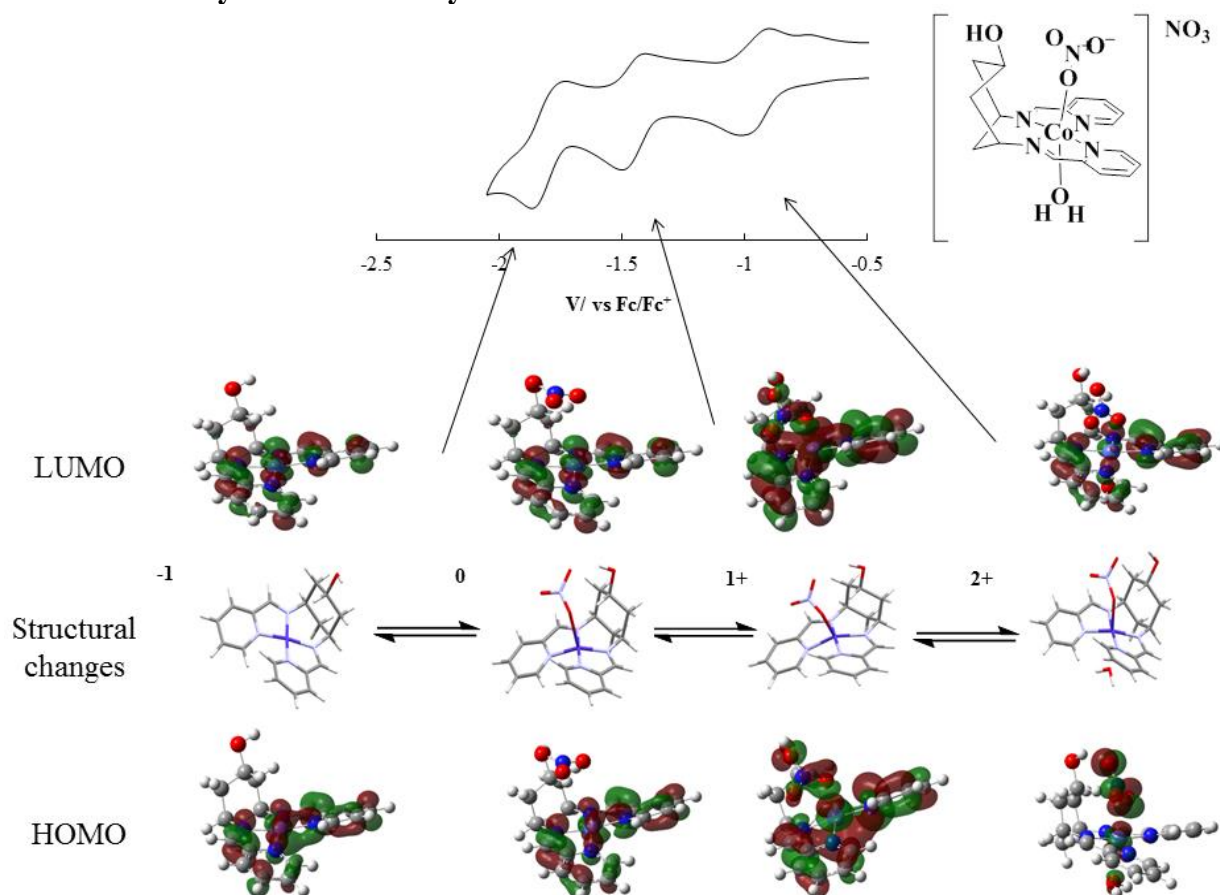


**Figure 4.38** Cyclic voltammetry of 1 mM **CoL2N** at GCE in acetonitrile at 100 mV/s. Corresponding DFT computed structures (*middle*), LUMO (*top*) and HOMO (*bottom*) are shown below with arrows indicating the couples. Overall charge on the complex is give by the number to the top left of each structure.



The DFT of **CoL2N** shows similar behaviour to **CoL1N**, on reduction to the 1+ state there is de-coordination/bond elongation of the axial aqua ligands, giving a 5-coordinate complex. However, on further reduction to the 0 state, the geometry and ligation remains the same. On further reduction to the -1 state, however, the axially bound nitrate is lost giving a square planar geometry. Overall the geometry of the iminopyridine chelate remains almost constant throughout the reduction events. The slight change in behaviour between the two complexes on the reduction of the 1+ state to the 0 state can be tentatively attributed to the distal hydroxyl group on the cyclohexane backbone in solution hydrogen bonding to the axial nitrate stabilising its interaction with metal.

The LUMOs of **CoL2N** show almost the same trend as in **CoL1N**, in the 2+ state, the LUMO is shown to be mainly focused on the ligand, and then in the +1 state it has mixed ligand metal behaviour, with a large metal contribution, therefore the couple associate with this assigned to the  $\text{Co}^{2+/+}$  couple of the metal. This is followed by the 0 and -1 states having mixed iminopyridine/metal character.

#### 4.5.9 DFT and cyclic voltammetry of CoL3N

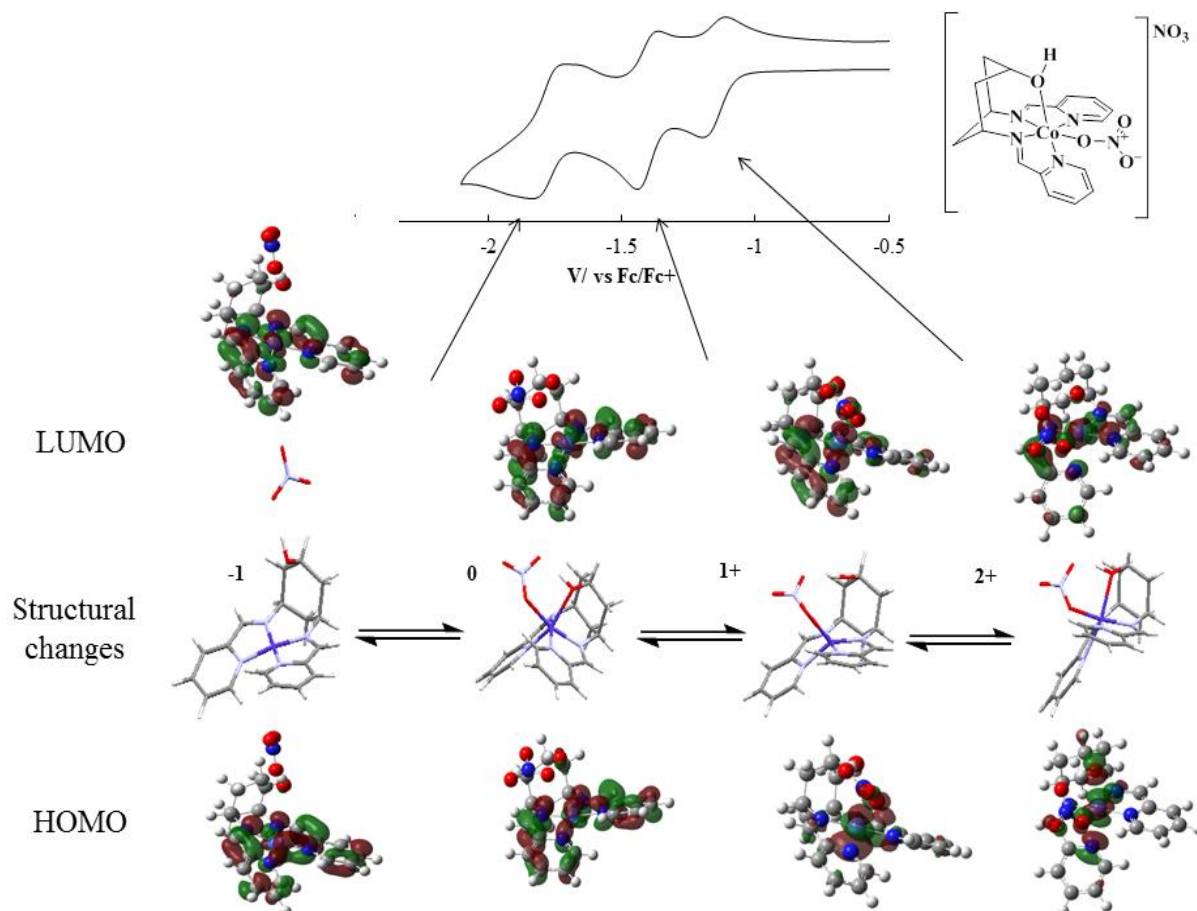


**Figure 4.39** Cyclic voltammetry of 1 mM **CoL3N** at GCE in acetonitrile at 100 mV/s. Corresponding DFT computed structures (*middle*), LUMO (*top*) and HOMO (*bottom*) are shown below with arrows indicating the couples. Overall charge on the complex is given by the number to the top left of each structure.

From the DFT of **CoL3N**, on reduction to the 1+ state there is de-coordination of the proximal hydroxyl ligand, giving a 5-coordinate complex and change in geometry from the trigonal prismatic geometry of the 2+ state to a distorted square pyramidal. On further reduction to the 0 state, there is a re-coordination of the proximal hydroxyl ligand giving a trigonal prismatic geometry. On further reduction to the -1 state, both the proximal hydroxyl and the nitrate decoordinate giving a square planar geometry.

For **CoL3N** in the 2+ state, there is a difference in LUMO compared to that of **CoL1N** and **CoL1N**, in that, instead of being largely ligand based there is also a proportion on the metal. For the 1+, 0 and -1 states the LUMO also has mixed metal ligand character. The

largest contribution from the metal appears to be seen in the LUMO of the 1+ state, and therefore the couple associated with this assigned to the  $\text{Co}^{2+/+}$  couple of the metal

In explaining the differences seen in the DFT and electrochemistry of **CoL3N** on reduction vs the other complexes, it is useful to think of molecular geometries and LFSE. The DDOPi (**9**, **L3**) ligand gives a trigonal prismatic geometry for the **CoL3N** in the 2+ oxidation state. As **CoL2N** in the 2+ oxidation state has a (HS)  $3d^7$  electronic configuration with the *bis*-iminopyridine and nitrate ligands, and as trigonal prismatic geometry gives a smaller LFSE, **CoL3N** must also be (HS)  $3d^7$ .<sup>102</sup> As shown in **section 3.3** the preference for trigonal prismatic or octahedral geometry is related to the electronic configuration and occupancy of orbitals. The highly irreversible behaviour of the  $\text{Co}^{3+/2+}$  couples of the **CoL3N** complexes compared to the other cobalt complexes presented can be attributed to redox coupled-spin crossover (RCSCO), the oxidation of high spin (HS)  $\text{Co}^{2+}$  to low spin (LS)  $\text{Co}^{3+}$ .<sup>197</sup> But, also to a change in geometry from trigonal prismatic geometry to octahedral, shown to be favoured for low spin  $d^6$ , which is the case for  $\text{Co}^{3+}$ .

On reduction of the trigonal prismatic high spin (HS)  $3d^7$   $\text{Co}^{2+}$  **CoL3N**, electron density is added to the  $e'$  level (of a trigonal prismatic ligand field), which is shown to favour neither trigonal prismatic or octahedral geometry, this is reflected in the DFT studies, giving distorted square pyramidal, for the  $3d^8$ , which is itself a Jahn-Teller distortion of the  $d_{z^2}$  of octahedral ligand field. This suggests that the complex would go from high spin (HS) to low spin, due to the removal of degeneracy from the d orbitals, as shown in **figure 4.40**. This would then suggest that a chemical one electron reduction may result in a diamagnetic complex, which could then be characterised spectroscopically by conventional  $^1\text{H}$ -NMR. Due to other priorities, this has not been undertaken in this work.

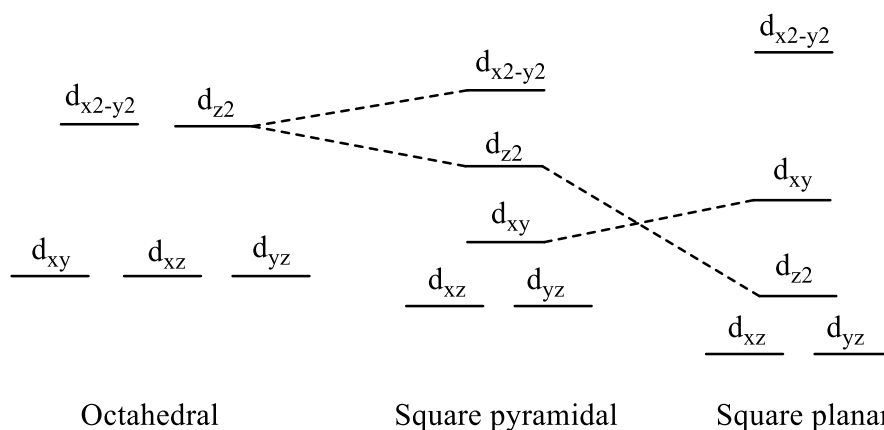


**Figure 4.40** Energy diagram of the axial distortions from octahedral to square planar.

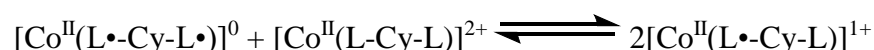
On further reduction to the neutral complex, electron density is added into the  $e''$  level of a trigonal prismatic energy system, shown to restore the balance towards trigonal prismatic geometry. This is seen by DFT through the re-coordination of the proximal hydroxyl, although this contrasts with the square-based pyramidal geometry observed for  $d^9$  Cu(II) – potentially due to more of the electron density being located on the ligands. The Co (0) and Cu (2+) systems are isoelectronic. But different charges and lower  $Z_{eff}$  of Co means electrons are likely to be located in different places. On further reduction of the complex to the -1 state, electron density is added to the  $e''$  level, to give a  $3d^{10}$  electronic configuration, and therefore there is no LFSE. By DFT the -1 state is shown to have a square planar geometry through de-coordination of the proximal hydroxyl, however, this is different to that found in the one electron reduction of **CuL3N** and the crystal structure of **ZnL3N** (**figure 3.9**), both with a  $3d^{10}$  electronic configuration giving trigonal prismatic geometry. This difference may be due to stabilisation of the large negative charge accumulated on **CoL3N** in the -1 state. As Co has lower  $Z/Z_{eff}$  so less electrons will be on Co.

#### 4.6.1 Electronic communication between redox centres

The thermodynamic stability of species with more than two oxidation states within a system can be calculated from the reduction potentials of the first and second reductions of the parent complex, ( $E_{1/2}(2)$  and  $E_{1/2}(3)$ , in the case of the cobalt complexes). The comproportionation constant,  $K_{com}$ , describes the equilibrium between them;



Using the cobalt complexes as an example this is;



And is given by;

$$K_{com} = e^{\left(\frac{n_1 \cdot n_2 \cdot \Delta E_{1/2} \cdot F}{R \cdot T}\right)}$$

$K_{com}$ , allows assignment of Robin and Day classification by describing communication between redox centers. For a Class I species,  $K_{com} < 4$ , and for Class III  $K_{com} > 10^6$ . Class II species have intermediate values. However, it is accepted that for  $K_{com} < 10^2$  the compound is Class I, for  $10^2 < K_{com} < 10^6$  the compound is Class II, and for  $K_{com} > 10^6$  the compound is Class III.<sup>198,199</sup>

**Table 4.8** Peak separations  $\Delta E_{1/2}$  between the first and second reductions of each of the metal complexes with their calculated comproportionation constants,  $K_{com}$ . () = difference between 2<sup>nd</sup> and 3<sup>rd</sup> reductions, [] = different isomer

	$\Delta E_{1/2} / \text{ mV}$	$K_{com}$
<b>ZnL1N</b>	90	$3.30 \times 10^1$
<b>MnL1N</b>	250	$1.70 \times 10^4$
<b>CoL1N</b>	530	$9.20 \times 10^8$
<b>CuL1N</b>	0 (1540)	1 ( $1.10 \times 10^{26}$ )
<b>ZnL2N</b>	110	$7.20 \times 10^1$
<b>MnL2N</b>	350	$8.30 \times 10^5$
<b>CoL2N</b>	490	$1.90 \times 10^8$
<b>CuL2N</b>	110 (1390)	$7.20 \times 10^1$ ( $3.20 \times 10^{23}$ )
<b>ZnL3N</b>	90 [160]	$3.3 \times 10^1$ [ $5.1 \times 10^2$ ]
<b>MnL3N</b>	210	$3.60 \times 10^3$
<b>CoL3N</b>	260	$2.50 \times 10^4$
<b>CuL3N</b>	1190	$1.30 \times 10^{20}$

[] = different isomers, () = second and third reductions used

The general trend in comproportionation constant,  $K_{com}$ , and thus delocalisation, shows an increase going across the period from the manganese complexes found to be class II, consistent with intermediate behaviour, to cobalt where the complexes are found to show class II and III, partially and fully delocalised behaviour. However, in the  $d^{10}$  case, Zn(II), the smallest values of  $K_{com}$ , are obtained, consistent with the class I fully localised behaviour that can be expected of a closed shell ion. In addition to this there is a general decrease in  $K_{com}$ , for DDOPi (**9**, **L3**) complexes compared to of DDP (**10**, **L1**) and DDOP (**5**, **L2**). This behaviour is most likely due to the fact that DDOPi (**9**, **L3**) gives trigonal prismatic geometry compared to the octahedral geometries found in DDP (**10**, **L1**) and DDOP (**5**, **L2**) in the +2 oxidation state.

This behaviour can be explained further using cobalt as an example. From the comproportionation constant,  $K_{com}$ , obtained for the cobalt complexes from the first two reductions, it can be seen that both **CoL1N** and **CoL2N** are found to be class III, with fully delocalised behaviour. **CoL3N**, however, is found to be class II, consistent with intermediate behaviour.

This difference is most probably caused by the difference geometry and thus orbitals involved in the reduction. **CoL3N** has trigonal prismatic geometry, compared to the octahedral geometry found in **CoL1N**, and **CoL2N**. The first reduction for the **CoL1N**, and **CoL2N** complexes were shown to be mainly *bis*-iminopyridine ligand based from LUMO of computed structures, with the second reduction also having a large contribution from the *bis*-iminopyridine ligand. In the octahedral geometry the two arms of the *bis*-iminopyridine both interact with the  $d_{x^2-y^2}$  metal orbitals, and thus the electrons can be delocalised through the orbital. Whereas in **CoL3N** the two arms of the *bis*-iminopyridine interact with different metal orbitals, and therefore delocalisation of the electrons through non-degenerate orbitals is harder.

The copper complexes give interesting behaviour, in **CuL1N** it was posulated that the first two reductions occur at the same potential, and thus would have no electronic communication between them. Whereas the difference in potential between the second and third reduction is large (1540 mV) which suggests communication between centres. **CuL2N** gives behaviour comparable to that of the zinc complexes of class I behaviour, suggesting no communication between reduction events. This is likely because one of the

reduction events gives copper(I) which has  $3d^{10}$  isoelectronic to zinc(II) and therefore comparable. **CuL3N**, however, gives different behaviour, and is postulated to change geometry from square based pyramidal to trigonal prismatic geometry, with the proximal hydroxyl bound to the copper centre. This has the effect of shifting the second reduction to more negative potential, and therefore the effect of this and the electronic communication between reductions cannot be disentangled.

# Chapter 5

## *Electrocatalysis*



## 5.1. Introduction to electrocatalysis

Electrocatalysts participate in electrochemical reactions by assisting in electron transfer to a reactant. The main parameters of characterisation of catalysis are as follows:

- 1) The overpotential ( $\eta$ ) is a thermodynamic parameter describing the additional potential, beyond the thermodynamic requirement, needed to drive a reaction at a specific rate.<sup>200</sup>
- (2) The half-wave potential ( $E_{cat/2}$ ) is defined as the point at which the catalytic wave reaches half of its maximum current,  $i_{p/2}$ .
- (3) The observed (or apparent) rate constant ( $k_{obs}/TOF_{max}$ ) describes the overall rate of homogeneous catalysis and is useful for determining mechanistic properties.<sup>201</sup>

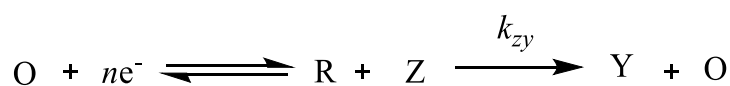
However, direct comparison between systems is often difficult because proton source, electrolyte, solvent, working electrode, and reference electrode vary between reports. In addition methods to define key properties, for example overpotential, differ between different research groups.

Cyclic voltammetry is the most commonly employed technique to analyse the electrocatalytic response of a system. Basic cyclic voltammetry is introduced and explained in **chapter 4**. Electrocatalytic processes may occur by many mechanisms with characteristic cyclic voltammetry responses, dependent on a number of different variables such as scan rate, catalyst and substrate concentrations and the rate constants of the different processes in the catalytic cycles.

Analysis of cyclic voltammogram curves for electrocatalytic processes can yield kinetic information, as well as indicating the thermodynamic overpotential. For example, under conditions that give pseudo first order kinetics, i.e. the concentration of one of the reactants is in excess (for example, the acid concentration),  $TOF_{max}$  can be deduced from the relationship between peak currents ( $i_p$ ) in the absence of substrate and in its presence when pseudo first order conditions occur ( $i_{cat[max]}$ ).

A simple EC' mechanism is shown below as a model to illustrate how electrocatalysis is described with cyclic voltammetry. An EC' mechanism is that in which E is a

heterogeneous electron transfer followed by a homogenous chemical reaction C with prime (') representing a catalytic process, this is illustrated in **scheme 5. 1**. Where O is the oxidised form of the electrocatalyst, which is reduced to R, the active form of the electrocatalyst, this reacts with substrate Z to give product Y and the re-oxidised form of the electrocatalyst (O), the rate of the homogenous chemical reaction is given by  $k_{zy}$ .



**Scheme 5.1** Illustration of an EC' mechanism of a heterogeneous electron transfer followed by a homogenous chemical reaction.

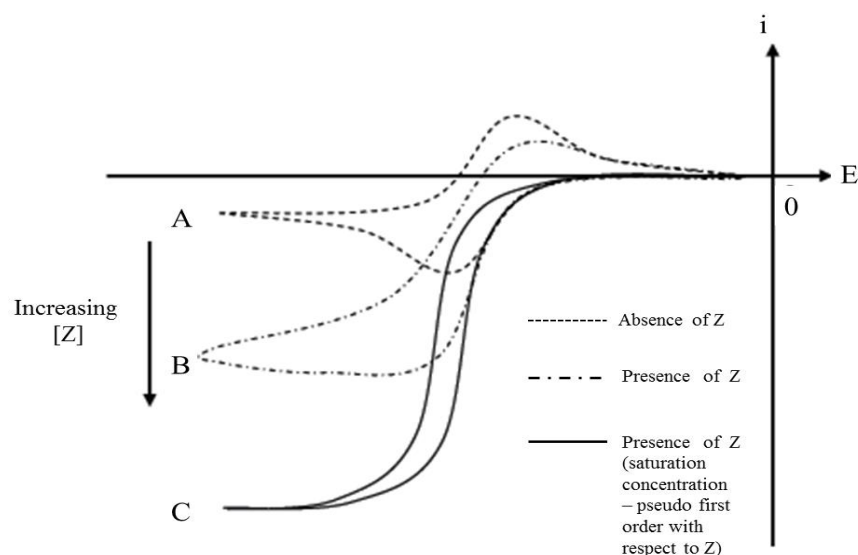


**Figure 5.1** Characteristic cyclic voltammograms responses for the EC' process.

For a reversible electron transfer as shown in **scheme 5.1**, the rate of electron transfer at any potential is always considerably more than the rate of mass transport. This gives a Nernstian equilibrium at the electrode surface, and a classical reversible cyclic voltammogram, where the two peaks for the redox couple are equal in size and shape, and are separated by c.a. 59 mV. This is illustrated by curve A in **figure 5.1**. However, if the rate of electron transfer is not considerably more than the rate of mass transport, the system is said to be irreversible. At low scan rates, the rate of electron transfer can still be larger than the rate of mass transport, and so therefore a reversible cyclic voltammogram is seen. However, as the scan rate is increased the rate of mass transport increases and becomes comparable to that of electron transfer. This results in a loss of reverse peak and an increase in peak separation on increasing scan rate.

$$k_{et} \gg k_{mass\ transport} = \text{reversible}$$

$$k_{et} \ll k_{mass\ transport} = \text{irreversible}$$

Under conditions where the rate of catalysis is slow ( $k_{zy}$ ), (or the scan rate is comparatively very fast) the chemical reaction has no effect on the cyclic voltammetry, and reversible conditions are seen as in curve A of **figure 5.1**. However, if the rate of catalysis is fast (or the scan rate is comparatively slow), catalysis of the reaction is seen and thus R reacts with substrate Z giving Y and the oxidised form O of the catalyst, giving an increase in the current passed at that potential, (i.e.  $i_{cat}$ ). This exceeds the current predicted from Randles-Sevick equation, as in curve B and C of **figure 5.1**. The value of  $i_{cat}$  increases with decreasing scan rate or increasing substrate concentration and the voltammogram peak becomes less defined as the limit of the catalysis is approached. When the limit is attained, the peak is replaced by a scan rate independent plateau as in curve C of **figure 5.1**. The current density of the plateau is given as;<sup>202</sup>

$$i_{cat} = -nFc_0\sqrt{Dk_{obs}} \quad \text{Eq 5.1}$$

$k_{obs}$ , can be deduced by dividing **Eq 5.1** by the Randles-Sevick equation to give;

$$\frac{i_{cat}}{i_p} = \frac{n}{0.4463} \sqrt{\frac{RT(k_{obs}[H^+]^x)}{Fv}} \quad \text{Eq 5.2}$$

Where  $i_p$  is the reductive current of a one electron reversible couple in the absence of a proton source, and  $i_{cat}$  is the peak reductive current of the catalytic wave in the presence of a proton source;

Under standard conditions this simplifies to;

$$TOF = k_{obs} = v \left( \frac{\frac{i_{cat}}{i_p}}{0.72} \right)^2 \quad \text{Eq 5.3}$$

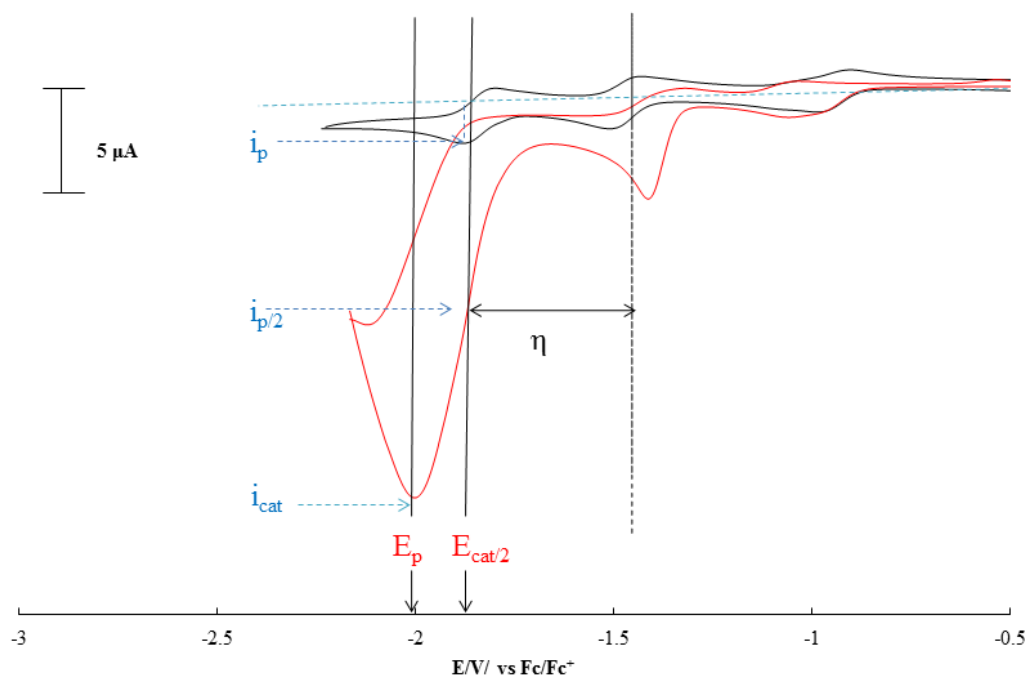


**Figure 5.2** Illustration of an electrocatalytic cyclic voltammogram with values shown used to calculate kinetic and thermodynamic parameters. The black dashed line is the thermodynamic potential for proton reduction.

Overpotential,  $\eta$ , is defined as the difference between the equilibrium potential for a given reaction (also called the thermodynamic potential) and the potential at which the catalyst operates at a specific current under specific conditions. There are a number of different approaches to do this by different groups, such as using the onset potential for the catalytic process; these can lead to inconsistencies in reported overpotentials. The most consistent method is to take the potential at half the catalytic current.<sup>203</sup>

A factor that affects the overpotential, and therefore should be accounted for is homoconjugation. Often, an acid (AH) and its conjugate base ( $A^-$ ) form a stable adduct ( $AHA^-$ ) through hydrogen bonding, this phenomenon is seen very frequently in acetonitrile, and is known as homoconjugation. It is described by the association constant,  $K_c$ , as shown in **scheme 5.2**. This means, therefore, that with increased concentrations of acid (AH) above  $1/K_c$ , there is a significant concentration of homoconjugate ( $AHA^-$ ), this in turn means that the strength of the acid is increased and thus the thermodynamic reduction potential becomes more positive in value. As acetic acid gives a large proportion of homoconjugation,  $\log_{10}K_c = 3.7$ , this must be compensated for Artero and

co-workers<sup>204</sup> showed that homoconjugation can be accounted for using a theoretical thermodynamic value for the most acidic couple present in solution accounting for the increased acidic strength from homoconjugation. In their publication they provide the theoretical values for common acids used in electrocatalytic studies, including acetic acid used in this work.



**Scheme 5.2** Homoconjugation of acids in solution.

$$\eta = \left| E_{H^+} - E_{\frac{cat}{2}} \right| \quad \text{Eq 5.4}$$

Where;  $E_{H^+}$  is the non-standard reduction potential for the  $\text{H}_2/\text{H}^+$  couple, and  $E_{\frac{cat}{2}}$  is the potential at half peak current of the catalytic wave.

$$E_{H^+} = E_{H^+}^{\theta} + \frac{RT}{nF} \ln \frac{[\text{H}^+]}{p\text{H}_2} \quad \text{Eq 5.5}$$

$$E_{H^+} = E_{H^+}^{\theta} - 0.05916V \times pH \quad \text{Eq 5.6}$$

Where the standard reduction potential for the  $\text{H}_2/\text{H}^+$  couple in acetonitrile is; <sup>205</sup>

$$E_{H^+ (MeCN)}^{\theta} = -0.0228 V \pm 0.008 V \text{ vs Fc/Fc}^+ \quad \text{Eq 5.7}$$

In acetonitrile this then becomes;

$$E_{H^+} = -0.0228 V - 0.05916V \times pKa \quad \text{Eq 5.8}$$

Where pKa is the pKa of the acid used in acetonitrile.

$$E_{H^+} = -1.42 V \text{ vs Fc/Fc}^+ \quad \text{Eq 5.9}$$

This gives the nonstandard reduction potential for the  $\text{H}_2/\text{H}^+$  couple in acetonitrile for acetic acid. However, **Eq 5.9** does not account for homoconjugation of acetic acid, as is explained previously. This is accounted for by Artero and co-workers,<sup>204</sup> as above, who tabulated a series of nonstandard reduction potentials for the  $\text{H}_2/\text{H}^+$  couple in acetonitrile for different concentrations of acetic acid. The theoretical value for the most acidic couple present in solution accounting for homoconjugation, at 0.1 M) is;

$$E_{\text{H}^+} = -1.23 \text{ V vs Fc/Fc}^+$$

Values used to calculate kinetic and thermodynamic parameters from the cyclic voltammetry are given in **figure 5.2**.

## 5.2. Screening of Complexes for Activity in Electrocatalytic Proton Reduction

The cyclic voltammetry of the **L1**, **L2** and **L3** complexes was performed in acetonitrile in the presence of a source of protons, and used as a method of screening the complexes for activity in the reduction of protons to dihydrogen. Acetic acid was chosen as a proton source due preliminary results suggesting its suitability.

### 5.2.1. Cobalt complexes

As shown in **figures 5.3** and **5.4** respectively, upon addition of increasing equivalents of acetic acid, the cyclic voltammetry of **CoL1N**, and **CoL2N** both show a shift to more negative potential for the first reductions at  $-0.85 \text{ V}$  and  $-0.94 \text{ V}$  respectively, and a large change in behaviour for the last two reductive couples at  $-1.37$  and  $-1.77 \text{ V}$ , and  $-1.45 \text{ V}$  and  $-1.81 \text{ V vs Fc/Fc}^+$  respectively, going from largely reversible to irreversible behaviour. The couples at  $-1.77 \text{ V}$  and  $-1.81 \text{ V vs Fc/Fc}^+$  in **CoL1N** and **CoL2N** respectively, also show a large increase in peak current, which increases linearly with increasing equivalents of acetic acid. As shown in **figure 5.5**, the electrochemistry of **CoL3N** in the presence of acetic acid gives more complicated behaviour. On the addition of acetic acid, the couples at  $-1.16 \text{ V}$ ,  $-1.40 \text{ V}$  and  $-1.8 \text{ V vs Fc/Fc}^+$  all shift to more negative potentials and go from being largely reversible in nature to irreversible. On increasing equivalents of acetic acid there is also a large increase in peak current for the last reductive process. This however is overlapped with another process which appears at

more positive potential when larger quantities of acetic acid are added. With very very high acid concentrations, this process appears to take over from the more negative process.

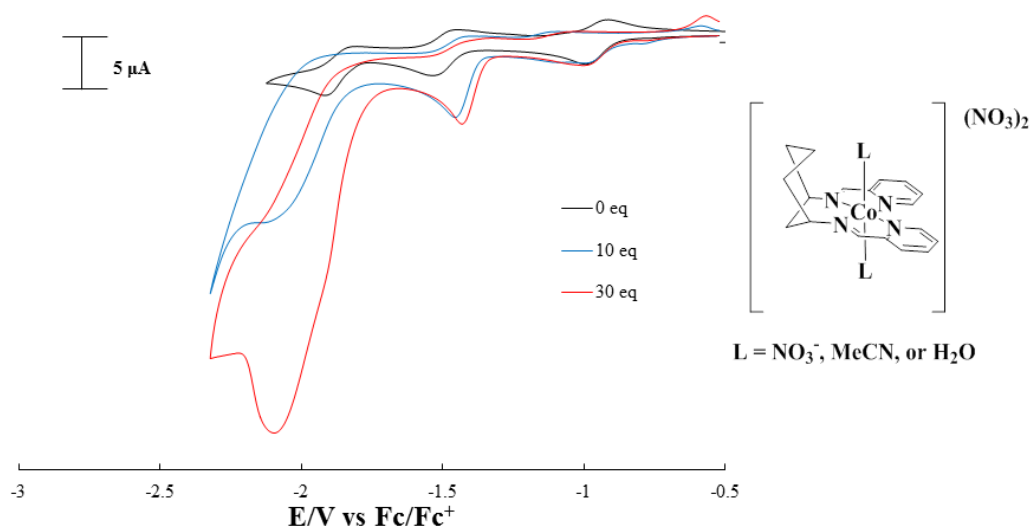


**Figure 5.3** Electrocatalytic response of 1 mM **CoL1N** in acetonitrile, in the presence of 10 and 30 equivalents of acetic acid, at a GCE.

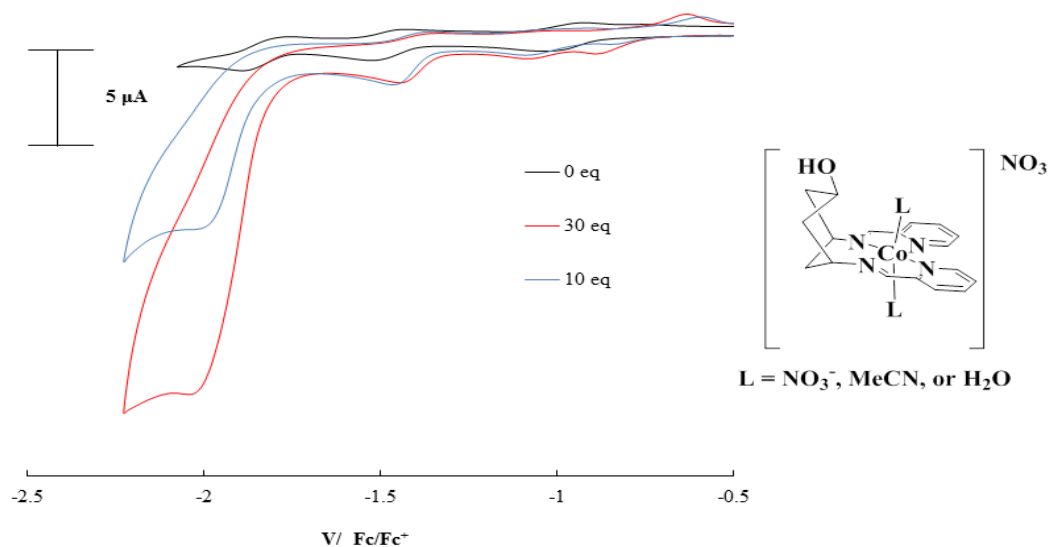


**Figure 5.4** Electrocatalytic response of 1 mM **CoL2N** in acetonitrile, in the presence of 10 and 30 equivalents of acetic acid, at a GCE.

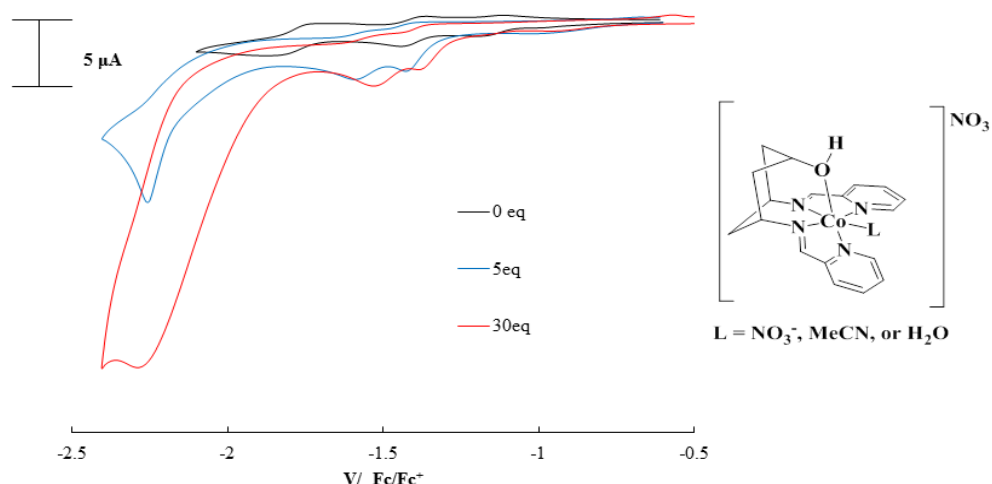


**Figure 5.5** Electrocatalytic response of 1 mM **CoL3N** in acetonitrile, in the presence of 5 and 30 equivalents of acetic acid, at a GCE. These quantities of acid are chosen to show the change in behaviour with increasing acid concentration, discussed below and later in the chapter.

Thus the CVs of the cobalt complexes **CoL1N**, **CoL2N**, and **CoL3N** all show a large enhancement in peak current of the last reductive process which increases on increasing equivalents of acetic acid. This increase in reductive current in the presence of a proton source suggests they are proton reduction electrocatalysts. The electrocatalytic behaviour is explored in more detail in **section 5.3.1**.

### 5.2.2 Copper complexes

As shown in **figure 5.6**, on addition of acetic acid to **CuL1N** the cyclic voltammetry shows the appearance of a large peak with  $E_p = -1.87$  V *vs* Fc/Fc<sup>+</sup>. This is also found with **CuL3N**, as shown in **figure 5.8**, where the cyclic voltammetry shows the appearance of a large peaks with  $E_p = -1.92$  and  $-2.04$  V *vs* Fc/Fc<sup>+</sup>. Such a large increase in reductive current in the presence of a proton source suggests electrocatalytic proton reduction. However, these catalytic waves appear to show cross-over, and the reverse oxidation spikes shifted to more positive potential and increase in current versus the acid free system. These observations are characteristic of nucleation and growth processes on the electrode surface.<sup>175</sup>



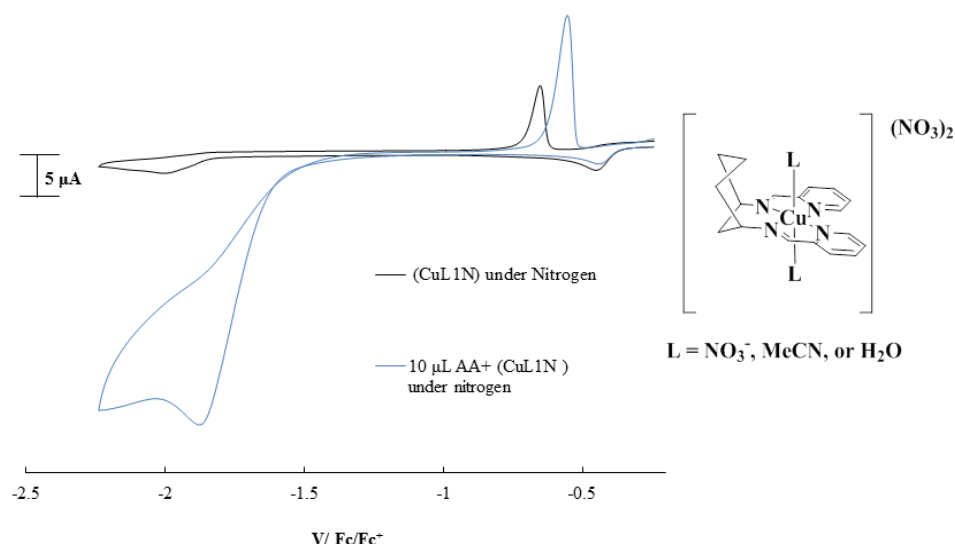


**Figure 5.6** Electrocatalytic response of 1 mM **CuL1N** in acetonitrile, in the presence of 6 equivalents of acetic acid, at a GCE.

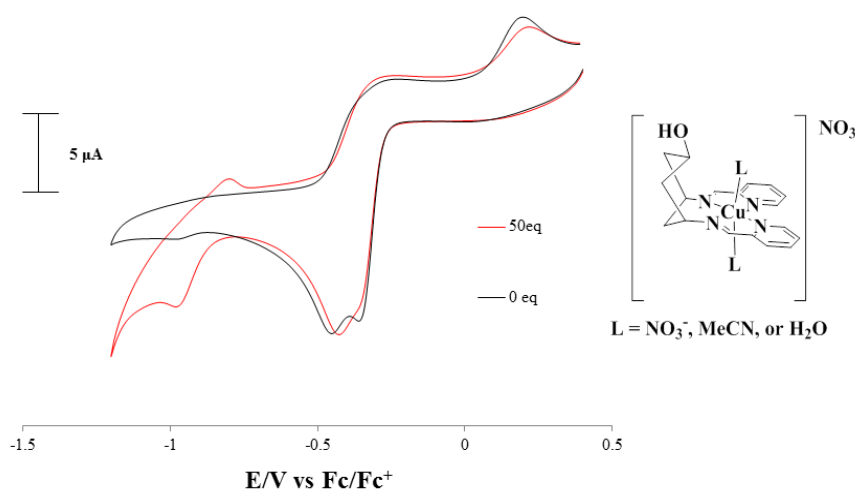


**Figure 5.7** Electrocatalytic response of 1 mM **CuL2N** in acetonitrile, the presence of 50 equivalents of acetic acid, at a GCE.

The other complex in this series, **CuL2N**, deposits on the electrode surface at highly reducing potentials even in the absence of a proton source, and in the presence of a proton source sweeping the current more negative than  $-1.2\text{ V vs Fc/Fc}^+$  results in its complete destruction. However, at less reducing potentials, in the presence of 50 equivalents of acetic acid it can be seen that the peaks at  $-0.35$  and  $-0.45\text{ V vs Fc/Fc}^+$  merge to give one peak at  $-0.43\text{ V vs Fc/Fc}^+$ , with the appearance of another quasi-reversible wave at  $-0.89\text{ V vs Fc/Fc}^+$ , as shown in **figure 5.7**. This may be a consequence of the partial proton

coupled reduction of the imino pyridine arms, as this would increase electron density on the nitrogen atoms and thus the copper centre making harder to reduce and therefore shift the  $\text{Cu}^{\text{II/I}}$  couple to more negative potential.

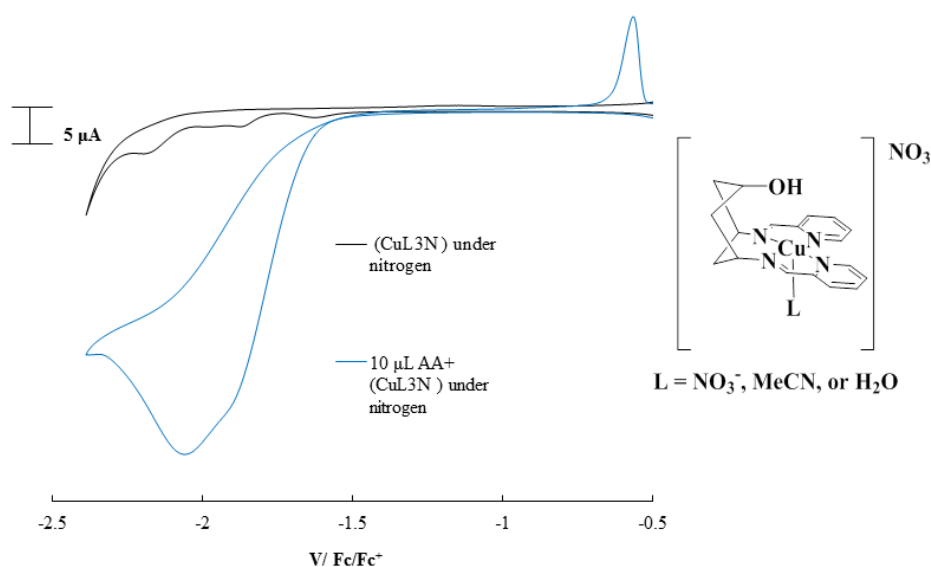


**Figure 5.8** Electrocatalytic response of 1 mM **CuL3N** in acetonitrile in the presence of 6 equivalents of acetic acid, at a GCE.

In conclusion the cyclic voltammetry of the copper complexes **CuL1N** and **CuL3N** show enhancement in peak current of a reductive process occurring at *ca.* -2 V *vs*  $\text{Fc/Fc}^+$  in the presence of a proton source, which increases on increasing equivalents of acetic acid. This increase in reductive current in the presence of a proton source is might suggest these complexes catalyse reduction of a protons. However, as seen most strongly with **CuL2N** the presence of acid also increases deposition and decomposition of the complexes on the electrode surface. The lack of stability of these complexes to protons under reducing conditions means that further investigation into their electrocatalytic proton reduction was discontinued. This type of behaviour has been reported previously for related copper ethylene-bis(acetylacetoniminato) complexes.<sup>206</sup>

### 5.2.3 Manganese complexes

**Figure 5.9** shows the voltammetric response resulting from addition of acetic acid to **MnL2N**. An increase in current is seen with acid and the growth of three peaks at  $E_p = -1.13, -1.64$  and  $-1.94$  V vs  $\text{Fc}/\text{Fc}^+$ . Increase in reductive current in the presence of a proton source suggests electrocatalytic proton reduction.

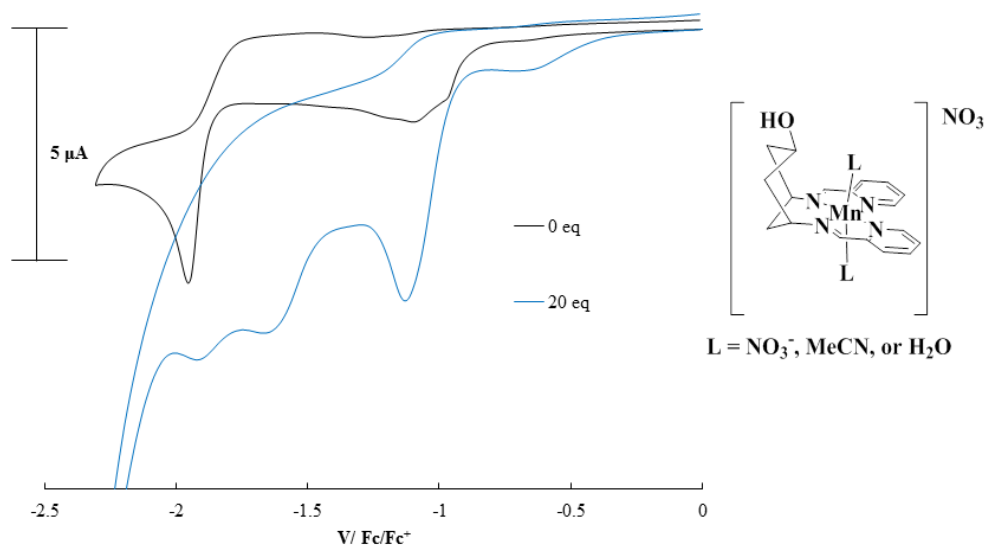


**Figure 5.9** Electrocatalytic response of 1 mM **MnL2N** in acetonitrile in the presence of 20 equivalents of acetic acid, at a GCE.

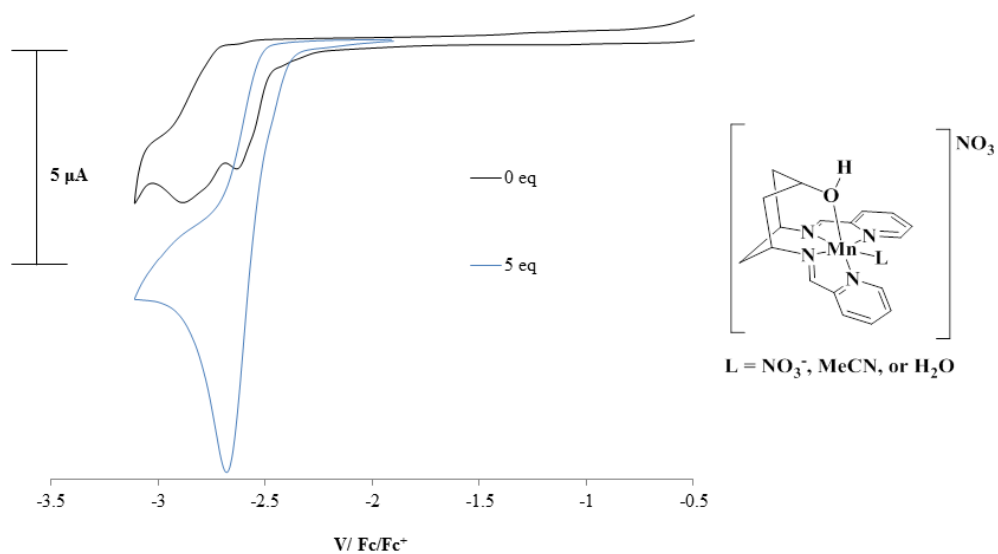


**Figure 5.10** Electrocatalytic response of 1 mM **MnL3N** in acetonitrile and in the presence of 5 equivalents of acetic acid, at a GCE.

However, in the case of manganese complexes the high overpotentials required to access the doubly reduced state makes this improbable.<sup>207</sup> The increase in current seen in **MnL2N** is most likely caused by the proton coupled reduction of the iminopyridine arms to the amines, and this explanation is supported by the observation that adding further acid gave no further enhancement in current or change in behaviour. There are only a few examples of manganese proton reduction electrocatalysts which have been published as of yet. Notably a manganese bipyridine catalyst published by Kubiak,<sup>208</sup> which has been shown to have a high TOF 5500 s<sup>-1</sup> and reasonable overpotential of 0.9 V. The bipyridine ligand framework is comparable to that of the iminopyridine ligand used in this work. However, unlike the manganese complexes in this work, the presence of back bonding carbon monoxide ligands may remove electron density from the manganese metal centre and thus make the doubly reduced state more accessible.

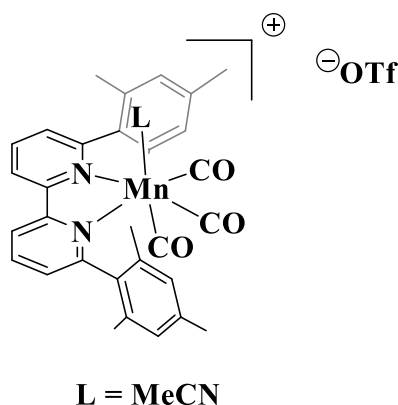


**Figure 5.11** Manganese electrocatalyst for proton reduction of TFA in MeCN.<sup>208</sup>

As shown in **figure 5.10**, in **MnL3N** the three one electron irreversible reductions at  $-2.66$  V,  $-2.81$  V and  $-2.87$  V *vs* Fc/Fc<sup>+</sup>, appear to combine to give one three electron irreversible peak at  $-2.66$  V *vs* Fc/Fc<sup>+</sup> in the presence of acetic acid. There is no further increase in the current of the process on increasing proton concentration further from here, therefore it is unlikely that this is due to the reduction of protons to dihydrogen. Thus, it appears that somehow addition of a proton source makes each of the reductions in the absence of a proton source equal in potential, and therefore this may indicate that the addition of a proton source changes the geometry from the trigonal prismatic geometry to distorted square based pyramidal geometry as suggested by DFT studies shown in **figure 5.12** but at lower potential. The specific proton source here, acetic acid, may assist

this structural change by hydrogen bonding to the proximal group, weakening its coordination to the metal centre. Any change in geometry likely only occurs after the first electron transfer: otherwise, we would expect the early reductive part of this CV in the presence of acid to resemble that of **MnL2N**.

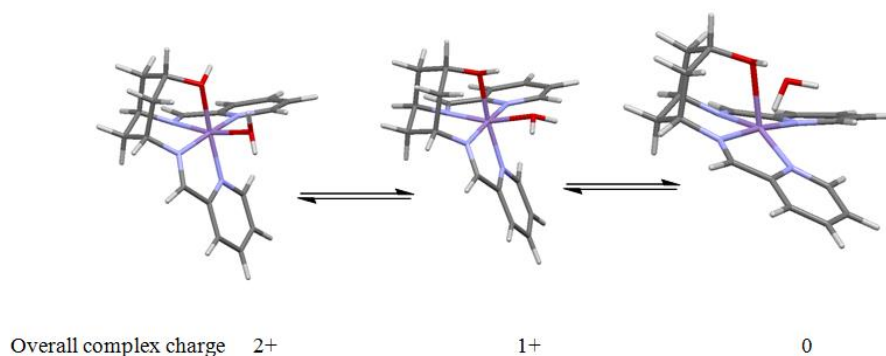


**Figure 5.12** DFT calculated structural changes in **MnL3N** on reduction from the 2+ to neutral oxidation state.

The investigation of **MnL1N** with a proton source gave rapid and complete decomposition of the complex on reduction.

#### 5.2.4 Nickel complex

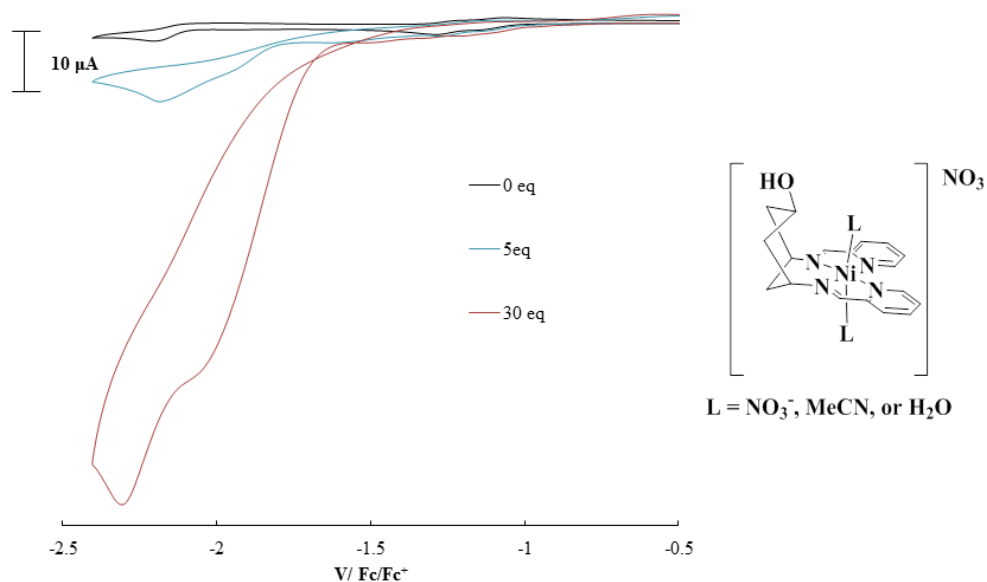


**Figure 5.13** Electrocatalytic response of 1 mM **NiL2C** in acetonitrile, the presence of 10 and 30 equivalents of acetic acid, at a GCE.

As shown in **figure 5.13**, on the addition of acetic acid to **NiL2C** the cyclic voltammetry shows the appearance of a large peak at *ca.*  $E_p = -2.25 \text{ V vs Fc/Fc}^+$ . With increasing equivalents of acetic acid another peak grows in at *ca.*  $E_p = -2.0 \text{ V vs Fc/Fc}^+$ , shown in **figure 5.13**. **NiL2C** shows one of the largest catalytic currents seen in this work for a given number of equivalents of acetic acid, for example a TOF of  $2000 \text{ s}^{-1}$  could be calculated from  $i_{cat}/i_p$  of 36 at 0.5 mM acetic acid is seen with an overpotential,  $\eta$ , of *ca.* 660 mV. However, these catalytic waves show cross-over, which is characteristic of nucleation and growth processes on the electrode surface.<sup>175</sup> This means that it is unclear whether the catalysis is coming from the complex, or something deposited on the electrode surface. If from the complex, the molecular catalyst would appear to be too unstable to be of further interest and if from deposits on the electrode surface, there would be much simpler routes to achieve a nickel functionalised electrode. For these reasons, and because attempts to synthesise and purify the other nickel complexes failed, work on electrocatalysis with **NiL2N** was discontinued.

#### 5.2.5 Aqueous buffered studies of CoL2N

Bis(iminopyridine) cobalt(II) complexes have previously been shown to have activity for hydrogen evolution in aqueous buffered solutions.<sup>44</sup> Therefore, the cyclic voltammetry of **CoL2N** was explored in aqueous medium at a gold-amalgam electrode.

A gold-amalgam electrode was used as the working electrode in these aqueous studies, as it is a good substitute for a mercury drop electrode, and still has a large potential range due to its large overpotential for proton reduction.<sup>209</sup>

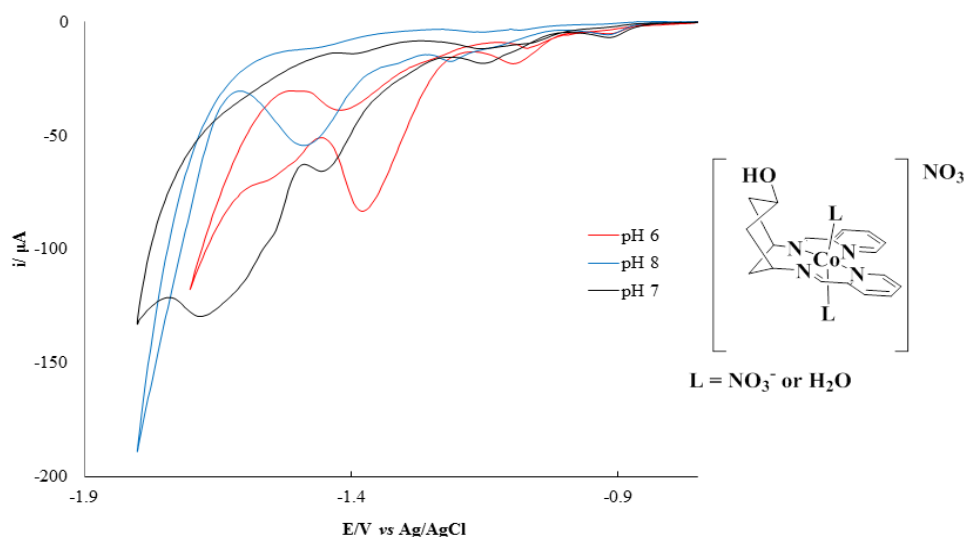


**Figure 5.14** Current normalised electrocatalytic response of 0.5 mM **CoL2N** in 50 mM, pH 6, 7, 8 aqueous phosphate buffers at 200 mV/s at a mercury-gold amalgam electrode.

**Table 5.1** Peak potentials,  $E_p$ , vs Ag/AgCl, for the current normalised electrocatalytic response of 0.5 mM **CoL2N** in 50 mM pH 6, 7, 8 aqueous phosphate buffers at 200 mV/s at a mercury-gold amalgam electrode.

pH	First reduction/ V	Second reduction/ V	Third reduction/ V	Fourth reduction / V
6	-0.91	-1.10	-1.38	-1.55
7	-0.91	-1.15	-1.46	-1.68
8	-0.92	-1.22	-1.49	

As shown in **figures 5.14**, the cyclic voltammetry of **CoL2N** in pH 6 sodium phosphate buffer gives four reductive peaks at  $E_p = -0.91, -1.10, -1.38$  and  $-1.55$  V vs Ag/AgCl. In pH 7 sodium phosphate buffer four reductive peaks are observed at  $E_p = -0.91, -1.149, -1.46$  and  $-1.68$  V vs Ag/AgCl. In pH 8 sodium phosphate buffer only three reductive peaks are seen at  $E_p = -0.92, -1.22$  and  $-1.49$  V vs Ag/AgCl.

A large peak current is seen at the peaks at ca.  $-1.4$  V vs Ag/AgCl, which increases with decreasing buffer pH, as seen in **figure 5.14**, indicative of proton reduction to dihydrogen. This behaviour is comparable to that seen in acetonitrile solution with acetic acid as the proton source **figure 5.4**. A half peak potential,  $E_{cat/2} = -1.35$  V vs Ag/AgCl represents an overpotential of ca. 740 mV at pH 7, using  $E_{H_2/H^+} = 0.0591 \cdot pH$ . However, reducing potentials in excess of  $-1.5$  V vs Ag/AgCl, with **CoL2N** in any aqueous buffer were seen

to causes deposition of an electroactive species on the gold-mercury amalgam electrode, therefore the stability of the complexes in aqueous buffers was investigated.

The stability of the complex at different pH in buffers was investigated via UV/Vis spectroscopy as shown in **figure 5.15**, to see which pH range and time scale is appropriate for the complex. These studies show that there is a significant change in the UV-vis spectrum within 5 minutes at pH 6, but that stability improves at pH 7 and mildly basic pH 8. The most probable decomposition pathway in aqueous solution is the hydrolysis of the iminopyridine arms to the corresponding amine and aldehyde.



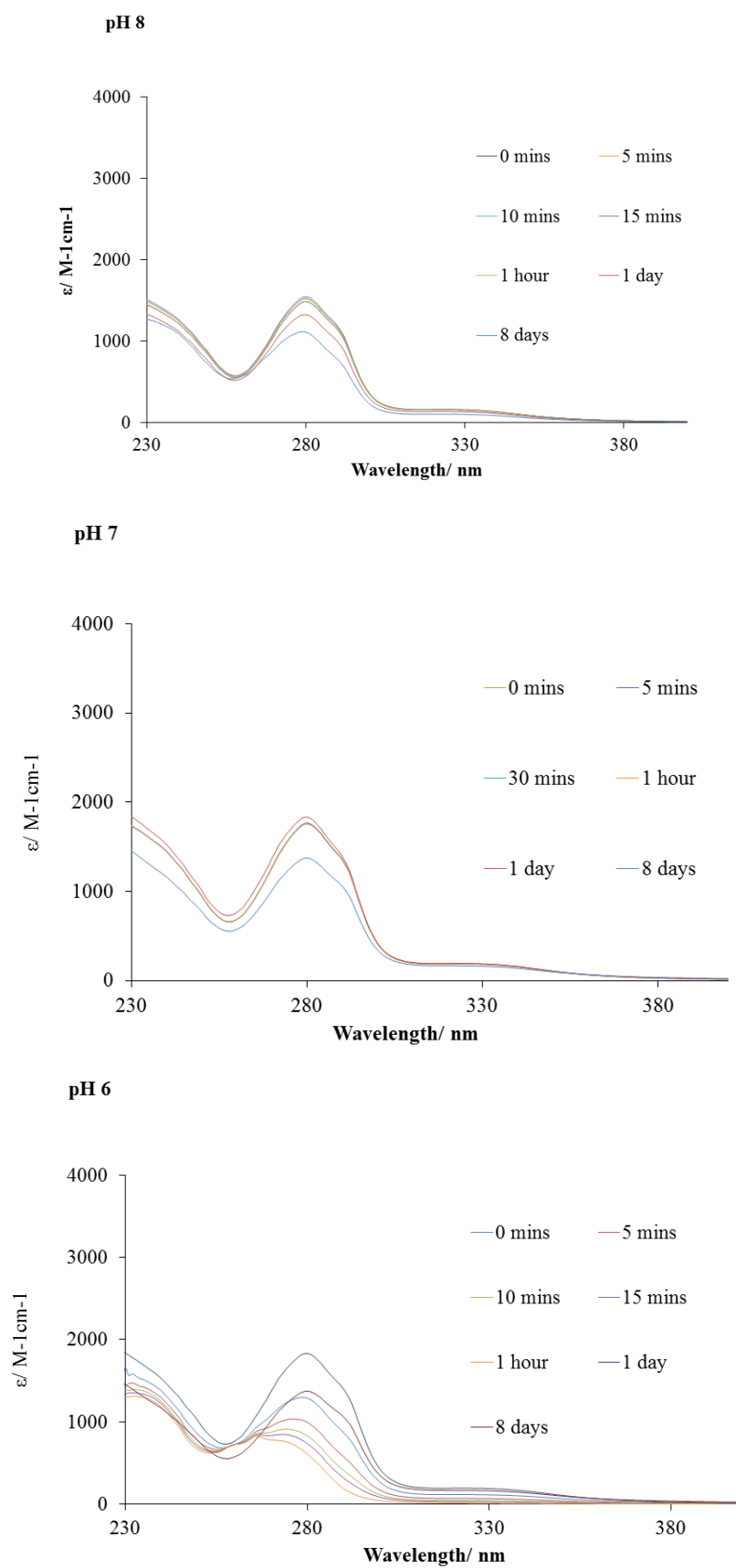


**Figure 5.15** UV-vis stability studies in pH 6, 7, 8 aqueous phosphate buffers, over 5 mins to 8 days for **CoL2N**

In conclusion; although the aqueous electrochemistry of **CoL2N** appears to show electrocatalytic activity, the results from this study lead to doubt in the analysis of Gray/Peters work.<sup>44</sup> Although there is a difference in ligand substitution at the imine (Me vs H), it is unclear whether the methyl group used by Gray and Peters would increase the stability of their catalyst, vs **CoL2N**. The methyl group could afford some steric protection, but on the other hand imine hydrolysis is acid catalysed, and the strong electron donation of the methyl group would increase the reactivity of the imine-N in the protonation step and make hydrolysis more likely. With the regard to this thesis, these problems with stability in aqueous media mean that further work is focused on the electrocatalytic activity and behaviour of the cobalt complexes in acetonitrile with acetic acid as a proton source.

### 5.3.0 Electrocatalysis using cobalt complexes at GCE

The remainder of this chapter is focused on the behaviour of the cobalt complexes as catalysts for reduction of protons to dihydrogen, as these were the most promising results from activity screening. To assist in comparison of catalysis by each of the complexes, the currents observed in the cyclic voltammetry of each complex with increasing concentration of acetic acid is normalised by taking the current of the cyclic voltammograms in the presence of a proton source,  $i_{cat}$ , in this case acetic acid and dividing it by the last reductive peak of the complex in the absence of proton source,  $i_p$ . This is then plotted vs the potential with reference to the ferrocene/ferrocenium couple (Fc/Fc<sup>+</sup>).

However, **it is important to note** that shortly before submission of this thesis was due, a bulk electrolysis experiment on **CoL3N** showed conclusively that for this complex, the main catalytic process observed is not reduction of protons to dihydrogen. Time has not permitted investigation of the other cobalt complexes, but this result means that the processes they catalyse are an open question – particularly in the case of the other nitrates. Despite this, analysis of turnover frequencies (TOF) and overpotentials ( $\eta$ ) performed for proton reduction have been retained – as they do reflect the kinetics and thermodynamics of a reductive process involving protons, even if the process is not clearly identified.

### 5.3.1 Electrocatalysis using Cobalt Complexes at GCE – Nitrate complexes Cyclohexane Based Complexes: CoL1N, CoL2N and CoL3N

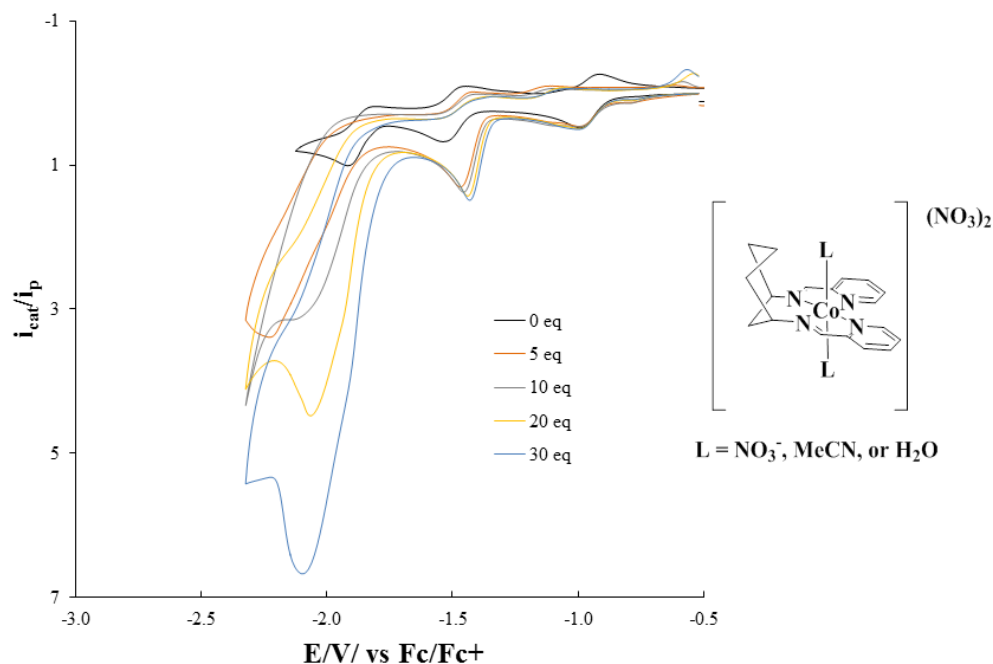


**Figure 5.16** Current normalised electrocatalytic response of 1 mM **CoL1N** in acetonitrile, in the presence of increasing equivalents of acetic acid, at a GCE.

As shown in **figure 5.16**, in the absence of a proton source, **CoL1N** gives three reductive couples at  $E_{1/2} = -0.85, -1.37$  and  $-1.77$  V vs  $\text{Fc/Fc}^+$ . In **chapter 4** these were assigned to a ligand based process, followed by a largely metal based process ( $\text{Co}^{\text{II/I}}$ ) and a mixed ligand metal ( $\text{Co}^{\text{I/0}}$ ) respectively as for the other octahedral cobalt complexes. In the presence of 5 equivalents of acetic acid, the first reduction initially shifts to more negative potential by 240 mV where it remains constant with increasing equivalence of acid. The second reduction becomes irreversible, at *ca.*  $E_p = -1.48$  V vs  $\text{Fc/Fc}^+$ , and shifts to more positive potential by 68 mV per  $-\log[\text{H}^+]$ . From the thermodynamic Nernstian analysis, the redox potential of a reaction at 298 K involving  $m$  protons and  $n$  electrons shifts by  $m/n \cdot 0.059$  V per tenfold change in proton activity ( $\log[\text{H}^+]$ ).<sup>210,211</sup> Therefore, this shift is symptomatic and most likely caused by a one electron one proton PCET (proton coupled electron transfer) event. The third reduction in the presence of acetic acid gives a large Faradaic current with *ca.*  $E_p = -2.2$  V vs  $\text{Fc/Fc}^+$ . However, at 10 eq of acetic acid this wave shifts more positive by 100 mV with comparable current to that at 5 eq of acetic acid, but on further addition of acid increases in Faradaic current on increasing equivalents of protons is indicative of electrocatalytic proton reduction. This peak also

shifts to more positive potential by 57 mV per  $-\log[\text{H}^+]$ , as for the second reduction, again symptomatic of a one electron one proton PCET event.<sup>210-212</sup>

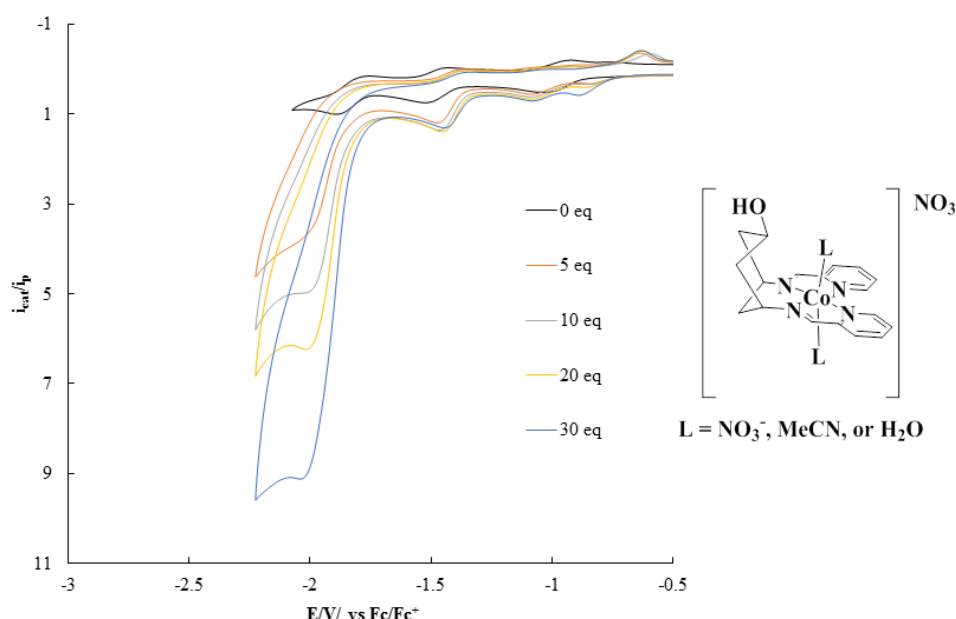


**Figure 5.17** Current normalised electrocatalytic response of 1 mM **CoL2N** in acetonitrile, the presence of increasing equivalents of acetic acid, at a GCE.

In **figure 5.17**, it can be seen that the electrocatalytic behaviour of **CoL2N** is almost the same as that of **CoL1N**. In the absence of a proton source, **CoL2N** gives three reductive couples at  $E_{1/2} = -0.94, -1.45$  and  $-1.81$  V vs  $\text{Fc}/\text{Fc}^+$ . In **chapter 4** these were assigned to a ligand based process, followed by a largely metal based process ( $\text{Co}^{\text{II/I}}$ ) and a mixed ligand metal ( $\text{Co}^{\text{I/0}}$ ) respectively as for the other octahedral cobalt complexes. In the presence of increasing equivalence of acetic acid, the first reduction remains largely unperturbed indicating that the complex is stable under the conditions but initially shifts to more negative potential by 117 mV with the addition of 5 eq of acetic acid. The second reduction becomes irreversible, at *ca.*  $E_p = -1.47$  V vs  $\text{Fc}/\text{Fc}^+$ , and shifts to more positive potential by 53 mV per  $-\log[\text{H}^+]$  – approximately consistent with a one electron one proton PCET event. From the DFT calculated HOMO and LUMO, analysis suggests that this is due to protonation and reduction of the metal centre presumably to give a metal hydride ( $\text{Co}^{\text{II}}\text{-H}$ ), as shown for similar cobalt electrocatalysts.<sup>86</sup> The third reduction in the presence of acetic acid gives a large Faradaic currents with *ca.*  $E_p = -2.01$  V vs  $\text{Fc}/\text{Fc}^+$ . This increase in Faradaic current on increasing equivalents of protons is indicative of electrocatalytic proton reduction. This peaks also shifts to more positive potential by 59

mV per  $-\log[\text{H}^+]$ , this shift as for the second reduction, is most likely caused by a one electron one proton PCET event.<sup>210,211</sup>

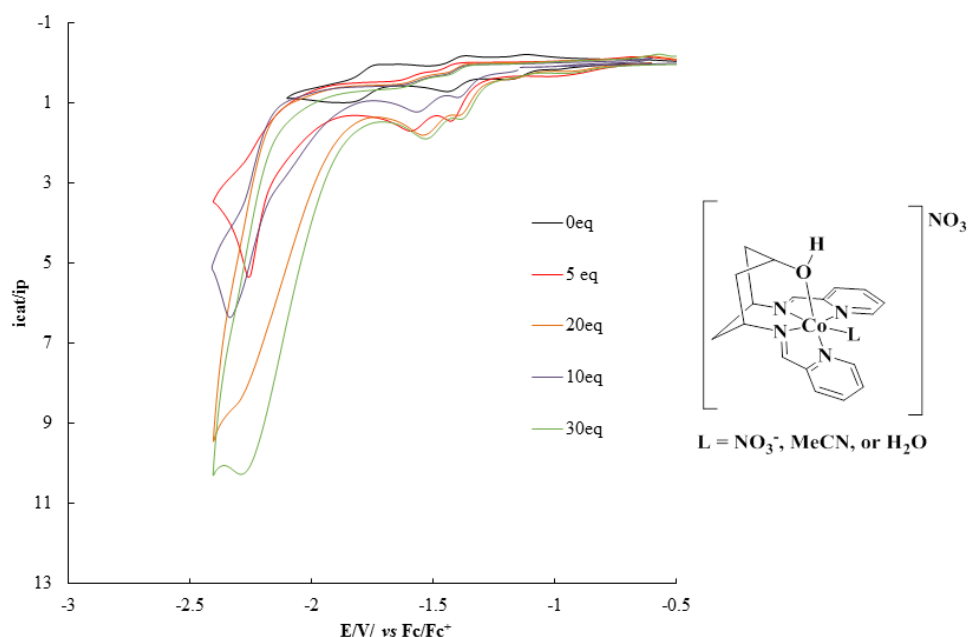


**Figure 5.18** Current normalised electrocatalytic response of 1 mM **CoL3N** in acetonitrile, in the presence of increasing equivalents of acetic acid, at a GCE.

As shown in **figure 5.18**, the electrocatalytic behaviour for **CoL3N** is different to that found for **CoL1N** and **CoL2N**. In the absence of a proton source, **CoL3N** gives three reductive couples at  $E_{1/2} = -1.16, -1.40$  and  $-1.80$  V vs  $\text{Fc}/\text{Fc}^+$ . In **chapter 4** these were shown to be a largely metal based process ( $\text{Co}^{\text{II/I}}$ ) and two mixed ligand metal ( $\text{Co}^{\text{I/0}}, \text{L}\cdot\text{Co-L}\cdot$ ) processes with more apparent ligand character for the last reduction.

In the presence of increasing equivalents of acetic acid, the first reduction ( $-1.16$  V), second reduction ( $-1.40$  V) and third reduction ( $-1.80$  V) all become irreversible. Initially all the peaks shift to more negative potential with increasing acetic acid concentration as shown in (d) of **figure 5.19**. However, from graph (d) from **figure 5.19** the trough of the curve of  $E_p$  or  $E_{p/2}$  vs  $[\text{H}^+]$ , shows a change in behaviour at *ca.* 0.0059 M “5.9 eq” of acetic acid for the couple at  $-1.16$  V, a change in behaviour at *ca.* 0.0052 M “5.2 eq” acetic acid for the couple at  $-1.4$  V, and a change in behaviour at *ca.* 0.008 M “8 eq” acetic acid for the couple at  $-1.8$  V. At these concentrations the potentials of the waves start to shift more positive.

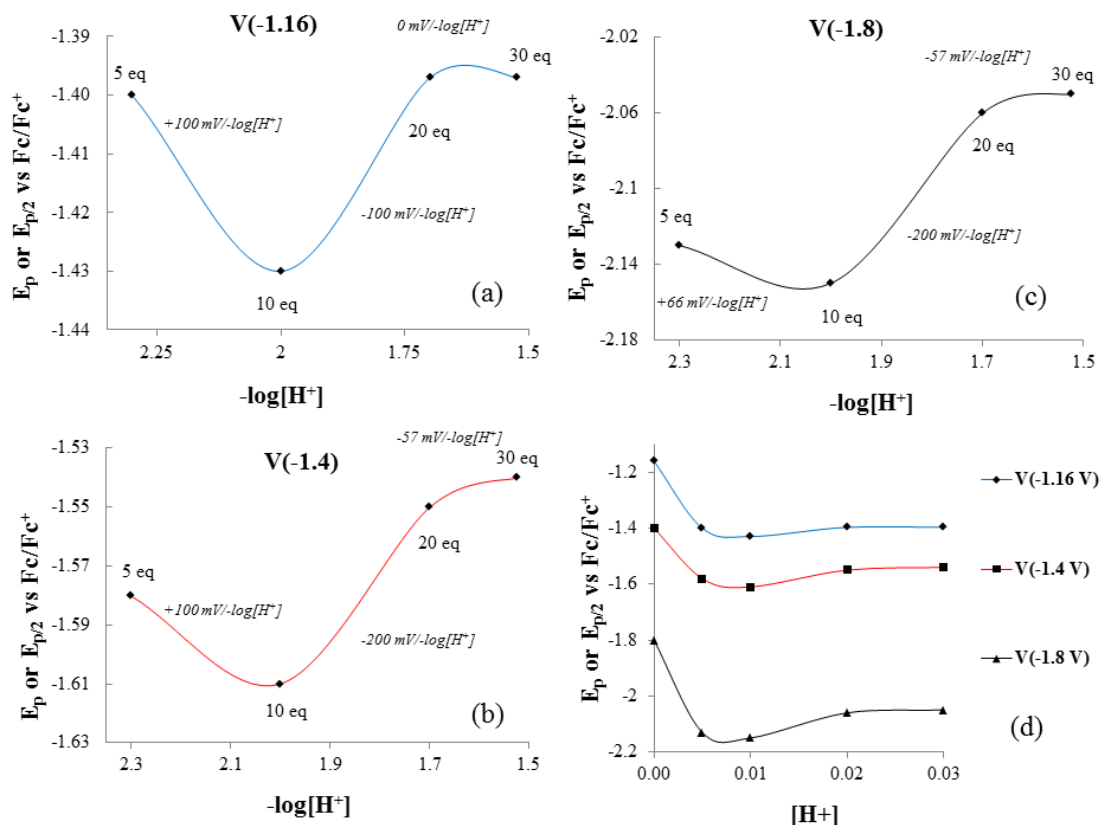


**Figure 5.19** Shifts in  $E_p$ , for one electron peaks, and  $E_{p/2}$  the catalytic peak, with the  $-\log[H^+]$  and increase in proton concentration for 1 mM **CoL3N** at a GCE electrode in acetonitrile, with 0.1 M TBABF<sub>4</sub> electrolyte. Where  $[H^+]$  = concentration of acetic acid. The equivalents of acid are shown as labels at the corresponding points, and the gradients of the lines are shown in *italics* for each section.

**Figures 5.19a to c** show the trends in potential for the three reductions independently, plotted against  $-\log[H^+]$ , with slopes in mV per  $-\log[H^+]$  annotated. Of these, those with a response to acid of *ca.* 60 mV per  $-\log[H^+]$  are likely to be associated with “normal”, one electron one proton PCET processes. However, the initial shifts in potential that occur from addition of 0 to 20 equivalents of acid are less easily explained – at 100 mV per  $-\log[H^+]$  or 200 mV per  $-\log[H^+]$  they do not correspond perfectly to two proton one electron (120 mV per  $-\log[H^+]$ ) or three proton one electron (180 mV per  $-\log[H^+]$ ) PCET, and it is also hard to justify transfer of such large numbers of protons. Thus, they may result from protonation dependent structural changes to form species which accept electrons at a different potential, thereby giving rise to large shifts. Paramagnetic  $^1\text{H}$ -NMR of **CoL3N** in the resting 2+ oxidation state in the presence of 170 mM and 340 mM of  $d^6$ -acetic acid is shown in **figure 5.20**. As the NMR spectrum remains almost constant with no new features present a negative ppm, this indicates there is no major change in structure in the resting 2+ oxidation state in the presence of a proton source – the other

cobalt complexes with different geometries show very different paramagnetic  $^1\text{H}$ -NMR spectra to **CoL3N** (see Chapter 3). Thus, the change in geometry can only occur after reduction.

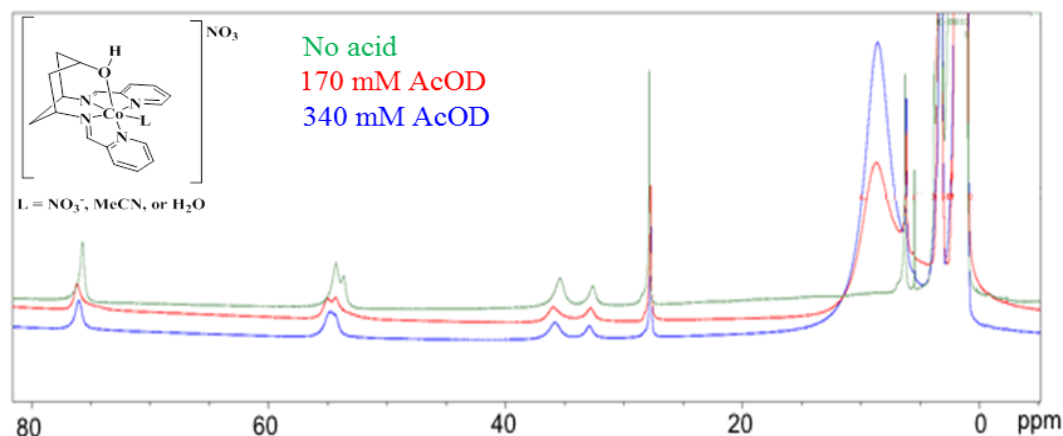


**Figure 5.20** Paramagnetic  $^1\text{H}$ -NMR of (**CoL3N**) in the resting  $2+$  state in acetonitrile sat.  $\text{TBABF}_4$  in the presence of 0 mM, 170 mM and 340 mM  $d^6$ -acetic acid.

From electrochemical data, the DFT studies shown in **section 4.4.6** and the analysis of the energetics of octahedral versus trigonal prismatic geometries (**section 3.3**) it can be postulated that at low and high acetic acid concentration, one ligand most probably the bound nitrate (or other coligand) of the cobalt(II) complex remains on reduction, giving a cobalt(I) species with the 5-coordinate pseudo square based pyramidal geometry seen from DFT.<sup>213</sup> On further reduction to a cobalt(0) species, work with other cobalt imine complexes and weak proton sources has shown that cobalt(II) hydrides result if the acid is strong enough to protonate the cobalt(0) centre.<sup>86</sup> In these published systems, this then leads to hydrogen evolution - either by bimolecular combination of two cobalt(II) hydride species, or via protonation of the metal hydride. On this basis, two main mechanisms have been proposed for proton reduction by **CoL3N**, at two concentration ranges of acid as illustrated in **figure 5.21**. Although it has subsequently been discovered that the primary catalytic pathway for **CoL3N** under the conditions used in this thesis is likely to be a reduction of solvent (acetonitrile), the initial steps leading to formation of a  $\text{Co}^{\text{II}}\text{-H}$  species are likely to still be relevant to this process.

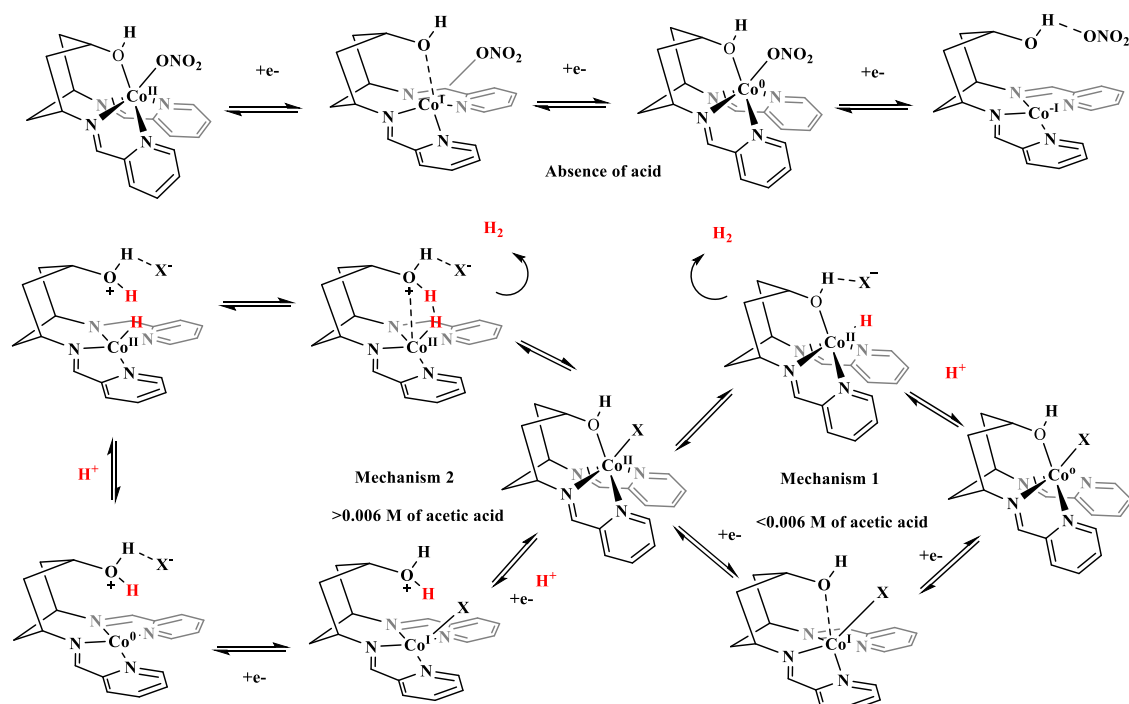


**Figure 5.21** Proposed mechanism of CoL3N in the presence of low and high concentrations of acetic acid

**Mechanism 1:** at low acid concentrations, below *ca.* 0.006 M of acetic acid, it can be proposed that the trigonal prismatic geometry largely remains, and the cobalt is reduced to give a cobalt(I) centre, which gives the pseudo square based pyramidal geometry seen from DFT. Reduction of this to the cobalt(0) species, then gives back the trigonal prismatic geometry, with the proximal hydroxyl bound. It can then be postulated that with loss of nitrate this can then be protonated by the weak acetic acid giving a cobalt(II) hydride species. This would either give hydrogen via bimolecular combination of two cobalt(II) hydride species, or via protonation of the metal hydride.

**Mechanism 2:** at high acid concentrations the large changes in potential suggest a large change in geometry of the complex, it can be suggested that the large change in structure of the complex on its reduction in the presence of *ca.* 0.006 M of acetic acid is most likely to be from a change in the resting state trigonal prismatic geometry to an octahedral or a pseudo square based pyramidal geometry comparable to that found in the copper(II) complex of the same ligand set **CuL3N**. This change in coordination would be encouraged by protonation, or more likely (given the high pK<sub>a</sub> of acetic acid), hydrogen bonding of the hydroxyl oxygen to acetic acid, weakening its ability to coordinate to Co. The resulting de-coordination of the hydroxyl would account for the more positive



reduction potentials as less electron density is donated to Co. As in **mechanism 1**, reduction of the Co(II) to the Co(I) species would give a pseudo square based pyramidal geometry as in the DFT. On further reduction to the Co(0) species however, the square pyramidal or square planar geometry would remain due to protonation (or hydrogen bonding) of the proximal hydroxyl. The proximal hydroxyl can then act as a proton relay, transferring the proton to the Co(0) metal centre forming a Co(II) hydride as found in other cobalt imine complexes with a weak proton source. This would either give hydrogen via bimolecular combination of two cobalt(II) hydride species, or via protonation of the metal hydride, which may be transferred via the proton relay. Re-coordination of the hydroxyl would aid the elimination of hydrogen and the regeneration of the catalyst, acting as a hemi-coordinate ligand.

### Propane-backbone complex: CoL4N

Although the main focus of this thesis is on the properties of the complexes of **L1**, **L2** and **L3**, with cyclohexane based backbones, as described in **chapter 3**, a cobalt complex with the same iminopyridine donor set and anion but with a propane backbone, **CoL4N**, was also synthesised. This allows investigation into the effects of the added rigidity and steric bulk provided by the cyclohexane on the electrochemistry and electrocatalysis.

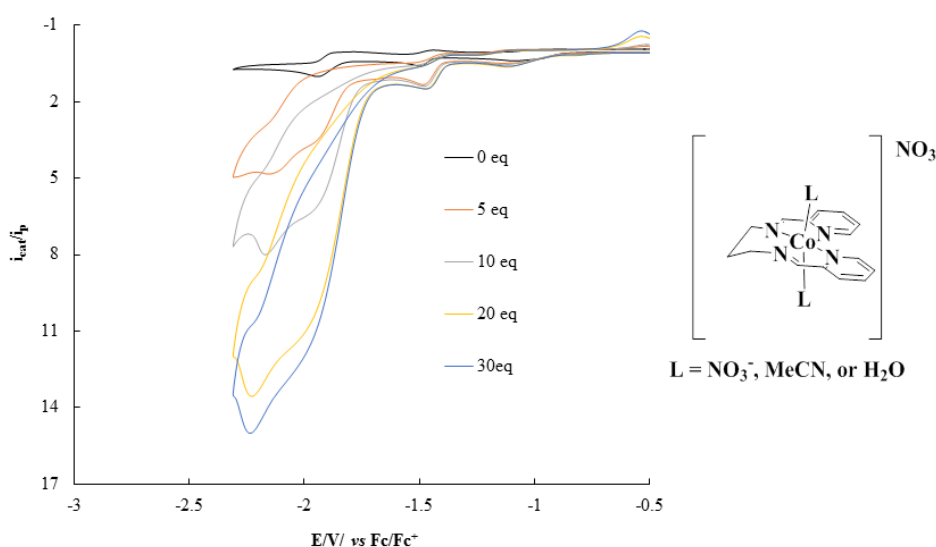


**Figure 5.22** Current normalised electrocatalytic response of 1 mM **CoL4N** in acetonitrile, in the presence of increasing equivalents of acetic acid, at a GCE.

**Figure 5.22** shows the electrocatalysis of proton reduction with **CoL4N**. In the absence of a proton source, **CoL4N** gives three reductive couples at  $E_{1/2} = -1.0, -1.44$  and  $-1.88$  V vs  $\text{Fc}/\text{Fc}^+$ . In **chapter 4** these were assigned to a ligand based process, followed by a largely metal based process ( $\text{Co}^{\text{II/I}}$ ) and a mixed ligand/metal based ( $\text{Co}^{\text{I/0}}$ ) respectively. In the presence of increasing quantities of acetic acid, the first reduction remains largely unperturbed indicating that the complex is stable under the conditions but shifts to more negative potential. The second reduction becomes irreversible, at *ca.*  $E_p = -1.46$  V vs  $\text{Fc}/\text{Fc}^+$ , and shifts to more positive potential. The third reduction splits into two overlapping peaks with large Faradaic currents with *ca.*  $E_p = -2.2$  V and  $-1.96$  V vs  $\text{Fc}/\text{Fc}^+$ . These increase in Faradaic current on increasing equivalents of protons, which is indicative of electrocatalytic proton reduction. These shifts in potential are most likely caused by acid dependent structural changes, as proposed for **CoL3N**, rather than PCET, as the shifts with proton concentration are not consistent with typical PCET mechanisms (i.e. 1 electron, 1 proton, 1 electron, 2 proton etc). Paramagnetic NMR shown in **section 3.5.4**, suggests intermediate behaviour in between trigonal prismatic and octahedral geometry seen in the other complexes. This could be caused by interconversion between the two geometries (**figure 5.23**), and presence of protons (or acetic acid) could influence the interconversion.

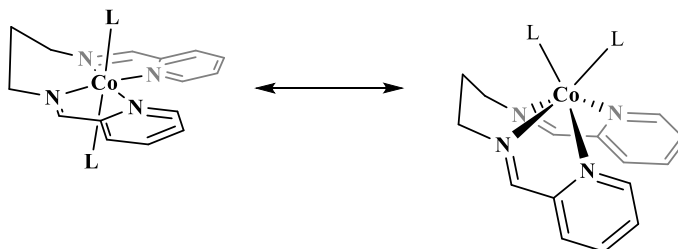


**Figure 5.23** Proposed exchange of geometry between trigonal prismatic and octahedral.

As all of the octahedral cobalt complexes with a cyclohexane backbone show a single catalytic wave, the split nature of the catalytic wave found in **CoL4N** may be caused by the above proposed fast exchange between octahedral and trigonal prismatic, and potential intermediate geometries. This would be facilitated by the more flexible propane backbone of **CoL4N**. Electrocatalytic waves from the different geometries would be expected to have different potentials, because of the difference in HOMO and LUMO energies caused by the different d-orbital splitting for the different geometries. This requires further experimentation to determine the exact cause, but it is worth noting that

pH controlled trigonal prismatic/octahedral switching has previously seen in dinuclear cobalt(II) complexes,<sup>214</sup>

### Summary of Catalytic Performance – Nitrate Complexes on GCE

Although direct acid reduction on GCE at acetic acid concentrations of greater than 0.04 M prevented from going to a higher acid regime to and pseudo first order conditions to give  $\text{TOF}_{\text{max}}$  for **CoL1N**, **CoL2N**, and **CoL3N**. Certain patterns in performance are found. It can be seen from **figure 5.24** and **table 5.3**, that **CoL4N** has both the lowest overpotential for the reductive process and the fastest turn over rate at a certain concentration of protons. However, it reaches proton saturation at much lower proton concentration than the other three complexes. It can also be seen that **CoL1N**, has comparable overpotential to **CoL4N**, but the slowest turn over rate of all of the catalysts described. **CoL3N** has the highest overpotential for the catalytic process, which is likely to be a consequence of the proximal hydroxyl group donating electron density to the metal centre, making it harder to reduce.

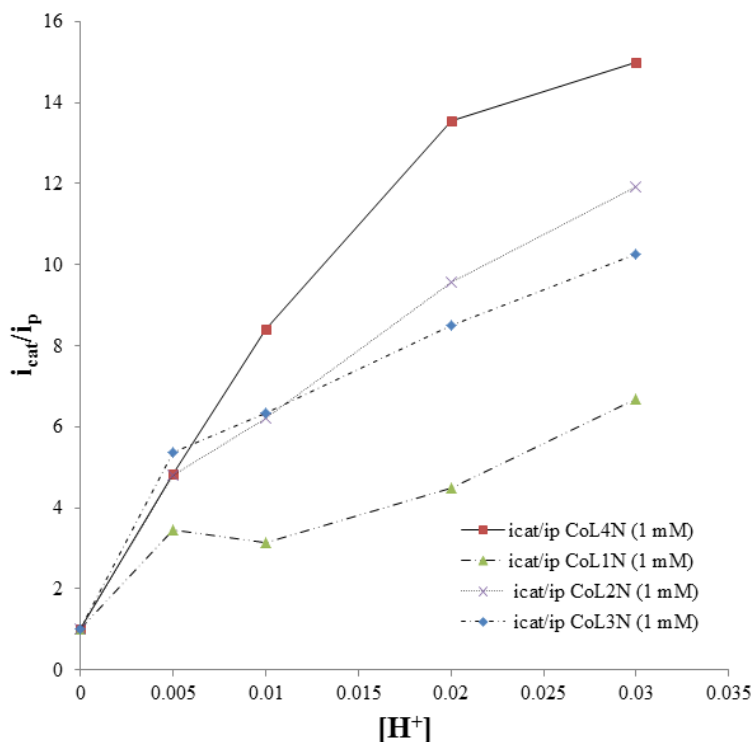


**Figure 5.24** Overlaid,  $i_{\text{cat}}/i_p$  versus  $[\text{H}^+]$  ( $[\text{H}^+] =$  acetic acid concentration) for **CoL4N**, **CoL1N**, **CoL2N** and **CoL3N** in the presence of increasing equivalents of acetic acid. Data taken from cyclic voltammograms shown in **figures 5.16 – 5.18** and **5.22**.

**Table 5.3** Overpotentials,  $\eta$ , for cobalt nitrate complexes in the presence of 0.02 M acetic acid at a 0.07 cm<sup>2</sup> GCE electrode. With the homoconjugation compensated thermodynamic potential of acetic acid,  $E_{H^+} = -1.23$  V vs Fc/Fc<sup>+</sup>. Data taken from cyclic voltammograms shown in **figures (5.18-21)**.

	$E_{cat/2}$ / V	$\eta$ / mV
<b>CoL4N (1 mM)</b>	-1.85	620
<b>CoL1N (1 mM)</b>	-1.85	620
<b>CoL2N (1 mM)</b>	-1.88	650
<b>CoL3N (1 mM)</b>	-2.06	830

### 5.3.2 Electrocatalysis using cobalt complexes at GCE – Tetrafluoroborate complexes

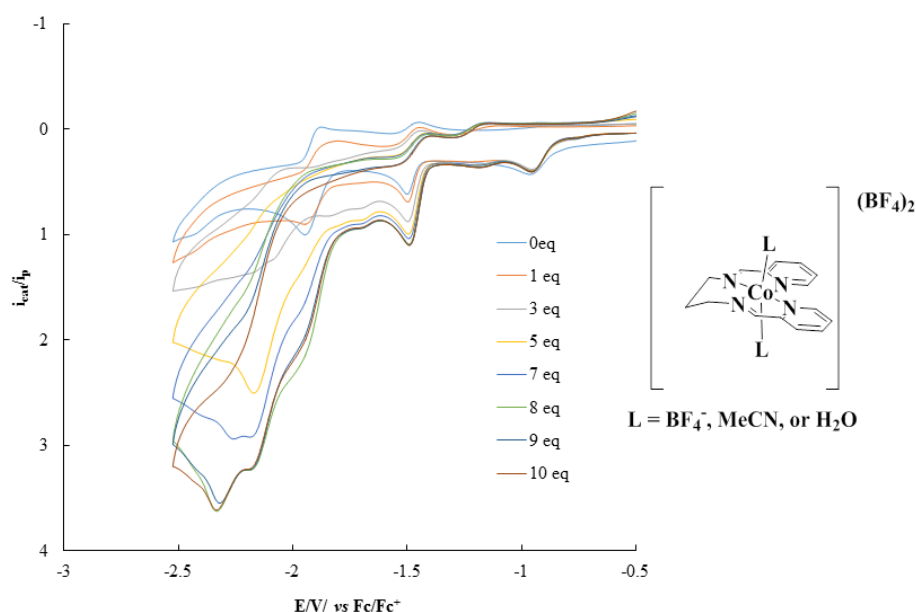


**Figure 5.25** Current normalised electrocatalytic response of 1 mM **CoL4B** in acetonitrile, in the presence of increasing equivalents of acetic acid, at a GCE.

The electrocatalytic behaviours of **CoL4B**, **CoL1B**, and **CoL3B** from **figures 5.25** to **5.27** respectively, are comparable to those seen for the nitrate based complexes. However, they generally have slightly lower overpotentials,  $\eta$ . **CoL4B** and **CoL1B** have an additional peak present within the main catalytic wave, this may be due to the added degree of coordinational freedom resulting from a completely non-coordinating anion, or due to coordination of acetate from the added acid. **CoL3B** on the other hand has almost identical electrochemical behaviour to **CoL3N**. All the tetrafluoroborate complexes,

however, reach pseudo first order conditions (i.e. a plateau in  $i_p$  as acid is added at much lower proton concentrations (0.01 M acetic acid) than do the nitrates (**figure 5.30**).

Overpotentials and turnover frequencies are summarised in **table 5.4**. This information enables a plot of  $\text{Log}(\text{TOF})$  vs  $\text{Log}(\eta)$  at 0.02 M acetic acid (**figure 5.31**) as a means to compare the activity of the complexes. The lower the  $\text{Log}(\eta)$  (overpotential) the lower the energy required to drive the catalyst, and the higher the  $\text{Log}(\text{TOF})$ , i.e. the turn over frequency, the faster the catalyst. Therefore, catalysts at the top left of the graph are the best, and poorer catalysts are situated towards the bottom and the right.

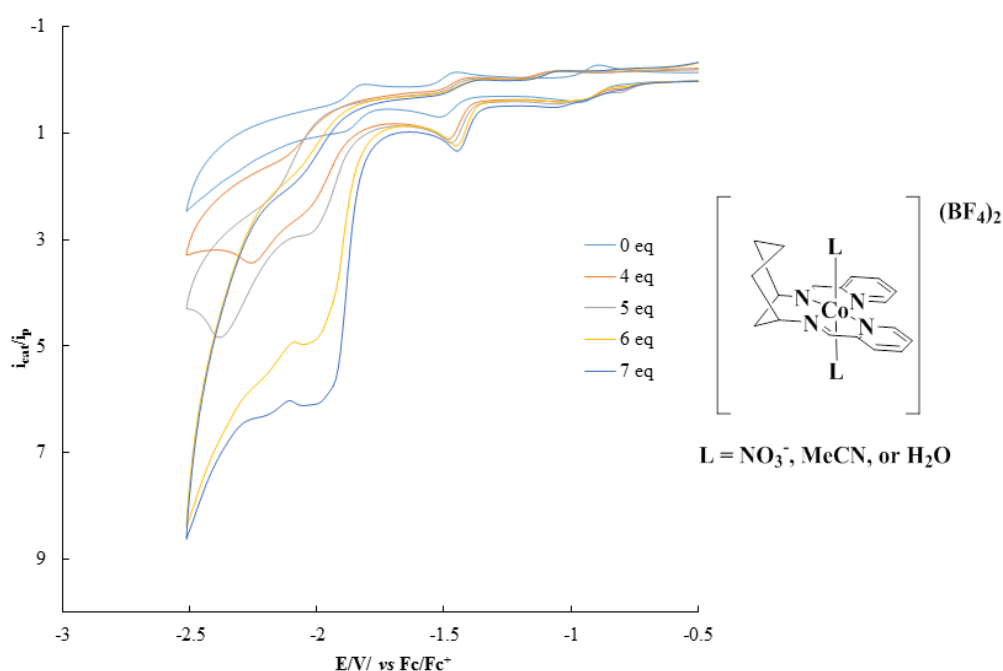


**Figure 5.26** Current normalised electrocatalytic response of 1 mM **CoL1B** in acetonitrile, the in presence of increasing equivalents of acetic acid, at a GCE.

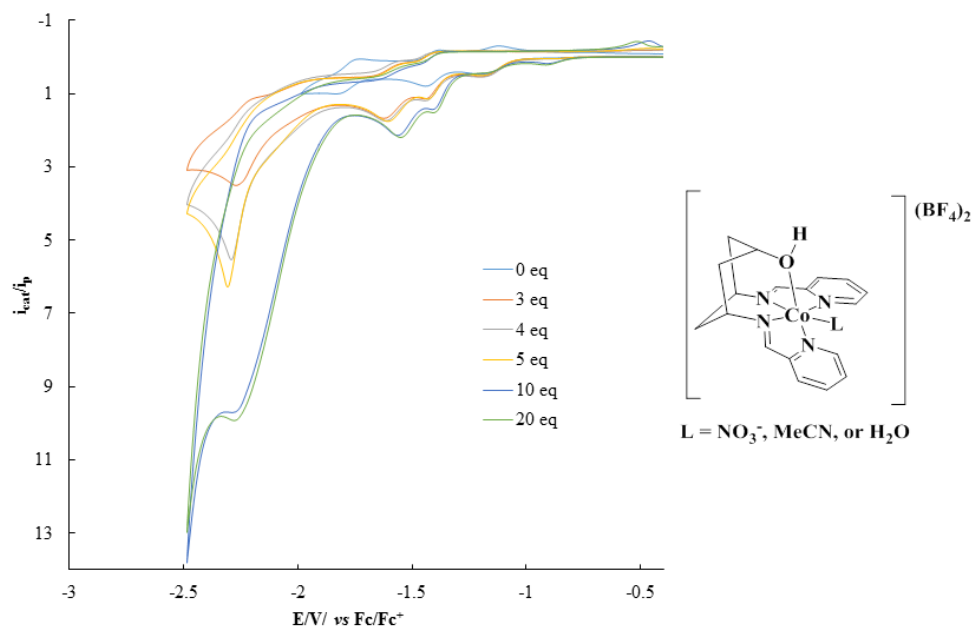


**Figure 5.27** Current normalised electrocatalytic response of 1 mM **CoL3B** in acetonitrile, in the presence of increasing equivalents of acetic acid, at a GCE.

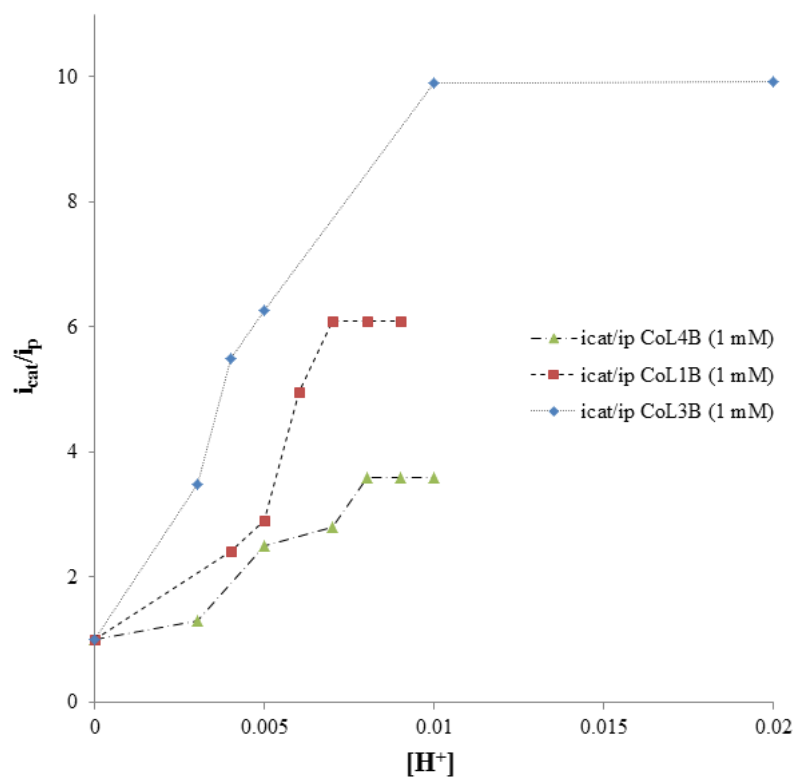


**Figure 5.28** Overlaid,  $i_{cat}/i_p$  versus  $[\text{H}^+]$ ,  $[\text{H}^+] =$  acetic acid concentration for 1 mM **CoL4N**, **CoL1N**, **CoL2N** and **CoL3N** in the presence of increasing equivalents of acetic acid. Data taken from cyclic voltammograms shown in **figure 5. 25 – 5.27**.

**Table 5.4** Overpotentials,  $\eta$ , for cobalt nitrate complexes in the presence of 0.01 M acetic acid or at the  $[H^+]$  of  $TOF_{max}$ , at a 0.07 cm<sup>2</sup> GCE electrode. With the homoconjugation compensated thermodynamic potential of acetic acid,  $E_{H^+} = -1.23$  V vs Fc/Fc<sup>+</sup>. Data taken from cyclic voltammograms shown in figures 5.27 to 5.29.

	$E_{cat}/2$ /V vs Fc/Fc <sup>+</sup>	$\eta$ / mV	TOF/s <sup>-1</sup>
<b>CoL4B (1 mM)</b> ( $TOF_{max} [H^+] = 0.01$ M)	-1.91	680	3
<b>CoL1B (1 mM)</b> ( $TOF_{max} [H^+] = 0.007$ M)	-1.87	640	7
<b>CoL3B (1 mM)</b> ( $TOF_{max} [H^+] = 0.01$ M)	-2.04	810	19

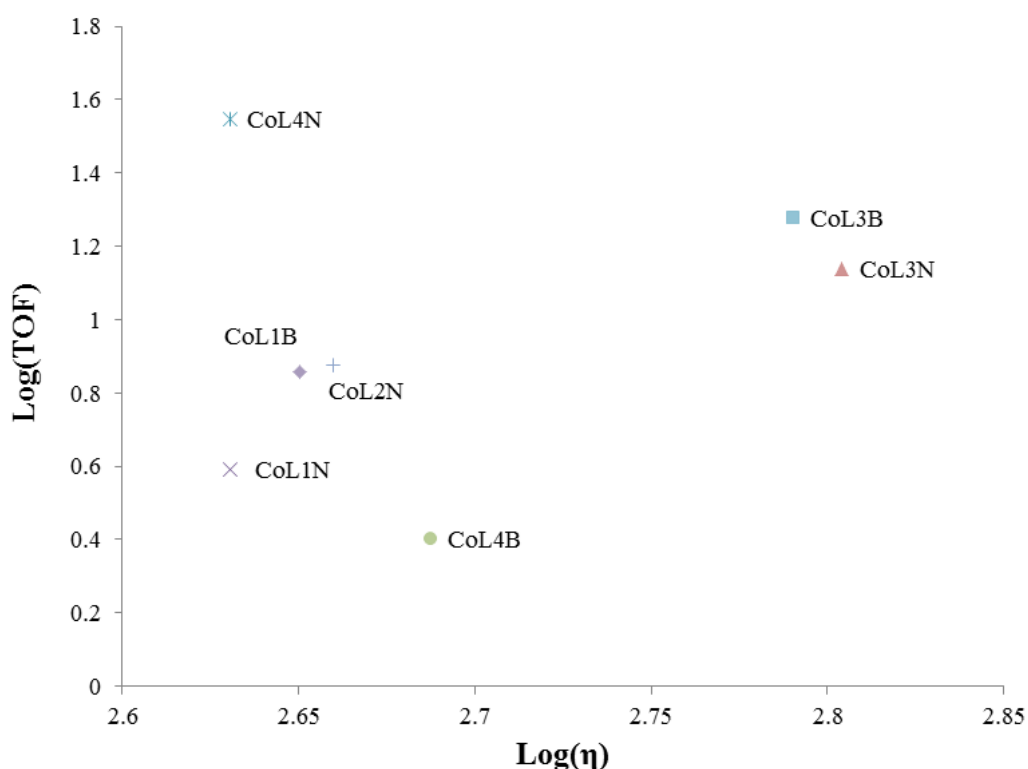


**Figure 5.29** Plot of Log(TOF) vs Log( $\eta$ ) at 0.02 M acetic acid or at  $TOF_{max}$  for 1 mM cobalt  $NO_3^-$  or  $BF_4^-$  complexes. Data taken from Table 5.3 and 5.4.

From figure 5.29 it can be seen that **CoL4N** is the best of the catalysts at 0.02 M of acetic acid. This suggests that the increase in flexibility of a catalyst helps to increase the TOF, this may be due to its ability of access a range of coordination modes and relax steric strain. Interestingly, the  $BF_4^-$  salt of the same complex, **CoL4B**, shows the worst activity, having one of the highest overpotentials and the lowest turn over frequencies. This suggests that the nitrate anion is actively helping catalysis, either by its involvement in the catalytic steps or by stabilisation of the complex, the latter being the most likely of

the two. This is because the tetrafluoroborate complexes tend to show ligand hydrolysis under standard conditions after a week, whereas the equivalent nitrate complexes can be kept indefinitely as solids in air. It could be expected that under highly reducing conditions in the presence of a proton source that this vulnerability to hydrolysis may increase and it is possible that interaction with nitrate in solution has a stabilising effect.

One thing unaccounted for is the stability of the complexes: **L4** complexes show the least stability followed by the **L1** and **L2**, with the most stable being the **L3** complexes. This was seen from the tendency of **L4** complexes to deposit on the electrode during the experiment, and to a lesser extent the complexes of **L1** and **L2**. However, **L3** complexes usually gave good data with minimal electrode fouling. Thus, the **L3** complexes show comparable activity with both anions and group together in **figure 5.31**. Interestingly **CoL1N**, **CoL1B**, and **CoL2N** are shown to have comparable electrocatalytic behaviour. As the fundamental ligand frameworks of the complexes are the same, the only things different between them are the distal hydroxyl in the cyclohexane backbone and the nitrate or tetrafluoroborate. The distal hydroxyl in the case of the nitrate complexes appears to stabilise the metal nitrate bond in the solid state, with the nitrate still bound on the side of the complex closest to the hydroxyl in the X-ray structure. This could be conceivably through H-bonding interactions with the nitrate. The results from **CoL1B** and **CoL2N** suggest that the distal hydroxyl has little or no effect on the turnover frequency at 0.02 M acetic acid concentration, and its effect on overpotential (*ca.* 10 mV increase) is within likely experimental errors. In all of the tetrafluoroborate complexes however, substrate saturation (pseudo 1st order conditions) were seen at low acid concentrations of 0.01 M (10 eq) however, in the nitrate complexes the substrate saturation concentration is found to far surpass this. However, this creates difficulties as at high concentrations of acetic acid direct acid reduction overlaps with the catalytic wave of the catalyst. This is shown in **figure 5.30**, illustrated by the growth of an additional peak at 40 eq (0.04 M) of acetic acid. **Figure 5.31** illustrates the electrocatalytic response of a GCE with and without **CoL2N** at the same concentrations of acetic acid. At low acid concentration there is little or no overlap between the direct acid reduction and the catalytic wave. However, as the concentration of acid increases the direct acid wave shows an increase in Faradaic current and a positive shift in potential. This means at higher acid concentrations (0.04 M) on GCE the direct acid reduction overlaps with that of the catalytic wave of the catalyst. This means that determination of substrate saturation



and therefore  $\text{TOF}_{\text{max}}$  for catalysts that have saturation points higher than this cannot be achieved with satisfactory accuracy. This is due to GCE having some activity for the proton reduction reaction.

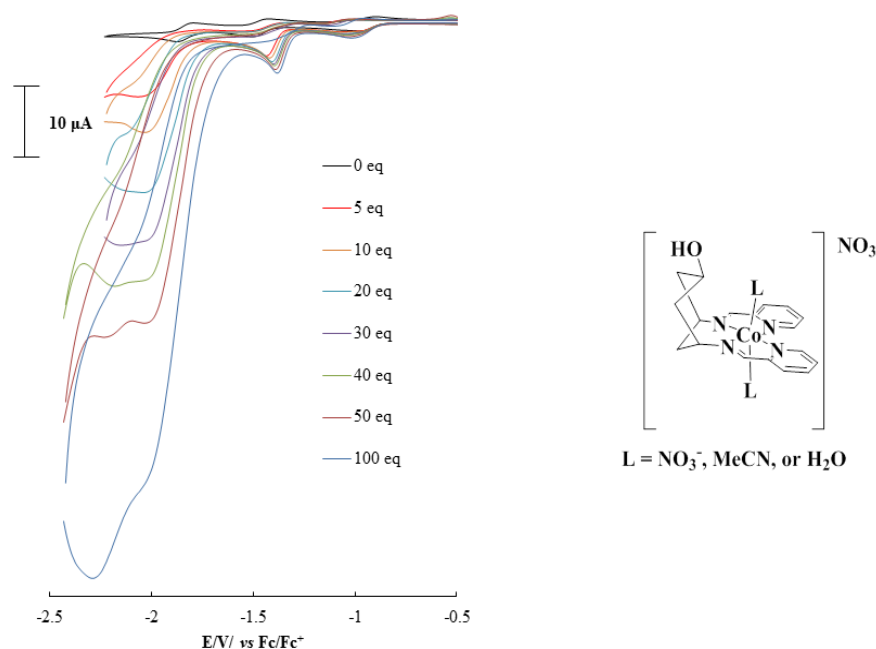


**Figure 5.30** Electrochemical response of 1 mM **CoL2N** in acetonitrile, with increasing equivalents of acetic acid, at a GCE and showing direct acid reduction overlap.

One way around this is to lower the concentration of the electrocatalyst, and therefore require a lower concentration of substrate to get to saturation pseudo first-order conditions. However, this needs to be within the detection limit of the electrode. Another is to change the working electrode surface to something with a larger overpotential and lower activity for proton reduction. Mercury has been shown to have a larger overpotential for proton reduction; however, it has problems associated with toxicity.<sup>215</sup> Moreover, the hanging mercury drop set up is expensive and unavailable at UEA, and we found the simple alternative of supporting a mercury drop on an Au electrode to be insufficiently stable in non-aqueous media in this system. An alternative carbon-based electrode surface, boron doped diamond (BDD) with additional benefits described below, was therefore chosen to study **CoL1N**, **CoL2N** and **CoL3N** under high acid concentrations, to give  $\text{TOF}_{\text{max}}$  under pseudo 1st order conditions.

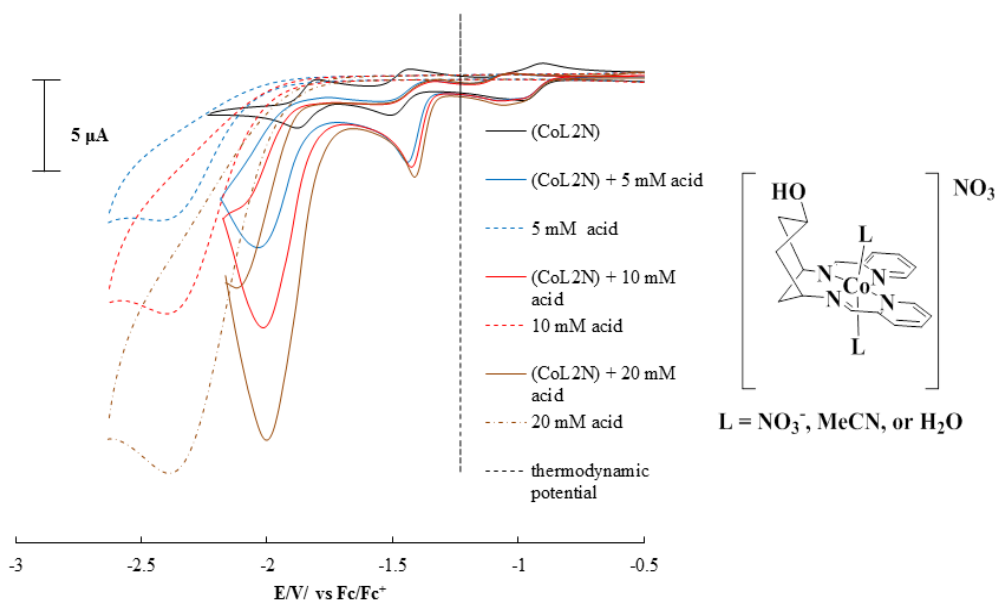


**Figure 5.31** Comparison of the electrocatalytic response of 1 mM  $\text{CoL}_2\text{N}$  vs acetic acid in acetonitrile, in the presence of increasing concentration of acetic acid, at a GCE.

#### 5.4.1 Boron Doped Diamond (BDD) background

Pure diamond is an insulator, however, the introduction of boron atoms into the diamond lattice of tetrahedral carbon atoms gives a p-type semiconductor, the boron atom inserts ‘holes’ into the structure due to its electron deficiency relative to carbon. Doping levels range from  $10^{18}$ - $10^{21}$  atoms  $\text{cm}^{-3}$ , the highest doping values give a *ca.* 1:100, boron to carbon ratio.<sup>216,217</sup> The conductivity of the BDD increases with increased doping due to the increase in number of boron acceptor states approximately 0.37 eV above the diamond valence band, as illustrated in **figure 5.32**.

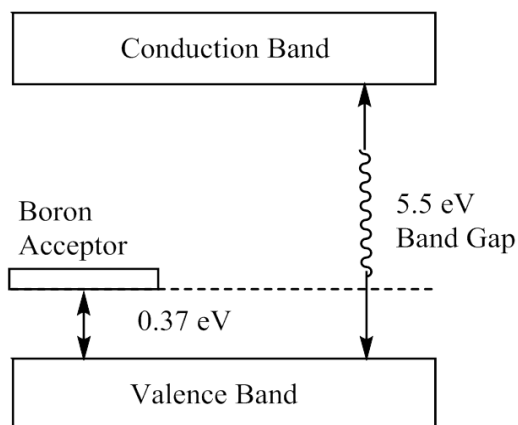


**Figure 5.32** Illustration of conduction and valence bands in boron doped diamond.

The electrical properties of BDD depend on a number of factors; on its boron doping level,<sup>218</sup> purity of the diamond and crystal orientation<sup>219</sup> and the surface termination.<sup>220-224</sup> BDD's have been shown to be a promising replacement electrode for dropping mercury electrode and other classical electrodes, as BDD has high chemical stability, a wide electrochemical window ( $>3$  V) and very low background currents.<sup>225</sup> At the highest levels of doping, at 1:100, boron to carbon ratio, films with a resistance  $< 0.1 \text{ } \Omega\cdot\text{cm}$  are achievable.<sup>226</sup>

BDD electrodes have very low background capacitance relative to other carbon based and metallic electrodes. Double-layer capacitance and background voltammetric currents are found to be an order of magnitude lower than observed for glassy carbon electrodes of the same geometric area. As a result signal-to-background noise is enhanced considerably, and detection limits may be reduced.<sup>227-229</sup> The low capacitance is attributed at H-terminated diamond electrodes to the relative absence of adsorbed species and carbon-oxygen functionalities that may be ionized.<sup>230</sup>

The electrochemical properties of BDD are largely dependent on the surface termination. The surface of an as-deposited BDD electrode is H-terminated, but this H-terminated surface is converted to an O-terminated surface on exposure to air, or an aqueous solution of a strong enough oxidiser.<sup>231-237</sup> The difference in carbon atom termination at the surface alters the kinetics of the redox reactions occurring at the surface due to the difference in electronic structure and surface energy between H-terminated and O-terminated surfaces. Therefore, it is important to match the electrode surface with the application. O-termination, for example, has a large hydrophilic surface area with a positive electron affinity favouring the formation of hydroxyl radicals ( $\bullet\text{OH}$ ) during anodic oxidation. It has however, a low electron transfer rate. H-terminated BDD electrodes have a hydrophobic low surface energy and negative electron affinity, with fast electron transfer.

238-240

Pre-treatment of the BDD electrode over time can lead to physical degradation, this is due to the pre-treatment methods acting to strip the boron doping from the electrode surfaces. Therefore the minimum cathodic pre-treatment needed for the electrochemical activation

of the BDD electrode, without producing any observable physical degradation, should be applied.<sup>241</sup>

#### 5.4.2 Electrochemistry with Boron Doped Diamond (BDD)

Prior to use in electrochemical experiments, boron doped diamond electrodes were activated by cycling the potential in aqueous 1 M HNO<sub>3</sub> between 0 and -3 V vs Ag/AgCl with stirring until stable reproducible curves were obtained (10 cycles with 0.1 V/s scan rate), to give a H-terminated electrode surface, as published by Bilewicz.<sup>242</sup>

**Figure 5.33** shows the comparison of the direct acid reduction of a high concentration 0.1 M at GCE and BDD in acetonitrile. It shows that at GCE  $E_p = -2.06$  V vs Fc/Fc<sup>+</sup> ( $i_{p/2} = -362$   $\mu$ A), and at BDD  $E_p = -2.29$  V vs Fc/Fc<sup>+</sup> ( $i_{p/2} = -70$   $\mu$ A), giving a 230 mV higher overpotential,  $\eta$ , at BDD, with 5 times less activity for proton reduction.

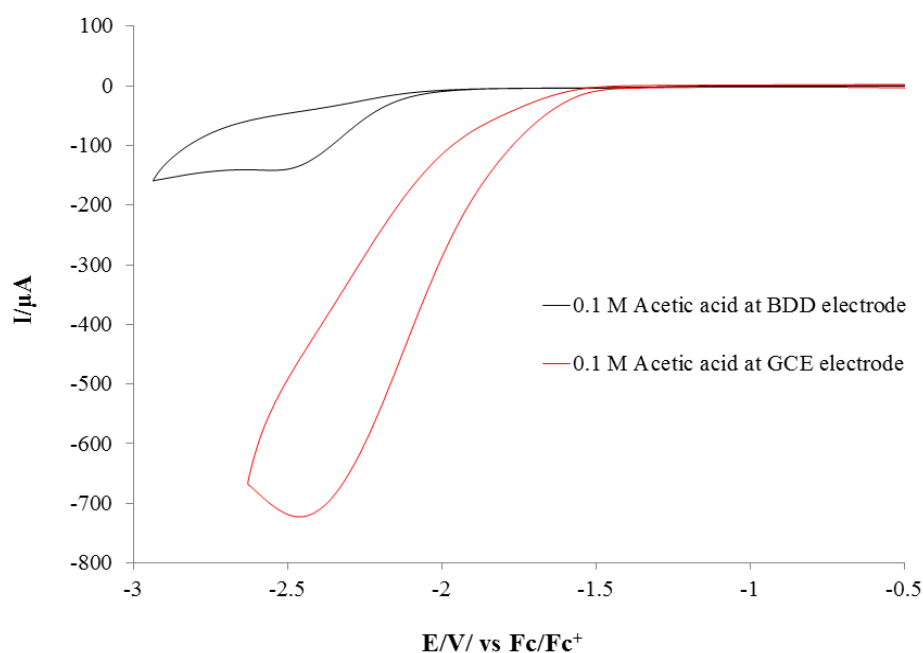


**Figure 5.33** Comparison of the direct acid reduction of 0.1 M acetic acid in acetonitrile at a GCE vs BDD with the same area (0.07 cm<sup>2</sup>).

The advantages of BDD electrodes; such as the smaller background currents, allowing analysis of smaller concentration of electrocatalysts, and the larger overpotential and lower activity for proton reduction have enabled the electrocatalytic studies of **CoL1N**,

**CoL2N** and **CoL3N** in the pseudo first order regime with respect to proton concentration and therefore determination of  $\text{TOF}_{\text{max}}$ .

### 5.5.1 Electrocatalysis of CoL1N, CoL2N and CoL3N at BDD electrode

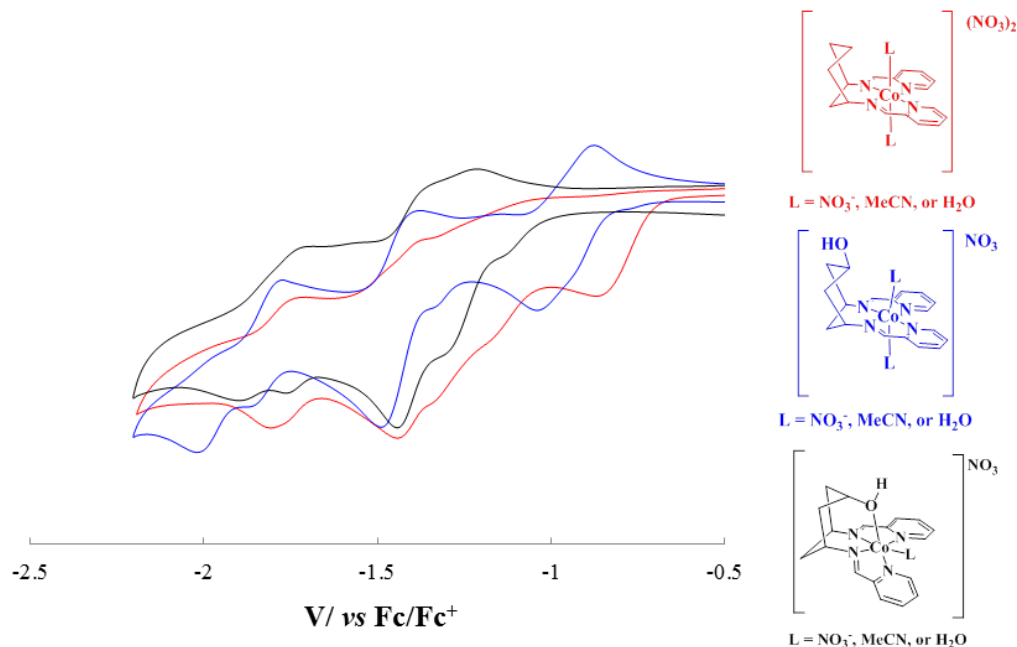


**Figure 5.34** Cyclic voltammetry of 0.1 mM **CoL1N** (red), **CoL2N** (blue), and **CoL3N** (black) in acetonitrile in the absence of a proton source at a 0.7 cm<sup>2</sup> BDD electrode, with 0.1 M TBABF<sub>4</sub> as electrolyte.

The redox behaviour of **CoL1N**, **CoL2N**, and **CoL3N** at 0.1 mM on BDD, as shown in **figure 5.34** is comparable to that on GCE at 1 mM in the absence of a proton source, giving roughly the same three one electron reductive couples. However, at 0.1 mM some splitting of last reduction in **CoL2N** and **CoL3N** is seen, this may be a consequence of concentration effects or residual water present within the acetonitrile. As at the lower concentration of complex, the equilibrium between water bound to the complex, and residual water in the acetonitrile will be pushed more to water bound to the metal centre.

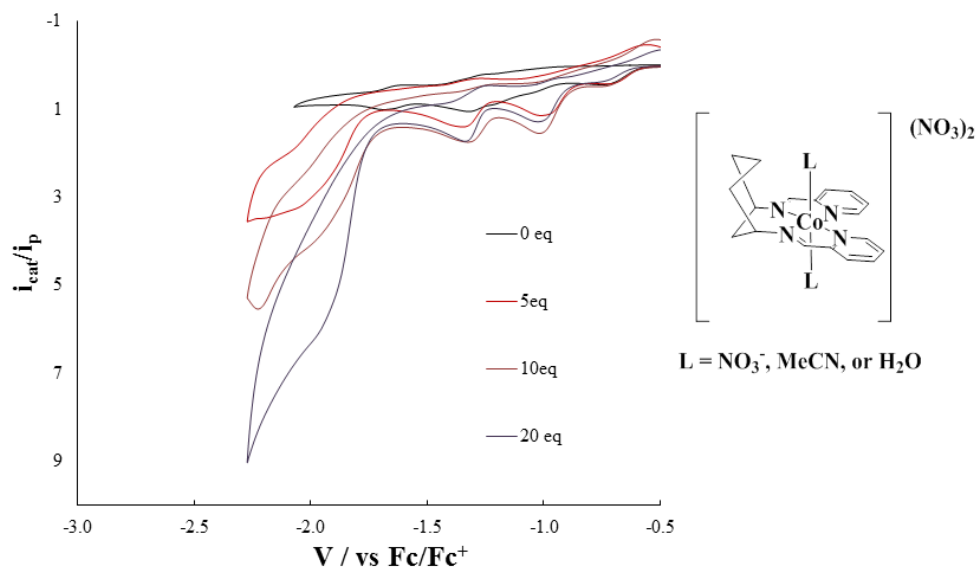


**Figure 5.35** Current normalised electrocatalytic response of 0.1 mM CoL1N in acetonitrile in the presence of increasing equivalents of acetic acid, at a BDD electrode.

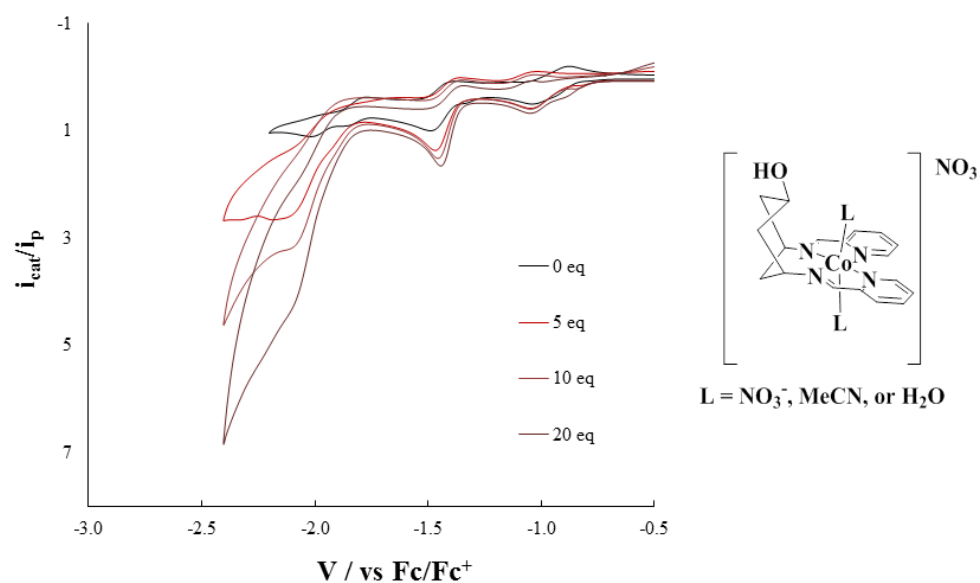


**Figure 5.36** Current normalised electrocatalytic response of 0.1 mM CoL1N in acetonitrile, in the presence of increasing equivalents of acetic acid, at a BDD electrode.

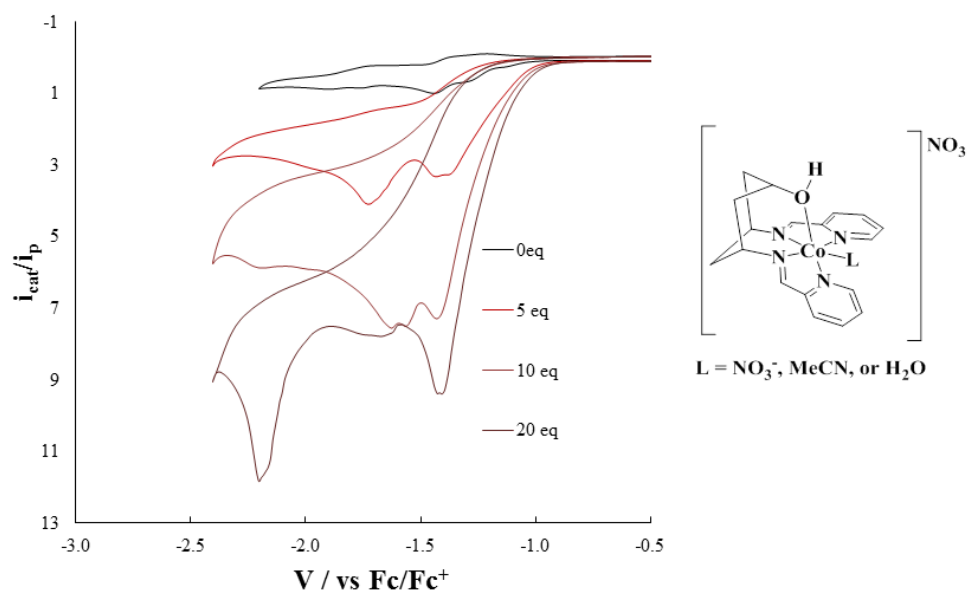


**Figure 5.37** Current normalised electrocatalytic response of 0.1 mM **CoL3N** in acetonitrile, the presence of increasing equivalents of acetic acid, at a BDD electrode.

As shown in **figure 5.35**, in the absence of a proton source, **CoL1N** gives three reductive couples at  $E_{1/2} = -0.85, -1.37$  and  $-1.77$  V *vs* Fc/Fc<sup>+</sup>. In **chapter 4** these were assigned to a ligand based process, followed by a largely metal based process (Co<sup>II/I</sup>) and a mixed ligand metal (Co<sup>I/0</sup>) respectively as for the other octahedral cobalt complexes. In the presence of 5 equivalents of acetic acid, the first reduction remains constant with increasing equivalents of acid at a potential  $-0.85$  V *vs* Fc/Fc<sup>+</sup>. The second reduction becomes irreversible, at *ca.*  $E_p = -1.48$  V *vs* Fc/Fc<sup>+</sup>, and shifts to more positive potential with increasing acid, with a shift symptomatic of PCET. The third reduction in the presence of acetic acid gives a large Faradaic current with *ca.*  $E_p = -2.2$  V *vs* Fc/Fc<sup>+</sup>. This increase in Faradaic current on increasing equivalents of protons suggests electrocatalytic proton reduction. This peak also shifts to more positive potential by 57 mV per  $-\log[\text{H}^+]$ , and as for the second reduction, is symptomatic and most likely caused by a one electron one proton PCET event.<sup>243,245</sup> Unlike at 1 mM, however, an additional wave is seen at  $-1.37$  V *vs* Fc/Fc<sup>+</sup> which remains roughly constant with increasing addition of acetic acid. It can be postulated that this additional wave is also a consequence of the effect of residual water on the lower concentration of the complex. The presence of an additional wave in the electrocatalytic studies of complexes in the presence intentionally added water at 1 mM on GCE has been seen in side studies of **CoL2N**, as illustrated in **figure 5.38**.

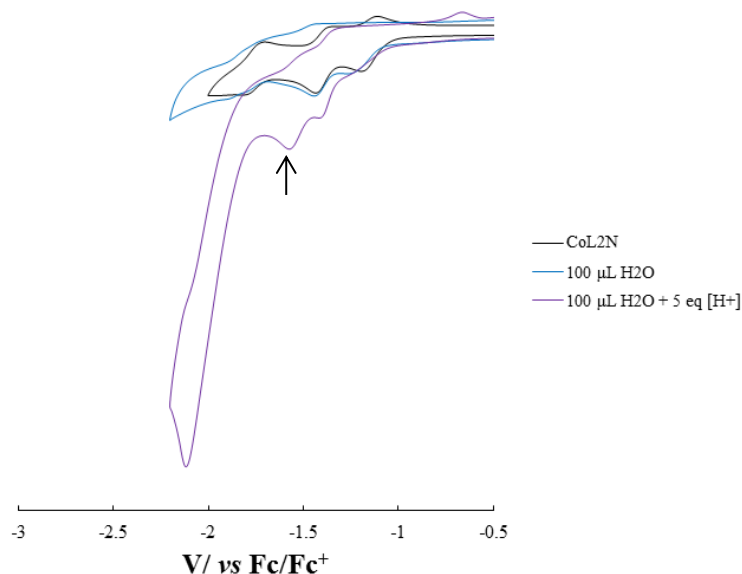


**Figure 5.38** Electrocatalytic response of 1 mM **CoL2N** in acetonitrile, the presence of 100  $\mu\text{L}$  of water, followed by 5 equivalents of acetic acid, at a GCE electrode. *The arrow illustrates the extra wave seen in the electrocatalytic response to protons with the addition of water.*

As shown in **figure 5.36**, the electrocatalytic behaviour for **CoL2N** is almost the same as found for **CoL1N**. In the absence of a proton source, **CoL2N** gives three reductive couples at  $E_{1/2} = -0.94, -1.45$  and  $-1.81$  V vs Fc/Fc<sup>+</sup>. In **chapter 4** these were assigned to a ligand based process, followed by a largely metal based process (Co<sup>II/I</sup>) and a mixed ligand metal (Co<sup>I/0</sup>) respectively as for the other octahedral cobalt complexes. In the presence of increasing equivalence of acetic acid, the first reduction remains largely unperturbed indicating that the complex is stable under the conditions but initially shifts to more negative potential by 110 mV with the addition of 5 eq of acetic acid. The second reduction becomes irreversible, at *ca.*  $E_p = -1.47$  V vs Fc/Fc<sup>+</sup>, and shifts to more positive potential by 53 mV per  $-\log[\text{H}^+]$ . From the thermodynamic Nernstian analysis, the redox potential of a reaction at 298 K involving  $m$  protons and  $n$  electrons shifts by  $m/n \cdot 0.059$  V per tenfold change in proton activity ( $\log[\text{H}^+]$ ).<sup>210</sup> Therefore, this shift is symptomatic and most likely caused by a one electron one proton PCET event.<sup>243</sup> From the DFT calculated HOMO and LUMO, analysis suggests that this is due to protonation and reduction of the metal centre presumably to give a metal hydride (Co<sup>II</sup>-H), as shown for similar cobalt electrocatalysts.<sup>246</sup> The third reduction in the presence of acetic acid gives a large Faradaic currents with *ca.*  $E_p = -2.01$  V vs Fc/Fc<sup>+</sup>. This increase in Faradaic current on increasing equivalents of protons suggests electrocatalytic proton reduction. This peaks also shifts to more positive potential by 59 mV per  $-\log[\text{H}^+]$ , this shift as for



the second reduction, is most likely caused by a one electron one proton PCET event.<sup>211,245</sup> **CoL2N** seems to be less sensitive to residual water at the lower concentration, as the electrocatalytic profile more closely reflects that at the higher catalyst concentration. This may be due to hydrogen bonding interactions of the distal hydroxyl group with the nitrate anion, which may favour having the nitrate bound to the cobalt metal centre.

As shown in **figure 5.37**, the electrocatalytic behaviour for **CoL3N** is different to that found for **CoL1N** and **CoL2N**. In the absence of a proton source, **CoL3N** gives three reductive couples at  $E_{1/2} = -1.16, -1.40$  and  $-1.80$  V *vs* Fc/Fc<sup>+</sup>. In **chapter 4** these were shown to be a largely metal based process (Co<sup>II/I</sup>) and two mixed ligand metal (Co<sup>I/0</sup>, L•-Co-L•) processes with more apparent ligand character for the last reduction.

In the presence of increasing equivalents of acetic acid, the first reduction ( $-1.16$  V), second reduction ( $-1.40$  V) and third reduction ( $-1.80$  V) all become irreversible.

Initially the peaks at  $E_{1/2} = -1.16, -1.40$  V *vs* Fc/Fc<sup>+</sup> shift to more negative potential and increase in Faradaic current with increasing concentration of acetic acid, until ca.  $0.016 - 0.02$  M of acetic acid, they reach ca.  $-1.40$  and  $-1.60$  V *vs* Fc/Fc<sup>+</sup> and decrease in Faradaic current. The peak at  $-1.80$  V, however, shifts to more positive potential and also increases in Faradaic current until it reaches ca.  $-1.60$  V merging with the second reduction, at ca.  $0.016$  M to  $0.02$  M of acetic acid where it decreases in current. At  $0.006$  M of acetic acid a catalytic wave at  $-2.2$  V is seen which increases with increasing acid and gives a large shift to more positive potential with increasing acid concentration until  $0.02$  M of acid where the catalytic current increases steadily at  $59$  mV per  $-\log[H^+]$ , (PCET) until the TOF<sub>max</sub> is reached at  $0.325$  M of acetic acid. This behaviour is comparable to that seen at  $1$  mM on GCE where there is a change shift in behaviour at  $0.006$  M and  $0.02$  M of acid, this therefore shows that this behaviour is independent on catalyst concentration and is only dependent on the concentration of acid present. An explanation for this behaviour is proposed in **section 5.31, Figure 5.21**.

**Table 5.6** Overpotentials,  $\eta$ , for cobalt nitrate complexes in the presence acetic acid taken at 0.02 M acetic acid concentraion, at a 0.07 cm<sup>2</sup> BDD electrode. With the thermodynamic potential of acetic acid,  $E_{H^+} = -1.23$  V vs Fc/Fc<sup>+</sup>. Data taken from cyclic voltammograms shown in **figures 5. 40** to **5.43**.

	$E_{cat/2}$ /V vs Fc/Fc <sup>+</sup>	$\eta$ / mV	TOF <sub>ma</sub> <sup>x</sup> /s <sup>-1</sup>
<b>CoL1N (0.1 mM) ( [H+] =0.02 M)</b>	-1.99	760	575
<b>CoL2N (0.1 mM) ([H+] =0.02 M)</b>	-1.95	720	8500
<b>CoL3N (0.1 mM) ([H+] =0.02 M)</b>	-2.00	770	28000

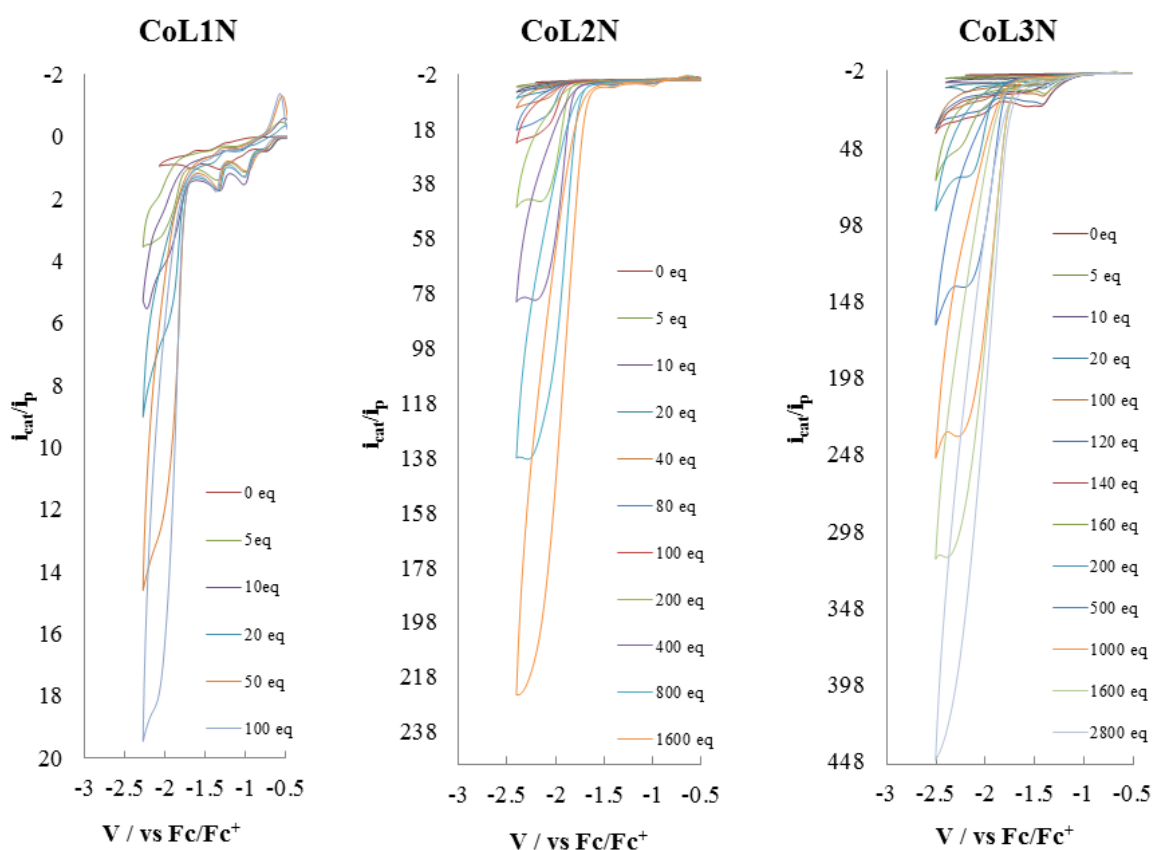


**Figure 5.39** Electrocatalytic response of 0.1 mM **CoL1N**, **CoL2N** and **CoL3N** in acetonitrile at a BDD electrode, the presence of increasing equivalents of acetic acid until pseudo first order conditions with respect to proton concentration is achieved.

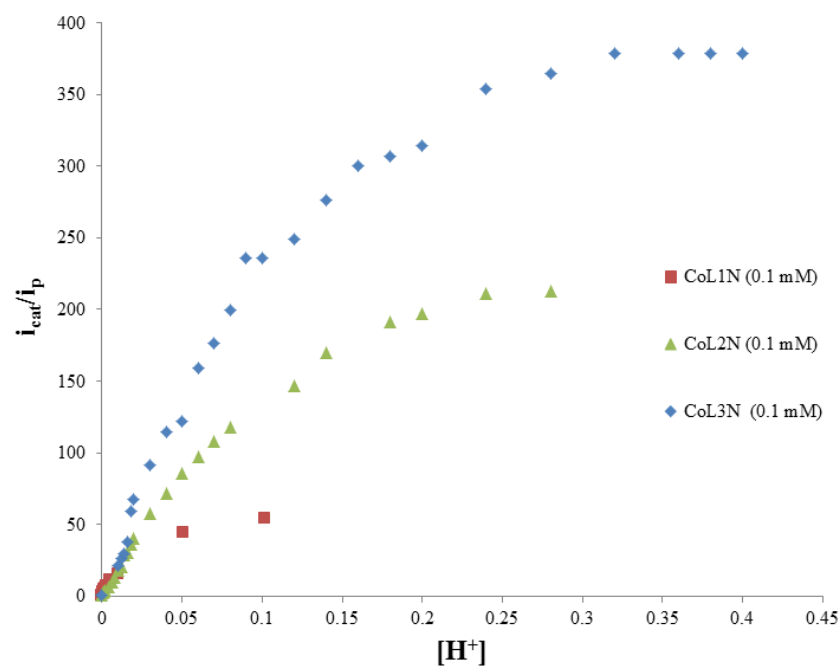


**Figure 5.40** Overlaid,  $i_{cat}/i_p$  versus  $[H^+]$ ,  $[H^+] =$  acetic acid concentration for 0.1 mM, **CoL1N**, **CoL2N** and **CoL3N** in the presence of increasing equivalents of acetic acid. Data taken from cyclic voltammograms shown in **figure 5.45**.

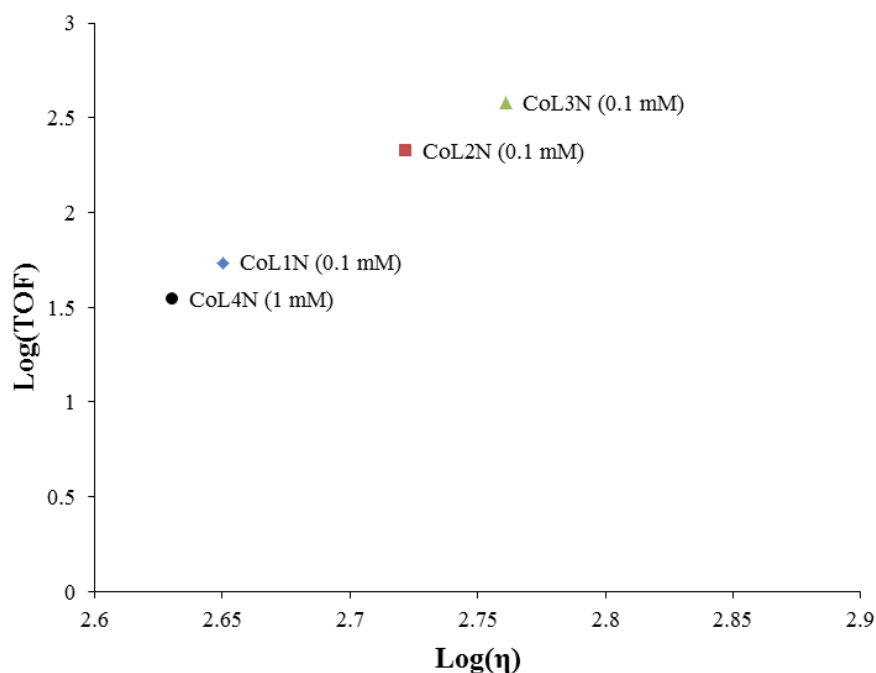


**Figure 5.41** Plot of  $\text{Log}(\text{TOF})$  vs  $\text{Log}(\eta)$  for **CoL4N** (1 mM), **CoL1N** (0.1 mM), **CoL2N** (0.1 mM), and **CoL3N** (0.1 mM), with  $\eta$  given at 0.01 M acetic acid and  $\text{TOF}_{\text{mas}}$  given at pseudo first order concentrations with respect to acetic acid. Data is taken from **table 5.3** and **table 5.6**. (Note: - **CoL4N** reaches  $\text{TOF}_{\text{max}}$  at 0.03 M  $[H^+]$  concentration, at this concentration on GCE there is confidence that little or no contribution from direct acid reduction is present, therefore data is used from 1 mM at GCE).

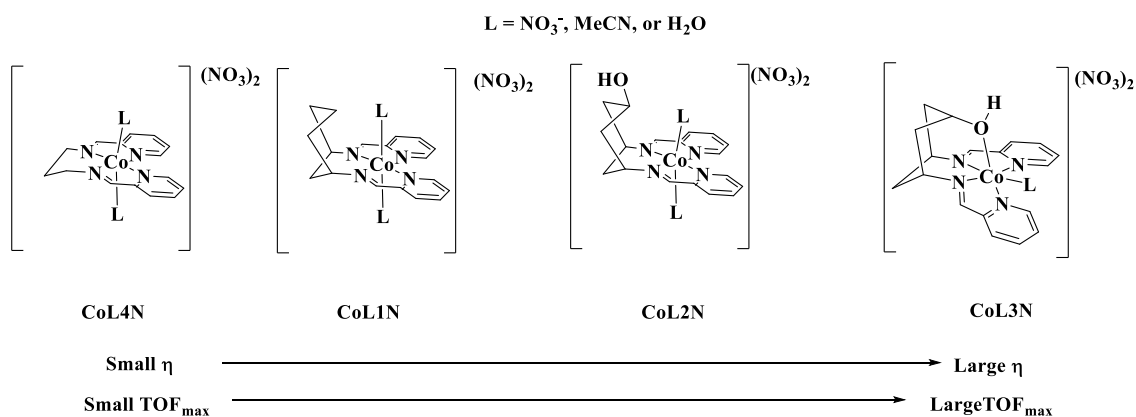


**Figure 5.42** Changes in catalyst structure and corresponding trends in catalytic parameters.

**Figure 5.41** shows the activity of **CoL4N**, **CoL3N**, **CoL2N**, and **CoL1N** in terms of overpotential and maximum turn over frequency (TOF) for catalytic response to protons (based on the originally presumed formation of  $\text{H}_2$ ). Although there are uncertainties in the precise nature of the catalytic process taking place, it is interesting to note an almost linear trend in  $\text{Log}(\text{TOF}_{\text{max}})$  vs  $\text{Log}(\eta)$  on going from **CoL1N** to **CoL3N**. **CoL4N** also seems to fit this trend, however as its  $\text{TOF}_{\text{max}}$  was determined at higher concentration it may not be directly comparable. These changes in catalytic parameters correlate well to the changes in the ligand structure, as illustrated in **figure 5.42**. As the *bis*-imino pyridine functionally remains constant for each complex, the governing factor is most likely the ligand backbone. Going from **CoL4N** with a propane backbone to **CoL1N** with a cyclohexane, the increase in overpotential may be explained in terms of the electron donating capacity of the ligand. The cyclohexane should donate more electron density to the nitrogens of the imino pyridines, therefore this would make the cobalt centre less electropositive and in turn make both the imino pyridine ligands and the cobalt centre harder to reduce. **CoL4N** shows the worst stability of the four catalysts and reaches pseudo first order conditions with respect to acid at *ca.* 0.03 M of acetic acid. Therefore, a possible reason for the increase in  $\text{TOF}_{\text{max}}$  is likely to be a consequence of the increased stabilisation from the increased steric bulk of the cyclohexane, increasing the complexes' stability to hydrolysis which is likely to be the main cause of deactivation. Another possibility may be that the increased rigidity of the cyclohexane could increase speed by minimising reorganisation energy and thus speeding electron transfer, as shown by Marcus theory.<sup>247</sup>

Going from **CoL1N** with a cyclohexane backbone to **CoL2N** with the cyclohexane and distal hydroxyl group, it is possible that the hydrogen bonding interactions between the distal hydroxyl and nitrate anions in solution may favour having one bound nitrate anion. Going from **CoL2N** with a distal hydroxyl to **CoL3N** with a proximal hydroxyl, it can be seen from **figures 5.40** and **5.39**, that **CoL3N** reaches pseudo first order conditions with respect to protons at ten times the acetic acid concentration of **CoL2N** and more than double that of **CoL1N** and **CoL4N** and therefore achieves a much higher  $\text{TOF}_{\text{max}}$  due to the added stability of the pentadentate over the tetradentate chelate, enabling the complex to reach a higher  $\text{TOF}_{\text{max}}$  before decomposition. Higher turn-over frequency may also be due to the proton relay effect as of the proximal hydroxyl group as described in **figure 5.21**. The increase in overpotential is likely to be caused by the proximal hydroxyl donating electron density to the cobalt centre and therefore making it less electropositive and therefore harder to reduce. Although for **CoL3N** it is shown below that the main catalytic process is not hydrogen evolution, formation of a cobalt hydride through the protonation of the metal centre is a likely key intermediate in any of the reductive processes occurring. Therefore, if the rate determining step is the protonation of the cobalt centre, then donation from the proximal hydroxyl may also favour this, by increasing the electron density on the cobalt, and therefore may have the effect of increasing the turn over rate.

#### 5.6.0 Bulk electrolysis using **CoL3N** catalyst at BDD electrode

Time did not allow for an in depth bulk electrolysis analysis of all the complexes. However initial results from the electrolysis of **CoL3N** at a BDD wafer are given. As **CoL3N** is the most stable of the catalysts and has the highest measured  $\text{TOF}_{\text{max}}$ , it was chosen for analysis.

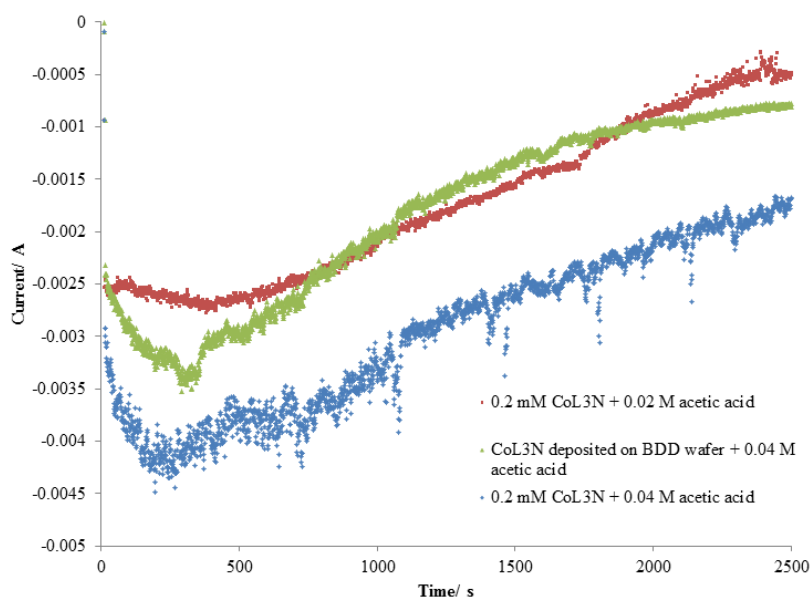


**Figure 5.43** Plot of chronoamperometry, current vs time for 0.2 mM **CoL3N** in acetonitrile with 0.02 M acetic acid at a 2.3 cm<sup>2</sup> BDD wafer (*red*), deposition product from bulk electrolysis of **CoL3N** in acetonitrile with 0.04 M acetic acid at a 2.3 cm<sup>2</sup> BDD wafer (*green*), 0.2 mM **CoL3N** in acetonitrile with 0.04 M acetic acid at a 2.3 cm<sup>2</sup> BDD wafer (*blue*)

### Bulk electrolysis 1

Bulk electrolysis of 1  $\mu\text{mol}$  **CoL3N** (concentration 0.2 mM) with 100  $\mu\text{mol}$  acetic acid for 2500 seconds (red trace in **figure 5.43**) at  $-2.3\text{ V vs Fc/Fc}^+$  (the  $E_p$  of the catalytic wave) gave 4.19 C of charge passed, equating to a theoretical  $2.17 \times 10^{-5}$  moles of  $\text{H}_2$  and consumption of *ca.* 43% of available protons. Direct calibration of the electrochemical cell under conditions without conducting electrolysis (injecting set volumes of hydrogen into the cell with electrolyte present, taking 150  $\mu\text{L}$  samples and injecting into a GC-TCD) gave a calibration of mV.s vs  $\text{H}_2$  volume in  $\mu\text{L}$  with the equation  $y = 0.854x + 79.543$  in the region of interest, where  $y$  is the GC-TCD response and  $x$  is the volume of hydrogen in the cell in  $\mu\text{L}$ . After electrolysis a 150  $\mu\text{L}$  sample of the headspace of the electrochemical cell was taken giving a GCE-TCD response of 110.7 mV.s, equating to 36.484  $\mu\text{L}$  of  $\text{H}_2$ , and thus  $1.629 \times 10^{-6}$  moles of  $\text{H}_2$  using the ideal gas equation. This gives a TON of 1.63, and a faradaic efficiency of 7.5% for hydrogen production. These results suggested that either the cell was not sealed correctly, or as the experiment time is relatively long, hydrogen was dissolving in the counter compartment and being re-oxidised by the platinum counter electrode, or that hydrogen production is not the main

catalytic process, as the catalytic current seen from cyclic voltammetry and the amount of charge passed in bulk electrolysis are far larger than the amount of hydrogen produced.

## **Bulk electrolysis 2**

Alterations to the 3-component cell were made to close the working compartment headspace from the counter electrode, and therefore prevent any reoxidation of hydrogen produced at the working electrode. Leak testing of the cell was also undertaken by injecting a certain volume of hydrogen in to the cell, and sampling after 15 and 30 mins. This gave negligible change in the GC response and therefore eliminated any hydrogen leak. Leak test of the set up after the bulk electrolysis run was also undertaken and showed a loss of H<sub>2</sub> of less than 5% in the 30 minutes after the end of the experiment. The previous reference electrode (Ag wire segregated by a frit) was replaced with a Metrohm non-aqueous Ag/AgCl reference electrode to eliminate problems with potential drift. Calibration of this cell with reduced headspace gave a relationship of mV.s vs injected H<sub>2</sub> volume in  $\mu\text{L}$  with the equation  $y = 1.973x + 91.633$  in the range relevant to the experiment. Where y is the GC-TCD response and x is the volume of hydrogen in the cell in  $\mu\text{L}$ .

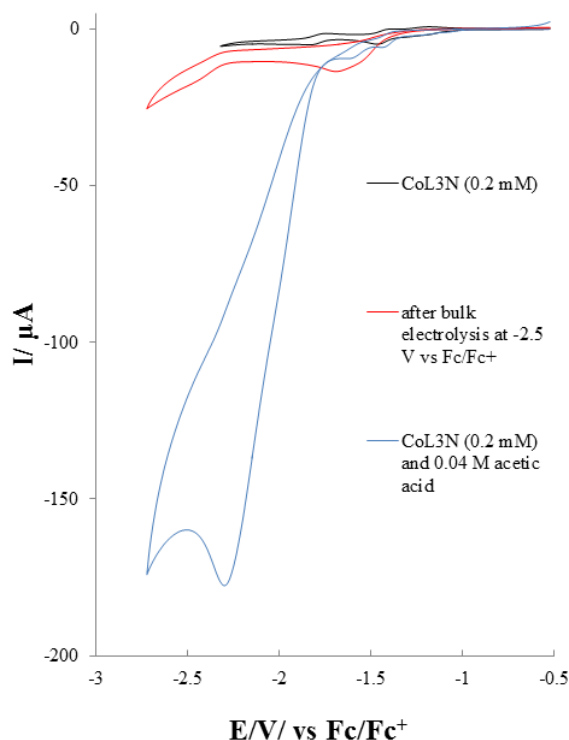


**Figure 5.44** Electrocatalytic response of 0.2 mM **CoL3N** in acetonitrile at a BDD voltammetry electrode, in the presence of 0.04 M acetic acid before and after electrolysis at -2.3 V vs Fc/Fc<sup>+</sup>.

In this set up, bulk electrolysis of 1  $\mu\text{mol}$  of **CoL3N** (concentration 0.2 mM) with 200  $\mu\text{mol}$  of acetic acid in acetonitrile for 2500 seconds (blue trace in **figure 5.43**) gave 7.385 C of charge passed equating to a theoretical  $7.65 \times 10^{-5}$  moles of  $\text{H}_2$  and consumption of *ca.* 76% of available protons (at the same potential as used above). To account for the possibility of hydrogen reacting or leaking during the bulk electrolysis experiment the headspace of the cell was sampled every 350 seconds, by injecting 200  $\mu\text{L}$  of argon into the headspace and removing 200  $\mu\text{L}$  samples then injecting 150  $\mu\text{L}$  into the GC-TCD. Removed hydrogen was then accounted for in determination of hydrogen produced by considering that 1.48% of the 13.5 mL headspace volume, and hence 1.48% of the  $\text{H}_2$  present, was removed in each sampling. Hydrogen production increased almost linearly through the experiment and therefore its loss through leakage or reaction does not appear likely. After electrolysis the overall GC-TCD response accounting for sampling was  $397 \text{ mV.s}^{-1}$  which using the cell calibration equates to 155  $\mu\text{L}$  of  $\text{H}_2$ , and thus  $7 \times 10^{-6}$  moles of  $\text{H}_2$  using the idea gas equation. This gives a TON of 7, and a faradaic efficiency of 18% for hydrogen production.



**Figure 5.45** shows the cyclic voltammetry of **CoL3N** before and after electrolysis at  $-2.3$  V vs  $\text{Fc}/\text{Fc}^+$ . The response after bulk electrolysis is comparable to that seen for the electrocatalytic response of **CoL3N** at lower acid concentrations, however less well defined, and therefore suggests that while at least some of the catalyst (**CoL3N**) may remain in solution, a significant percentage of it has formed another species after bulk electrolysis.

While this result is better than the first run, the low Faradaic efficiency obtained in a cell that showed satisfactory performance in a leak test makes it very clear that production of  $\text{H}_2$  is not the main catalytic process for **CoL3N**.

### Bulk electrolysis 3

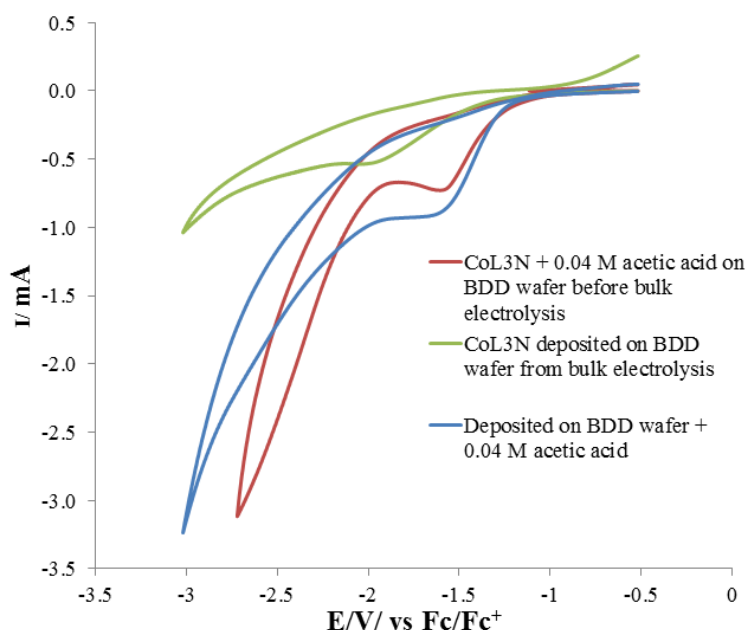


**Figure 5.45** Cyclic voltammetry of 0.2 mM **CoL3N** in the presence of 0.04 M acetic acid before electrolysis at  $-2.3$  V vs  $\text{Fc}/\text{Fc}^+$ , the deposited species on the electrode after electrolysis in clean electrolyte, and the deposited species in the presence of 0.04 M acetic acid, at a  $2.3 \text{ cm}^2$  BDD wafer.

The BDD wafer electrode from bulk **electrolysis 2** had a deposited species at the end of the experiment, and its cyclic voltammetry is shown in **figure 5.49**. This suggests either the catalyst forms a film on the working electrode surface, or that a species is deposited on the electrode surface from the decomposition of **CoL3N**. The electrode with a deposited species from **CoL3N** was run under the same conditions in fresh electrolyte

and 200  $\mu\text{mol}$  (0.04 M) acetic acid for 2500 seconds to investigate this (shown in green in **figure 5.43**). The charge passed was 4.6 C, equating to a theoretical  $2.4 \times 10^{-5}$  moles of  $\text{H}_2$  and consumption of *ca.* 24% of available protons. After electrolysis the overall GC-TCD response accounting for sampling was  $591 \text{ mV.s}^{-1}$  which using the cell calibration equates to 253  $\mu\text{L}$  of  $\text{H}_2$ , and thus  $1.13 \times 10^{-5}$  moles of  $\text{H}_2$ . Using the ideal gas equation this gives a faradaic efficiency of 47% for hydrogen production.

This result lends weight to the conclusion above that reduction of protons to dihydrogen is not the primary electrocatalytic process for **CoL3N** under these conditions, and that the catalytic phenomenon observed in measurements with **CoL3N** is largely molecular in nature. This is because substantially more current is passed with **CoL3N** present, but the quantity of hydrogen obtained is smaller.

#### 5.6.1 Conclusions from initial bulk electrolysis studies and further work

Further work and optimisation of bulk electrolysis conditions is required determine the fate of the *ca.* 80% of electrons that are not used to produce hydrogen in this system, and to uncover the ability of **CoL3N** to produce hydrogen under conditions where other processes do not dominate.

From the initial bulk electrolysis investigations of **CoL3N**, it can be concluded that although the complex or a deposited species on the electrode formed from **CoL3N** does catalyse proton reduction to hydrogen, this is not the main process catalysed by **CoL3N**. The amount of charge passed in bulk electrolysis far exceeds the volume of hydrogen produced. The excess charge passed cannot be accounted for in the two electron two proton reduction of the iminopyridine ligands as this would be only account for 0.193 C of charge.

The fact that more charge is passed with **CoL3N** present than with the deposited species on the electrode surface in the presence of the same concentration of acetic acid, and that more hydrogen is produced from the charge passed in the case of the deposited species, shows that the molecular catalyst has a lower activity for hydrogen production, but a much higher activity for the other electrocatalytic reductive processes occurring

From the composition of the electrolyte solution there are several possibilities; the reduction of acetonitrile to ethylamine or other amines; the multielectron multi proton reduction of nitrate to a number of products such as  $\text{NO}_2$ ,  $\text{NO}_2^-$ ,  $\text{HNO}_2$ ,  $\text{NO}$ ,  $\text{N}_2\text{O}$ ,  $\text{N}_2$ ,  $\text{NH}_2\text{OH}$  and  $\text{NH}_4^+$ ,<sup>248</sup> and the reduction of acetate to ethanal and ethanol.

From the cyclic voltammetry experiments with **CoL3B**, at GCE in **figure 5.30** it can be seen that the complex gives pseudo first order conditions at 0.01 M of acetic acid. Whereas **CoL3N** required the use of BDD electrode and low concentration 0.2 mM to achieve pseudo first order conditions with respect to proton concentration of 0.34 M. As the only difference between the two complexes is the nitrate counter anions, nitrate may be implicated in the catalytic process. This type of behaviour has been published recently for a protoporphyrin complex able to reduce nitrate to a number of products but having selectivity for  $\text{NH}_2\text{OH}$  formation.<sup>250</sup> The catholyte solution of **bulk electrolysis 2** was tested after electrolysis with ninhydrin, by spotting the solution on a TLC plate and developing with an ethanolic solution of ninhydrin, these gave a blue spot indicative of ammonia or primary and secondary amines.<sup>251</sup> A possible quantitative determination method for ammonia has been described by Pickett and co-workers,<sup>251</sup> at the end of the electrolysis ammonia in the catholyte is purged into an aqueous acid trap and is identified and estimated by the indophenol test. The indophenol test employs two reagents: reagent A (phenol and  $\text{Na}_2[\text{Fe}(\text{CN})_5(\text{NO})]$  in distilled water); and reagent B (sodium hydroxide and sodium hypochlorate). These are in turn added to the analyte solution, and if ammonia is present give a characteristic blue colour. The concentration of ammonia can be determined from a calibration curve measuring the UV/Vis absorbance at 625 nm.

However, each **CoL3N** introduces only two nitrates. Even complete reduction of these to ammonia could only account for 20% of the charge passed in **bulk electrolysis 2** above. And alternative explanations of a positive ninhydrin test would be hydrolysis or other fragmentation of **CoL3N**, or reduction of solvent – for example acetonitrile to ethylamine. Reduction of solvent as an explanation is favoured by a positive ninhydrin test obtained from **bulk electrolysis 3**, where **CoL3N** is absent and the yield of  $\text{H}_2$  is higher – implying that reduction of solvent occurs regardless but is favoured by **CoL3N**. Such a reduction could be acetonitrile to ethylamine or other products, and the electrochemical four proton

four electron reductions of nitriles such as benyl cyanide have previously been seen at cobalt electrodes.<sup>252</sup> Electrocatalytic studies in other solvent such as DMF and DCM should give different responses to protons in the form of acetic acid. If acetonitrile is implicated in the catalytic response, determination of main products of electrolysis could possibly achieved through separation from the catholyte solution via acid-base extraction followed by <sup>1</sup>H-NMR analysis in combination with GC-MS, should allow its determination. Reduction of acetate to ethanal and or ethanol could be determined by careful fractional distillation of the catholyte solution and analysis by <sup>1</sup>

## **Chapter 6.0**

*Conclusions and further work*

## 6.1 Conclusions

A series of first row transition metal complexes of zinc, manganese, cobalt, nickel and copper based on cyclohexane-supported *bis*-imino pyridines with different ligand backbones of cyclohexane, and cyclohexanol were synthesised, where hydroxyl is either distal or proximal to the metal centre.

Coordination chemistry of the ligand sets developed gave a range of geometries. Ligands (**10**, **L1**) and (**5**, **L2**) both give octahedral geometries, whereas (**9**, **L3**) gives trigonal prismatic geometry with Zn, Mn and Co, and square-pyramidal geometry with Cu. Complexes synthesised were characterised by x-ray crystallography when crystals of suitable quality could be grown, plus elemental analysis, infra-red spectroscopy, and mass spectrometry. In addition  $^1\text{H}$  and  $^{13}\text{C}$  NMR spectra were obtained for zinc complexes and paramagnetic  $^1\text{H}$ -NMR for cobalt complexes.

All of the complexes synthesised were shown to give rich electrochemistry, largely due to the redox non-innocent *bis*-imino pyridine ligands. Furthermore, the presence or absence and position of a hydroxyl group distal/proximal to the metal centre are shown to have a large effect on the cyclic voltammetry. Evidence for molecular motion in **ZnL3N** and **CuL3N** is seen involving the interconversion between different geometries from the electrochemistry: specifically trigonal prismatic and octahedral or square-based pyramidal, this is through the coordination and de-coordination of the proximal hydroxyl.

Electrocatalysis was focused on the series of cobalt complexes as these were shown to give the largest response to acetic acid, and less evidence for decomposition or deposition than found for example with nickel. The electrochemistry of **CoL3N** and **CoL3B**, containing the proximal hydroxyl, in the presence of acetic acid protons both show a change in behaviour on increasing proton concentration, which is most likely caused by a change in geometry on protonation (or hydrogen bonding to acetic acid) and reduction.

Electrocatalytic response to protons for the cobalt nitrate based complexes gives high turn overs of electrons passed per second, indicating a fast rate of catalysis. Catalytic parameters,  $\eta$ , and  $\text{TOF}_{\text{max}}$ , of the cobalt complexes follow a trend in increasing  $\eta$  and  $\text{TOF}_{\text{max}}$  from the propane backbone, to cyclohexane backbone, to the distal cyclohexanol,

to the proximal cyclohexanol. This indicates that increase in rigidity increases the rate of catalysis, but increases the energy required. Coordination of the proximal hydroxyl group, as seen in **CoL3N** and **CoL3B** also has a clear influence on the catalytic process, giving rise to both higher  $\eta$  and higher  $\text{TOF}_{\text{max}}$ . These effects may result both from relay of protons to the metal centre by the  $-\text{OH}$  group, and increased reactivity of any resulting hydride species due to electron donation from  $-\text{OH}$  to the cobalt centre.

Bulk electrolysis of **CoL3N** with acetic acid indicates that proton reduction to hydrogen is not the primary electrocatalytic process for this complex, due to a Faradaic yield of  $\text{H}_2$  (*ca.* 18%) than is produced in the absence of the complex (47%). A positive nihydriin test of the catholyte after bulk electrolysis indicates presence of amines, and suggests reduction of acetonitrile solvent is in fact the main process.

## 6.2 Further work

- Address the nature of the reductive processes occurring during bulk electrolysis of **CoL3N** and of the other cobalt catalysts. As previously stated, there are three possible substrates other than protons in solution: nitrate, acetonitrile and acetate. Initial identification of these – in particular potential organic products such as amines, aldehydes or alcohols can be performed by mass spectroscopic analysis of the catholyte. However, this is unlikely to be quantitative. GC-MS (or LC-MS) would enable quantification by linking quantitative chromatography to mass spectral identification. In addition to this, amine products (for example ethylamine) can be confirmed and identified by using an acid-base extraction to separate from the catholyte, followed by  $^1\text{H}$ -NMR analysis in combination with GC-MS as suggested above. If the process is nitrate or acetonitrile reduction to ammonia, purging the catholyte solution into an acid trap and performing an indophenol test will reveal its presence. Moreover, the concentration of ammonia can be determined from a calibration curve measuring the UV/Vis absorbance at 625 nm. Reduction of acetate to ethanal and/or ethanol could be determined by careful fractional distillation of the catholyte solution and analysis by  $^1\text{H}$ -NMR, although this is unlikely to be more practically viable than GC-MS unless performed at large scale.

- In support of the above experiments, investigation into the electrocatalytic response of **CoL3N** and the other cobalt based complexes with acetic acid (or other acids) in other solvents other than acetonitrile should be performed. This would provide a rapid indication of whether this behaviour is from reduction of acetonitrile and might also enable the true activity of these complexes towards the HER to be established, in the absence of competing substrates.
- Investigations into the change in geometry of **CoL3N** in the presence of acetic acid, and whether this behaviour is dependent on the presence of acetate or if it is seen with other acids with different conjugate bases. The change in geometry could possibly be investigated through  $^1\text{H-NMR}$ , by reducing the complex chemically in the presence of acetic acid. Although the  $2+$  complex is paramagnetic, reduction of the complex in the presence of acid is likely to result in a square-planar or square based pyramidal geometry, as seen in the DFT studies conducted with this work. Therefore, this should give a  $d^8$  diamagnetic species and therefore a  $^1\text{H-NMR}$  comparable to that of **ZnL1N** and **ZnL2N**. Investigations could also be conducted via UV/Vis spectro-electrochemistry, or EPR spectro-electrochemistry.
- Further investigations into the molecular motion of **ZnL3N** by electrochemistry over a wider range of scan rates and temperature range along with variable temperature  $^1\text{H-NMR}$  studies.
- Investigations into the effect of anions on the electrochemical response of cobalt complexes to a proton source.
- Further investigations into the change in geometry of **CuL3N** on reduction. This could possibly be achieved through  $^1\text{H-NMR}$ , through reducing the complex chemically to give the  $d^{10}$  complex that would be expected to give a  $^1\text{H-NMR}$  comparable to that of **ZnL3N**.



# Chapter 7

*Experimental*

## 7.1 General experimental

### 7.1.1 Materials

Tetrahydrofuran (THF) was distilled over sodium wire under nitrogen; triethylamine (TEA) was distilled at reduced pressure over KOH and stored over KOH under nitrogen; acetonitrile (MeCN) was distilled over CaH<sub>2</sub> under nitrogen, and dichloromethane was distilled over P<sub>2</sub>O<sub>5</sub> and K<sub>2</sub>CO<sub>3</sub> under nitrogen. Pyridine was distilled and over KOH under nitrogen. Ethanol was dried over 4Å molecular sieves. *cis,cis*-1,3,5-Cyclohexanetriol dihydrate was obtained from Bujno Chemicals and dried under high vacuum for 24 hours at 50 °C (until weighing confirmed that all water had been removed). *cis*-1,3-Diaminocyclohexane was obtained from TCI chemicals. All other reagents and solvents were obtained as ACS grade from Sigma-Aldrich, Alfa Aesar or Fisher Scientific and used as supplied. Deuterated solvents were obtained from Goss Scientific. Tosyl chloride (Aldrich) was recrystallised from ethyl acetate after washing with 10% NaOH solution. Unless otherwise stated, all column chromatography was performed over silica gel.

### 7.1.2 Methods

With the exception of the hydrogenations and complexations with nitrate and chloride metal salts, all syntheses were carried out under an atmosphere of oxygen-free nitrogen using standard schlenk techniques. For the synthesis of **CoB**, **CoL4B**, **CoL1B** and **CoL3B**, anhydrous solvents were degassed under nitrogen for 20 minutes prior to use, and other reagents were degassed by freeze thaw cycles.

TLC plates were developed using an ultraviolet lamp, KMnO<sub>4</sub> dip or iodine chamber.

FT-IR spectra described as a thin film on CaF<sub>2</sub> were acquired by adding of a drop of a concentrated solution of an analyte in a volatile solvent onto a CaF<sub>2</sub> plate and allowing for the evaporation of the solvent to give a thin film, before measuring the spectrum.

Paramagnetic <sup>1</sup>H NMR for cobalt complexes were recorded using the following parameters; Line broadening (LB) = 2, Acquisition Time (AQ) = 0.5 s, Delay (D<sub>1</sub>) = 0.1 s, Sweep Width (SW) = 333.18 ppm, number of scans = 512.

### 7.1.3 DFT methods

DFT calculations were performed using the Gaussian 09 suite of programs.<sup>253</sup> Structures were optimized in the gas phase using the PBE<sup>256</sup> pure functional from crystal structures obtained from the structures in the 2+ oxidation state. The optimized structure was then used as a starting point for optimization calculations of the 1+, 0, and -1 structures of the complexes. In each case, carbon nitrogen and hydrogen were treated with the 6-311g(d,p) basis set with metal centers described with the lanl2dz<sup>255</sup> basis set with effective core potential. Where required, structures were re-optimized in acetonitrile using the SMD solvent scheme of reference 254. All structures were confirmed as minima by frequency analysis. Diagrams showing the complexes and HOMO and LUMO molecular orbitals were then generated using Gaussview to try to understand where reductions were based on the complexes, and most likely places for protonation to occur.

### 7.1.4 Instrumentation

---

<b>Elemental analysis</b>	London Metropolitan University Elemental Analysis Service
<b>Mass spectrometry</b>	UK National Mass Spectrometry Service, Swansea University
<b>FT-IR spectroscopy</b>	Perkin Elmer FT-IR spectrum BX and Bruker FT-IR XSA spectrometers
<b>UV-vis spectroscopy</b>	Agilent Cary 60 UV-vis spectrophotometer
<b>NMR spectroscopy</b>	Bruker AC 300 (300 MHz) and Bruker Ascend 500 (500 MHz) spectrometers. All shifts are quoted with respect to TMS using the solvent signals as secondary standard
<b>X-ray crystallography</b>	Oxford Diffraction XCalibur 3 diffractometer (UEA), or Rigaku AFC 12 goniometer (National Crystallography service) equipped with an

enhanced sensitivity (HG) Saturn724+ detector and  
FR-E+ SuperBright molybdenum rotating anode  
generator with HF Varimax optics (100 $\mu$ m focus).

## Electrochemistry

Autolab (PGStat 302N, and PGStat 30)  
potentiostat/galvanostat

---

### 7.1.5 Compound numbering

Organic compounds are numbered in the order in which their syntheses are described in the ligand synthesis and characterisation, chapter 3, with ligands described by their respective names and Ln, where n = the number of the ligand used in the respective metal complex. Coordination compounds are given identification by the central metal, M followed by ligand, Ln, n = 1, 2, 3 or 4, followed by N to denote nitrate, Cl to denote chloride and B to denote tetrafluoroborate, for example **CoL1N**.

### 7.1.6 Notation for NMR, MS and IR spectra

Wherever possible, NMR spectra have been fully assigned using diagrams of the structures, labels for protons ( $H_a$ ,  $H_b$  etc), and the following notation.

NMR: s – singlet; d - doublet; t – triplet; q – quartet; qi – quintet; se – sextet; dd, dt, td, tt – doublet of doublets etc; p before any other letter signifies the prefix pseudo.

Coupling constants for pseudo multiplets are not given as these are the result of second order coupling from non-equivalent protons with similar constants. Note also that assignment is necessarily incomplete for compounds **14** and **15**. In these cases only the resonances for protons geminal to functional groups can be clearly identified, due to overlapping resonances making recognition of peak shape and or multiplicity impossible.

ES-MS:  $[M]^+$  - molecular ion;  $[M-Na]^+$  - molecule plus a sodium ion.

EI-MS:  $[M]^+$  - molecular ion;  $[M-X]^+$  - molecular ion minus fragment X.

IR: sh – shoulder; vw – very weak; w – weak; m – medium; s – strong; vs – very strong.

### 7.1.7 A note on the purity of imine ligands

For all of the Schiff-base products (before complexation), that is (**18**, **L4**), (**10**, **L1**), (**5**, **L2**) and (**9**, **L3**), small quantities of unreacted 2-pyridine carboxyaldehyde are always observed in NMR of the products even after precipitation or crystallisation. Purification by column chromatography or distillation was not possible as the conditions result in the hydrolysis of the imine groups. For this reason, elemental analysis for these ligands was not obtained. However, all other characterisation data matches the correct products, and elemental analysis and structural data from X-ray crystallography provides unequivocal proof that the target ligands were synthesised.

### 7.1.8 Electrochemical methods

All electrochemical procedures were carried out using an Autolab PGStat 30 potentiostat/galvanostat, using GPES or Nova software. Cyclic voltammetry (CV) experiments were performed in a single-compartment or a conventional three-electrode cell with a Ag/AgCl reference electrode (3M NaCl, saturated AgCl) or a pseudo-reference Ag wire electrode separated by a glass frit. Glassy carbon (GCE), gold amalgam (Au/Hg), or boron doped diamond (BDD) were used as working electrodes with a Pt wire or gauze auxiliary electrode. Acetonitrile was freshly distilled (from CaH<sub>2</sub>), with TBABF<sub>4</sub> used as the supporting electrolyte. Solutions containing ca. 0.1 - 1 mM of analyte and 0.1 M electrolyte were degassed by purging with nitrogen for 20 minutes before the experiment and during the measurements a nitrogen atmosphere was maintained. All  $E_{1/2}$  values were calculated from  $(E_{pa} + E_{pc})/2$  at a scan rate of 100 mV s<sup>-1</sup> and referenced to internal standard ferrocene (Fc/Fc<sup>+</sup>). Bulk electrolysis was performed using chronoamperometry in a three-compartment cell where both reference and counter electrode were separated by a glass frit. A 3×1×0.1 cm BDD wafer was used as a high surface area working electrode, a Pt gauze counter electrode and as a pseudo-reference electrode an Ag wire was used, or a Metrom non-aqueous Ag/AgCl.

Prior to use in electrochemical experiments, boron doped diamond electrodes were activated by cycling the potential in aqueous 1 M HNO<sub>3</sub> between 0 and -3 V vs Ag/AgCl

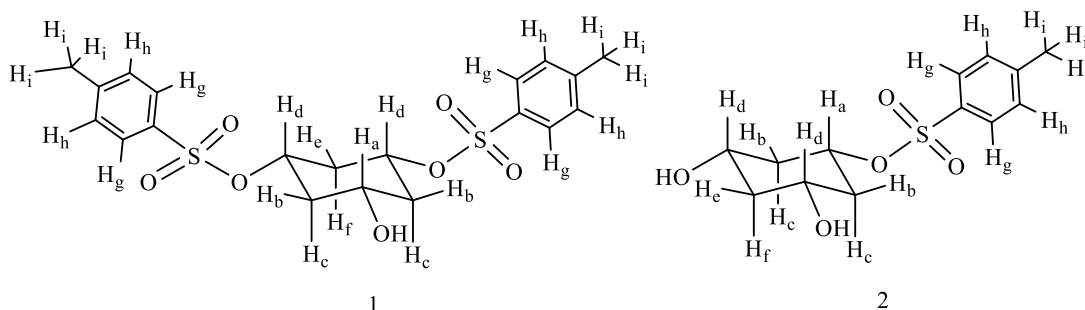
with stirring until stable reproducible following curves were obtained (10 cycles with 0.1 V/s scan rate), to give a H-terminated electrode surface, as published by Bilewicz.<sup>255</sup>

#### 7.1.9 Preparation of [NBu<sub>4</sub>] [BF<sub>4</sub>] electrolyte

A solution of tetrabutylammonium hydrogen sulfate (169.0 g, 0.498 mol) in distilled water (200 mL) was added to a solution of sodium tetrafluoroborate (54.6 g, 0.498 mol) in distilled water (200 mL) with vigorous stirring for 30 minutes giving a white precipitate. This precipitate was collected, washed three times with water (200 mL), and dried. The air dried solid was dissolved in freshly distilled dichloromethane and dried over magnesium sulphate overnight before being filtered off and washed with dried dichloromethane. The resulting filtrate was slowly added to dry diethyl ether (1.5 L) with vigorous stirring. A white precipitate of [NBu<sub>4</sub>] [BF<sub>4</sub>] was obtained which was collected by filtration and dried *in vacuo* for 24 hours.

## 7.2 Ligand synthesis

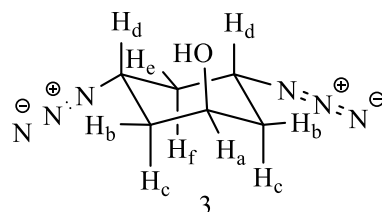
### 7.2.1 *cis*-1,3-Ditosyloxy-*trans*-5-hydroxycyclohexane (**1**) and *cis*-1,3-dihydroxy-5-tosyloxycyclohexane (**2**)



To a vigorously stirred solution of dry *cis,cis*-1,3,5-cyclohexanetriol (0.787 g, 0.596 mmol) in pyridine (13 mL, 16 mmol) at 0 °C was added dropwise a solution of freshly purified and dried tosyl chloride (2.38 g, 1.25 mmol) in pyridine (4 mL, 0.48 mmol) and stirred for 6 hours at 0 °C. The reaction mixture was then allowed to slowly warm to room temperature with stirring overnight. After the reaction was seen to complete by TLC, ethyl acetate (40 mL) was added, and the resulting mixture was washed with (10 mL) of 1 M HCl, followed by water (10 mL), saturated sodium carbonate (10 mL), and brine (10 mL). The organic layer was then dried over sodium sulphate, and the solvent removed to give the crude tosylated compound which was absorbed on the minimum of silica. Flash chromatography with ethyl acetate: hexane (2:1), gave compound **1** as an off white sticky solid (1.503 g, 0.358 mmol, 57%). <sup>1</sup>H-NMR (300 MHz, CDCl<sub>3</sub>): δ 7.73 (d, 4H, *J* = 8 Hz, H<sub>g</sub>), 7.33 (d, 4H, *J* = 8 Hz, H<sub>h</sub>), 4.32 (*m*, 2H, H<sub>d</sub>), 3.53 (*m*, 1H, H<sub>a</sub>), 2.44 (s, 6H, H<sub>i</sub>), 2.23-2.15 (*m*, 3H, 2H<sub>b</sub> + H<sub>e</sub>), 1.60 (*m*, 1H, H<sub>f</sub>), 1.42 (*m*, 2H, H<sub>c</sub>). <sup>13</sup>C-NMR (75 MHz, CDCl<sub>3</sub>): δ 145.2 (Ar, C), 133.8 (Ar, C), 130.0 (Ar,CH), 127.6 (Ar, CH), 74.1 (CH), 64.4 (CH), 40.3 (CH<sub>2</sub>), 37.7 (CH<sub>2</sub>), 21.7 (CH<sub>3</sub>). *m/z* (ESI<sup>+</sup>) 441.10 [M+H]<sup>+</sup>. FTIR (thin film on CaF<sub>2</sub>) cm<sup>-1</sup>: 3540 (s), 2958 (m), 2870 (w), 1598 (m), 1495 (w), 1469 (w), 1356 (s), 1173 (s), 1096 (m). Elemental analysis for C<sub>26</sub>H<sub>36</sub>O<sub>10</sub>S<sub>2</sub> calcd (found) %: C 54.63 (54.59), H 5.37 (5.41). Also isolated as the second product from the same column was **2** as a white solid (0.04 g, 0.149 mmol, 25%). <sup>1</sup>H-NMR (300 MHz, CDCl<sub>3</sub>): δ 7.77 (d, 2H, *J* = 9 Hz, H<sub>g</sub>), 7.34 (d, 2H, *J* = 9 Hz, H<sub>h</sub>), 4.47 (*m*, 1H, H<sub>a</sub>), 3.68 (*m*, 2H, H<sub>d</sub>), 2.45 (s, 3H, H<sub>i</sub>), 2.21-2.122 (*m*, 3H, 2H<sub>b</sub> + H<sub>e</sub>), 1.58 (*m*, 1H, H<sub>c</sub>), 1.39 (*m*, 2H, H<sub>f</sub>). <sup>13</sup>C-NMR (75 MHz, CDCl<sub>3</sub>): δ 145.0 (Ar, C), 134.3 (Ar, C), 130.0 (Ar,CH), 127.8 (Ar, CH), 75.8 (CH), 65.4 (CH), 42.6 (CH<sub>2</sub>), 40.4 (CH<sub>2</sub>), 21.8 (CH<sub>3</sub>). *m/z* (ESI<sup>+</sup>) 595.16 [2M+Na]<sup>+</sup>. FTIR (thin film on CaF<sub>2</sub>)

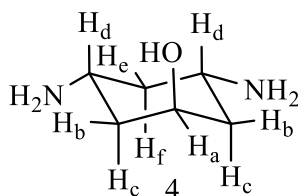
cm<sup>-1</sup>: 3348 (b), 2947 (sh), 2866 (w), 1597 (m), 1467 (m), 1349 (s), 1189 (s), 1174 (s), 1096 (s), 1024 (s), 953 (s), 928 (s). Elemental analysis for C<sub>13</sub>H<sub>18</sub>O<sub>7</sub>S, calcd (found) %: C 54.38 (54.53), H 6.37 (6.34).

### 7.2.2 *cis*-3,5-Diazido-*trans*-hydroxycyclohexane (**3**)



To *cis*-1,3-ditosyloxy-*trans*-5-hydroxycyclohexane (**1**) (3.34 g, 8.106 mmol) in anhydrous DMF (56 mL) was added sodium azide (5.27 g, 81.06 mmol). The resulting suspension was stirred at 70 °C for 16 hours before cooling, addition of EtOAc (40 mL) and removal of salts by filtration. The salts were washed with EtOAc, the washings combined with the filtrate and washed with water (3 × 40 mL), and the aqueous layer back extracted with EtOAc (2 × 40 mL). Combination of the organic layers, drying over MgSO<sub>4</sub> and removal of solvent at reduced pressure, followed by column chromatography on silica (37.5% to 75% EtOAc in hexane), afforded compound **3** as a pale-yellow oil (0.996 g, 5.47 mmol, 68 %). <sup>1</sup>H-NMR (300 MHz, CDCl<sub>3</sub>): δ 4.39 - 4.32 (m, 1 H, H<sub>a</sub>), 3.77 (m, 2H, H<sub>d</sub>), 2.37 - 2.29 (m, 1 H, H<sub>e</sub>), 2.12 - 2.02 (m, 2 H, H<sub>b</sub>), 1.46 (m, 2H, H<sub>c</sub>), 1.38 (m, 1H, H<sub>f</sub>). <sup>13</sup>C-NMR (125 MHz, CDCl<sub>3</sub>): δ 65.7 (CH), 54.07 (CH), 37.5 (CH<sub>2</sub>), 36.9 (CH<sub>2</sub>). *m/z* (ESI<sup>+</sup>) 205.08 [M+Na]<sup>+</sup>. FTIR (thin film on CaF<sub>2</sub>) cm<sup>-1</sup>: 3417 (m), 2935 (m), 2860 (w), 2489 (vs), 1248 (s), 1129 (s). Elemental analysis for C<sub>6</sub>H<sub>10</sub>N<sub>6</sub>O, calcd (found) %: C 39.62 (39.68), H 5.34 (5.45), N 45.82 (45.87).

### 7.2.3 *cis*-3,5-Diamino-*trans*-hydroxycyclohexane (**4**)

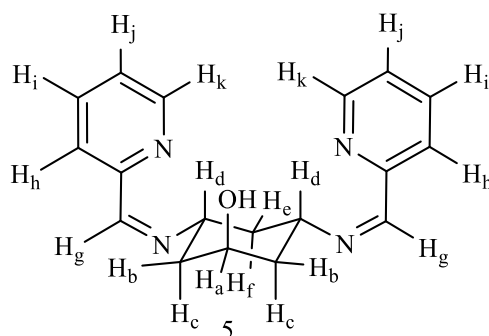


To *cis*-3,5-diazido-*trans*-hydroxycyclohexane (**3**) (0.400 g, 2.2 mmol) in ethanol (21 mL) separated into 6 × 3.5 mL aliquots was added 10% Pd/C catalyst (0.006 g) per aliquot. The mixture was agitated for 18 hours at 30 °C, under a hydrogen atmosphere of 620 kPa



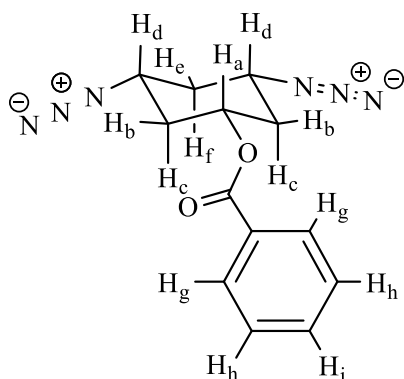
before the catalyst was removed by gravity filtration. Evaporation of the solvent gave product **4** as an off white solid (0.264 g, 2.024 mmol, 92%).  $^1\text{H-NMR}$  (300 MHz,  $\text{CD}_3\text{OD}$ ):  $\delta$  4.17 (*m*, 1H,  $\text{H}_a$ ), 2.93 (*m*, 2H,  $\text{H}_d$ ), 2.00 - 1.90 (*m*, 1H,  $\text{H}_e$ ), 1.89 – 1.78 (*m*, 2H,  $\text{H}_b$ ), 1.18 (*m*, 2H,  $\text{H}_c$ ), 0.88 (*m*, 1H,  $\text{H}_f$ ).  $^{13}\text{C-NMR}$  (125 MHz,  $\text{CD}_3\text{OD}$ ):  $\delta$  66.60 (CH), 45.26 (CH), 44.47 ( $\text{CH}_2$ ), 41.23 ( $\text{CH}_2$ ).  $m/z$  ( $\text{ESI}^+$ )  $\text{M}^+$  130.2. IR (thin film on  $\text{CaF}_2$ )  $\text{cm}^{-1}$ : 3336 (sh), 2929 (sh), 1571 (s), 1468 (s), 1386 (s), 1333 (s), 1139 (w), 1004 (w), 980 (m).

#### 7.2.4 *cis*-3,5-Bis[(2-Pyridinyleneamin)]-*trans*-hydroxycyclohexane (**5**, **L2**)



A methanolic solution (2 mL) of 2-pyridinecarboxaldehyde (0.587 g, 5.48 mmol) was added to a solution of *cis*-3,5-diamino-*trans*-hydroxycyclohexane (**4**) (0.300 g, 2.27 mmol) and triethylamine (0.115 g, 1.14 mmol) in methanol (50 mL). The mixture was refluxed under nitrogen for 20 hours and the volume was then reduced giving brown oil. This was extracted from water with chloroform ( $3 \times 25$  mL), the organic layer back-extracted with water ( $3 \times 25$  mL) and dried over  $\text{MgSO}_4$ . The brown oil was then dissolved diethyl ether (5 mL), and precipitated by the addition of hexane. Filtration and drying under vacuum gave the product **5** (0.685 g, 92%) as a light brown solid.  $^1\text{H-NMR}$  (300 MHz,  $\text{CDCl}_3$ ):  $\delta$  8.58 (dd, 2H,  $J = 5, 2$  Hz,  $\text{H}_k$ ), 8.41 (s, 2H,  $\text{H}_g$ ), 7.94 – 7.91 (*m*, 2H,  $\text{H}_h$ ), 7.67 (*m*, 2H,  $\text{H}_i$ ), 7.24 (*m*, 2H,  $\text{H}_j$ ), 4.40 (*m*, 1H,  $\text{H}_a$ ), 3.90 (*m*, 2H,  $\text{H}_d$ ), 2.01–1.80 (*m*, 6H,  $2\text{H}_b + 2\text{H}_c + \text{H}_e + \text{H}_f$ ).  $^{13}\text{C-NMR}$  (125 MHz,  $\text{CDCl}_3$ ):  $\delta$  160.7 (CN-imine), 154.7 (py -CN), 149.5 (py -CN), 136.7 (py -C), 124.9 (py -C), 121.7 (py -C), 66.6 (CH), 62.9 (CH), 41.2 ( $\text{CH}_2$ ), 39.8 ( $\text{CH}_2$ ).  $m/z$  ( $\text{ESI}^+$ ) 331.15  $[\text{M}+\text{Na}]^+$ . FTIR (thin film on  $\text{CaF}_2$ )  $\text{cm}^{-1}$ : 3353 (m), 2928 (m), 2859 (m), 1644 (s), 1132 (s).

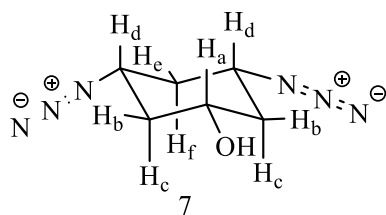
### 7.2.5 *cis,cis*-3,5-Diazidocyclohexyl benzoate (**6**)



6

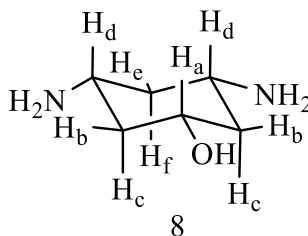
A solution of *cis*-3,5-diazo-*trans*-hydroxycyclohexane (0.56 g, 3.1 mmol) in anhydrous THF (5 mL) was cooled to -50 °C (dry ice/acetone bath) under nitrogen. Benzoic acid (0.62 g, 4.9 mmol) and triphenylphosphine (1.29 g, 4.9 mmol) were then added to the cooled solution in quick succession, followed by the dropwise addition of DEAD (0.86 mL, 4.9 mmol). The reaction mixture was then allowed to warm to room temperature over *ca.* 2 hours and stirred for a further hour at room temperature until completion of the reaction was shown by TLC (hexane: ethyl acetate, 95:5). Ether (10 mL) was added to the reaction mixture, which was then washed with 1 M HCl (10 mL), water (10 mL), saturated sodium bicarbonate solution (10 mL) and brine (10 mL). The ethereal layer was then dried over MgSO<sub>4</sub> and the solvent removed and left overnight for crystals of triphenylphosphine oxide to form. The resulting mixture was taken up in ethyl acetate and evaporated to dryness on silica gel, before purification by column chromatography (hexane: ethyl acetate, 95:5 to 60:40) gave the product **6** as a yellow oil (0.556 g, 62%). <sup>1</sup>H-NMR (500 MHz, CDCl<sub>3</sub>): δ 8.02 (dd, *J* = 7.5, 1 Hz, 2 H, H<sub>g</sub>), 7.58 (tt, *J* = 7.5, 1 Hz, 1 H, H<sub>i</sub>), 7.51-7.47 (m, 2H, H<sub>h</sub>), 5.00 (*m*, 1 H, H<sub>a</sub>), 3.46 (*m*, 2H, H<sub>d</sub>), 2.5-2.44 (m, 2H, H<sub>b</sub>), 2.37-2.3 (m, 1H, H<sub>e</sub>), 1.53 (*m*, 2H, H<sub>c</sub>), 1.40 (*m*, 1H, H<sub>f</sub>). <sup>13</sup>C-NMR (125 MHz, CDCl<sub>3</sub>): δ 165.8 (Ar-COO, C), 133.5 (ArC), 129.86 (ArC), 129.84 (ArC), 128.64 (ArC), 68.4 (CH), 55.1 (CH), 36.8 (CH<sub>2</sub>), 36.6 (CH<sub>2</sub>). *m/z* (ESI<sup>+</sup>) 259.12 [M-N<sub>2</sub>+H]<sup>+</sup>. FTIR (thin film on CaF<sub>2</sub>) cm<sup>-1</sup>: 3324 (w), 2956 (m), 2880 (m), 2506 (w), 2104 (s, sh), 1716 (s, sh), 1604 (m). Elemental analysis for C<sub>13</sub>H<sub>14</sub>N<sub>6</sub>O<sub>2</sub>, calcd (found) %: C 54.54 (54.71), H 4.93 (5.04), N 29.36 (29.46).

### 7.2.6 *cis*-3,5-Diazido-*cis*-hydroxycyclohexane (**7**)



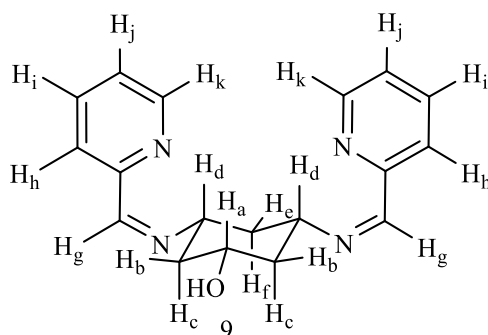
To a solution of *cis,cis*-3,5-diazidocyclohexyl benzoate (**6**) (100 mg, 0.35 mmol) in anhydrous methanol (2 mL) was added dropwise a solution of sodium methoxide in methanol (0.5 M, 2 mL). After the solution had stirred for 4 hours at room temperature, the solution was washed through Amberlite IR-120 (plus) (prewashed with methanol). Removal of the solvent and purification by column chromatography (hexane: EtOAc 9:1, then 4:6) yielded **7** as a yellow oil, (50 mg, 79 %).  $^1\text{H-NMR}$  (500 MHz,  $\text{CDCl}_3$ ):  $\delta$  3.72 (*m*, 1H,  $\text{H}_a$ ), 3.35 (*m*, 2H,  $\text{H}_d$ ), 2.37 – 2.20 (*m*, 3H,  $2\text{H}_b + \text{H}_e$ ), 1.34 (*m*, 1H,  $\text{H}_f$ ), 1.327 (*m*, 2H,  $\text{H}_c$ ).  $^{13}\text{C-NMR}$   $\delta$  (125 MHz,  $\text{CDCl}_3$ ): 66.4 (CH), 55.2 (CH), 40.0 ( $\text{CH}_2$ ), 36.5 ( $\text{CH}_2$ ).  $m/z$  ( $\text{ESI}^+$ ) 205.08  $[\text{M}+\text{Na}]^+$ . FTIR (thin film on  $\text{CaF}_2$ )  $\text{cm}^{-1}$ : 3330 (br), 2926 (s), 2858 (s), 2486 (s), 2094 (sh). Elemental analysis for  $\text{C}_{13}\text{H}_{14}\text{N}_6\text{O}_2$ , calcd (found) %: C 39.56 (39.80), H 5.53 (5.67), N 46.13 (45.89).

### 7.2.7 *cis*-3,5-Diamino-*cis*-hydroxycyclohexane (**8**)



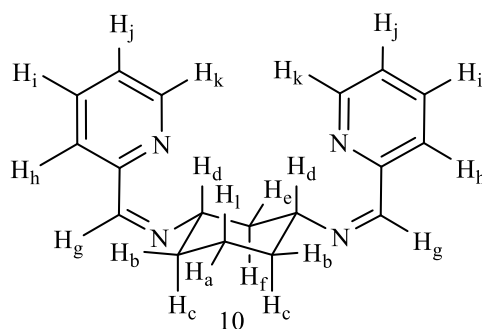
10% Pd/C (0.020 g, mmol) was added to a solution of *cis*-3,5-diazido-*cis*-hydroxycyclohexane (**7**) (0.126 g, 0.691 mmol) in ethanol (3.5 mL). This was treated with hydrogen at 620 kPa, at 30 °C with stirring for 18 hours. Removal of Pd/C by filtration, followed by evaporation of the solvent gave the product as a white solid (0.085 g, 0.65 mmol, 94%).  $^1\text{H-NMR}$  (500 MHz,  $\text{D}_2\text{O}$ ):  $\delta$  3.68 (*m*, 1H,  $\text{H}_a$ ), 3.74 (*m*, 2H,  $\text{H}_d$ ), 2.1-2.04 (*m*, 2H,  $\text{H}_b$ ), 1.96 – 1.90 (*m*, 1H,  $\text{H}_e$ ), 1.04 (*m*, 2H,  $\text{H}_c$ ), 0.90 (*m*, 1H,  $\text{H}_f$ ).  $^{13}\text{C-NMR}$  (125 MHz,  $\text{D}_2\text{O}$ ):  $\delta$  67.03 (CH), 45.70 (CH), 42.7 ( $\text{CH}_2$ ), 42.41 ( $\text{CH}_2$ ).  $m/z$  ( $\text{ESI}^+$ ) 153.09  $[\text{M}+\text{Na}]^+$ . FTIR (thin film on  $\text{CaF}_2$ )  $\text{cm}^{-1}$ : 3279 (sh), 2929 (sh), 1596 (s), 1554 (s), 1458 (s), 1356 (s), 1284 (s), 1257 (w), 1022 (w), 910 (m).

### 7.2.8 *cis*-3,5-Bis[(2-pyridinyleneamin)]-*cis*-hydroxycyclohexane (**9**, L3)



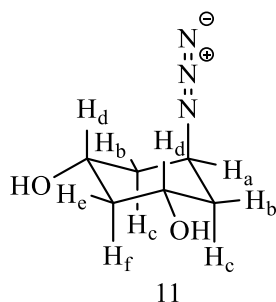
A methanolic solution (5 mL) of 2-pyridinecarboxaldehyde (0.41 g, 3.54 mmol) was added to a solution of *cis*-3,5-diamino-*cis*-hydroxycyclohexane (**8**) (0.230 g, 1.77 mmol) and triethylamine (0.09 g, 0.88 mmol) in methanol (40 mL). The mixture was refluxed under nitrogen for 20 hours and the volume was then reduced to give a brown oil. This was extracted from water with chloroform (3 × 50 mL), the organic layer back-extracted with water (3 × 50 mL) and dried over MgSO<sub>4</sub>. The brown oil was then dissolved in the minimum of diethyl ether and precipitated by addition of hexane, filtration and drying under vacuum gave the product **9** (0.481 g, 1.55 mmol, 86%) as a cream solid. <sup>1</sup>H-NMR (500 MHz, CDCl<sub>3</sub>): δ 8.65 (dd, 2H, *J* = 5, 2 Hz, H<sub>k</sub>), 8.44 (s, 2H, H<sub>g</sub>), 8.02 - 7.99 (m, 2H, H<sub>h</sub>), 7.74 (*m*, 2H, H<sub>i</sub>), 7.32 (*m*, 2H, H<sub>j</sub>), 3.97 (*m*, 1H, H<sub>a</sub>), 3.55 (*m*, 2H, H<sub>d</sub>), 2.19-2.12 (*m*, 2H, H<sub>b</sub>), 1.97 (*pq*, 1H, H<sub>f</sub>), 1.89-1.81 (*m*, 1H, H<sub>e</sub>), 1.74 (*pq*, 2H, 2H<sub>c</sub>). <sup>13</sup>C-NMR (125 MHz, CDCl<sub>3</sub>): δ 160.8 (CN-imine), 154.7 (py -CN), 149.6 (py -CN), 136.7 (py -C), 124.9 (py -C), 121.7 (py -C), 65.6 (CH), 42.6 (CH<sub>2</sub>), 40.7 (CH<sub>2</sub>). *m/z* (ESI<sup>+</sup>) 331.15 [M+Na]<sup>+</sup>. FTIR (thin film on CaF<sub>2</sub>) cm<sup>-1</sup>: 3352 (br, sh), 3059 (w), 3010 (w), 2935 (s), 2860 (s), 2217 (w), 1645 (s), 1588 (s), 1567 (s), 1469 (s), 1436 (s), 1337 (s), 1225 (s), 1086 (s), 1026 (m), 992 (w).

### 7.2.9 *cis*-1,3-Bis(2-pyridinylenamine] cyclohexane (**10**, L1)



*cis*-1,3-Diaminocyclohexane (0.88 mmol, 0.122 mL) was added to a solution of 2-pyridinecarboxaldehyde (1.85 mmol, 0.192 mL) and triethylamine (0.44 mmol, 0.06 mL) and refluxed in dry MeOH (60 mL) overnight. The solvent was then removed under reduced pressure and the resultant oil re-dissolved in DCM, which was washed with distilled water and the organic layer dried over MgSO<sub>4</sub>. The volume was reduced under vacuum to *ca* 5 mL then hexane was added and put in the freezer overnight forming **10** as brown crystals (0.2 g, 0.7 mmol, 80%). <sup>1</sup>H-NMR (500 MHz, DOCD<sub>3</sub>): δ 8.06 (dd, 2H, *J* = 5, 2 Hz, H<sub>k</sub>), 8.46 (s, 2H, H<sub>g</sub>), 8.04 – 8.016 (m, 2H, H<sub>h</sub>), 7.9 (*m*, 2H, H<sub>i</sub>), 7.47 (*m*, 2H, H<sub>j</sub>), 3.56 (*ptpt*, 2H, H<sub>d</sub>), 1.97 (*m*, 2H, 2H<sub>c</sub>), 1.90 - 1.80 (*m*, 3H, H<sub>e</sub> + 2H<sub>b</sub>), 1.72 – 1.61 (*m*, 3H, H<sub>f</sub> + H<sub>a</sub> + H<sub>l</sub>). <sup>13</sup>C-NMR (125 MHz, CDCl<sub>3</sub>): δ 160.12, 154.82, 149.43, 136.52, 124.62, 121.48, 68.17, 41.31, 33.18, 22.88. FTIR (thin film on CaF<sub>2</sub>) cm<sup>-1</sup>: 1600 (s). *m/z* (ESI<sup>+</sup>): [M+Na] 315.16.

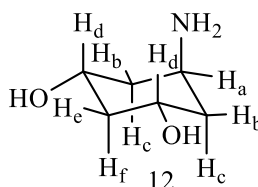
### 7.2.10 *cis*-1,3-Dihydroxy-*trans*-5-azidocyclohexane (**11**)



To a solution of *cis*-1,3-dihydroxy-5-tosyloxycyclohexane (**2**) (1.088 g, 3.80 mmol) in dry DMF (10 mL) was added sodium azide (1.24 g, 19.1 mmol). The resulting suspension was stirred at 70 °C for 16 hours before it was allowed to cool and acetone (25 mL) was added to precipitate the salts. The salts were filtered off and washed with acetone (3 ×

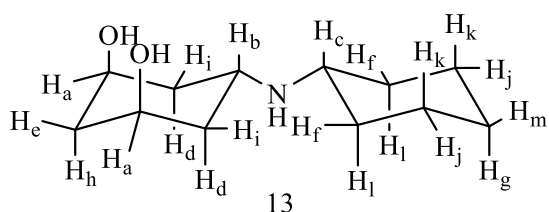
20 mL), and the filtrate evaporated under vacuum before purification by column chromatography on silica (EtOAc, then 10% - 30% <sup>i</sup>PrOH in EtOAc) yielded the title compound as a yellowish crystalline solid (0.473 g, 3.01 mmol, 80%). <sup>1</sup>H-NMR (300 MHz, CD<sub>3</sub>OD): δ 4.11 (*m*, 1H, H<sub>a</sub>), 3.85 (*m*, 2H, H<sub>d</sub>), 2.19 - 2.13 (*m*, 1H, H<sub>e</sub>), 2.01 - 1.95 (*m*, 2H, H<sub>b</sub>), 1.52 - 1.45 (*m*, 2H, H<sub>c</sub>), 1.317 (*m*, 1H, H<sub>f</sub>). <sup>13</sup>C-NMR (125 MHz, CD<sub>3</sub>OD): δ 70.0 (CH), 57.6 (CH), 44.2 (CH<sub>2</sub>), 38.8 (CH<sub>2</sub>). *m/z* (ESI<sup>+</sup>): 158 [M-H]<sup>+</sup>, 130 [MH - N<sub>2</sub>]<sup>+</sup>, 112 [M - N<sub>2</sub> - OH]<sup>+</sup>. FTIR (thin film on CaF<sub>2</sub>) cm<sup>-1</sup>: 3322 (b), 2936 (sh), (N<sub>3</sub>) 2109 (vs), 1461 (sh), 1371 (*m*), 1311(sh), 1268 (sh), 1114 (*s*) 1080(*s*), 1037 (sh), 928 (*m*). Elemental analysis for C<sub>6</sub>H<sub>11</sub>N<sub>3</sub>O<sub>2</sub>, calcd (found) %: C 45.85 (46.11), H 7.05 (7.10), N 26.73 (25.88).

### 7.2.11 *cis*-1,3-Dihydroxy-*trans*-5-aminocyclohexane (**12**)



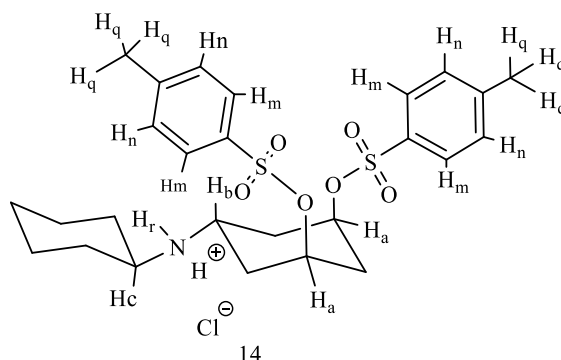
To 27 mg of 10% Pd/C catalyst was added *cis*-1,3-dihydroxy-*trans*-5-azidocyclohexane (**11**) (0.359 g, 2.28 mmol) in ethanol (20 ml). The resulting suspension was stirred under hydrogen at 620 kPa, 30 °C for 18 hours. Filtration of the catalyst and evaporation of the solvent, followed by trituration with ether gave **12** as a white solid (0.285g, 2.17 mmol, 95%). <sup>1</sup>H-NMR (500 MHz, D<sub>2</sub>O): δ 3.97 (*m*, 2H, H<sub>d</sub>), 3.31 (*m*, 1H, H<sub>a</sub>), 2.09 – 1.99 (*m*, 1H, H<sub>e</sub>), 1.70 (*m*, 2H, H<sub>b</sub>), 1.52 – 1.45 (*m*, 2H, H<sub>c</sub>), 1.33 (*m*, 1H, H<sub>f</sub>). <sup>13</sup>C-NMR (125 MHz, D<sub>2</sub>O): δ 65.1 (CH), 43.7 (CH), 41.2 (CH), 39.4 (CH). *m/z* (ESI<sup>+</sup>): 132.2 [M-H]<sup>+</sup>, 114.1 [OH]<sup>+</sup>. FTIR (thin film on CaF<sub>2</sub>) cm<sup>-1</sup>: 3342 (*s*), 3273 (*m*), 2929 (*m*), 2852 (*m*), 1626 (*m*). Elemental analysis for C<sub>6</sub>H<sub>13</sub>NO<sub>2</sub>, calcd (found) %: C 54.94 (55.16), H 9.99 (10.15), N 10.68 (10.44).

### 7.2.12 *cis*-3,5- Dihydroxy-*trans*-cyclohexylaminocyclohexane (**13**)



To *cis*-1,3-dihydroxy-*trans*-5-aminocyclohexane (**12**) (56 mg, 0.426 mmol) in methanol (5 mL) was added cyclohexanone (51 mg, 53  $\mu$ L, 0.512 mmol) and stirred under reflux for 15 hours. The solution was then allowed to cool to room temperature and toluene (20 mL), cyclohexanone (53  $\mu$ L, 0.512 mmol) and ammonium formate (96 mg, 1.534 mmol) added. The resulting mixture was refluxed in a Dean-Stark apparatus for 18 hours. Evaporation of the solvent gave a brown residue which was dissolved in DCM (20 mL) and washed with KOH (1 mL, 20 M). The aqueous layer was washed with DCM (3  $\times$  20 mL), and the organic layers combined dried over  $\text{MgSO}_4$ . Concentration of the solvent to *ca.* 2 mL gave **13** as cream needles (60 mg, 66 %) after 3 days at room temperature, which were collected and washed with hexane (20 mL).  $^1\text{H-NMR}$  (500 MHz,  $\text{CDCl}_3$ ):  $\delta$  4.23 (*m*, 2H,  $\text{H}_a$ ), 3.43 (*m*, 1H,  $\text{H}_b$ ), 2.59 (*m*, 1H,  $\text{H}_c$ ), 2.14 – 2.07 (*m*, 2H,  $\text{H}_i$ ), 2.03 – 1.96 (*m*, 1 H,  $\text{H}_e$ ), 1.92 – 1.86 (*m*, 2H,  $\text{H}_f$ ), 1.76 – 1.68 (*m*, 1H,  $\text{H}_j$ ), 1.67 – 1.58 (*m*, 2H,  $\text{H}_d$ ), 1.36 – 1.28 (*m*, 2H,  $\text{H}_l$ ), 1.28 – 1.20 (*m*, 2H,  $\text{H}_k$ ), 1.19 – 1.10 (*m*, 2H,  $\text{H}_m + \text{H}_g$ ), 1.04 (*pq*, 1H,  $\text{H}_h$ ).  $^{13}\text{C-NMR}$  (125 MHz,  $\text{D}_2\text{O}$ ):  $\delta$  68.1 (CH), 53.2 (CH), 43.0 (CH), 40.6 (CH), 37.6 (CH), 34.2 (CH), 26.1 (CH), 25.24 (CH).  $m/z$  ( $\text{ESI}^+$ ): 214.18 [ $\text{M} + \text{H}$ ] $^+$ . FTIR (thin film on  $\text{CaF}_2$ )  $\text{cm}^{-1}$ : 3267 (b), 2927 (s), 2852 (s), 1448 (s), 1260 (s), 1075 (s), 1017 (s). Elemental analysis for  $\text{C}_{12}\text{H}_{24}\text{NO}_2\text{Cl}$  calcd (found): %: C 57.70 (56.73), H 9.40 (9.69), N 5.61 (5.67).

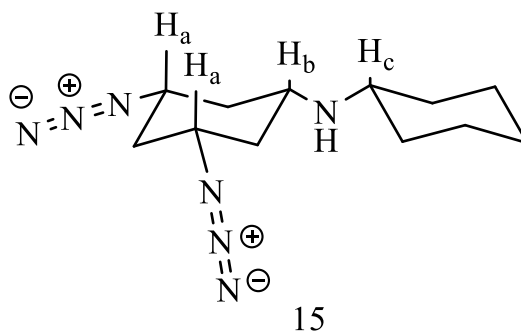
### 7.2.13 *cis*-3,5-Ditosyloxy-*trans*-cyclohexylaminocyclohexane hydrochloride (**14**)



To a stirred solution of *cis*-3,5-dihydroxy-*trans*-cyclohexylaminocyclohexane (**13**) (116 mg, 0.54 mmol) in freshly distilled pyridine (7 mL) at 0 °C was added tosyl chloride (1.03 g, 0.544 mmol). This was left to slowly warm to room temperature over 6 hours and then stirred for a further 3 days. The resulting mixture was added to a stirred slurry of ice giving the formation of a brown precipitate, which was collected and taken up into DCM (20 mL) and washed with water (3 × 15 mL). Drying of the organic layer over MgSO<sub>4</sub>, and evaporation gave **14** as a brown precipitate (119 mg, 0.214 mmol, 40 %). <sup>1</sup>H-NMR (500 MHz, CDCl<sub>3</sub>): δ 8.58 (s, 1H, H<sub>r</sub>), 7.75 (d, 4H, *J* = 8 Hz, H<sub>n</sub>), 7.30 (d, 4H, *J* = 8 Hz, H<sub>m</sub>), 4.9 - 4.86 (m, 2H, H<sub>a</sub>), 3.65-3.55 (m, 1H, H<sub>b</sub>), 2.86 - 2.75 (m, 1H, H<sub>c</sub>), 2.43 (s, 6H, O-Ts-Me, H<sub>q</sub>), 2.14 - 2.03 (m, 2H), 2.01 - 1.93 (m, 1H), 1.93 - 1.83 (m, 2H), 1.77 - 1.69 (m, 2H), 1.69 - 1.51 (m, 4H), 1.48 - 1.32 (m, 2H), 1.20 - 1.01 (m, 3H). <sup>13</sup>C-NMR (125 MHz, D<sub>2</sub>O): δ 149.5 (ArC), 144.9 (ArC), 141.9 (ArC), 133.9 (ArC), 130.08 (ArC), 129.17 (N<sup>+</sup>-C), 127.9 (ArC), 125.9 (N<sup>+</sup>-C), 74.9 (Ts-Me), 24.7 (CH), 21.8 (CH), 21.5 (CH). *m/z* (ESI<sup>+</sup>): 692.2 [M+OTs+H]<sup>+</sup>, 522.2 [M+H]<sup>+</sup>. FTIR (thin film on CaF<sub>2</sub>) cm<sup>-1</sup>: 3417 (b), 2936 (m), 2860 (m), 2552 (m), 2460 (m), 1921 (w), 1595 (s), 1494 (s), 1453 (s), 1359 (m), 1306 (w), 1262 (w), 1175 (s). Elemental analysis for C<sub>26</sub>H<sub>35</sub>NO<sub>6</sub>ClS<sub>2</sub> calcd (found) %: C 56.05 (56.54), H 6.33 (6.31), N 2.51 (2.47).

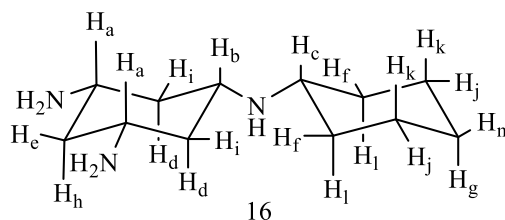


### 7.2.14 *cis*-3,5-Diazido-*cis*-cyclohexylaminocyclohexane (**15**)



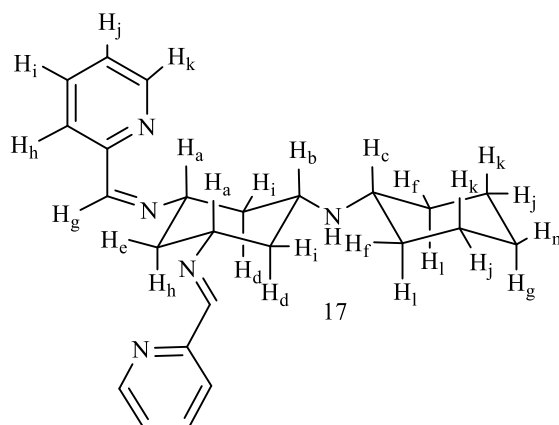
To *cis*-3,5-ditosyloxy-*trans*-cyclohexylaminocyclohexane hydrochloride (**14**) (119 mg, 0.214 mmol) in anhydrous DMF (5 mL) was added sodium azide (0.360 g, 5.48 mmol). The resulting suspension was stirred at 70 °C for 2 days before cooling, addition of DCM (30 mL) and removal of salts by filtration. The salts were washed with DCM (3 × 30 mL), the washings combined with the filtrate and washed with water (3 × 30 mL), and the aqueous layer back extracted with DCM (2 × 30 mL). Combination of the organic layers, drying over MgSO<sub>4</sub> and removal of solvent *in vacuo*, followed by column chromatography on silica with 1:19 EtOAc : hexane, followed by EtOAc, afforded **15** as a pale yellow oil (0.033 g, 0.125 mmol, 50 %). <sup>1</sup>H-NMR (500 MHz, CDCl<sub>3</sub>): δ 3.30 (*m*, 2H, H<sub>a</sub>), 2.81 – 2.67 (*m*, 1H, H<sub>b</sub>), 2.64 – 2.52 (*m*, 1H, H<sub>c</sub>), 2.30-2.19 (*m*, 3H), 1.87-1.79 (*m*, 2H), 1.76-1.69 (*m*, 2H), 1.66-1.56 (*m*, 1H), 1.37-0.97 (*m*, 8H). <sup>13</sup>C-NMR (125 MHz, CDCl<sub>3</sub>): δ 56.2 (CH), 49.3 (CH), 45.5 (CH), 36.9 (CH), 36.17 (CH), 31.3 (CH), 26.0 (CH), 25.1 (CH). *m/z* (ESI<sup>+</sup>): 264.19 [M+H]<sup>+</sup>. FTIR (thin film on CaF<sub>2</sub>) cm<sup>-1</sup>: 2927 (s), 2854 (s), 2079 (vs), 1450 (s), 1374 (s).

### 7.2.15 *cis*-3,5-Diamino -*cis*-cyclohexyl-cyclohexylamine (16)



10% Pd/C (20 mg) was added to a solution of *cis*-3,5-diazido-*cis*-cyclohexylaminocyclohexane (**15**) (0.033 g, 0.125 mmol) in ethanol (3.5 mL). This was treated with hydrogen at 620 kPa, 30 °C with stirring for 18 hours. Removal of Pd/C by filtration, followed by evaporation of the solvent gave the product (**16**) as yellow oil (0.022 g, 0.10 mmol, 82%). <sup>1</sup>H-NMR (500 MHz, CD<sub>3</sub>OD): δ 2.74 (*ptpt*, 1H, H<sub>b</sub>), 2.69 (*ptpt*, 2H, H<sub>a</sub>), 2.63 (*ptpt*, 1H, H<sub>c</sub>), 2.09–1.98 (m, 3H, 2H<sub>i</sub> + H<sub>e</sub>), 1.94–1.86 (m, 2H, H<sub>f</sub>), 1.79–1.72 (m, 2H, H<sub>j</sub>), 1.69–1.61 (m, 1H H<sub>m</sub>), 1.35–1.24 (m, 2H, H<sub>k</sub>), 1.23–1.00 (m, 3H, H<sub>l</sub> + H<sub>g</sub>), 0.94 (*pq*, 1H, H<sub>h</sub>), 0.88 (*pq*, 2H, H<sub>d</sub>). *m/z* (ESI<sup>+</sup>): 212.21 [M+H]<sup>+</sup>. FTIR (thin film on CaF<sub>2</sub>) cm<sup>-1</sup>: 3270 (b), 2927 (s), 2854 (s), 1658 (w), 1573 (w), 1450 (m).

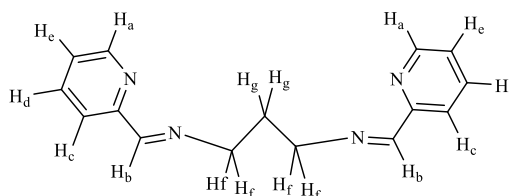
### 7.2.16 *cis*-3,5-Bis[(2-Pyridinyleneamin)]-*cis*-(aminocyclohexyl)-cyclohexane (17)



A methanolic solution (2 mL) of 2-pyridinecarboxaldehyde (36 µL, 0.035 mmol) was added to a solution of *cis*-3,5-diazido-*cis*-cyclohexyl-cyclohexylamine (0.022 g, 0.1025 mmol) and triethylamine (12 µL, 0.09 mmol) in methanol (50 mL). The mixture was refluxed under nitrogen for 20 hours and the volume was then reduced giving red/brown oil. This was extracted from water with DCM (3 × 25 mL), the organic layer back-extracted with water (3 × 25 mL) and dried over MgSO<sub>4</sub>. The brown oil was then dissolved in the minimum of diethylether and precipitated by the addition of hexane,

filtration and drying under vacuum gave the product (0.040 g, 0.0943 mmol, 92%) as a brown/red solid (10% 2-pyridine carboxaldehyde).  $^1\text{H-NMR}$  (500 MHz,  $\text{CDCl}_3$ ):  $\delta$  8.62 (dd, 2H,  $J = 4, 1.6 \text{ Hz}$ ,  $\text{H}_k$ ), 8.43 (s, 2H,  $\text{H}_g$ ), 8.01 – 7.97 (m, 2H,  $\text{H}_h$ ), 7.72 (m, 2H,  $\text{H}_i$ ), 7.72 (m, 2H,  $\text{H}_j$ ). 3.53 (m, 2H,  $\text{H}_a$ ), 2.97 (m, 1H,  $\text{H}_b$ ), 2.61 (m, 1H,  $\text{H}_c$ ), 2.1 – 2.02 (m, 1H,  $\text{H}_e$ ), 1.98 (m, 1H,  $\text{H}_h$ ), 1.9–1.82 (m, 2H,  $\text{H}_i$ ), 1.75–1.66 (m, 2H,  $\text{H}_f$ ), 1.64 – 1.55 (m, 1H,  $\text{H}_m$ ), 1.49 (m, 2H,  $\text{H}_d$ ), 1.30–0.93 (m, 4H,  $2\text{H}_l + 2\text{H}_k$ ), 0.89–0.79 (m, 1H,  $\text{H}_g$ ).  $^{13}\text{C-NMR}$  (125 MHz,  $\text{CDCl}_3$ ): 160.5 (C=N), 154.8 (py -CN), 149.5 (py -CN), 136.7 (py -C), 124.8 (py -C), 121.6 (py -C), 66.6 (CH) 53.4 (CH), 50.3 (CH) 41.2 ( $\text{CH}_2$ ), 41.1 ( $\text{CH}_2$ ), 34.4 ( $\text{CH}_2$ ), 26.2 ( $\text{CH}_2$ ), 25.3 ( $\text{CH}_2$ ).  $m/z$  ( $\text{ESI}^+$ ): 390.26  $[\text{M}+\text{H}]^+$ . FTIR (thin film on  $\text{CaF}_2$ )  $\text{cm}^{-1}$ : 3377 (mb), 3056 (m), 2928 (NH), 2853 (NH), 1645 (s) (C=N), 1588 (s), 1469 (s), 1434 (s), 1322 (w).

#### 7.2.17 N,N'-Bis(2-pyridylmethylene)-1,3-diaminopropane (**L4 18**)

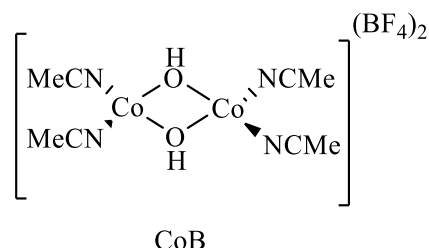


18, L4

1,3-Diamino propane (0.74 g, 10 mmol) and 2-pyridine carboxaldehyde (2.14 g, 20 mmol) were added to ethanol (20 mL), and refluxed under an atmosphere of nitrogen for 17 hours. The solvent was removed under vacuum, yielding a brown oil. Volatiles were removed by three washings of diethyl ether (10 mL), after which the oil was dissolved in a minimum volume of dichloromethane and an excess of diethyl ether was added, causing precipitation of a grey solid. The mixture was filtered, and the solvent was removed from the filtrate under vacuum, yielding DDPP (**18, L4**) (2.07 g, 8.20 mmol, 82%) as a reddish-brown oil.  $^1\text{H-NMR}$  (500 MHz,  $\text{CDCl}_3$ ):  $\delta$  8.57 (dd, 2H,  $J = 5, 2 \text{ Hz}$ ,  $\text{H}_a$ ), 8.35 (s, 2H,  $\text{H}_b$ ), 7.93 (m, 2H,  $\text{H}_c$ ), 7.66 (m, 2H,  $\text{H}_d$ ), 7.24 (m, 2H,  $\text{H}_e$ ), 3.73 (td, 4H,  $J = 6.8, 1.4 \text{ Hz}$ ,  $\text{H}_f$ ), 2.10 (p, 2H,  $J = 6.8 \text{ Hz}$ ,  $\text{H}_g$ ).  $^{13}\text{C-NMR}$  (500 MHz;  $\text{CDCl}_3$ ,  $\delta$ ): 160.38, 152.69, 147.55, 134.66, 122.81, 119.39, 57.11, 29.82.  $m/z$  ( $\text{ESI}^+$ ): 253.14  $[\text{M}+\text{H}]^+$ . FTIR (thin film on  $\text{CaF}_2$ )  $\text{cm}^{-1}$ : 3054 (w), 2924 (w), 2846 (m), 1650 (s) 1586 (s).

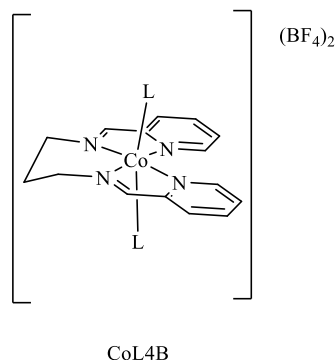
### 7.3 Metal complex synthesis

#### 7.3.1 $[\text{Co}_2(\text{OH})_2(\text{MeCN}_4)](\text{BF}_4)_2$ (**CoB**)



Acetonitrile (80 mL) was added to  $[\text{Co}(\text{H}_2\text{O})_6](\text{BF}_4)_2$  (5.01 g, 20.82 mmol), stirred and heated to reflux for *ca.* 144 hours, with a Soxhlet extractor attached containing 4 Å molecular sieves. The mixture was filtered via cannula, yielding a clear pink solution. The solvent was then removed under vacuum, and precipitated through the addition of diethyl ether (20 mL), filtration and drying yielded (**CoB**) (3.86 g, 8.07 mmol, 54%) as a pale pink/orange solid. FTIR (MeCN solution)  $\text{cm}^{-1}$ : 3396 (m), 3006 (w), 2944 (m), 2316 (s), 2288 (s). Elemental analysis for  $\text{C}_8\text{H}_{14}\text{Co}_2\text{N}_4\text{O}_2 \text{ B}_2\text{F}_8$  calcd (found) %: C 19.62 (19.97), H 2.88 (2.94), N 11.40 (11.40).

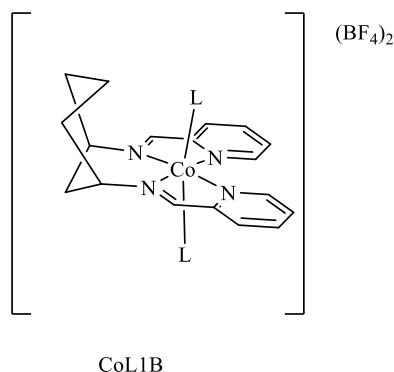
#### 7.3.2 $[\text{Co}(\text{DDPP})\text{L}_2](\text{BF}_4)_2$ (**L** = solvent, **CoL4B**)



**L4** (63 mg, 0.25 mmol) in acetonitrile (25 mL) was added dropwise to a solution of (**CoB**) (0.12 g, 0.25 mmol) in acetonitrile (2.5 mL), with stirring at room temperature. Once all (**CoB**) was added, the reaction was continued for a further 30 minutes, yielding a brown solution. The solvent was removed under vacuum, and the residue dissolved in a minimum of DCM and precipitated with an excess of diethyl ether with cooling, filtering yielded (**CoL4B**) (0.12 g, 0.21 mmol, 84%) as a brown solid.  $^1\text{H}$ -NMR (500 MHz;  $\text{CD}_3\text{CN}$ ,  $\delta$ ): 86.38, 54.99, 43.52, 29.31, 14.06, 8.52, 4.82, -77.91.  $^{19}\text{F}$ -NMR (500 MHz,  $\text{CD}_3\text{CN}$ ,  $\delta$ ): -148.78. FTIR (MeCN solution)  $\text{cm}^{-1}$ : 2879 (w), 1639 (s), 1598 (s).  $m/z$

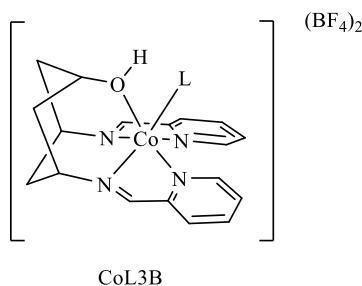
(ESI<sup>+</sup>): 176.05 [M-2BF<sub>4</sub>-NCMe]<sup>2+</sup>. Elemental analysis is consistent with hydrolysis of one BF<sub>4</sub> to F<sup>-</sup> with loss of BF<sub>3</sub> *in vacuo* - for C<sub>15</sub>H<sub>16</sub>CoN<sub>4</sub>BF<sub>5</sub> calcd (found) %: C 43.20 (42.97), H 3.87 (3.51), N 13.43 (13.58).

### 7.3.3 [Co(DDP)L<sub>2</sub>](BF<sub>4</sub>)<sub>2</sub> (L = solvent, CoL1B)



**L1** (0.03 g, 0.1 mmol) was dissolved in acetonitrile (7 mL). The solution was added dropwise to a solution of **CoB** (48 mg, 0.1 mmol) in acetonitrile (1 mL), whilst stirring at room temperature. Once all **L1** was added, the reaction was continued for a further 30 minutes, yielding a brown solution. The solvent was removed under vacuum, and the residue was dissolved in a minimum of acetonitrile and precipitated by the addition of excess diethyl ether, yielding a brown precipitate, which with filtration isolated **CoL1B** (0.05 mg, 0.08 mmol, 80%) as a brown solid. <sup>1</sup>H-NMR (500 MHz; CD<sub>3</sub>CN): δ 96.77, 52.47, 45.32, 34.21, 9.71, 5.00, 3.57, -22.27, -24, 26, -62.26, -95.35, -112.93. <sup>19</sup>F-NMR (500 MHz; CD<sub>3</sub>CN): δ -149.52 (s). FTIR (MeCN solution) cm<sup>-1</sup>: 3014 (m), 1636 (s). ESI-MS Calc. For *m/z* (ESI<sup>+</sup>): 438.10 [M-2BF<sub>4</sub>-NCMe]<sup>2+</sup>.

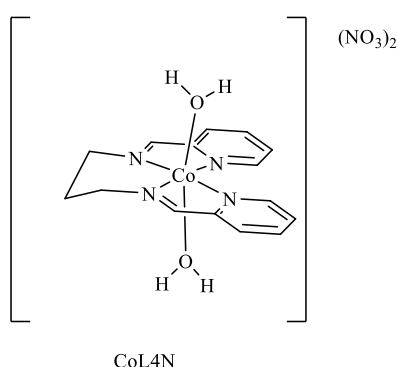
### 7.3.4 [Co(DDOPi)(L)](BF<sub>4</sub>)<sub>2</sub> (L = solvent, CoL3B)



**L3** (32 mg, 0.1 mmol) was dissolved in acetonitrile (10 mL). The solution was added dropwise to a solution of **L3** (48 mg, 0.1 mmol) in acetonitrile (1 mL), whilst stirring at room temperature. Once all **L3** was added, the reaction was continued for a further 30

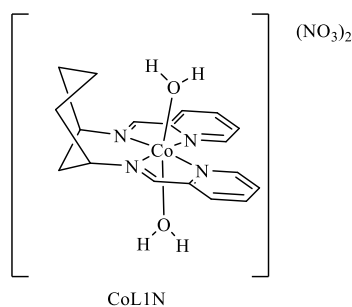
minutes, affording a brown solution. The solvent was removed under vacuum, and the residue dissolved in diethyl ether, forming a brown precipitate. The mixture was filtered, yielding **CoL3B** (40 mg, 0.07 mmol, 70%) as a brown solid.  $^1\text{H-NMR}$  (500 MHz,  $\text{CD}_3\text{CN}$ ):  $\delta$  78.53, 58.12, 56.14, 54.86, 38.55, 32.13, 27.63, 15.89, 9.92, 5.53, 3.35, 1.05.  $^{19}\text{F-NMR}$  (500 MHz,  $\text{CD}_3\text{CN}$ ,  $\delta$ ): -149.46 (s). FTIR (MeCN solution)  $\text{cm}^{-1}$ : 3308 (br), 2866 (m), 1639 (s), 1601 (s).  $m/z$  ( $\text{ESI}^+$ ): 183.55  $[\text{M}-2\text{BF}_4-\text{NCMe}]^{2+}$ . Elemental analysis for  $\text{CoC}_{18}\text{N}_4\text{H}_{22}\text{B}_2\text{F}_8\text{O}_2\cdot\text{H}_2\text{O}$  calcd (found) %: C 36.90 (36.23), H 4.30 (3.99), N 9.56 (9.77).

### 7.3.5 $[\text{Co}(\text{DDPP})(\text{H}_2\text{O})_2(\text{NO}_3)_2]$ (**CoL4N**)



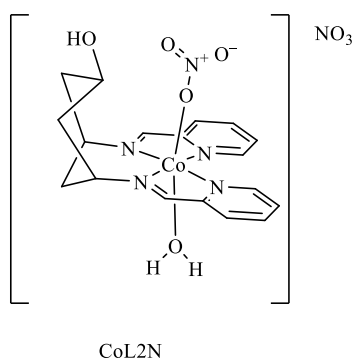
**L4** (33 mg, 0.132 mmol) as a 0.01 M methanolic solution (13.2 mL) was added dropwise over 3.5 hours to a solution of  $\text{Co}(\text{NO}_3)_2\cdot 6\text{H}_2\text{O}$  (34.9 mg, 0.115 mmol) in methanol (0.5 mL). A colour change from pink to orange was observed. After the addition was complete the solution was stirred for a further 30 minutes, reduced to *ca* 2 mL and set to crystallise by  $\text{Et}_2\text{O}$  diffusion. After 12 hours orange-brown crystals of **CoL4N** were formed (23 mg, 0.0575 mmol, 23%).  $^1\text{H-NMR}$  (300 MHz,  $\text{CD}_3\text{OD}$ ):  $\delta$  68.52, 61.74, 36.71, 19.3, 4.94, 3.29, 2.07, -60.  $m/z$  ( $\text{ESI}^+$ ): 310.06  $[\text{M}+ -\text{N}_2\text{O}_6\text{H}]$ . IR (MeOH)  $\text{cm}^{-1}$ : 1650 (s). Elemental analysis for  $\text{C}_{18}\text{H}_{20}\text{CoN}_6\text{O}_6$  calcd (found) %: C 41.39 (41.7), H 3.71 (3.5), N 19.31 (19.20).

### 7.3.6 Co[DDP](NO<sub>3</sub>)<sub>2</sub> (CoL1N)



**L1** (0.021 g, 0.07185 mmol) as a 0.01 M methanolic solution (7 mL) was added dropwise over 3.5 hours to a solution of Co(NO<sub>3</sub>)<sub>2</sub>·6H<sub>2</sub>O (0.022 g, 0.007185 mmol) in methanol (1 mL). A colour change from pink to orange was observed. After the addition was complete the solution was stirred for a further 30 minutes, reduced to *ca* 3 mL and set to crystallise by Et<sub>2</sub>O diffusion. After 12 hours orange-brown crystals of **CoL1N** were formed (40 mg, 0.062 mmol, 86%). <sup>1</sup>H-NMR (300 MHz, CD<sub>3</sub>OD): δ 73.63 - 77.67, 64.86, 37.61, 22.46, 1.60 - 3.07, 1.51 - 1.98, 0.91 - 1.05, -6.75, -15.99, -16.6, -38.08, -36.36, -50.12, -59.33, -57.14. *m/z* (ESI<sup>+</sup>): 350.09 [M<sup>+</sup> - N<sub>2</sub>O<sub>6</sub>H]. IR (MeOH) /cm<sup>-1</sup>: 1650 (s). Elemental analysis for C<sub>18</sub>H<sub>20</sub>CoN<sub>6</sub>O<sub>6</sub> calcd (found) %: C 45.48 (45.30), H 4.24 (4.10), N 17.68 (17.90).

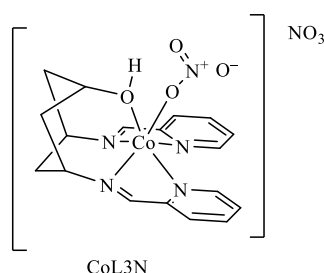
### 7.3.7 Co[DDOP](NO<sub>3</sub>)<sub>2</sub> (CoL2N)



**L2** (23 mg, 0.7 mmol) as a 0.01 M methanolic solution (8 mL) was added dropwise over 3.5 hours to a solution of Co(NO<sub>3</sub>)<sub>2</sub>·6H<sub>2</sub>O (27 mg, 0.07 mmol) in methanol (1 mL). A colour change from pink to orange was observed. After the addition was complete the solution was stirred for a further 30 minutes, reduced to *c.a.* 2 mL and set to crystallise by Et<sub>2</sub>O diffusion. After 24 hours orange-brown crystals of *cis*-3,5-*bis*[2-pyridinyleneamin]-*trans*-hydroxycyclohexane-κ<sup>4</sup>-N,N',N'',N'''-nitrato-aquacobalt(II)

nitrate were formed (10 mg, 0.019 mmol, 27 %).  $^1\text{H-NMR}$  (300 MHz,  $\text{CD}_3\text{OD}$ ):  $\delta$  74 (br), 64.8, 37.3, 22.2, 4.8, 3.8, -15.9, -17.4 (sh), -37.5 (br), -50.3 (sh), -59.3 (sh).  $m/z$  ( $\text{ESI}^+$ ): 429.08  $[\text{M-H}_2\text{O-NO}_3]^+$ . FTIR (diamond anvil)  $\text{cm}^{-1}$ : 3331(br) (OH), 2940 (w) (CH), 1646 (m) (C=N), 1599 (s), 1569 (w), 1480 (w), 1422 (m), 1376 (m), 1293 (coordinated  $\text{NO}_3^-$ ), 1070 (m) (C-O). Elemental analysis for  $\text{C}_{18}\text{H}_{22}\text{CoN}_6\text{O}_8$  calcd (found) %: C 42.45 (42.48), H 4.35 (4.34), N 16.50 (16.27).

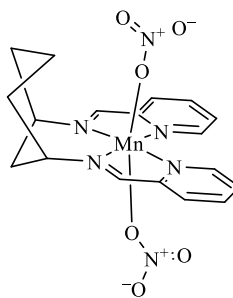
### 7.3.8 $\text{Co}[\text{DDOPI}](\text{NO}_3)_2$ (**CoL3N**)



**L3** (20 mg, 0.06 mmol) as a 0.01 M methanolic solution (7 mL) was added dropwise over 3.5 hours to a solution of  $\text{Co}(\text{NO}_3)_2 \cdot 6\text{H}_2\text{O}$  (23 mg, 0.06 mmol) in methanol (0.5 mL). A colour change from pink to brown was observed. After the addition was complete the solution was stirred for a further 30 minutes, reduced to *c.a.* 2 mL and set to crystallise by  $\text{Et}_2\text{O}$  diffusion. After 1-week brown crystals of **CoL3N** were grown by  $\text{Et}_2\text{O}$  diffusion (7.8 mg, 0.018 mmol, 30%).  $^1\text{H-NMR}$  (300 MHz,  $\text{CD}_3\text{OD}$ ):  $\delta$  66 (sh), 47, 41, 35 (br), 28 (sh), 23 (br), 7, 5, 1, 0.  $m/z$  ( $\text{ESI}^+$ ): 429.08  $[\text{M-NO}_3]^+$ . FTIR (thin film on  $\text{CaF}_2$ )  $\text{cm}^{-1}$ : 3096 (m) (OH), 2929 (w) (CH), 1650 (m) 1599 (s) (C=N), 1446 (s), 1391 (s), 1309 (coordinated  $\text{NO}_3^-$ ), 1128 (m) (C-O). Elemental analysis for  $\text{C}_{18}\text{H}_{20}\text{CoN}_6\text{O}_7$ , calcd (found) %: C 44.0 (43.56), H 4.10 (4.15), N 17.11 (16.94).



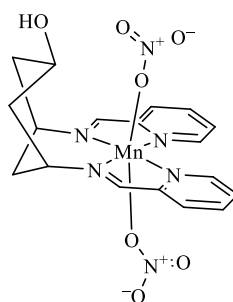
### 7.3.9 Mn[DDP](NO<sub>3</sub>)<sub>2</sub> (MnL1N)



MnL1N

**L1** (33 mg, 0.11 mmol) as a 0.01 M methanolic solution (12.6 mL) was added dropwise over 3.5 hours to a solution of Mn(NO<sub>3</sub>)<sub>2</sub>·6H<sub>2</sub>O (28 mg, 0.11 mmol) in methanol (0.5 mL). The solution deepened in colour from pale to darker yellow. After the addition was complete the solution was stirred for a further 30 minutes, reduced to *c.a.* 3 mL at the rotary evaporator and set to crystallise by Et<sub>2</sub>O diffusion. After 2 hours pale yellow needles of **MnL1N** were formed (27.9 mg, 0.059 mmol, 52%). FTIR (thin film on CaF<sub>2</sub>) cm<sup>-1</sup>: 2941 (w) (CH), 2922 (w), 1635 (s) 1592 (s) (C=N), 1478 (s), 1442 (s), 1300 (coordinated NO<sub>3</sub><sup>-</sup>), 1260 (s). *m/z* (ESI<sup>+</sup>): 473.14 [M-NO<sub>3</sub>]<sup>+</sup>. Elemental analysis for C<sub>18</sub>H<sub>20</sub>MnN<sub>6</sub>O<sub>6</sub>·H<sub>2</sub>O, calcd (found) %: C 44.18 (44.51), H 4.53 (4.25), N 17.17 (17.11)

### 7.3.10 Mn[DDOP](NO<sub>3</sub>)<sub>2</sub> (MnL2N)

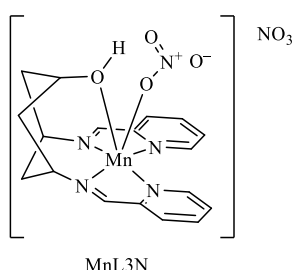


MnL2N

**L2** (82 mg, 0.26 mmol) as a 0.01 M methanolic solution (28.9 mL) was added dropwise over 3.5 hours to a solution of Mn(NO<sub>3</sub>)<sub>2</sub>·6H<sub>2</sub>O (65 g, 0.26 mmol) in methanol (0.5 mL). The solution deepened in colour from pale to darker yellow. After the addition was complete the solution was stirred for a further 30 minutes, reduced to *c.a.* 3 mL at the

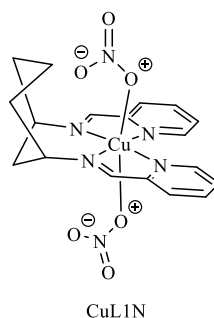
rotary evaporator and set to crystallise by Et<sub>2</sub>O diffusion. After 2 hours yellow crystals of **MnL2N** were formed (20 g, 0.059 mmol, 16%). *m/z* (ESI<sup>+</sup>): 429.08 [M-H<sub>2</sub>O-NO<sub>3</sub>]<sup>+</sup>. FTIR (thin film on CaF<sub>2</sub>) cm<sup>-1</sup>: 3368 (br, m) (OH), 2936 (w) (CH), 2902 (w), 1644 (s) 1596 (s) (C=N), 1444 (s), 1389 (s), 1308 (coordinated NO<sub>3</sub><sup>-</sup>), 1260 (s), 1060 (C-O). Elemental analysis for C<sub>18</sub>H<sub>20</sub>MnN<sub>6</sub>O<sub>7</sub>, calcd (found) %: C 44.36 (44.07), H 4.14 (4.32), N 17.25 (17.01).

### 7.3.11 Mn[DDOP](NO<sub>3</sub>)<sub>2</sub> (**MnL3N**)



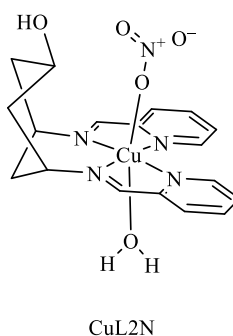
**L3** (14 mg, 0.04347 mmol) as a 0.01 M methanolic solution (4.8 mL) was added dropwise over 3.5 hours to a solution of Mn(NO<sub>3</sub>)<sub>2</sub>·6H<sub>2</sub>O (22 mg, 0.04347 mmol) in methanol (0.5 mL). The solution deepened in colour from pale to darker yellow. After the addition was complete the solution was stirred for a further 30 minutes, reduced to *c.a.* 2 mL and set to crystallise by Et<sub>2</sub>O diffusion. After 12 hours yellow crystals of **MnL3N** were grown by Et<sub>2</sub>O diffusion (7.2 mg, 0.01478 mmol, 34%). *m/z* (ESI<sup>+</sup>): 429.08 [M-NO<sub>3</sub>]<sup>+</sup>. FTIR (thin film on CaF<sub>2</sub>) cm<sup>-1</sup>: 2919 (w) (CH), 2848 (w), 1653 (s) 1559 (s) (C=N), 1541 (s), 1457 (s), 1395(s) 1301 (coordinated NO<sub>3</sub><sup>-</sup>), 1129 (s), 1011 (C-O). Elemental analysis for C<sub>18</sub>H<sub>20</sub>MnN<sub>6</sub>O<sub>7</sub>, calcd (found) %: C 44.36 (44.44), H 4.14 (4.17), N 17.25 (17.09)

### 7.3.12 Cu[DDP](NO<sub>3</sub>)<sub>2</sub> (CuL1N)



**L1** (27 mg, 0.0915 mmol) as a 0.01 M methanolic solution (10.2 mL) was added to a solution of Cu(NO<sub>3</sub>)<sub>2</sub>·6H<sub>2</sub>O (27 mg, 0.0915 mmol) in methanol (0.5 mL) and stirred for 16 hours at room temperature. A colour change from blue to dark green was observed. After which the solution was reduced to *c.a.* 3 mL at the rotary evaporator and set to crystallise by Et<sub>2</sub>O diffusion. After 12 hours dark green crystals of **CuL1N** formed (18 mg, 0.0375 mmol, 41%). *m/z* (ESI<sup>+</sup>): 417.09 [M-NO<sub>3</sub>]<sup>+</sup>. FTIR (thin film on CaF<sub>2</sub>) cm<sup>-1</sup>: 3445 (m) (OH), 3079 (w) (CH), 2936 (w) (CH), 2359, 1645 (s) 1604 (s) (C=N), 1484 (s), 1378 (s), 1335 (coordinated NO<sub>3</sub><sup>-</sup>), 1226 (m) (C-O). Elemental analysis for C<sub>18</sub>H<sub>22</sub>CuN<sub>6</sub>O<sub>7</sub>, calcd (found) %: C 43.42 (43.15), H 4.45 (4.38), N 16.88 (16.49).

### 7.3.13 Cu[DDOP](NO<sub>3</sub>)<sub>2</sub> (CuL2N)



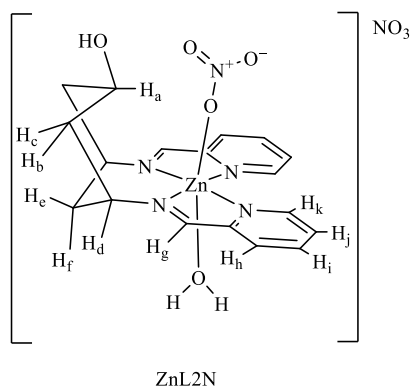
**L2** (70 mg, 0.266 mmol) as a 0.01 M methanolic solution (20 mL) was added to a solution of Cu(NO<sub>3</sub>)<sub>2</sub>·6H<sub>2</sub>O (55 mg, 0.266 mmol) in methanol (1 mL) and stirred for 16 hours at room temperature. A colour change from blue to dark green was observed. After which the solution was reduced to *c.a.* 3 mL at the rotary evaporator and set to crystallise by Et<sub>2</sub>O diffusion. After 12 hours dark green crystals of **CuL2N** were formed (60 mg, 0.117



ZnL1N

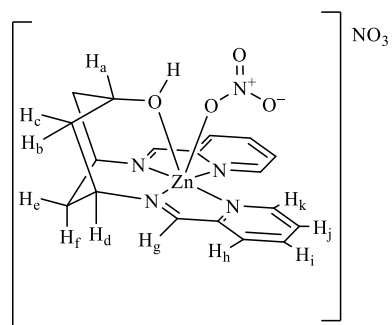
245

### 7.3.16 Zn[DDOP](NO<sub>3</sub>)<sub>2</sub> (ZnL2N)



**L2** (44 mg, 0.14 mmol) as a 0.01 M methanolic solution (15.6 mL) was added to a solution of Zn(NO<sub>3</sub>)<sub>2</sub>·6H<sub>2</sub>O (36 mg, 0.14 mmol) in methanol (0.5 mL) and stirred for 2 hours at room temperature. The colour of the solution remained pale yellow throughout. After which the solution was reduced to *c.a.* 2 mL at the rotary evaporator and set to crystallise by Et<sub>2</sub>O diffusion. After 12 hours colourless needles of **ZnL2N** were formed (13.3 mg, 0.0258 mmol, 18 %). <sup>1</sup>H-NMR (500 MHz, CD<sub>3</sub>OD): δ 9.19 (d, 2H, *J* = 4.8 Hz, H<sub>k</sub>), 8.9 (s, 2H, H<sub>g</sub>), 8.44 (*ptd*, 2H, H<sub>i</sub>), 8.16 (d, 2H, *J* = 7.57 Hz, H<sub>h</sub>), 8.08–8.03 (m, 2H, H<sub>j</sub>), 4.64 – 4.54 (m, 2H, H<sub>d</sub>), 4.35 (*ptpt*, 1H, H<sub>a</sub>), 2.30–2.23 (m, 4H, 2H<sub>b</sub> + H<sub>e</sub> + H<sub>f</sub>), 2.04 (*ptd*, 2H, H<sub>c</sub>). <sup>13</sup>C-NMR (125 MHz, CD<sub>3</sub>OD): δ 164.2 (C=N), 151.4 (ArC), 148.1 (ArC), 143.5 (ArC), 131.0 (ArC), 130.2 (ArC), 65.5 (CH), 61.0 (CH), 43.4 (CH<sub>2</sub>), 33.8 (CH<sub>2</sub>). *m/z* (ESI<sup>+</sup>): 434.08 [M-H<sub>2</sub>O-NO<sub>3</sub>]<sup>+</sup>. FTIR (thin film on CaF<sub>2</sub>) cm<sup>-1</sup>: 3368 (s) (OH), 2932 (m) (CH), 2361 (CH), 1653 (s) (C=N), 1601 (s), 1570 (w), 1559 (w), 1541(w), 1386 (s) (NO<sub>3</sub><sup>-</sup>), 1309 (s) 1065 (s), 1020 (w) (C-O). Elemental analysis for C<sub>18</sub>H<sub>22</sub>ZnN<sub>6</sub>O<sub>8</sub>, calcd (found) %: C 41.92 (42.00), H 4.30 (4.25), N 16.29 (15.89).

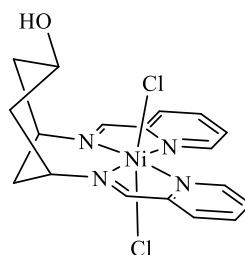
### 7.3.17 Zn[DDOP](NO<sub>3</sub>)<sub>2</sub> (ZnL3N)



ZnL3N

**L3** (48 mg, 0.1512 mmol) as a 0.01 M methanolic solution (16.8 mL) was added to a solution of Zn(NO<sub>3</sub>)<sub>2</sub>·6H<sub>2</sub>O (40 mg, 0.1512 mmol) in methanol (1 mL) and stirred for 2 hours at room temperature. The colour of the solution remained pale yellow throughout. After which the solution was reduced to *c.a.* 2 mL at the rotary evaporator and set to crystallise by Et<sub>2</sub>O diffusion. After 12 hours colourless needles crystals of **ZnL3N** were grown by Et<sub>2</sub>O diffusion (18 mg, 0.0363 mmol, 24%). <sup>1</sup>H-NMR (500 MHz, CD<sub>3</sub>OD): δ 8.91 (d, 2H, *J* = 4.8 Hz, H<sub>k</sub>), 8.73 (s, 2H, H<sub>g</sub>), 8.31 (*ptd*, 2H, H<sub>i</sub>), 8.01 (d, 2H, *J* = 7.5 Hz, H<sub>h</sub>), 7.92 (m, 2H, H<sub>j</sub>), 4.57 (*pp*, 2H, H<sub>d</sub>), 4.54 (*pp*, 1H, H<sub>a</sub>), 2.57 (dt, 1H, *J* = 14.7, 3.3 Hz, H<sub>f</sub>), 2.38 (*dpt*, 2H, *J* = 14.6 Hz, H<sub>b</sub>), 2.32- 2.26 (m, 2H, H<sub>c</sub>), 2.12 (*dpt*, 1H, *J* = 12.9 Hz, H<sub>e</sub>). <sup>13</sup>C-NMR (125 MHz, CD<sub>3</sub>OD): δ 160.6 (C=N), 151.1 (ArC), 148.7 (ArC), 143.0 (ArC), 130.3 (ArC), 129.3 (ArC), 68.6 (CH), 64.2 (CH), 39.1 (CH<sub>2</sub>), 38.7 (CH<sub>2</sub>). *m/z* (ESI<sup>+</sup>): 371.08 [M<sup>+</sup>-H<sup>+</sup>-2(NO<sub>3</sub>)]. FTIR (thin film on CaF<sub>2</sub>) cm<sup>-1</sup>: 3223 (s) (OH), 2925 (m) (CH), 2853 (CH), 1742 (s), 1656 (s) (C=N), 1599 (s), 1446 (s), 1386 (s) (NO<sub>3</sub><sup>-</sup>), 1311 (s) 1034 (s), 1014 (w) (C-O). Elemental analysis for C<sub>18</sub>H<sub>20</sub>ZnN<sub>6</sub>O<sub>7</sub>, calcd (found): % C 43.43 (43.65), H 4.05 (3.95), N 16.88 (16.73).

### 7.3.18 Ni[DDOP]Cl<sub>2</sub> (NiL2C)



NiL2C

**L2** (70 mg, 0.226 mmol) as a 0.01 M methanolic solution (20 mL) was added dropwise to NiCl<sub>2</sub>·6H<sub>2</sub>O (54 mg, 0.226 mmol) in methanol (5 mL) and the resulting yellow solution stirred for 2 hours, before the volume was reduced to *ca* 3 mL *in vacuo*. Diffusion of ether into the methanolic solution over 36 hours produced large, green block crystals of the title compound (24 mg, 0.0491 mmol, 22%). FTIR (thin film on CaF<sub>2</sub>) cm<sup>-1</sup>: 3501 (s) (OH), 3058 (w), 2919 (w) (CH), 1648 (m) (C=N), 1599 (s), 1481 (w), 1446 (w), 1389 (w), 1308 (m), 1219 (w), 1158 (w), 1120 (w), 1050 (m) (C-O), 1015 (w), 978 (w), 782 (s), 638 (w). Elemental analysis for C<sub>19</sub>H<sub>26</sub>Cl<sub>2</sub>N<sub>4</sub>NiO<sub>3</sub>, calcd (found): % C 47.41 (47.15), H 4.86 (4.85), N 12.29 (11.93).



## References

- <sup>1</sup> Newton, J.; *Uncommon Friends: Life with Thomas Edison, Henry Ford, Harvey Firestone, Alexis Carrel, and Charles Lindbergh. New York: Harcourt, 1987.*
- <sup>2</sup> R.K. Pachauri and L.A. Meyer, IPCC, **2014**: Climate Change 2014: Synthesis Report. Contribution of Working Groups I, II and III to the Fifth Assessment Report of the Intergovernmental Panel on Climate Change. *IPCC*, Geneva, Switzerland, 151.
- <sup>3</sup> BP: Statistical Review of World Energy, Workbook (xlsx), London,  
[http://www.iea.org/publications/freepublications/publication/KeyWorld\\_Statistics\\_2015.pdf](http://www.iea.org/publications/freepublications/publication/KeyWorld_Statistics_2015.pdf) (accessed 17/05/2017)
- <sup>4</sup> Key World Energy Statistics 2015, *IEA*. **2015**, 37, 8;  
<http://www.iea.org/publications/freepublications/> (accessed 17/05/2017)
- <sup>5</sup> Hoffert, M. I.; Caldeira, K.; Jain, A. K.; Haites, E. F.; Harvey, L. D. D.; Potter, S. D.; Schlesinger, M. E.; Schneider, S. H.; Watts, R. G.; Wigley, T. M. L.; *Nature.*, **1998**, 395, 881-884.
- <sup>6</sup> Lewis, N. S. & Nocera, D. G; *Pro. Natl. Acad. Sci USA.*, **2006**, 103, 15729-15735.
- <sup>7</sup> 2013 World population data sheet; population reference Bureau: Washington, DC, **2013**;  
<http://www.prb.org/wpds/2013/> (accessed 19/05/2017)
- <sup>8</sup> Cook, T. R.; Dogutan, D. K.; Reece, S. Y.; Surendranath, Y.; Teets, T. S. & Nocera, D. G.; *Chem. Rev.*, **2010**, 110, 6474-6502.
- <sup>9</sup> [www.worldcoal.org](http://www.worldcoal.org) (accessed 20/05/2017)
- <sup>10</sup> Abbott, D.; *Proc. IEEE*, , **2010**, 98, 42-66.
- <sup>11</sup> Lewis, N. S. & Nocera, D. G; *Pro. Natl. Acad. Sci USA.*, **2006**, 103, 15729-15735.
- <sup>12</sup> Lewis, N. S.; *AAAS.*, **2007**, 315, 798-801.
- <sup>13</sup> Pitts, R.; Buttery R.; Pinches, S.; *Phys. World*, **2006**, 19, 20-26.
- <sup>14</sup> Bolton, J. R. & Hall, D. O.; *Annual Review Energy, Annual Reviews*, **1979**, 4, 353-401.
- <sup>15</sup> Rand, D. & Dell, R.; *J. Power Sources*, **2005**, 144, 568-578.
- <sup>16</sup> Schuiling, R. D.; Badescu, V.; Cathcart, R. B.; Seoud, J. & Hanekamp, J. C.;  
*IJGENVI, Inderscience Publishers*, **2007**, 7, 341-343.
- <sup>17</sup> Pollack, H. N.; Hurter, S. J.; Johnson, J. R.; *Rev. Geophys.* **1993**, 31, 267-280.
- <sup>18</sup> <http://www.wwindea.org/wwea-half-year-report-worldwind-wind-capacity-reached-456-gw/>- accessed 19/12/2016
- <sup>19</sup> Marsh, G.; *Renewable Energy Focus, Elsevier BV*, **2007**, 8, 42-45.

- <sup>20</sup> Hamlen, R. D.; Atwater, T. B. in *Handbook of Batteries*, 3rd ed.; Linden, D.; Reddy, T. B., Eds.; New York: McGraw-Hill, **2002**.
- <sup>21</sup> Goodenough, J. B.; Abruna, H. D.; Buchanan, M.V.; *Technology and Applied R&D Needs for Electrical Energy Storage; A Resource Document for Basic Research Needs for Electrical Energy Storage*, Washington, DC: U.S. Department of Energy, **2007**.
- <sup>22</sup> Palacin, M. R.; *Chem. Soc. Rev.* **2009**, 38, 2565.
- <sup>23</sup> Jin., S-H.; Jiang D.; LI Xue-qin, Sun J-W.; *Journal Zhejiang University Sci.*, **2004**, 5, 897-899.
- <sup>24</sup> Schulz, H.; *Applied Catalysis A: General*, **1999**, 186, 3–12.
- <sup>25</sup> Reece, S. Y.; Hamel, J. A.; Sung, K.; Jarvi, T. D.; Esswein, A. J.; Pijpers J. J. H.; Nocera, D. G.; *Science*, **2011**, 334, 645-648.
- <sup>26</sup> Bolton J.R., Hall D.O.; *Ann. Rev. Energy*, **1979** 4, 353–401.
- <sup>27</sup> Iordanova, N.; Hammes-Schiffer, S. J.; *Am. Chem. Soc.*, **2002**, 124, 4848-4850.
- <sup>28</sup> Binstead, R. A.; Meyer, T. J. J.; *Am. Chem. Soc.*, **1987**, 109, 3287-3289.
- <sup>29</sup> Farrer, B. T.; Thorp, H. H.; *Inorg. Chem.*, **1999**, 38, 2497-2501.
- <sup>30</sup> Weinberg, D.R.; Gagliardi, C. J.; Hull, J. F.; Murphy, C. F.; Kent, C. A.; Westlake, B. C.; Paul, A.; Ess, D. H.; McCafferty, D. G. and Meyer, T. J.; *Chem. Rev.*, **2012**, 112, 4016-4093.
- <sup>31</sup> Artero, V.; Fontecave, M.; *Chem. Soc. Rev.*, **2013**, 42, 2338-2341.
- <sup>32</sup> Rzaeva, M.P.; Salamov, O.M.; Kerimov, M.K.; *Int. J. Hydrog. Energy*, **2001**, 26, 195–201.
- <sup>33</sup> Yilanci, A.; Dincer, I.; Ozturk, H.K.; *Prog. Energy Combust Sci.*, **2009**, 35, 231–244.
- <sup>34</sup> Subbaraman, R.; Tripkovic, D.; Strmcnik, D.; Chang, K-C.; Uchimura, M.; Paulikas, A. P.; Stamenkovic, V.; Markovic, N. M.; *Science*, **2011**, 334, 1256–1260.
- <sup>35</sup> Yin, H. J.; Zhao, S. L.; Zhao, K. Muqsit, A.; Tang, H. J.; Chang, L.; Zhao, H. J.; Gao, Y.; Tang, Z. Y.; *Nat. Commun.*, **2015**, 6, 6430–6442.
- <sup>36</sup> Frey, M.; *Chem Bio Chem*, **2002**, 3, 153–160.
- <sup>37</sup> Steinfeld, A.; *Sol Energy*, **2005**, 78, 603–615.
- <sup>38</sup> Tard, C.; Pickett, C. J.; *Chem. Rev.*, **2009**, 109, 2245-2274.
- <sup>39</sup> Tard, C.; Liu, X.; Ibrahim, S. K.; Bruschi, M.; De Gioia, L.; Davies, S. C.; Yang, X.; Wang, L.-S.; Sawers, G.; Pickett, C. J.; *Nature*, **2005**, 433, 610 - 613.
- <sup>40</sup> Ghosh, S.; Hogarth, G.; Hollingsworth, N.; Holt, K. B.; Kabir, S. E.; Sanchez, B. E.; *Chem. Commun.*, **2014**, 50, 945-947.
- <sup>41</sup> Ghosh, S.; Sanchez, B. E.; Richards, I.; Haque, M. N.; Holt, K. B.; Richmond,

- M. G.; Hogarth, G.; *J. Organomet Chem.*, **2016**, 812, 247-253.
- <sup>42</sup> Fisher, B. J.; Eisenberg, R.; *J. Am. Chem. Soc.*, **1980**, 102, 7361–736.
- <sup>43</sup> Hu, X.; Brunschwig, B. S.; Peters, J. C.; *J. Am. Chem. Soc.*, **2007**, 129, 8988–8998.
- <sup>44</sup> Stubbert, B. D.; Peters, J. C.; Gray, H. B.; *J. Am. Chem. Soc.*, **2011**, 133, 18070–18073.
- <sup>45</sup> Kellett, R. M.; Spiro, T. G.; *Inorg. Chem.*, **1985**, 24, 2373–2377.
- <sup>46</sup> Abdel-Hamid, R.; El-Sagher, H. M.; Abdel-Mawgoud, A.M.; Nafady, A.; *Polyhedron.*, **1998**, 17, 4535-4541.
- <sup>47</sup> Connolly, P.; Espenson, J. H.; *Inorg. Chem.*, **1986**, 25, 2684–2688.
- <sup>48</sup> Hu, X. ; Cossairt, B. M. ; Brunschwig, B. S. ; Lewis, N. S. ; Peters J. C. ; *Chem. Commun.*, **2005**, 4723-4725.
- <sup>49</sup> Kosuke, I.; in *Acid–Base Dissociation Constants in Dipolar Aprotic Solvents*, Oxford: Blackwell Scientific Publications, **1990**.
- <sup>50</sup> McCrory, C. C. L.; Uyeda, C.; Peters J. C.; *J. Am. Chem. Soc.*, **2012**, 134, 3164–3170.
- <sup>51</sup> Artero, V.; Fontecave, M.; *Coord. Chem. Rev.*, **2005**, 249, 1518–1535.
- <sup>52</sup> Helm, M. L.; Stewart, M. P.; Morris Bullock, R.; DuBois, M. R.; DuBois, D. L.; *Science*, **2011**, 333, 863-866.
- <sup>53</sup> Lakadamyali, F.; Kato, M.; Muresan, N. M.; Reisner, E.; *Angew. Chem. Int. Ed.*, **2012**, 51, 9381-9384.
- <sup>54</sup> Lakadamyali, F.; Reisner, R.; *Chem. Commun.*, **2011**, 47, 1695-1697.
- <sup>55</sup> Bauer, R.; Werner, H. A. F.; *Int. J. Hydrog. Energy*, **1994**, 19, 497-499.
- <sup>56</sup> Mondal, B.; Sengupta, K.; Rana, A.; Mahammed, A.; Botoshansky, M.; Dey, S. G.; Gross, Z.; Dey, A.; *Inorg. Chem.* **2013**, 52, 3381–3387.
- <sup>57</sup> Huynh, M. H. V.; Meyer, T. J.; *Chem Rev.*, **2007**, 107, 5044-5064.
- <sup>58</sup> Costentin, C.; *Chem. Rev.*, **2008**, 108, 2145-2179.
- <sup>59</sup> Mayer, J. M.; *Proton-Coupled Electron Transfer*, **2013**, 2112-2114.
- <sup>60</sup> Hammes-Schiffer, S.; Stuchebrukhov, A. A.; *Chem. Rev.*, **2010**, 110, 6939-6960.
- <sup>61</sup> Rakowski DuBois, M.; DuBois D. L.; *Chem. Soc. Rev.*, **2009**, 38, 62-72.
- <sup>62</sup> Rakowski DuBois, M.; DuBois, D. L.; *Comptes Rendus Chimie*, **2008**, 11, 805-817.
- <sup>63</sup> Moore, E. J.; Sullivan, J. M.; Norton, J. R.; *J. Am. Chem. Soc.*, **1986**, 108, 2257-2263.
- <sup>64</sup> Van der Vlugt, J. I.; Rauchfuss, T. B.; Whaley, C. M.; Wilson, S. R.; *J. Am. Chem. Soc.*, **2005**, 127, 16012-16013.
- <sup>65</sup> Berning, D. E.; Miedaner, A.; Curtis, C. J.; Noll, B. C.; Rakowski DuBois, M. C.; DuBois, D. L.; *Organometallics*, **2001**, 20, 1832-1839.

- <sup>66</sup> Curtis, C. J.; Miedaner, A.; Ellis, W. W.; DuBois, D. L.; *J. Am. Chem. Soc.*, **2002**, *124*, 1918-1925.
- <sup>67</sup> Frazee, K.; Wilson, A. D.; Appel, A. M.; Rakowski DuBois, M.; DuBois, D. L.; *Organometallics*, **2007**, *26*, 3918-3924.
- <sup>68</sup> Wilson, A. D.; Newell, R. H.; McNevin, M. J.; Muckerman, J. T.; Rakowski DuBois, M.; DuBois, D. L.; *J. Am. Chem. Soc.*, **2006**, *128*, 358-366.
- <sup>69</sup> Volbeda, A.; Fontecilla-Camps, J. C.; *J. Chem. Soc., Dalton Trans.*, **2003**, 4030-4038.
- <sup>70</sup> Nicolet, Y.; de Lacey, A. L.; Vernède, X.; Fernandez, V. M.; Hatchikian, E. C.; Fontecilla-Camps, J. C.; *J. Am. Chem. Soc.*, **2001**, *123*, 1596-1601.
- <sup>71</sup> Barton, B. E.; Olsen, M. T.; Rauchfuss, T. B.; *J. Am. Chem. Soc.*, **2008**, *130*, 16834-16838.
- <sup>72</sup> Curtis, C. J.; Miedaner, A.; Ciancanelli, R. F.; Ellis, W. W.; Noll, B. C.; DuBois, M. R.; DuBois, D. L. *Inorg. Chem.* **2003**, *42*, 216-227.
- <sup>73</sup> Berning, D. E.; Noll, B. C.; DuBois, D. L.; *J. Am. Chem. Soc.*, **1999**, *121*, 11432-11447.
- <sup>74</sup> Berning, D. E.; Miedaner, A.; Curtis, C. J.; Noll, B. C.; DuBois, M. R.; DuBois, D. L.; *Organometallics*, **2001**, *20*, 1832-1839.
- <sup>75</sup> Curtis, C. J.; Miedaner, A.; Ellis, W. W.; DuBois, D. L.; *J. Am. Chem. Soc.*, **2002**, *124*, 1918-1925.
- <sup>76</sup> Curtis, C. J.; Miedaner, A.; Ciancanelli, R.; Ellis, W. W.; Noll, B. C.; Rakowski DuBois, M.; DuBois, D. L.; *Inorg. Chem.*, **2003**, *42*, 216-227.
- <sup>77</sup> Kilgore, U. J.; Roberts, J. A. S.; Pool, D. H.; Appel, A. M.; Stewart, M. P.; Rakowski DuBois, M.; Dougherty, W. G.; Kassel, W. S.; Morris Bullock, R.; DuBois, D. L.; *J. Am. Chem. Soc.*, **2011**, *133*, 5861-5872.
- <sup>78</sup> Pool, D. H.; Stewart, M. P.; O'Hagan, M.; Shaw, W. J.; Roberts, J. A. S.; Morris Bullock, R.; DuBois, D. L.; *Pro. Natl. Acad. Sci USA*, **2012**, *109*, 15634-15639.
- <sup>79</sup> Helm, M. L.; Stewart, M. P.; Bullock, R. M.; Rakowski DuBois, M.; DuBois, D. L.; *Science*, **2011**, *333*, 863-866.
- <sup>80</sup> Shaw, W. J. ; Jain, A.; Lense, S.; Linehan, J. C.; Raugei, S.; Cho, H.; DuBois, D. L.; *Inorg. Chem.*, **2011**, *50*, 4073-4085.
- <sup>81</sup> Shaw, W. J. ; Jain, A. ; Reback, M. L.; Lindstrom, M. L.; Thogerson, C. E.; Helm, M. L.; Appel, A. M.; *Inorg. Chem.*, **2012**, *51*, 6592-6602.
- <sup>82</sup> Kilgore, U. J.; Roberts, J. A. S.; Pool, D. H.; Appel, A. M.; Stewart, M. P.; Rakowski DuBois, M.; Dougherty, W. G.; Kassel, W. S.; Bullock, R. M.; DuBois, D. L.; *J. Am. Chem. Soc.*, **2011**, *133*, 5861-5872.

- <sup>83</sup> DuBois, D. L.; Jacobsen, G. M.; Yang, J. Y.; Twamley, B.; Wilson, A. D.; Bullock, R. M.; Rakowski DuBois, M.; *Energy Environ. Sci.*, **2008**, 1, 167-174
- <sup>84</sup> DuBois, D. L.; Wiedner, E. S.; Yang, J. Y.; Dougherty, W. G.; Kassel, W. S.; Bullock, R. M.; Rakowski DuBois, M.; *Organometallics*, **2010**, 29, 5390-5401.
- <sup>85</sup> Nocera, D. G.; Lee, C. H.; Dogutan, D. K.; *J. Am. Chem. Soc.*, **2011**, 133, 8775-8777.
- <sup>86</sup> Artero, V.; Baffert, C.; Fontecave, M.; *Inorg. Chem.*, **2007**, 46, 1817-1824.
- <sup>87</sup> Urbach, F. L.; Sarneski, J. E.; Turner, L. J.; Busch, D. H.; *Inorg. Chem.*, **1968**, 7, 2169-2171.
- <sup>88</sup> Wentworth, R. A. D.; Felten, J. J.; *J. Am. Chem. Soc.*, **1968**, 90, 621-626.
- <sup>89</sup> Lions, F.; Martin, K. V.; *J. Am. Chem. Soc.*, **1957**, 79, 1572-1575.
- <sup>90</sup> Greener, B.; Cronin, L.; Wilson, G. D.; Walton, P. H.; *J. Chem. Soc., Dalton Trans.*, **1996**, 401-403.
- <sup>91</sup> Cronin, L.; Foxon, S.P.; Lusby, P.J.; Walton, P.; *J. Biol. Inorg. Chem.*, **2001**, 6, 367-377.
- <sup>92</sup> Greener, B.; Walton, P. H.; *J. Chem. Soc., Dalton Trans.*, **1997**, 3733-3740.
- <sup>93</sup> Cronin, L.; Foxon, S. P.; Lusby, P. J.; Walton, P. H.; *J. Biol. Inorg. Chem.*, **2001**, 6, 367-377.
- <sup>94</sup> Wass, D. F.; Ebrahimpour, P.; Haddow, M. F.; *Inorg. Chem.*, **2013**, 52, 3765-3771.
- <sup>95</sup> G. Seeber, Ph.D thesis, University of Birmingham, **2003**
- <sup>96</sup> Gajda, T.; Szorcsik, A.; Matyuska, F.; Bényei, A.; Nagy, N. V.; Szilágyi, R. K.; *Dalton Trans.*, **2016**, 45, 14998-15012.
- <sup>97</sup> Fielden, J.; Long, D.-L.; Evans, C.; Cronin, L.; *Eur. J. Inorg. Chem.*, **2006**, 2006, 3930-3935.
- <sup>98</sup> J. Fielden, PhD thesis, University of Glasgow, **2004**
- <sup>99</sup> Cronin, L.; Fielden, J.; Sprott, J.; *New J. Chem.*, **2005**, 29, 1152-1158.
- <sup>100</sup> Fielden, J.; Long, D.-L.; Cronin, L.; *Chem. Commun.*, **2004**, 2156-2163.
- <sup>101</sup> Seidel, W. W.; Arias, M. D. I.; Schaffrath, M.; Jahnke, M. C.; Hepp, A.; Pape, T.; *Inorg. Chem.* **2006**, 45, 4798-4792.
- <sup>102</sup> Cronin, L.; Kögerler, P.; Fielden, J.; Long, D.-L.; Speldrich, M., *Dalton Trans.*, **2012**, 41, 4927-4934.
- <sup>103</sup> Rauchfuss, T. B.; Barton, B. E.; Olsen, M. T.; *J. Am. Chem. Soc.*, **2008**, 130, 16834-13835.
- <sup>104</sup> Elchert, B.; Jie, L.; Wang, J.; Hui, Y.; Rai, R.; Ptak, R.; Ward, P.; Takemoto, J. Y.; Bensaci, M.; Chang, C-W. T., *J. Org. Chem.*, **2004**, 69, 1513-1523.
- <sup>105</sup> Carolyn R. Bertozzi, *J. Am. Chem. Soc.* **2005**, 127, 2686-2695.

- <sup>106</sup> DuBois, D. L. ; Rakowski DuBois, M. ; Wilson, A. D.; Newell, R. H.; McNevin, M. J.; Muckerman, J. T.; *J. Am. Chem. Soc.*, **2006**, *128*, 358–366.
- <sup>107</sup> Cook, J. M.; Zhou, H.; Liao, X.; *Org. Lett.*, **2004**, *6* , 249–252.
- <sup>108</sup> Furó, I.; *Journal of Molecular Liquids*, **2005**, *117*, 117-137.
- <sup>109</sup> Clayden, J. **2001**. Organic chemistry. Oxford: Oxford University Press. ISBN 0-19-850346-6.
- <sup>110</sup> O'Connor, D.; Lauria, A.; Bondi, S. P.; Saba, S.; *ChemInform*, **2011**, *52*, 129-132.
- <sup>111</sup> Karplus, M.; *J. Am. Chem. Soc.*, **1963**, *85*, 2870-2882.
- <sup>112</sup> Minch, M. J. **1994**. "Orientational Dependence of Vicinal Proton-Proton NMR Coupling Constants: The Karplus Relationship". *Concepts in Magnetic Resonance* *6*, 41-46.
- <sup>113</sup> Garcia de la Vega, J. M.; San Fabian, J.; Crespo-Otero, R.; Pérez, C.; Suardíaz, R.; Contreras, R. H.; *J. Chem. Theory Comput.*, **2008**, *4* (9), 1494–1500.
- <sup>114</sup> Winstein, S.; Carter, P.; Anet, F. A. L.; Bourn, A. J. R.; *J. Am. Chem. Soc.*, **1965**, *87*, 5247–5249.
- <sup>115</sup> Garbisch, E. W.; Griffith, M. G.; *J. Am. Chem. Soc.*, **1968**, *90*, 6543.
- <sup>116</sup> Baldwin, J. E.; Morgera, K. B.; James, S.; Hudson, B. S.; Allis, D. G.; O'Leary, D. J.; *J. Am. Chem. Soc.*, **2008**, *130*, 13659–13663.
- <sup>117</sup> Abraham, R. J.; Warne, M. A; Griffiths, L., *J. Chem. Soc., Perkin Trans.* , **1997**, *2*, 2151-2160.
- <sup>118</sup> Rissanen, K.; Valkonen, J.; Jäntti, A.; *Acta Chemica Scandinavica*, **1998**, *52*, 1010-1016.
- <sup>119</sup> Texas A&M University, Preparation of First-Row Transition Metal Acetonitrile Solvated Cations from the Aquo-Solvated Cations. **2010**. 1st ed. [ebook] Texas: The Dunbar Research Group, pp.2-3. Available at:  
<http://www.chem.tamu.edu/rgroup/dunbar/Syntheses%20of%20Common%20Starting%20Materials.pdf> [Accessed 12 Jan. 2017].
- <sup>120</sup> Curzon, E. H.; Herron, N.; Moore, P.; *J. Chem. Soc., Dalton Trans.*, **1980**, 574-578.
- <sup>121</sup> Steed, J. W.; Turner, D. R.; Hursthouse, M. B.; Light M. E.; *Chem. Commun.*, **2004**, 1354-1355.
- <sup>122</sup> Jahn, H. A.; Teller, E.; *Proc. R. Soc.A.*, **1937**, *161*, 220-235.
- <sup>123</sup> Hoskins, B.F.; *Coord. Chem. Rev.*, **1973**, *9* , 365–388.
- <sup>124</sup> Addison, A. W.; Rao, T. N.; Reedijk, J.; van Rijn, J.; Verschoor, G. C.; *J. Chem. Soc., Dalton Trans.*, **1984**, 1349 – 1355.
- <sup>125</sup> Cremades, E.; Echeverría, J.; Alvarez, S.; *Chem. Eur. J.*, **2010**, *16*, 10380-10396.

- <sup>126</sup> Wentworth, R. A. D.; Dahl, P. S.; Huffman, C. J.; Gillum, W. O.; Streib, W. E.; Huffman, J. C.; *Inorg. Chem.*, **1982**, *21*, 3060-3063.
- <sup>127</sup> Yousif, Y. Z.; *Polyhedron*, **1992**, *11*, 1411-1418.
- <sup>128</sup> Bertini, I.; Luchina, C.; Parigi, G. “*Solution NMR of Paramagnetic molecules*”; Elsevier: Amsterdam, **2001**, pp.1-376.
- <sup>129</sup> Banci, L.; Bertini, I.; Luchinat, C. “Nuclear and electron relaxation. The magnetic nucleus-unpaired electron coupling in solution”; VCH: Weinheim, **1991**, pp. 1-208.
- <sup>130</sup> Bertini, I.; Luchinat, C.; Parigi, G.; *Progr. NMR Spectrosc.* **2002**, *40*, 249-273.
- <sup>131</sup> Hrobark, P.; Reviakine, R.; Arbuzniyov, A. V.; Makina, O.L.; Malkin, V. G.; Koler, M.; *J. Chem. Phys.*, **2007**, *126*, 024107.
- <sup>132</sup> Kruck, M.; Sauer, D.C.; Ederd, M.; Wadepohl, H.; Gade, L. H.; *Dalton Trans.*, **2011**, *40*, 10406-10415.
- <sup>133</sup> Friebolin, H.; “*Basic One- and Two- Dimension NMR Spectroscopy*”, VCH: Weinheim, **2010**.
- <sup>134</sup> Drago, R. S.; “*Physical Methods in Inorganic Chemistry*”, Philadelphia: W.B. Saunders, **1977**.
- <sup>135</sup> Hausser, K. H.; Brunner, H.; “*Encyclopedia of Nuclear Magnetic Resonance*”; Eds. Grant, D.; Harris, R. K.; Chichester: Wile, **1996**, pp. 1864-1869.
- <sup>136</sup> La Mar, G. N.; W. DeW. Horrocks, Jr.; Holm, R. H.; (ed.); *NMR of Paramagnetic Molecules*, New York: Academic Press, **1973**.
- <sup>137</sup> Bertini, I.; Luccinat, C.; *Coord. Chem. Rev.*, **1996**, *150*, 1-20.
- <sup>138</sup> Kohler, F.H.; *Magnetism: Molecules to Materials*, ed. J. S. Miller, M. Drillon, Wiley-VCH, Weinheim, **2001**, p. 379–430.
- <sup>139</sup> Bertini, I.; Luchinat, C.; Parigi, G.; *Prog. Nucl. Magn. Reson. Spectrosc.*, **2002**, *40*, 249-253.
- <sup>140</sup> Bertini, I.; Luchinat, C.; Parigi, G.; Pierattelli, R.; *ChemBioChem*, **2005**, *6*, 1536-1546.
- <sup>141</sup> Rastrelli, F.; Bagno, A.; *Chem.–Eur. J.*, **2009**, *15*, 7990-7996.
- <sup>142</sup> Kaupp, M.; Kohler, F. H.; *Coord. Chem. Rev.*, **2009**, *253*, 2376-2380.
- <sup>143</sup> Kohler, F. H.; *Magnetism: Molecules to Materials*, ed. J. S. Miller, M. Drillon, Wiley-VCH: Weinheim, **2001**, p. 379–430.
- <sup>144</sup> Pennanen, T. O.; Vaara, J.; *Phys. Rev. Lett.*, **2008**, *100*, 133002-133032.
- <sup>145</sup> Mao, J.; Zhang, Y.; Oldfield, E.; *J. Am. Chem. Soc.*, **2002**, *124*, 13911-13923.
- <sup>146</sup> Knorr, R.; Hauer, H.; Weiss, A.; Polzer, H.; Ruf, F.; Löw, P.; Dvortsák, P.; Böhrer, P.; *Inorg. Chem.*, **2007**, *46*, 8379-8384.

- <sup>147</sup> Fernández, P.; Pritzkow, H.; Carbó, J.; Hofmann, P.; Enders, M.; *Organometallics*, **2007**, 26, 4402-4413.
- <sup>148</sup> Roquette, P.; Maronna, A.; Reinmuth, M.; Kaifer, E.; Enders M.; Himmel, H.-J.; *Inorg. Chem.*, **2011**, 50, 1942-1953.
- <sup>149</sup> Golding, R. M.; Stubbs, L. C.; *Magn. Reson. Chem.*, **1979**, 33, 627-647.
- <sup>150</sup> Ruiz-Morales, Y.; Schreckenbach, G.; Ziegler, T.; *Organometallics*, **1996**, 15, 3920-3923.
- <sup>151</sup> Dewar, M. J. S.; Hashmall, J. A.; Trinajstić, N.; *J. Am. Chem. Soc.*, **1970**, 92, 5555-5563.
- <sup>152</sup> Howell, J. O.; Goncalves, J. M.; Amatore, C.; Klasinc, L.; Wightman, R. M.; Kochi, J. K.; *J. Am. Chem. Soc.*, **1984**, 106, 3968.
- <sup>153</sup> A.C.Fisher, *Electrode dynamics-primer*, Oxford University Press, **1996**.
- <sup>154</sup> Brownson, D. A. C.; Banks, C. E.; “Interpreting Electrochemistry” in *The Handbook of Graphene Electrochemistry*. London: Springer London. **2014**.
- <sup>155</sup> Matsuda, H.; Ayabe, Y.; *Z. Electrochem.*, **1955**, 59, 494–503.
- <sup>156</sup> Zanello, P.; *Inorganic electrochemistry: theory, practise and applications*. RSC, **2003**.
- <sup>157</sup> Crow, D. R.; *Principles and Applications of Electrochemistry*, 4<sup>th</sup> Edition, Cheltenham: Taylor & Francis, **1994**.
- <sup>158</sup> Ananikov, V. P.; Piroyan, A. O.; Gaiduk, K. A.; Beletskaya, I. P.; Khrustalev, V. N.; Antipin, M. Y.; *Russ. J. Org. Chem.*, **2009**, 45, 1743-1754.
- <sup>159</sup> Piskunov, A. V.; Ershova, I. V.; Gulenova, M. V.; Pashanova, K. I.; Bogomyakov, A. S.; Smolyaninov, I. V.; Fukin, G. K.; Cherkasov, V. K.; *Russian Chemical Bulletin*, **2015**, 64, 642-649.
- <sup>160</sup> Neese, F.; Wieghardt, K.; Ray, K.; Petrenko, T.; *Dalton Trans.*, **2007**, 1552-1566.
- <sup>161</sup> Boillot, M.-L.; Floquet, S.; Simaan, A. J.; Rivière, E.; Nierlich, M.; Thuéry, P.; Ensling, J.; Gülich, P.; Girerd, J.-J.; *Dalton Trans.*, **2005**, 1734-1742.
- <sup>162</sup> Don, M.-J.; Yang, K.; Bott, S. G.; Richmond, M. G.; *Journal of Chemical Crystallography*, **1996**, 26, 335-340.
- <sup>163</sup> Boyer, J. L.; Cundari, T. R.; DeYonker, N. J.; Rauchfuss, T. B.; Wilson, S. R.; *Inorg. Chem.*, **2009**, 48, 638-645.
- <sup>164</sup> Wieghardt, K.; Bill, E.; Ghosh, P.; Weyhermüller, T.; *J. Am. Chem. Soc.*, **2003**, 125, 3967-3979.
- <sup>165</sup> Griffith, W. P.; *Transition Metal Chemistry*, **1993**, 18, 250–256.



- <sup>166</sup> Fedushkin, I. L.; Skatova, A. A.; Khvoinova, N. M.; Lukoyanov, A. N.; Fukin, G. K.; Ketkov, S. Yu.; Maslov, M. O.; Bogomyakov, A. S.; Makarov, V. M.; *Russian Chemical Bulletin*, **2013**, 62, 2122-2131.
- <sup>167</sup> Wieghardt, K.; Muresan, N.; Chlopek, K.; Weyhermüller, T.; Neese, F.; *Inorg. Chem.*, **2007**, 46, 5327-5337.
- <sup>168</sup> Wieghardt, K.; Lu, C. C.; Bill, E.; Weyhermüller, T.; Bothe, E.; *J. Am. Chem. Soc.*, **2008**, 130, 3181-3197.
- <sup>169</sup> Westerhausen, M.; Bollwein, T.; Makropoulos, N.; Schneiderbauer, S.; Suter, M.; Nöth, H.; Mayer, P.; Piotrowski, H.; Polborn, K.; Pfitzner, A.; *Eur. J. Inorg. Chem.*, **2002**, 389–404.
- <sup>170</sup> Bard, A. J.; *The Electrochemistry of Organic Compounds in Aprotic Solvents, Methods and Applications*, IUPAC, Department of Chemistry, University of Texas, **1971**, p. 385.
- <sup>171</sup> O'Reilly, I. E.; Elving, P. J.; *J. Am. Chem. Soc.*, **1972**, 94, 7941-7944.
- <sup>172</sup> Nadra, J.; Givadinovitch, H.; Devand, M.; *J. Chem. Res., Synop.*, **1983**, 192.
- <sup>173</sup> Toomey Jr., J. E.; *Advances in Heterocyclic Chemistry*, **1984**, 37, 167 – 215.
- <sup>174</sup> Andrieux, C. P.; Saveant, J. M.; *J. Electroanal. Chem.*, **1971**, 33, 453-461.
- <sup>175</sup> Bonou, L.; Eyraud, M.; Crousier, J.; *J. Appl. Electrochem.*, **1994**, 24, 906—910.
- <sup>176</sup> Darwent, B. B.; *National Standard Reference Data Series*, National Bureau of Standards, no. 31, Washington, **1970**.
- <sup>177</sup> Benson, S. W.; *J. Chem. Educ.*, **1965**, 42, 502.
- <sup>178</sup> Kerr, J. A.; *Chem. Rev.*, **1966**, 66, 465.
- <sup>179</sup> Wekesa, M.; Uddin, M. D. J.; Sobhi, H. F.; *Int. J. Chem. Res.*, **2011**, 2, 34-37.
- <sup>180</sup> Hoffmann, R.; Howell, J.M.; Rossi, A.R.; *J. Am. Chem. Soc.*, **1976**, 9, 98-102.
- <sup>181</sup> Dong, Y.; Shigematsu, T.; Kumamoto, T.; *Google Patents*, **2013**.
- <sup>182</sup> Zolezzi, S.; Spodine, E.; Decinti, A.; *Polyhedron*, **2002**, 21, 55-59.
- <sup>183</sup> Cotton, F. A.; Wilkinson, G.; *Advanced Inorganic Chemistry*, Wiley Interscience: New York, NY, USA, **1988**.
- <sup>184</sup> Krivokapic, I.; Zerara, M.; Daku, M. L.; Vargas, A.; Enachescu, C.; Ambrus, C.; Tregenna-Piggott, P.; Amstutz, N.; Krausz, E.; Hauser, A.; *Coord. Chem. Rev.*, **2007**, 251, 364-376.
- <sup>185</sup> Hendry, P.; Ludi, A.; *Adv. Inorg. Chem.*, **1990**, 35, 117-120.
- <sup>186</sup> Harding, P.; Harding, D. J.; Daengngern, R.; Thurakitsaree, T.; Schutte, B. M.; Shaw, M. J.; Tantirungrotechai, Y.; *Polyhedron*, **2012**, 42, 291-301.

- <sup>187</sup> Turner, J. W.; Schultz, F. A.; *Coord. Chem. Rev.*, **2001**, *81*, 219–221.
- <sup>188</sup> Buhks, E.; Dixon, M.; Jortner, J.; Navon, G.; *Inorg. Chem.*, **1979**, *18*, 2014–2017.
- <sup>189</sup> Endicott, J. F.; Brubaker, G. R.; Ramasami, T.; Kumar, K.; Dwarakanath, K.; Cassel, J.; Johnson, D.; *Inorg. Chem.*, **1983**, *22*, 3754.
- <sup>190</sup> Hammershøi, A.; Geselowitz, D.A.; Taube, H.; *Inorg. Chem.*, **1984**, *32*, 979–992.
- <sup>191</sup> Bernhardt, P.V.; Jones, L.A.; Sharpe, P.C.; *Inorg. Chem.*, **1997**, *36*, 2420–2432.
- <sup>192</sup> Anson, F. C.; Collins, T. J.; Coots, R. J.; Gipson, S. L.; Richmond, T. G.; *J. Am. Chem. Soc.*, **1984**, *106*, 5037–5038.
- <sup>193</sup> Koikawa, M.; Gotoh, M.; Ōkawa, H.; Kida, S.; Kohzuma, T.; *J. Chem. Soc., Dalton Trans.*, **1989**, 1613–1616.
- <sup>194</sup> Martin, D. J.; McCarthy, B. D.; Donley, C. L.; Dempsey, J. L.; *Chem. Commun.*, **2015**, *51*, 5290–5293.
- <sup>195</sup> De-alwis, D.C.L.; Schultz, F.A.; *Inorg. Chem.*, **2003**, *42*, 3616–3619.
- <sup>196</sup> Harding, P.; Harding, D.; Daengngern, R.; Thurakitsaree, T.; Schutte, B. M.; Shaw, M. J.; Tantirungrotechai, Y.; *Polyhedron*, **2012**, *42* (1), 291–301.
- <sup>197</sup> Hendry, P.; Ludi, A., *Adv. Inorg. Chem.*, **1990**, *35*, 117–198.
- <sup>198</sup> Zanello, P.; *Inorganic Electrochemistry: Theory, Practice, and Application*, 1st ed., Royal Society of Chemistry, **2003**.
- <sup>199</sup> Robin, M. B.; Day, P.; Emeleus, H.; Sharpe, A., Eds.; *Adv. Inorg. Chem.*, **1968**, *10*, 247 – 422.
- <sup>200</sup> Bard, A. J.; Faulkner, L. R.; *Electrochemical Methods: Fundamentals and Applications*, 2nd ed.; Hoboken, NJ: John Wiley & Sons, Inc., **2001**.
- <sup>201</sup> Costentin, C.; Savéant, J.-M.; *Chem. Electro. Chem.*, **2014**, *1*, 1226–1236.
- <sup>202</sup> Dempsey, J. L.; Rountree, E. S.; McCarthy, B. D.; Eisenhart, T. T.; *Inorg. Chem.*, **2014**, *53*, 9983–10002.
- <sup>203</sup> Appel, A. M.; Helm, M. L.; *ACS Catal.*, **2014**, *4*, 630–633.
- <sup>204</sup> Fourmond, V.; Jacques, P.-A.; Fontecave, M.; Artero, V.; *Inorg. Chem.*, **2010**, *49*, 10338–10347.
- <sup>205</sup> Roberts, J. A. S.; Bullock, R. M.; *Inorg. Chem.*, **2013**, *52*, 3823–3835.
- <sup>206</sup> Udugala-Ganehenegge, M. Y.; Dissanayake, N. M.; Liu, Y.; Bond, A. M.; Zhang, J.; *Transition Met. Chem.*, **2014**, *39*, 819–830.
- <sup>207</sup> Grice, K. A.; Kubiak, C. P.; *Adv. Inorg. Chem.*, **2014**, *66*, 163–188.
- <sup>208</sup> Kubiak, C. P.; Sampson, M. D.; *Inorg. Chem.*, **2015**, *54*, 6674–6676

- <sup>209</sup> Evans, D. H.; Felton, G. A. N.; Glass, R. S.; Lichtenberger, D. L.; *Inorg. Chem.*, **2006**, 45, 9181–9184.
- <sup>210</sup> Mayer, J. M.; *Annu. Rev. Phys. Chem.* **2004**, 55, 363–390.
- <sup>211</sup> Wasylenko, D; Ganesamoorthy, C; Borau-Garcia, J; Berlinguette, C.; *Chem. Commun.*, **2011**, 47, 4249–4251.
- <sup>212</sup> Singh, W; Mirmohades, M; J., R; White, T; Hammarström, L; Thapper, A; Lomoth, R; Ott, S.; *Chem. Commun.*, **2013**, 49, 8638-8640.
- <sup>213</sup> Massoud, S. S.; Broussard, K. T.; Mautner, F. A.; Vicente, R.; Saha, M. K.; Bernal, I.; *Inorg. Chim. Acta*, **2008**, 361, 123–131.
- <sup>214</sup> Wendelstorf, C.; Krämer, R.; *Angew. Chem. Int. Ed.*, **1997**, 36, 2791-2793.
- <sup>215</sup> Evans, D. H.; Felton, G. A. N.; Glass, R. S.; Lichtenberger, D. L.; *Inorg. Chem.*, **2006**, 45, 9181–9184.
- <sup>216</sup> Compton, R.G.; Foord, J.S.; Marken, F.; *Electroanalysis*, **2003**, 15, 1349-1363.
- <sup>217</sup> Luong, J.H.T.; Male, K.B.; Glennon, J.D.; *Analyst*, **2009**, 134, 1965-1979.
- <sup>218</sup> Wei, J. J.; Li, Ch. M.; Gao, X. H.; Hei, L. F.; Lvun, F. X.; *Appl. Surf. Sci.*, **2012**, 258, 6909-7244.
- <sup>219</sup> Fortunato, W.; Chiquito, A. J.; Galerani, J. C.; Moro, J. R., *J. Mater. Sci.*, **2007**, 42, 7331-7336.
- <sup>220</sup> Szunerits, S.; Jama, C.; Coffinier, Y.; Marcus, B.; Delabouglise, D.; Boukherroub, R.; *Electrochem. Commun.*, **2006**, 8, 1185-1190.
- <sup>221</sup> H. Martin, A. Argoitia, U. Landau, A. B. Anderson, and J. C. Angus. *J. Electrochem. Soc.*, **1996**, 143, 133-136.
- <sup>222</sup> Xu, J.; Granger, M. C.; Chen, Q.; Strojek, J. W.; Lister, T. E.; Swain, G. M.; *Analytical Chemistry*. **1997**, 69, 591-597.
- <sup>223</sup> Goeting, C. H.; Marken, F.; Gutierrez-Sosa, A.; Compton, R. G.; Foord, J. S.; *Diam. Relat. Mater.*, **2000**, 9, 390-396.
- <sup>224</sup> Girard, H.; Simon, N.; Ballutaud, D.; Herlem, M.; Etcheberry, A.; *Diam. Relat. Mater.*, **2007**, 16, 316-325.
- <sup>225</sup> Swain, G. M.; Ramesham, R.; *Anal. Chem.*, **1993**, 65, 345-351.
- <sup>226</sup> Luong, J.H.T.; Male, K.B.; Glennon, J.D.; *Analyst*, **2009**, 134, 1965-1979.
- <sup>227</sup> Xu, J.; Granger, M. C.; Chen, Q.; Strojek, J. W.; Lister, T. E.; Swain, G. M.; *Analytical Chemistry*. **1997**, 69, 591-597.
- <sup>228</sup> Wang, J.; Swain, G.M.; Mermoux, M.; Lucazeau, G.; Zak, J.; Strojek, J.W.; *New Diamond Front. Carbon Technol.* **1999**, 9, 317-321.

- <sup>229</sup> Xu, J.; Chen, Q.; Swain, G.M.; *Anal. Chem.*, **1998**, 70, 3146-3154.
- <sup>230</sup> Granger, M.C.; Swain, G.M.; *J. Electrochem. Soc.*, **1999**, 146, 4551-4558.
- <sup>231</sup> Salazar-Banda, G. R.; Andrade, L. S.; Nascente, P. A. P.; Pizani, P. S.; Rocha-Filho, R. C.; Avaca, L. A.; *Electrochim. Acta.*, **2006**, 51, 4612-4619.
- <sup>233</sup> Notsu, H.; Yagi, I.; Tatsuma, T.; Tryk, D. A.; Fujishima, A.; *Electrochem. Solid-State Lett.*, **1999**, 2, 5220-5224.
- <sup>234</sup> Notsu, H.; Yagi, I.; Tatsuma, T.; Tryk, D. A.; Fujishima, A.; *J. Electroanal. Chem.*, **2000**, 492, 31-37.
- <sup>235</sup> Notsu, H.; Fukazawa, T.; Tatsuma, T.; Tryk, D. A.; Fujishima, A.; *Electrochem. Solid-State Lett.*, **2001**, 4, 1-3.
- <sup>236</sup> Ferro, S.; De Battisti, A.; *J. Electroanal. Chem.*, **2002**, 533, 177-185.
- <sup>237</sup> Chaplin, B. P.; Hubler, D. K.; Farrell, J.; *Electrochim. Acta*, **2013**, 89, 122 -131.
- <sup>238</sup> Suffredini, H. B.; Pedrosa, V. A.; Codognoto, L.; Machado, S. A. S.; Rocha-Filho, R. C.; Avaca, L. A.; *Electrochim. Acta.*, **2004**, 49, 4021-4026.
- <sup>239</sup> Bachmann, P. K.; Eberhardt, W.; Kessler, B.; Lade, H.; Radermacher, K.; Wiecher, D. U.; Wilson, H.; *Diam. Relat. Mater.*, **1996**, 5, 1378-1383.
- <sup>240</sup> Kiran, R.; Scorsone, E.; de Sanoit, J.; Arnault, J.-C.; Mailley, P.; Bergonzo, P.; *J. Electrochem. Soc.*, **2013**, 160, 67-73.
- <sup>241</sup> Salazar-Banda, G. R.; de Carvalho, A. E.; Andrade, L. S.; Rocha-Filho, R. C.; Avaca, L. A.; *J. Appl. Electrochem.*, **2010**, 40, 1817–1827.
- <sup>242</sup> Stolarczyk, K.; Nazaruk, E.; Rogalski, J.; Bilewicz, R. *Electro. Communications*, **2007**, 9, 115-118.
- <sup>243</sup> Wasylenko, D; Ganesamoorthy, C; Borau-Garcia, J; Berlinguette, C.; *Chem. Commun.*, **2011**, 47, 4249–4251.
- <sup>245</sup> Singh, W; Mirmohades, M; Jane, R; White, T; Hammarström, L; Thapper, A; Lomoth, R; Ott, S.; *Chem. Commun.*, **2013**, 49, 8638-8640.
- <sup>246</sup> V.; Baffert, C.; Fontecave, M.; *Inorg. Chem.*, **2007**, 46, 1817–1824.
- <sup>247</sup> Marcus, R. A.; *J. Chem. Phys.*, **1956**, 24, 966-978.
- <sup>248</sup> Da Cunha, M. C. P. M.; De Souza, J. P. I.; Nart, F. C.; *Langmuir*, **2000**, 16, 771–777.
- <sup>249</sup> Koper, M. T. M.; Shen, J.; Birdja, Y. Y.; *Langmuir*, **2015**, 31, 8495–8501.
- <sup>250</sup> West, R.; *J. Chem. Educ.*, **1965**, 42, 386.
- <sup>251</sup> Pickett, C. J; Ryder, K S.; Talarmin, J.; *J. Chem. Soc., Dalton Trans.*, **1986**, 0, 1453-1457.

- <sup>252</sup> Krishnan, V.; Muthukumaran, A.; Udupa, H. V. K.; *J. Appl. Electrochem.*, **1979**, *9*, 657–659.
- <sup>253</sup> Frisch, M. J.; Trucks, G. W.; Schlegel, H. B.; et al.; Gaussian 09, Revision B.01 *Gaussian 09, Revision B.01, Gaussian, Inc., Wallingford CT*. **2009**.
- <sup>254</sup> Ho, J.; Ertem, M. Z.; *J. Phys. Chem. B*, **2016**, *120*, 1319–1329.
- <sup>254</sup> Stolarczyk, K.; Nazaruk, E.; Rogalski, J.; Bilewicz, R.; *Electrochem. Commun.*, **2007**, *9*, 115 – 118.
- <sup>255</sup> Hay, P.J.; Wadht, W.R., *J.Chem. Phys.*, **1985**, *1*, 270-283.
- <sup>256</sup> Adamo, C.; Barone, V., *J.Chem. Phys.*, **1999**, *110*, 6158-6170.